

Photoresponse of Molecular Tunnel Junctions: Converting Photons to Charge Carriers and Probing Internal Energy Levels

by

Jerry Alfred Fereiro

A thesis submitted in partial fulfillment of the requirements for the degree of

Doctor of Philosophy

Department of Chemistry  
University of Alberta

© Jerry Alfred Fereiro, 2015

# Abstract

Molecular electronics seeks to build circuitry using organic components with at least one dimension in the nanoscale domain. Progress in the field has been inhibited by the difficulty in determining the energy levels of molecules after being perturbed by interactions with the conducting contacts. We show the conductance of seven different aromatic molecules covalently bonded to carbon implies a modest range ( $<0.5$  eV) in the observed transport barrier despite widely different free molecule HOMO energies ( $>2.0$  eV range). Upon bonding, electronic inductive effects modulate the energy levels of the system, resulting in compression of the tunneling barrier. Modification of the molecule with electron donating or withdrawing groups modulate both the molecular orbital energies and the contact energy level, resulting in a levelling effect which compresses the tunneling barrier into a range much smaller than expected. While the value of the tunneling barrier can be varied by using a different class of molecules (alkanes), using only aromatic structures results in a similar equilibrium value for the tunnel barrier for different structures resulting from partial charge transfer between the molecular layer and the substrate. Thus, the system does not obey the Schottky-Mott limit, and the interaction between the molecular layer and the substrate acts to influence the energy level alignment. These results indicate that the entire system must be considered to understand the impact of a variety of electronic factors that act to determine the tunnel barrier.

The photocurrent spectra for large-area aliphatic and aromatic molecular tunnel junctions with partially transparent copper top contacts have been measured. The effect of variation of the molecular structure and thickness are discussed. Internal photoemission (IPE), a process

involving optical excitation of hot carriers in the contacts followed by transport across internal system barriers, is dominant when the molecular component does not absorb light. The IPE spectrum contains information regarding energy level alignment within a complete, working molecular junction, with the photocurrent sign indicating transport through either the occupied or unoccupied molecular orbitals. At photon energies where the molecular layer absorbs, a secondary phenomenon is operative in addition to IPE. In order to distinguish IPE from this secondary mechanism, the effect of the source intensity as well as the thickness of the molecular layer on the observed photocurrent has been shown. Our results clearly show that the IPE mechanism can be differentiated from the secondary mechanism by the effects of variation of experimental parameters. IPE may provide valuable information regarding interfacial energetics in intact, working molecular junctions, as long as the secondary mechanism is avoided.

# Preface

This thesis is based on the research I have done at University of Alberta between January 2010 and April 2015. The nature and extent of my contribution to the work that has been included in the thesis are briefly summarized below.

Chapter 2 of this thesis has been published as Sayed Y. Sayed\*, Jerry A. Fereiro\*, Haijun Yan, Richard L. McCreery, Adam J. Bergren. “Charge transport in molecular electronic junctions: Compression of the molecular tunnel barrier in the strong coupling regime”. *Proceedings to National Academy of Science (PNAS-USA)*. 2012, vol. 109, No.29, 11498-11503. It’s an equally contributed first author paper where I was responsible for the data collection and spectral and further data analysis. Dr. Sayed. Y. Sayed, Dr. Haijun Yan, Dr. Adam J. Bergren assisted in the experiments. Dr. Richard L. McCreery, Adam J. Bergren and Dr Sayed Y. Sayed were involved in the planning stage of the project and also contributed to the manuscript edits. Professor Richard L. McCreery and Dr. Adam J. Bergren were the supervisory authors and were involved in the concept formation, data analysis, and manuscript composition.

Chapter 3 of this thesis has been published in *JACS* as Jerry A. Fereiro, Richard L. McCreery and Adam J. Bergren, “Direct optical determination of interfacial transport barriers in molecular tunnel junctions” *Journal of American Chemical Society (JACS)*. 2013, vol. 135, No.26, 9584-9587. I was responsible for the data collection, spectral and further data analysis and wrote the first draft of the manuscript. Dr Adam J. Bergren and Professor Richard L. McCreery provided assistance in the experiments and were involved in the manuscript composition. Professor Richard L. McCreery and Dr. Adam J. Bergren were the supervisory authors and were involved in the concept formation, data analysis, and manuscript composition.

Chapter 4 of this thesis has been published in *JACS* as Jerry A. Fereiro, Mykola Kondratenko, Richard L. McCreery and Adam J. Bergren Thomas, “Internal Photoemission in molecular junctions: Parameters for interfacial barrier determination” *Journal of American Chemical Society (JACS)*. 2015, vol. 137, No.3, 1296-1304. I was responsible for the data collection, spectral and further data analysis and wrote the initial draft of the manuscript. Dr Mykola Kondratenko helped in fabricating NDI and Ferrocene samples. Dr Adam J. Bergren and Professor Richard L. McCreery provided assistance in the experiments and were involved in the manuscript composition. Professor Richard L. McCreery and Dr. Adam J. Bergren were the supervisory authors and were involved in the concept formation, data analysis, and manuscript composition.

To my parents

Father, *Joseph Alfred Fereiro*

Mother, *Philomina Alfred*

for their continuous support, encouragement, and endless love  
throughout my life.

# Acknowledgements

Working as a graduate student in University of Alberta was a wonderful and challenging experience to me. In the University I met some people who were instrumental directly or indirectly in shaping up my academic career. It would have been impossible for me to success in my doctoral work without the precious support of these personalities.

First and foremost, I like to thank my parents for their affection and continuous support. I thank them for giving me full freedom to make my own decision, and giving me the strength and support to chase my dreams. My little brother also deserves wholehearted thanks as well.

I would like to sincerely thank my supervisor, Prof. Richard L. McCreery for his guidance and support throughout this programme, especially for the confidence he had in me. It was only due to his valuable guidance, and ever friendly nature that I was able to complete my research work in a respectable manner. I am very grateful to Dr. Adam J. Bergren for inspiring me to become an independent researcher and helped me to realize the power of critical thinking. I was able to interact with him on routine basis, which helped me to learn many basic things.

My sincere thanks must also go to the members of my thesis advisory and exam committee: Professors McDermott, Mark Freeman, Nils Petersen and John Veinot. They generously gave their time to offer me valuable comments toward improving my work. I would like to specially thank my mentor, Jerly sir in a special way; I express my heartfelt gratefulness to him for introducing me to the world of chemistry. I express my sincere thanks to all the present and past members of our group namely Bryan Szeto, Dr. Rajesh Pillai, Dr. Sayed Y Sayed, Dr. Haijun Yan, Dr. Rajesh Kumar, Dr. Mykola Kondratenko, Ahktar Bhayat, Dr. Amar Mahmoud &

Xiangyu Chen who have provided a diverse and friendly environment that has not only shaped me as a good researcher but also as a good person. I like to thank Matthew Schneider for editing my thesis.

Amazingly, I managed to meet some people outside of the department, and it turns out that many of them have been among my most critical and constant supporters. I would not be the same person without the friendships of Dr. Praveen V.K, Dr. Dinesh Nair, Dr. Javix Thomas, Dr. Swaroop Sasidharanpillai, Dr. Yogesh Godwal, Dr. Mahesh Kate and Krishna Ramachandran.

I would also remember the beautiful friends that I met from Chemistry Graduate Student Society and ABCampus, who sincerely helped me to improve my leadership skills and all the events that we organized together. To my family here in Edmonton-“Edmonton Super team” & “11323 University Ave” thank you all for your understanding and encouragement in my many moments of crisis. Your friendship makes my life a wonderful experience, I cannot list all the names here, but you are always on my mind.

Thank you, Lord, for always being there for me.

# TABLE OF CONTENTS

<b>Chapter 1: Introduction</b>	<b>Pages</b>
1.1 Molecular electronics.....	01
1.2 Components of a molecular junction.....	03
1.2.1 Self-Assembled monolayers.....	04
1.2.2 Langmuir-Blodgett films.....	05
1.2.3 Covalently bonded molecules on carbon and silicon.....	06
1.3 Electron transport in molecular junctions.....	08
1.3.1 Tunnelling mechanism.....	08
1.3.2 Hopping mechanism.....	10
1.4 Metal Organic Interfaces.....	12
1.5 Work function.....	14
1.5.1 Work function measurement techniques.....	15
1.5.1.1 Measuring work function using UPS.....	16
1.5.1.2 Measuring work function using KP .....	17
1.6 Vacuum level.....	18
1.7 Gap states.....	20
1.7.1 Interface free of gap states (Schottky-Mott model).....	21
1.7.2 Interface dominated by gap states.....	22
1.8 Investigation methods.....	23
1.8.1 Photoelectron spectroscopy.....	23
1.8.2 Inverse photoelectron spectroscopy.....	27

1.8.3 Other spectroscopic investigation methods.....	28
1.9 Research objectives.....	30
1.10 References.....	31

**Chapter 2: Charge transport in molecular electronic junctions: compression of the molecular tunnel barrier in the strong coupling regime**

2.1 Introduction.....	42
2.2 Junction fabrication and electrical characterization.....	44
2.2.1 Junction fabrication.....	44
2.2.2 Molecular structures used in this study.....	47
2.2.3 Conditions for film growth.....	47
2.2.4 Electrical characterization.....	49
2.3 AFM and UPS measurements.....	52
2.3.1 AFM measurements.....	52
2.3.2 UPS measurements.....	54
2.4 Experimental results and discussion.....	56
2.5 Statistical Analysis.....	68
2.6 Conclusions.....	72
2.7 References.....	73

**Chapter 3: Direct optical determination of interfacial transport barriers in molecular tunnel junctions**

3.1 Introduction.....	80
3.1.1 Internal photoemission (IPE) Vs. External photoemission.....	82

3.1.2	Fowler theory.....	86
3.1.2.1	Determination of barrier height using the Fowler method.....	87
3.2	Junction fabrication and electrical characterization.....	90
3.2.1	Junction fabrication.....	90
3.2.2	Molecular structures used in this study.....	92
3.2.3	Electrical characterization.....	92
3.3	AFM and UPS measurements.....	93
3.3.1	AFM measurements.....	93
3.3.2	UPS measurements.....	93
3.4	Experimental apparatus.....	94
3.4.1	Laser experimental apparatus.....	94
3.4.2	Lock-In amplifier experimental apparatus.....	95
3.5	Calibration of experimental apparatus.....	96
3.5.1	Oscilloscope calibration apparatus.....	98
3.5.2	Phase calibration using photodiode.....	99
3.5.3	Dependence of phase & photocurrent on chopper frequency.....	100
3.5.4	Assigning photocurrent sign for molecular junctions.....	101
3.5.5	Verification of phase using laser experiment.....	102
3.5.6	Analysis of bolometric mechanism.....	104
3.6	Conversion of photocurrent to yield.....	105
3.7	Background correction and noise level.....	106
3.8	Thin film optical property calculation.....	107
3.9	UV-Vis absorption spectra of chemisorbed molecules.....	111

3.9.1 Method for determining the absorption spectra of molecular layers on PPF .....	111
3.9.2 Optical absorption spectra of different molecules used in the study.....	113
3.9.3 Yield vs. Energy photocurrent spectrum.....	114
3.10 Conclusion.....	116
3.11 References.....	116

**Chapter 4: Internal photoemission in molecular junctions: parameters for interfacial barrier determinations**

4.1 Introduction.....	121
4.1.1 Optical absorption spectra for different molecules.....	122
4.1.2 Structure and absorption spectra for NDI and ferrocene molecular layers.....	123
4.2 Experimental section.....	123
4.3 Results and discussion.....	126
4.3.1 Photocurrent yield spectrum for alkane and BrP junctions.....	128
4.3.2 Fowler plots for alkane and BrP junctions.....	129
4.3.3 Alumina junctions.....	131
4.4 Proposed mechanism for alkane and BrP Junctions.....	133
4.5 Differentiating IPE from other photocurrent generating mechanisms.....	137
4.5.1 Relationship between absorption spectrum and photocurrent spectrum.....	137
4.5.2 Overlay of photocurrent yield, absorption vs. energy spectrum.....	138
4.5.3 Photocurrent vs. excitation intensity.....	141
4.5.4 NDI and Ferrocene molecular junctions.....	146
4.5.5 Thickness test.....	148

4.5.6 Fowler plots.....	151
4.6 Proposed mechanism for ferrocene and NDI.....	155
4.7 Conclusion.....	157
4.8 References.....	158

**Chapter 5: Photoresponse of Aromatic molecules in molecular tunnel junctions: converting photons to charge carriers**

5.1 Introduction.....	162
5.2 Single layer organic photovoltaic devices compared to carbon molecular junctions.....	163
5.3 Experimental section.....	166
5.4 Results and discussion.....	166
5.4.1 IPE to molecular absorption (MA) mechanism.....	167
5.5 Proposed model.....	171
5.6 Thickness dependence.....	174
5.7 Changing the top contact.....	177
5.7.1 Comparison of photocurrent spectrum with carbon and copper top contact.....	179
5.7.2 Varying the thickness of carbon top contact.....	180
5.7.3 Thickness study on BTB molecules using carbon top contacts.....	181
5.8 Conclusion.....	183
5.9 Future work.....	184
5.10 References.....	188
<b>Bibliography.....</b>	<b>192</b>

## LIST OF TABLES

Table 2.1: Calculated HOMO energies for the free, gas phase molecule (Gaussian, B3LYP-631G (d)). $\phi_{+est} = E_f - E_{HOMO}$ , and $\phi_{-est} = E_{LUMO} - E_f$ . NP = nitrophenyl, AQ = anthraquinone, NAB = nitroazobenzene, BrB = Bromophenyl, EB = Ethynylbenzene, AB = azobenzene, and BTB=bisthienylbenzene.....	57
Table 2.2: Values of apparent work function, work function shift, the onset of the molecular HOMO energy measured using UPS, and the barrier obtained from fitting the data to a modified form of the Simmons tunneling model.....	64
Table 2.3: Summary of the number of points in the attenuation plot for each molecule, the average value of ' $\beta$ ', and the resulting standard deviation in ' $\beta$ ' calculated using eqn 2.2.....	70
Table 2.4: Calculated values for $\sigma$ pooled.....	70
Table 2.5: Student's t-values for comparison of ' $\beta$ ' values for different molecules. Those that are greater than $t_{95\%}$ are highlighted.....	71
Table 2.6: Summary of the number of junctions made for each molecule.....	71
Table 2.7: Measured values of ' $\beta$ ' for each molecule and the uncertainty due to the standard deviation of the molecular layer thickness measurements.....	72
Table 3.1: Summary of the different type of molecules used, and their measured thickness and standard deviation data from the AFM measurements.....	93
Table 3.2: Different molecules used for UV-Vis solution absorption studies and their concentration used for this study.....	114
Table 4.1: Summary of optical absorption data for molecular layers.....	140
Table 4.2: $R^2$ correlation coefficient for both I photo vs. incident power and the (I photo) <sup>2</sup> vs. incident power for all the molecules used in this study at different energies.....	148
Table 4.3: Summary of barrier heights obtained using three different methods.....	152
Table 4.4: Fowler intercepts for each molecule along with their errors.....	154

## LIST OF FIGURES

Figure 1.1: Schematic of the components of a generic molecular electronic junction.....	03
Figure 1.2: Comparison of surface bonding properties of several substrate/molecules systems commonly used in molecular electronics.....	04
Figure 1.3: Schematic illustration of the preparation of Langmuir-Blodgett films.....	06
Figure 1.4: Schematic energy levels for a tunnel junctions (A) normal (B) under bias. $M_1$ and $M_2$ refer to metallic contacts, with the shaded area indicating filled electronic states, $\phi_e$ and $\phi_h$ indicates the electron and the hole-injection barriers.....	08
Figure 1.5: Schematic energy levels diagram for diffusive tunneling. ' $\alpha$ ' is the potential well depth of N sites spaced apart by a distance "a".....	10
Figure 1.6: Schematic representation of energetic models of electron migration through DNA system.....	11
Figure 1.7: Energy diagram of an interface between a molecular film and a metal surface.....	13
Figure 1.8: Schematic energy diagram of a metal, showing the work function.....	15
Figure 1.9: UPS of gold surface.....	17
Figure 1.10: Vacuum level close to the surface ( $E_{vac}(s)$ ) and vacuum level at infinity ( $E_{vac}(\alpha)$ ).....	18
Figure 1.11: (A) Electron and dipole layer with a representative extension L with the distance x between them (B) The potential energy of the electron by the dipole layer.....	19
Figure 1.12: Electronic structure of a typical (organic) semiconductor-metal interface, showing relevant energy levels on both sides, the electron affinity (EA) and ionization energy (IE) of the semiconductor, the interface dipole $\Delta$ , the interface density of gap states and charge neutrality level ECNL, and the electron and the hole injection barriers.....	20
Figure 1.13: Principle of UPS study of an organic/metal interface. a) Photoemission from the metal. b) Photoemission from the organic layer deposited on the metal surface.....	25
Figure 1.14: Shows the UPS spectra of metal and organic material with the energy of an emitted electron with an arbitrary origin as the abscissa.....	26

Figure 1.15: Schematic of photoemission spectroscopy (PES) process on metallic sample. Picture adapted from Rudy Schalf tutorial lesson.....	27
Figure 1.16: Schematic of IPES in “Isochromat” mode. Electrons with particular kinetic energy are emitted from the electron gun. At the sample surface they recombine into empty states above the Fermi level and photons are emitted. A detector with a narrow(0.6eV) fixed energy window (10eV) counts emitted photons. Variation of the electron kinetic energy allows to scan through the unoccupied states, resulting in IPES spectrum.....	28
Figure 1.17: Schematic illustration of possibilities in two photon photoemission involving (A) unoccupied states below the vacuum level (B) and an occupied state below the Fermi level. ....	29
Figure 2.1: Flow chart for fabrication of carbon based molecular junction.....	46
Figure 2.2: Molecular structures used in this study. NP = Nitrophenyl, AQ = Anthraquinone, NAB = Nitroazobenzene, BrP = Bromophenyl, EB = Ethynylbenzene, AB = Azobenzene, and BTB = Bisthiénylbenzene.....	47
Figure 2.3: Cyclic voltammograms of (1AQ, BTB, 2AQ, AB) diazonium ions on carbon (PPF) in 0.1M TBABF <sub>4</sub> in acetonitrile. Single scan was used for all the molecules with a scan rate of 200mV/s.....	48
Figure 2.4: Cyclic voltammograms of 2AQ (4scans) (a), AB (10 scans) (b) diazonium ions on carbon (PPF) in 0.1M TBABF <sub>4</sub> in acetonitrile. The largest voltammetric current was observed on the first scan, and then decreased with successive scans.....	49
Figure 2.5: Wiring schematics for four-wire measurements of current-voltage ( <i>i-V</i> ) behavior of molecular junctions. <i>V</i> refers to the bias voltage from a digital-to-analog converter, and ADC1 stands for the analog-to-digital channel for current. ADC0 monitors the voltage and has a differential input in the case of a four-wire arrangement. <i>D</i> and <i>S</i> denote drive and sense, respectively; <i>S</i> leads correspond to high-impedance voltage monitors.....	50
Figure 2.6: $\ln J-V$ curves for 1AQ (a), BTB (b), 2AQ (c), BrP (d), AB (e) and NAB (f) as a function of thickness. Error bars for $\ln J (\pm \sigma)$ are included, but are smaller than the width of the lines for all molecules except BrP.....	51
Figure 2.7: J-V curves for 1AQ (a), BTB (b), 2AQ (c), BrP (d), as a function of thickness. Error bars for $J (\pm \sigma)$ are included, except for BTB.....	52
Figure 2.8: AFM image of a trench made in a molecular layer of NP on PPF.....	53
Figure 2.9: Fitting of the data generated as a histogram from the AFM data .....	54

Figure 2.10: (A) Close-up of the HBEC region for unmodified PPF and four samples modified with different molecular structures.....	54
Figure 2.11: UPS spectra used for the determination of $E_{\text{HOMO, onset}}$ values for different molecules: AB, EB, BrP, 1-AQ, 2-AQ, NP and BTB.....	55
Figure 2.12: (A) Schematic of a carbon/molecule/Cu molecular junction with a multilayer of azobenzene sandwiched between carbon and Cu. (B) Corresponding energy level diagram showing the Fermi level of the contacts offset from the molecular energy levels, where the closest occupied level (in this case the HOMO) represents a barrier for hole tunneling ( $\phi$ ). Filled orbitals in the contacts are indicated by shading. A parallel situation can be drawn for electron tunneling through a barrier determined by the LUMO.....	56
Figure 2.13: Representative examples of $J$ - $V$ curves on a semi-logarithmic scale for two molecules, NP (A) and EB (B). (C) The corresponding attenuation plots show conductance values at 0.1 V, Junction area = 0.0013 cm <sup>2</sup> .....	59
Figure 2.14: (A) Overlay of attenuation plots for eight different molecules constructed from $J$ - $V$ curves with different thicknesses of each structure. The lines are least squares regression lines for aliphatic ( $\beta = 8.7 \text{ nm}^{-1}$ ) and all aromatic ( $2.7 \text{ nm}^{-1}$ ) molecules. ‘ $\beta$ ’ determined by least squares for each aromatic molecule are listed in table 2.1.....	61
Figure 2.15: Energy level diagram showing the vacuum level shift induced by the molecular dipole for the molecules.....	63
Figure 2.16: UPS spectra in the HBEC region for NAB on three different metals.....	65
Figure 2.17: (A) Energy levels before bonding the molecules to the carbon substrate, where the hole transport barrier is defined by the Schottky-Mott rule ( $\phi_{\text{SM}}$ ), and spans a 2.3 eV range. (B) $E_{\text{HOMO, onset}}$ energy, measured using UPS for molecules bonded to PPF. The numbers next to each molecule are the estimated tunneling barriers based on the indicated orbital energies.....	67
Figure 3.1: Energy level diagram showing a non-resonant tunnel barrier for holes (HOMO-mediated transport) and electrons (LUMO-mediated transport).....	82
Figure 3.2: Light of different energy (wavelength), incident on the surface of the metal (potassium, work function $\phi_{\text{work}} = 2\text{eV}$ ). Only photons of energy greater than the work function of the metal eject electrons from surface of metal.....	83
Figure 3.3: Plot of Kinetic energy of the ejected electrons vs. the frequency of the incident photons.....	84
Figure 3.4: Idealized cartoon representation of potassium metal (energy level) showing external photoemission (photoelectric effect).....	84
Figure 3.5: Idealized cartoon representation of energy level diagram showing internal photoemission (IPE) process, where $\phi_{\text{barr}}$ denotes the interfacial barrier height.....	85

Figure 3.6: (A) Idealized energy level alignment diagram of Al/Al <sub>2</sub> O <sub>3</sub> /Al sandwich structure. (B) Fowler intercept for the Al/Al <sub>2</sub> O <sub>3</sub> junction.....	87
Figure 3.7: (A) Experimental apparatus used for Al/Al <sub>2</sub> O <sub>3</sub> junction by Goodman and co-workers. (B) Energy level diagram for the Al/Al <sub>2</sub> O <sub>3</sub> junction.....	88
Figure 3.8: (A) Experimental apparatus used for Al/Al <sub>2</sub> O <sub>3</sub> junction by Goodman and co-workers showing the direction of flow of electrons at low energy (B) direction of flow of electrons at high energy.....	88
Figure 3.9: (A) Photocurrent yield spectrum reported for Al/Al <sub>2</sub> O <sub>3</sub> junction (B) Fowler plot obtained from the positive regime of the photocurrent spectrum (C) Fowler plot obtained from negative regime of the photocurrent spectrum.....	89
Figure 3.10: Idealized Energy level representation of Al/Al <sub>2</sub> O <sub>3</sub> junction with barrier values obtained from Fowler plot.....	90
Figure 3.11: (A) Schematic of molecular attachment through diazonium reduction, where aryl radical formation is through one-electron electrochemical reduction. (B) Schematic of molecular attachment through oxidation of a primary amine, where radical formation is through one-electron electrochemical oxidation.....	91
Figure 3.12: The structures of all the molecules used in this study. (A) NDI; (B) Anthraquinone; (C) Azobenzene; (D) Ferrocene; (E) Bromophenyl; (F) Nitroazobenzene; (G) Alkane (C <sub>12</sub> H <sub>25</sub> N). In most cases, molecular layers were multilayers of several molecules.....	92
Figure 3.13: (A) J-V curves for a series of BrP and C12 junctions with two different Y axis scales. Error bars represent one standard deviation of current density for four junctions on one sample.....	92
Figure 3.14: UPS measurement of the HOMO onset energy for C12 on PPF.....	94
Figure 3.15: Experimental apparatus for DC laser illumination and photocurrent measurement.....	94
Figure 3.16: Apparatus with Xe arc continuum source, modulation by an optical chopper and detection with Lock-In -Amplifier (LIA).....	96
Figure 3.17: Direct DC measurement of photocurrent for a BrP junction using 458nm laser illumination. Positive photocurrent corresponds to electrons flowing from the Cu to PPF electrode in the external circuit.....	97
Figure 3.18: Apparatus with Xe arc continuum source, modulation by an optical chopper and calibration using an Oscilloscope.....	98

Figure 3.19: (A) Photoresponse of the photodiode (ON and OFF) overlaid with trigger from the chopper. (B) Photoresponse of AB junction overlaid with the trigger from chopper, indicating a real response from molecular junction.....	99
Figure 3.20: (A) Photocurrent spectrum of the photodiode obtained from LIA experimental apparatus (B) the phase spectrum obtained from the LIA for the photodiode. (C) Zero-phase adjusted spectrum for photodiode.....	100
Figure 3.21: (A) Photoresponse of photodiode vs. chopper frequency. (B) Photodiode phase as a function of chopper frequency.....	100
Figure 3.22: (A) Photoresponse of an AB junction vs. chopper frequency. (B) Phase of the AB junction as a function of chopper frequency.....	101
Figure 3.23: (A) Overlay of phase spectrum of AB junction and photodiode. (B) Overlay of phase spectrum of AB and Bromophenyl junctions obtained from the LIA apparatus.....	102
Figure 3.24: (A) Direct DC measurement of photocurrent for a BrP junction using 458nm laser illumination, showing positive photocurrent. (B) Direct DC measurement of photocurrent for a BrP junction using 458nm laser illumination, showing negative photocurrent.....	103
Figure 3.25: Oscilloscope trace of photocurrent versus time for 400 nm wavelength at 400 Hz for a photodiode (red curve) and a molecular junction (blue curve), showing that the response time of the molecular junction is faster than 250 $\mu$ s. This lag time is due to the mechanical limit of the chopper wheel in the experimental setup, shown by the overlay of the photodiode response. Although the electronic response time of the photodiode is 50 ns, it shows a similar rise time to the molecular junction.....	104
Figure 3.26: Variation of the measured photocurrent for a molecular junction (red curve) and photodiode (blue curve).....	105
Figure 3.27: Power density of Xe arc/monochromator with bandpass of 13 nm, measured at the sample position.....	106
Figure 3.28: Background noise continuously measured for 28 hrs.....	107
Figure 3.29: (A) Film star calculation carried out on PPF/molecule/Cu system. %T at 532nm is plotted as a function of thickness, where Cu/molecule interface is defined as X=0 (B) Model showing the light transmission through different layers such as Cu (20nm), molecular layer (5nm) and PPF (200nm). Molecular layers are multilayers but for simplicity shown as monolayers.....	108
Figure 3.30: Film star calculation showing the % of reflected & transmitted light at 532nm vs. the thickness of copper interface.....	109

Figure 3.31: Film star calculation showing the overlay of % of transmitted light at 532 & 780nm vs. the thickness of copper interface.....	110
Figure 3.32: The photocurrent yield obtained by varying the molecular layer thickness with three different copper top contact thicknesses.....	110
Figure 3.33: (A) Absorption spectra of quartz (red) only, Quartz with optically transparent photoresist film (OTPPF-blue) and finally the Quartz/OTPPF surface modified with azobenzene to make Quartz/OTPPF/Azobenzene (green). (B): Schematic representation of the sample....	112
Figure 3.34: Absorption spectrum of azobenzene (3.4 nm) obtained from figure 3.32.....	113
Figure 3.35: Optical absorption spectra C12, AQ, AB, NAB, and BrP following subtraction of OTPPF spectrum.....	113
Figure 3.36: Normalized absorption solution spectra of different molecules (BP, NP, NAB, AB and NBP) used in this study.....	114
Figure 3.37: Photocurrent yield as a function of energy for molecular junctions containing alkane (red triangles) and bromophenyl (black circles) molecular layers. The y-axis error bars are $\pm$ one standard deviation for three (BrP) or six (C12) junctions, while the overall length of the x-axis error bars represent the band pass of the spectrometer (13 nm).....	115
Figure 4.1: (A): Optical absorption spectra C12, AQ, AB, NAB, and BrP following subtraction of OTPPF spectrum. (B): Method for determining onset of optical absorption.....	122
Figure 4.2: Absorption spectra of Fc (A) and NDI (B) films on OTPPF (both NDI & Fc are 3-4nm thick), after subtraction of the OTPPF spectrum. Multilayers of molecules are formed; however monolayers are shown for simplicity.....	123
Figure 4.3: Schematic representation of the junction structure.....	124
Figure 4.4: Energy level diagram showing a non-resonant tunnel barrier for holes (HOMO-mediated transport, blue arrows) and electrons (LUMO-mediated transport, red arrows).....	127
Figure 4.5: (A) Overlay of the optical absorption spectra for the alkane (C12, blue curve) and bromophenyl (BrP, black curve) on optically transparent carbon. (B) Photocurrent yield as a function of energy for molecular junctions containing alkane (red triangles) and bromophenyl (black circles) molecular layers. The y-axis error bars are $\pm$ one standard deviation for three (BrP) or six (C12) junctions, while the overall length of the x-axis error bars represent the band pass of the spectrometer (13 nm).....	128
Figure 4.6: (A) Fowler plots for two different junctions where positive photocurrent is observed at PPF. (B) Fowler plots for negative photocurrent for the same two junctions. Extrapolated thresholds for each case are given.....	130

Figure 4.7: A) Photocurrent yield spectra for two junctions (Al/AlOx/Cu, red curve and carbon/C12/Cu, black curve). (B): Corresponding Fowler plots with extrapolated barrier values .....	132
Figure 4.8: (A) Diagram of the IPE mechanism for excitation of holes from Cu to carbon. (B) Diagram for electron transport from Cu to carbon. The alignment of the occupied system orbitals (OSOs) and unoccupied system orbitals (USOs) relative to the contact Fermi levels determine the sign of the observed photocurrent and the energy threshold for onset.....	133
Figure 4.9: Energy level diagrams constructed based on IPE characterization (A) Alkane (B) BrP molecule.....	134
Figure 4.10(A): Photocurrent yield spectrum for five different junctions (BrP (Blue curve), C12 (black), AQ (green), AB (red) and NAB (violet)). (B): Shows the same data on an expanded Y axis, with the photon energies indicated where the curves cross the X axis.....	137
Figure 4.11: An overlay of photocurrent yield and absorption spectra for four different junctions; black line indicates the optical absorption spectra of the molecular layer corrected for PPF absorption and the coloured line indicates the measured photocurrent spectrum of a particular molecular junction (A) AQ, (B) AB, (C) BrP, and (D) NAB.....	139
Figure 4.12: Expanded view of figure 4.10(B), showing positive photocurrent for AB junction (red curve) obtained from diode laser at two different energies (1.46eV and 1.54eV).....	141
Figure 4.13: Photocurrent vs. light intensity curves for (A) Al/AlOx/Cu, blue curve at 2.6eV (476nm) (B) Carbon/AQ/Cu at 1.8eV (688nm), red curve and 2.4eV (516nm), green curve (C) Carbon/BrP/Cu at 2.4eV (516nm), green curve and 2.7eV (458nm), blue curve (D) carbon/AB/Cu at 2.4eV (516nm), green curve and 2.7eV (458nm), blue curve.....	144
Figure 4.14: Photocurrent vs. intensity plot for an alkane junction at 2.4 eV (458 nm) and 2.7 eV (516 nm).....	145
Figure 4.15: Overlay of Photocurrent yield (colored lines) and absorbance spectra (black lines), for Fc (A) and NDI (B). (C) Photocurrent vs. Intensity for PPF/Fc/Cu at 2.4eV (green line), and 1.8eV (red) (D) Photocurrent vs. intensity for PPF/NDI/Cu at 2.7eV and 1.9eV.....	147
Figure 4.16: Photocurrent yield spectra for increasing molecular layer thicknesses, as indicated. (A) Ferrocene (B) NDI (C) AB (D) NAB.....	149
Figure 4.17: Yield vs. thickness plots of (A) Fc, (B) NDI, (C) AB and (D) NAB junctions....	150
Figure 4.18: (A) Fowler plots for BrP, NDI, Fc and AQ (B) shows the Fowler plot of AB.....	152
Figure 4.19: (A) Proposed diagram of the IPE mechanism for OSO mediated transport of electrons from PPF to Cu for the ferrocene molecule. (B): Diagram for electron transfer from Cu to carbon through the USO for the NDI molecule. The alignment of the occupied system orbitals (OSOs) and the unoccupied orbitals (USOs) relative to the contact Fermi levels determines the sign of the observed photocurrent and the energy threshold for onset.....	155

Figure 5.1: (A) Single layer photovoltaic cell, in which indium tin oxide (ITO) serves as a transparent high work-function electrode and Al serves as a low work-function electrode (picture adopted from reference(21)). (B) carbon/molecule/Cu device.....	164
Figure 5.2: Single-layer photovoltaic cell, in which indium tin oxide (ITO) serves as a transparent high work-function electrode and Al serves as low work-function electrode.....	165
Figure 5.3: (A) Overlay of photocurrent spectrum of AQ (green) and C12 (Black) junctions (B) Overlay of absorption spectrum of AQ (green) and C12 (black) molecules.....	168
Figure 5.4: An overlay of photocurrent yield and absorption spectra for DAB junctions; black line indicates the optical absorption spectra of the molecular layer corrected for PPF absorption and the coloured line indicates the measured photocurrent spectrum of a particular molecule..	170
Figure 5.5: Proposed idealized schematic representation leading to photocurrent generation and different steps involved with the process: (1) exciton generation (2) exciton diffusion (3) charge transfer state generation (4) charge separation (5) charge collection.....	172
Figure 5.6: The steps and loss mechanisms of converting light power into electric power. Light which is not converted to electricity is converted to heat.....	173
Figure 5.7: Photocurrent yield spectra for increasing molecular layer thickness, as indicated. (A) Fc (B) NDI.....	175
Figure 5.8: photocurrent yield vs. thickness plots of (A) Ferrocene (B) NDI at two different photon energies. The Inset in figure B shows the enlarged plot of NDI at 2.0eV.....	176
Figure 5.9:(A) Schematic energy-level representation for ITO/polymer/Al devices (B) Schematic energy-level representation for Carbon/molecule/copper devices. HOMO and LUMO levels are generic, i.e. not for a particular molecular structure.....	178
Figure 5.10: Comparison of photocurrent yield spectra of AB junctions with similar molecular layer thickness but different top contact. (Cu (20nm, red curve) and C(10nm)/Cu(10nm), blue curve).....	180
Figure 5.11: Comparison of photocurrent yield spectra of AB junctions with similar molecular layer thickness but different carbon top contact thickness. (C(10nm)/Cu(10nm), brown curve and C(5nm)/Cu(15nm), green curve).....	181
Figure 5.12: (A) Overlay of photocurrent yield spectra of BTB junctions with different thickness using carbon as top contact (B) Yield vs. thickness data for BTB junctions at 3.2 eV.....	182
Figure 5.13: Different modification pathways for formation of molecular bilayers via click chemistry.....	184

Figure 5.14: (A) two-layer photovoltaic cell. The electron accepting C60-layer contacts the Au electrode, while the electron donating MEH-PPV layer contacts the ITO electrode. (B) Bilayer molecular junction resembling the two-layer photovoltaic cell..... 185

Figure 5.15: Exciton dissociation at the donor-acceptor interface. The electron goes to the acceptor while hole stays in the donor..... 186

Figure 5.16: Schematic representation of the molecular photovoltaic device..... 187

## LIST OF ABBREVIATION

AB	Azobenzene
ACN	Acetonitrile
AQ	Anthraquinone
AU	Absorbance Unit
BP	Biphenyl
BrP	Bromophenyl
BTB	Bisthienylbenzene
C-AFM	Conducting Atomic Force Microscopy
CB	Conduction Band
CPD	Contact Potential Difference
EA	Electron Affinity
EB	Ethynylbenzene
EQE	External Quantum Efficiency
Fc	Ferrocene
HBEC	High Binding Energy Cut-off

HOMO	Highest Occupied Molecular Orbital
HOSO	Highest Occupied System Orbital
IE	Ionization Energy
IPE	Internal Photoemission
IPES	Inverse Photoelectron Spectroscopy
KP	Kelvin Probe
LB	Langmuir-Blodgett
LIA	Lock-in Amplifier
LUMO	Lowest Unoccupied Molecular Orbital
LUSO	Lowest Unoccupied System Orbital
MA	Molecular Absorption
NAB	Nitroazobenzene
NDI	Naphthalene di-imide
NEXAFS	Near-Edge X-ray Absorption Fine Structure
NP	Nitrophenyl
OFET	Organic Field Effect Transistor
OLED	Organic Light Emitting Diodes

OPV	Organic Photovoltaic
OTPPF	Optically transparent Pyrolyzed Photoresist Film
PES	Photoelectron Spectroscopy
PPF	Pyrolyzed Photoresist Film
2PPE	2-Photon Photoemission
QCM	Quartz Crystal Microbalance
SAMs	Self-Assembled Monolayers
STM	Scanning Tunneling Microscopy
TBABF <sub>4</sub>	Tetrabutylammonium Tetrafluoroborate
UPS	Ultraviolet Photoelectron Spectroscopy
VB	Valence Band
VL	Vacuum Level
WF	Work Function

# Chapter-1

## Introduction

### 1.1 Molecular electronics:

Molecular electronics, as its name implies, use a single molecule or ensemble of molecules as functional elements in electronic circuits. Since the size of components in integrated circuits is followed the exponential decrease with time known as Moore's law for >30 years, it is a simple matter to suggest that the ultimate integrated circuits will be constructed at the molecular or atomic level. Such a scenario was suggested by an eminent physicist and visionary Richard Feynman in a lecture at an American Physical Society meeting at Caltech, 1959 (1). The field of molecular electronics started with the landmark papers of Aviram and Ratner (2) in which they proposed the possibility of creating a unimolecular rectifier. Since then, the field of molecular electronics has drawn continuous attention from researchers in different disciplines. Some have defined it as technology that utilizes only single molecules rather than allowing a group of molecules, but this definition is far too limiting. Molecular electronics can be defined as a technology utilizing single molecules, small group of molecules, carbon nanotubes, or nanoscale metallic or semiconductor wires to perform electronic functions (3). From the broader definition, it can be suggested that any device utilizing molecular properties is a molecular electronic device.

The first significant breakthrough in molecular electronics was the invention of scanning tunneling microscopy (STM) in 1981 (4). With STM imaging the surface at molecular and atomic scale became possible. A second set of advances underlying molecular electronics was the

emergence of chemically modified surfaces, particularly in electrochemical studies (5-8). These advances led to the ability to place monolayers of organic molecules on the surface of various materials, including conductors and semi-conductors, which serve as a starting point for a molecular junction. Research efforts in the field of molecular electronics have seen dramatic growth since the 1990s, partially because of the development of self-assembled monolayers (SAMs) and the increasing sophistication of micro-fabrication technology.

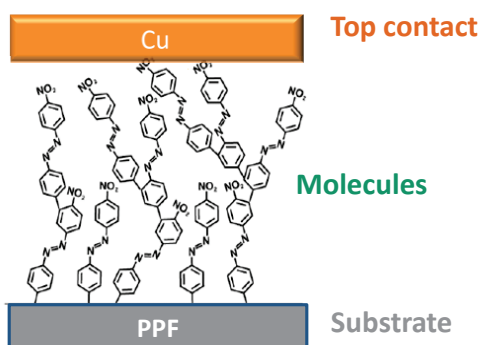
One potential advantage of organic molecules for electronics is that they provide a cheap means to fabricate microchips. In addition, organic molecules can be readily self-assembled or grafted onto a substrate, which provides a potential “bottom-up” approach to build functional molecular electronic devices. Another advantage of organic molecules lies in their versatility and chemical tailorability. There are a great variety of molecules available with versatile electronic, optical, magnetic or photonic properties which can be readily tailored or tuned by molecular engineering and provide unlimited possibilities for technological exploration.

Molecular electronics should not be confused with the vast field of organic electronics, which includes organic light emitting diodes (OLED), organic field effect transistors (OFET), organic photovoltaics and conducting polymer devices. The fundamental differences between organic electronics and molecular electronics are as follows: *a)* dimensions: molecular electronic devices have at-least one dimension in a nanometer scale (usually 1-5 nm), while the organic layers in organic devices are often hundreds of nanometers or even micrometers in thickness. *b)* Charge transport mechanism: The charge transport in organic electronic devices is mainly governed by “hopping” mechanism with a thermally activated energy barrier whereas for the molecular electronic devices (SAMs and LB films) there are other mechanisms such as tunneling. Localized regions of order exist often in organic electronic devices where tunnelling/band-like

transport can take place in smaller domains, with hopping in between domains *c)* order: unlike organic electronic devices, the molecules in molecular electronic devices are usually ordered (SAMs and LB films) with a well-defined orientation (9).

## 1.2 Components of a molecular junction:

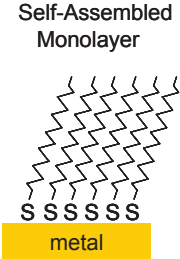
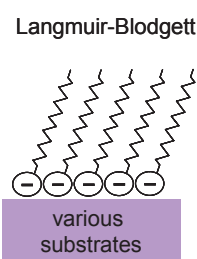
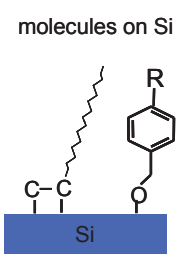
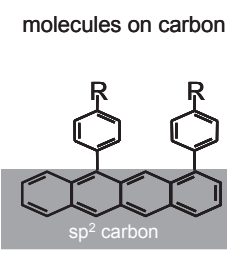
The physical components of a molecular junction include contacts, molecules and interfaces. A molecular junction usually consists of a single molecule or ensemble of molecules sandwiched between two electrodes (see figure 1.1). The two electrodes can either be conductors or semiconductors and are often fabricated separately. The construction of the molecular junction usually adopts a ‘bottom-up’ approach where one electrode is first fabricated as a substrate and then the molecules are assembled or grafted onto the substrate followed by forming a second “contact” deposited on top of the molecular layer. Significant components of the molecular junction are the interfaces between the molecules and the electrodes. It is supposed that the interface between the molecules and the contacts can play a significant role in determining device characteristics(10).



**Figure 1.1:** Schematic of the components of a generic molecular electronic junction:

Substrates used in molecular junctions include metals like Au (11-13), Ag (14, 15), Pt (16, 17), Carbon (18, 19) or Hg (14, 15) etc. Depending on how the molecules are attached to the

substrates, three classes of substrate/molecule systems are available: self-assembled monolayers (SAMs), Langmuir-Blodgett (LB) films and covalently-bonded molecular layers on carbon or silicon substrates. A comparison of the surface bonding properties for these three examples is given in figure 1.2.

	Self-Assembled Monolayer	Langmuir-Blodgett	molecules on Si	molecules on carbon
				
Bond type	metal-S	various	Si-C, Si-O-C	C-C
Bond Strength	~ 40 kcal/mol or 1.7 eV	< 10 kcal/mol or < 0.5 eV	80-100 kcal/mol or 3.5 - 4 eV	80-100 kcal/mol or 3.5 - 4 eV
Surface dipole	yes	yes	varies	very weak

**Figure 1.2:** Comparison of surface bonding properties of several substrate/molecules systems commonly used in molecular electronics.

### 1.2.1 Self-assembled monolayers:

Self-assembled monolayers (SAMs) on metals were one of the first systems used to make molecular junctions, in conjunction with the scanning tunnelling microscope (STM) tip to complete the circuit (20). SAMs are considered ordered molecular assemblies formed by spontaneous adsorption of organic molecules onto the substrate surface. A variety of molecular species can form SAMs on different metals such as Au (21, 22), Ag (23), Cu (23), Pt (24), Pd (25), and Hg (26) or on semiconductors such as GaAs (27) and InP (28). The self-assembly of organic monolayers on the electrode (29-31) is considered to be a promising approach for the fabrication of molecular electronic devices. Thiols have been widely used to connect the organic molecules to noble metals because of the ease of preparation and their ability to form structurally well-defined monolayers on metal surfaces. To date, most molecular electronic junctions have

been primarily based on a Metal-Molecule-Metal (MMM) structure using thiolates on Au substrate as a typical system. Even though these materials form well-ordered monolayers they lack the stability required for many applications in electronic circuits. Thiols do not provide an efficient pathway for charge transport due to the local character of the sulphur 3p orbitals involved in the thiolate-metal bond (32, 33). SAMs are also known to have defects between grain boundaries (34). The low energy-barrier for molecular desorption and diffusion is another obstacle for the applicability of thiols in electronic devices, limiting the device stability and the product shelf life of organic-based devices (31). Damage of SAMs by evaporated metals and metal penetration through SAMs has also been well documented in the literature (35, 36).

### **1.2.2 Langmuir-Blodgett films:**

The Langmuir-Blodgett (LB) technique is an effective tool for transferring well-ordered molecular films at the air-water interface onto a solid support, permitting a degree of control over the molecule-surface interaction or contact, as it is applicable for forming both chemisorbed and physisorbed films (37). LB films are formed by amphiphilic molecules with a hydrophilic 'head' and a hydrophobic 'tail' which assembles at the air-liquid interface. The layer of molecules on a liquid surface is termed a Langmuir monolayer and after transfer it is called a Langmuir-Blodgett film. The preparation of LB films involves spreading amphiphilic molecules over the surface of the sub-phase (usually water), and then compressing or expanding the surface with a barrier (usually made of Teflon), followed by transferring the film onto a solid substrate. LB films provide a level of control over the orientation and placement of molecules in monolayer and multilayer assemblies that are difficult to achieve otherwise. The formation of multilayers with good control of thickness can be achieved in a layer-by-layer deposition fashion by repeating the formation steps. The bonding strength of the electrostatic force between molecules and the

substrate in LB films ( $< 10$  Kcal/mol) is weaker than the Au-S (40 Kcal/mol) in SAMs. LB metal-organic assembly also has the potential for the exploration of different more common metal/thiol self-assembly method. However, the preparation of the LB films is a tedious process and requires a specific apparatus, which makes them much less popular than SAMs for use in molecular electronics.

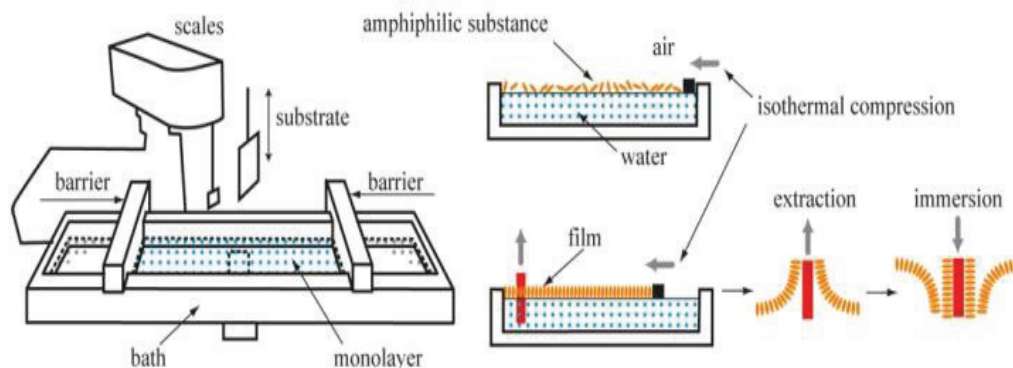


**Figure 1.3:** Schematic illustration of the preparation of Langmuir-Blodgett films.

### 1.2.3 Covalently bonded molecules on Carbon and silicon:

Carbon materials such as graphite, glassy carbon and diamond, etc., have long been used as electrode materials in electrochemistry. The advantage of using carbon materials includes low cost, wide electrochemical-potential window, and relatively inert electrochemistry (38). Carbon surfaces can also be modified with organic molecules by electrochemical, thermal, or photochemical methods (39-41). The McCreery group has employed a carbon material of pyrolyzed photoresist films (PPF) as a substrate for molecular electronics (42). PPF behaves electronically like a metal but with lower conductivity and density of electronic states. Furthermore PPF can easily be modified by the electrochemical reduction of diazonium ions or the electrochemical oxidation of primary amines. The C-C bond formed by covalent bonding of organic molecules by diazonium reduction is much stronger than the Au-S bond in SAMs or

electrostatic force in LB films, with a bonding energy of 80-100 kcal/mol. The covalent C-C bond can withstand more harsh conditions during the top electrode formation, especially by physical vapour deposition. By using covalently bonded molecular layers using diazonium chemistry on carbon substance it has been shown that the direct deposition of some materials (Cu (43-45), Si (46), and Carbon (47)) does not destroy or disrupt the molecular layers. Gold (Au) can penetrate the molecular layers (44, 47), resulting in short circuits, and Ti (44) resulted in the degradation of the molecules. However, highly reproducible molecular junctions have been demonstrated using covalently bonded molecular layers with directly deposited Cu or carbon contacts (48).

Silicon is another commonly-used substrate in molecular electronics. It provides a great potential of integrating molecular electronic devices into current silicon-based microelectronics technology. Silicon has a well-defined surface crystal structure and can offer versatile surface reaction to form strong covalent Si-C or Si-O-C bonds. The silicon surface crystal structure can serve as a template for the translational order of the molecules and dictate the orientation of the molecular layer (49). The interaction of Si electronic bands and molecular levels may lead to some interesting effects and this interaction can be modulated by changing Si doping level to potentially modify and control charge transport across the device.

Understanding of the electrical behaviour i.e. direct current-voltage (I-V) measurements is a requirement for molecules arranged into metal-molecule-metal junctions. The common methods available for obtaining I-V behaviour include mechanical break junctions (50, 51), cross-wire junctions (52), scanning tunnelling microscopy (STM) (53, 54), and conducting atomic force microscopy (c-AFM) (55, 56). Molecular-conductance values obtained from such devices not

only depend on the inherent molecular features, but also on other important parameters, such as metal-molecule contact, the orientation of the molecule, the nature and type of the molecule, etc.

### 1.3 Electron transport in molecular junctions:

Several mechanisms like coherent tunneling, activated transfer between potential wells, various hopping modes, etc., have been reported for electron transport through single molecules or a collection of molecules oriented in parallel. A molecular junction generally refers to a two-terminal device consisting of two contacts with a monolayer of molecules oriented between them (57). If the two contacts of a tunnel junction are close enough for their wave functions to overlap electrons can tunnel across the gap. In the simplest case tunneling is coherent and controlled by the barrier height and the gap spacing. For coherent junctions no redox reaction occurs and the current is independent of the temperature.

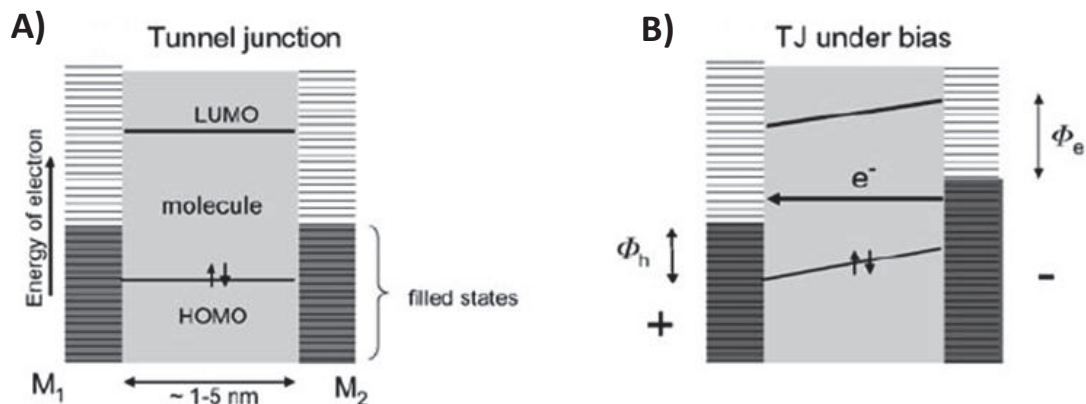


**Figure 1.4:** Schematic energy levels for a tunnel junctions (A) normal (B) under bias.  $M_1$  and  $M_2$  refer to metallic contacts, with the shaded area indicating filled electronic states,  $\phi_e$  and  $\phi_h$  indicates the electron and the hole-injection barriers. Picture adopted from reference (57).

#### 1.3.1 Tunneling mechanism:

Classical tunneling is often explained with the “Simmons model” based on the probability of an electron traversing a barrier of given thickness and height (58). The rate of coherent

tunnelling decreases exponentially with the thickness of the barrier, and is stated in its simplest form using the Simmons relation (59).

$$(Eqn 1.1) \quad J = \frac{q^2 V}{h^2 d} (2m\phi)^{\frac{1}{2}} \exp\left[-\frac{4\pi d}{h} (2m\phi)^{\frac{1}{2}}\right]$$

where  $J$ = current density,  $q$ = electron charge,  $V$ = applied voltage,  $h$  = Planck's constant,  $m$ = electron mass,  $\phi$ = barrier height, and  $d$ = barrier thickness. This equation shows only the linear term for a rectangular tunnel barrier but shows the exponential dependence on thickness "d". In the figure given above (figure 1.4), 'd' is the distance between the conductors, typically 1-5 nm. The above equation can be simplified to the form:

$$(Eqn 1.2) \quad J = J_0 e^{-\beta d}$$

where 'β' is the attenuation factor for the molecules, has units of inverse nm. By comparing the equations, we know that β is proportional to the square root of the barrier height.

$$(Eqn 1.3) \quad \beta = 2 \sqrt{2m(\phi - \frac{V}{2})/\hbar^2}$$

According to the above equation, 'β' should decrease slowly with a change in voltage and approach zero as 'V' approaches 2φ. Lower 'β' value means less attenuation of the current per unit distance or more efficient tunnelling.

Sometimes electrons interact with the orbitals and the electronic structure of the molecules, enhancing the tunneling rate and making "through bond" tunneling more efficient than "through space" tunneling. This process of "through bond" tunneling is known as "superexchange" tunneling (60-62). The tunneling process, with or without (through space tunneling) the super exchange mechanism, should not depend on temperature. Tunneling is generally not effective

over great distances greater than a few nm. Electron transport over such distance is usually attributed to more complex phenomena such as “incoherent tunneling” or “hopping”.

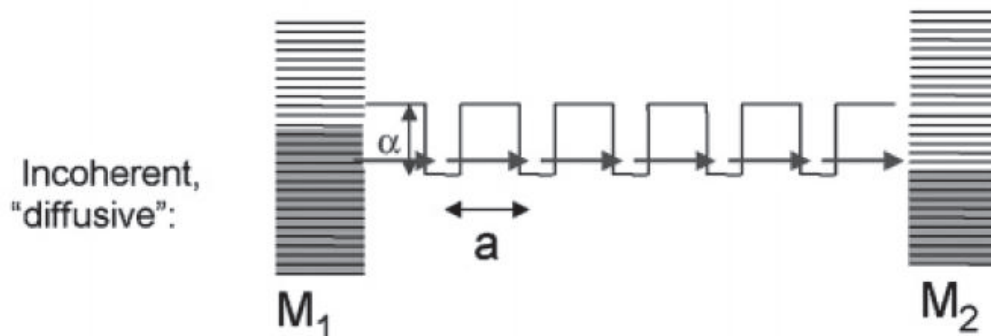


**Figure 1.5:** Schematic energy levels diagram for diffusive tunneling. ‘ $\alpha$ ’ is the potential well depth of  $N$  sites spaced apart by a distance “ $a$ ”.  $M_1$  and  $M_2$  are the metallic contacts (63).

The Incoherent tunneling model proposes that the electron tunnels coherently along a series of sites which are characterized by potential wells (see figure 1.5) (64). The electron spends enough time (residence time) in the well that the phase of the electron is disturbed and the process should be viewed as a series of discrete steps. It is important to understand that the electron tunnels through the barrier between the sites, and the process is independent of temperature.

### 1.3.2 Hopping mechanisms:

Electron transport can exceed distances greater than the upper limit for tunneling by a multistep hopping process. In this mechanism, the total distance ‘ $d$ ’ is split up into a series of short ET steps. The hopping model was first developed for DNA (see figure 1.6). This model stemmed from the observation that DNA is a charge-carrier and that the efficiency of charge transfer states scales with the number of guanine base pairs (65). The overall electron transfer rates do not follow the exponential dependence on distance, but rather scale algebraically with

the number of hopping steps 'n'. If  $K_n$  as the hopping rate,  $\eta$  takes values between 1 and 2 (66), and equation 1.4 applies.

(Eqn 1.4)

$$K_{ET} \propto K_n n^{-\eta}$$

thus the main characteristics of sequential electron-transport by hopping are the occurrence of chemical intermediates, i.e. oxidised (reduced) bridge units that function as relays, and the resulting weak distance-dependence of ET across such bridges. The superexchange mechanism shows strong exponential distance-dependence whereas electron hopping exhibits only weak distance-dependence. As with incoherent tunnelling, the electron may traverse one or more sites, but the difference between the tunneling and hopping is the involvement of nuclear or the re-organizational motion (67). Electron transfer does not occur until the thermal motion of the nuclei results in a favourable molecular geometry, and transport is temperature dependent.

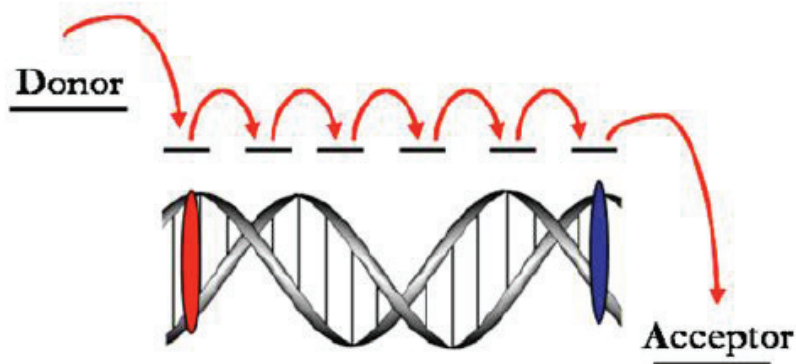


**Figure 1.6:** Schematic representation of energetic models of electron migration through DNA system. In this hopping model, donor orbitals are energetically close to those of the bridge. Charge occupies the bridge hopping between discrete molecular orbitals.

Hopping involves electron motion over the barrier (meaning that the reorganizational energy must rearrange for electron transfer to occur), while tunneling involves electron transfer through the barrier (meaning that there is a finite probability of finding an electron on the other side of

the barrier, without requiring nuclear motion). Hopping involves a series of transfers between relatively stable redox sites and does not exhibit the exponential distance dependence of coherent tunneling but instead varies as  $d^{-1}$ . The time an electron resides in various potential wells relative to the time for molecular re-organization is the key parameter in assessing the importance of nuclear motion to electron transport (68).

Fowler-Nordheim tunneling refers to an enhanced tunneling which occurs at high electric fields when the applied voltage exceeds the barrier height and is well beyond the linear voltage behaviour implied by the Simmons relation. Fowler-Nordheim tunneling is independent of temperature but decreases exponentially with distance.

#### **1.4 Metal-Organic interfaces:**

In the past decade, much research and development has been focussed on the energetics at metal-organic interfaces. While the properties of conventional metal, semiconductor, or insulator films are well understood, the fundamentals of interfaces with molecules are not completely understood. The energetics at these interfaces is significant since they control charge injection and transport through the devices (69-72). Understanding the factors that determine the electronic properties of these interfaces is an important goal in interfacial research.

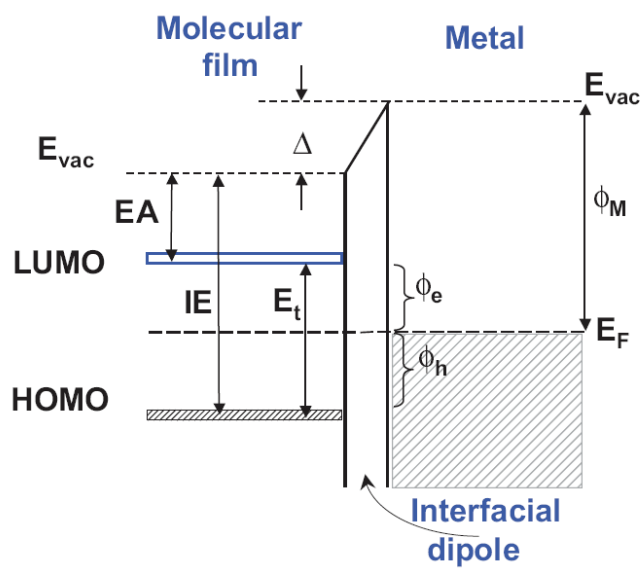


**Figure 1.7:** Energy diagram of an interface between a molecular film and a metal surface. Figure adopted from reference (71).

The interface electronic-structure of a typical metal-organic interface is shown in figure 1.7. Important electronic levels are the electrode Fermi level ( $E_F$ ); the highest and the lowest occupied molecular orbitals (HOMO, LUMO); and the Vacuum level ( $E_{vac}$ ) of each material. The work function of the electrode ( $\phi_M$ ), the ionization energy (IE), and the electron affinity (EA) are defined as the energy difference between the vacuum and the LUMO levels for the molecules. The interface shift between the vacuum levels of the two materials, or the interface dipole barrier is denoted as  $\Delta$ . Central to the charge carrier-injection through the interface are the electron and hole-injection barriers,  $\phi_e$  and  $\phi_h$ , respectively.

Most of the research efforts in recent decades were aimed at providing the energy levels for defining barriers to electronic charge carrier injection and transport. In order to predict the barrier for charge carrier transport between molecules and the contacts of a molecular junction requires understanding of both the occupied and the unoccupied energy levels at the interface. If the

interaction between the molecule and the contacting materials is only van der Waals type of force then the prediction is simple. In most cases the interaction becomes complex due to strong chemical interactions between the molecule and the contacts. The well-known valence and conduction bands of inorganic semiconductors are replaced by transport states such as the HOMO and the LUMO levels of the molecule. The relative position of the contact Fermi level and charge-neutrality level of this induced density of states defines charge transfer across the interface and the interface energetics (73, 74). Experimental results (75, 76) indicate that metal/organic interfaces generally do not follow the Mott-Schottky model (77) and the interfacial electronic structure is dominated by the charge exchange between the contact material and the interfaces. Electronic states resulting from interfacial chemistry generally dominate the energetics (78), and the energetics can depend on chemical bonding and molecular orientation. Previous reports shows that in molecular electronics the charge transport is more efficient when the interface is reactive, i.e. when a chemical bond is formed between the molecules and the substrate (51). This result shows that the behavior of the electronic system might be different from that of the isolated components, emphasizing the importance of interface characterization.

## 1.5 Work Function:

*Work function in metals:* For metals, the valence bands are filled with electrons up to the Fermi energy ( $E_F$ ). The energy difference between the Fermi energy and the vacuum level corresponds to the work function ( $\phi$ ). The work function is described as the minimum amount of energy needed to remove an electron from the metal into a vacuum. Figure 1.8 shows the schematic energy level diagram of a metal. The work function of the surface is strongly affected by the condition of the surface. Contamination present on the surface can change the work function substantially (69). Substrate preparation can affect the composition as well as electrical

characteristics of the given surface. A clean metal surface has relatively high energy at the surface, where the molecules of ambient atmosphere ( $N_2$ ,  $H_2O$ , hydrocarbons) get adsorbed. This can lead to a difference in work function between “clean” and “exposed to air” metal surfaces (79). These changes are a result of the formation of electric dipoles at the surface, which change the energy that an electron needs to leave the sample. Due to the sensitivity of the work function to chemical changes on the surface, its measurement can give valuable insight into the condition of a given metal surface.

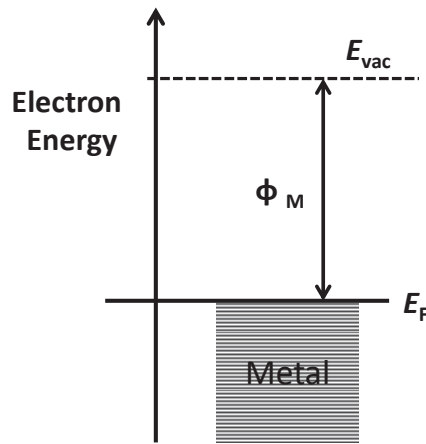


**Figure 1.8:** Schematic energy diagram of a metal, showing the work function.

### 1.5.1 Work function measurement techniques:

The work function of a given material can be measured with ultraviolet photoelectron spectroscopy (UPS) and a Kelvin probe (KP). UPS allows the measurement of the absolute work function whereas KP only gives the contact potential difference (CPD) between the actual probe and the sample surface. Calibration with PES allows calibration of KP results to yield absolute values.

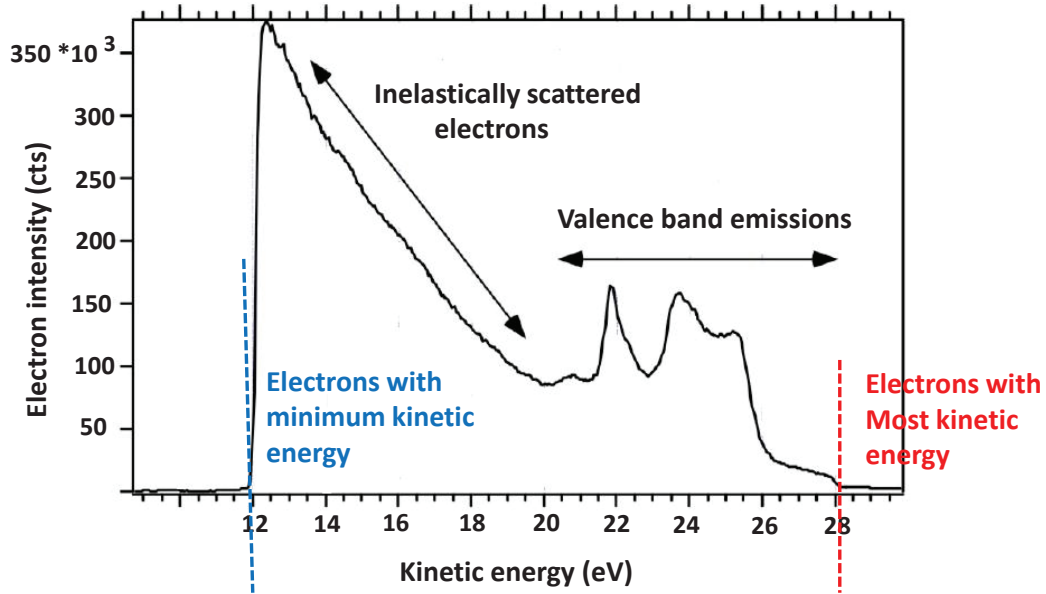
### 1.5.1.1 Measuring work function using UPS:

Figure 1.9 shows the UPS spectrum of a gold sample (80). The Fermi level separates the occupied and the empty states. There are no actual energy levels at the Fermi level and the Fermi level is a statistical concept (70). UPS works only with the occupied states, since there need to be electrons that can be photoemitted, i.e. states above the Fermi level are empty and do not emit electrons. Further to the left from the Fermi level at low-binding energies the valence bands structures are visible. They are the electrons with maximum kinetic energy detected at the detector. Then there is a high-binding energy cut off where the spectrum ends. The electrons at the secondary cut off edge are the slowest electrons of the spectrum. The electrons responsible for the secondary edge and the increasing tail before the secondary cut-off edge are inelastically scattered electrons which were initially emitted from the valence band states but lost energy through scattering processes on their way to the sample surface. Inelastically scattered electrons will have enough energy to escape into vacuum and will be detected as secondary electrons. Knowing the binding energy of electrons right at the secondary edge, we can determine the work function, which is the difference between the kinetic energy measured at the detector for the electrons at the cut off plus the photon energy, and the energy of the electrons originating from the Fermi level of the sample. The “X” axis can be displayed either in kinetic or binding energy. Work function can be calculated using eqn (1.5).

(Eqn 1.5)

$$\phi_m = E_K^{\min} + h\nu - E_K^{\max}$$

Therefore, the calculated work function of gold sample in this case is  $(12.0+21.2-28.0) = 5.2$  eV (see figure 1.9), where 21.21 eV is the energy of the HeI radiation source used ( $h\nu$ ).



**Figure 1.9:** UPS of gold using He (1) (21.2 eV) excitation.

### 1.5.1.2 Work function using KP:

A Kelvin probe (KP) cannot be used to measure the absolute work function of the material, since it can only detect the difference between the work functions of the probe and substrate. Therefore, to measure the work function of a material with KP a calibration measurement needs to be carried out. Considering the example with Au, a certain KP contact potential measured relative to the Au surface would be assigned 5.2 eV. Then the unknown sample could be measured using the KP. If the work function of the unknown sample is smaller than the Au work function, then KP would yield a negative contact potential, while if it is larger then a positive contact potential would be detected. Adding the contact potential value obtained from this to the Au work function value would then yield the actual work function of the sample. Contamination can change the work function of the reference and so obtaining an absolute work function value in air becomes difficult. HOPG (highly oriented pyrolytic graphite) does not form interface

dipole, therefore its work function (4.6 eV) value is not significantly changed under typical ambient condition and it is commonly used as the standard.

## 1.6 Vacuum level:

The vacuum level of a finite size sample ( $E_{\text{vac}}(s)$ ) is defined as the energy of an electron at rest just outside the surface of the solid. For metals, this distance is also where the image potential is essentially zero (70). The distance just outside the solid means the distance between the electrons and the surface is larger than the interatomic distance but smaller than the size of the crystal surface(70). The ( $E_{\text{vac}}(s)$ ) is involved with the measurement of  $I$ ,  $A$  and  $\phi$ (81, 82). The vacuum level at infinity ( $E_{\text{vac}}(\infty)$ ) is defined as the energy of an electron at rest at infinite distance from the surface. Fermi level is constant and ( $E_{\text{vac}}(\infty)$ ) can be viewed as a level at a fixed energy from the Fermi level. ( $E_{\text{vac}}(\infty)$ ) is an virtual level that is experimentally not accessible.

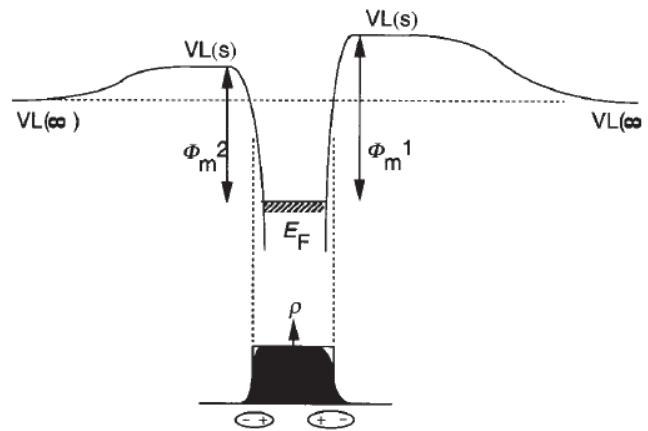


**Figure 1.10:** vacuum level close to the surface ( $E_{\text{vac}}(s)$ ) and vacuum level at infinity ( $E_{\text{vac}}(\infty)$ ). Figure adapted from reference (73). The back region shows the electron density in the metal, with tailing at the surface to form a surface dipole layer.

For a metal, the difference between the energies of ( $E_{\text{vac}}(\infty)$ ) and ( $E_{\text{vac}}(s)$ ) is mostly due to the surface dipole layer formed by the tailing of electron cloud at the surface(83, 84). The tailing of the negatively charged electron cloud into vacuum makes the vacuum side negative, while the

lack of electrons inside the surface makes the bulk side positive (see figure 1.10). In addition when the electron crosses the surface dipole on its way out of the solid, the potential energy is raised by an amount equal to the dipole energy barrier and as the electron moves away from the (finite-size) surface, the dipole field and the potential energy decrease (see figure 1.11).

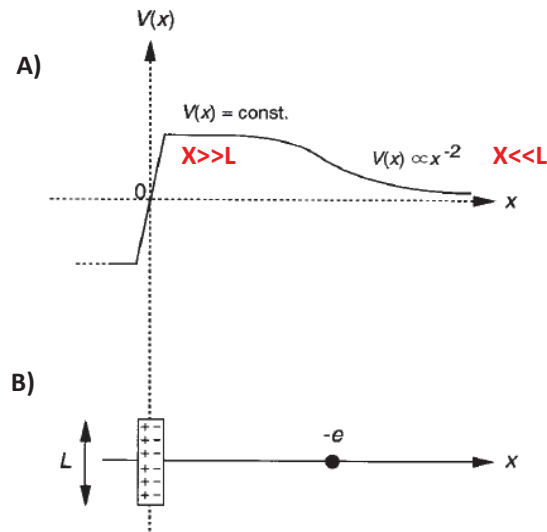


**Figure 1.11:** (A) Electron and dipole layer with a representative extension  $L$  with the distance  $x$  between them. (B) The potential energy of the electron by the dipole layer. Figures adapted from reference (73).

The flat portion of the dipole just outside the surface in figure 1.11 (A) is the region of  $(x \ll L)$ . As the distance from the surface becomes larger than the extension of the sample surface  $(x \gg L)$ , the effect of the surface dipole layer diminishes, and the energy of the free electron gradually converges to a common value, which corresponds to  $V_L(\alpha)$ .

## 1.7 Gap states:

The interface electronic structure of a typical metal-organic interface is given in figure 1.12. The density of the interface gap states,  $D_{is}$ , is schematically represented between the HOMO and LUMO, and the interface shift between the vacuum levels of the two materials, or interface dipole barrier, is denoted as  $\Delta$ . Considering the standard case for metal-semiconductor interface (76), gives the following equation for the electron injection barrier.

$$\phi_{Bn} = S (\phi_M - EA) + (1 - S) E_{CNL}$$

$$S = \frac{1}{1 + 4\pi e^2 \delta D_{is}}$$

$\delta$  is the effective metal-semiconductor distance, and  $E_{CNL}$  is the charge neutrality level of the interface states. If the interface  $E_F$  is above the  $E_{CNL}$ , the net charge in the interface state is negative, and a dipole with corresponding sign develops across the interface and vice versa.

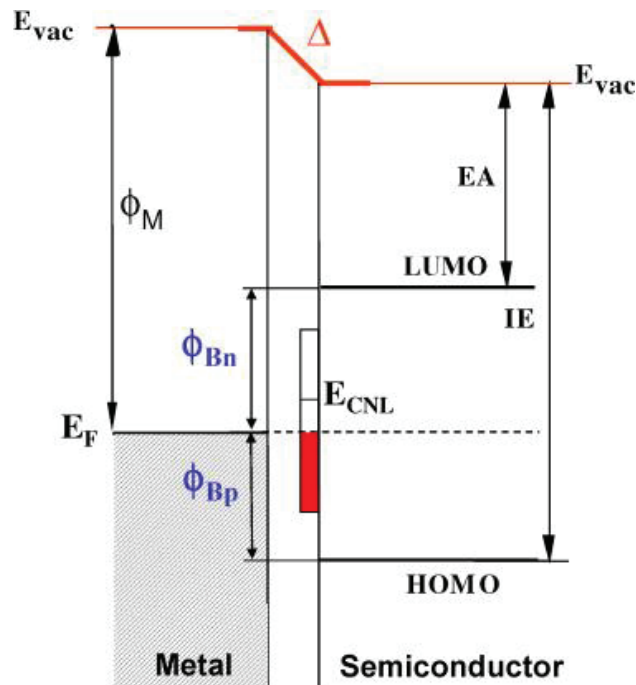


**Figure 1.12:** Electronic structure of a typical (organic) semiconductor-metal interface, showing relevant energy levels on both sides, the electron affinity (EA) and ionization energy (IE) of the semiconductor, the interface dipole  $\Delta$ , the interface density of gap states and charge neutrality level  $E_{CNL}$ , and the electron and the hole injection barriers. Picture adapted from reference (69).

### 1.7.1 Interface free of gap states (Schottky-Mott model):

The Schottky-Mott limit assumes a vanishingly small density of interface states  $D_{is}$ , a situation where there is no interaction between metal-semiconductor interfaces. The position of the molecular level ( $E_{Vac}(s)$ ) with respect to the electrode  $E_F$  follows from vacuum level alignment, or  $\Delta=0$ . The electron tunnelling barrier  $\phi_e$  in this case will be equal to the difference between the electrode work function  $\phi_M$  and the organic electron affinity EA. The hole tunneling barrier will be equal to  $\phi_h = IE - \phi_M$ . The interface parameter “S” – defined as the derivative of the electron barrier with respect to the electrode work function and can be used to describe the dependence on the barrier on the electrode (69). The interface will depart from the simple Schottky-Mott rule if the work function of the electrode decreases to reach the semiconductor EA, causing a large electron transfer from the metal to the LUMO of the organic film. A similar situation occurs when the charge transfer happens from the organic HOMO to the metal, as the electrode work function increases and reaches the semiconductor IE. The extensive study carried out in the past decade shows that the interfaces formed by spin coating polymer films on metal electrodes, and interfaces formed by evaporating small molecule films on contaminated metal surfaces follow the Schottky-Mott limit (85, 78).

Whereas, metal-on-polymer and metal-on-small molecule interfaces made by vacuum metal thermal evaporation of the metal and small molecule-on-clean metal surfaces depart from Schottky mott rule (75, 76). The reorganization of the surface metal electronic structure happens when an atom or molecule is deposited on a metal surface due to the columbic repulsion between its electron density and the surface metal electrons locally suppressing the tail of electron wave functions that spills in to the vacuum (see figure 1.10). The reduction in the work function associated with this effect should not be viewed as resulting from the formation of an interface

dipole, but simply due to the modification by the “external” surface component to the work function of the metal.

### **1.7.2 Interface dominated by gap states:**

If the density of interface states is excess ( $5 \times 10^{13} \text{ cm}^{-2} \text{ eV}^{-1}$ ) with energy, in the gap of the semiconductor then it has a significant impact in the position of the interface  $E_F$  (69). The parameter ‘S’ approaches zero for large  $D_{is}$ , leading to a Fermi level position defined by the charge neutrality level of the interface states. When  $D_{is}$  is large enough, the Fermi level excursion range will be limited due to the presence of significant density of states, and eventually lead to  $E_F$  pinning. The origin of interfaces can be either due to chemical (chemical bonds) or defects between the semiconductor and the metal (94). When a metal is vacuum evaporated on a molecular film, it leads to the formation of metal induced defects in the organic material, which exhibit filled or empty electronic states that overlap with the original gap of the semiconductor(95).

The metal electron wave function at the metal-semiconductor interface tails into the semiconductor (96, 97). The proximity of the metal surface and the overlap between the continuum of metal states and semiconductor states induces a density of interface states in the gap of the semiconductor known as metal induced gap states (MIGS), this concept at the semiconductor interface is now applied to weakly interacting molecular organic interface (98, 99). The charge neutrality level is calculated by integrating the local density of states in the MIGS and imposing that the total number of electrons up to charge neutrality level equals the number of electrons in the neutral molecule. As the density increases the parameter “S” decreases and the interface Fermi level position and associated barriers become increasingly dependent of the metal work function(69). The electron distribution across the interface depends on the magnitude

of the metal work function relative to the charge neutrality level position (see figure 1.12). If the work function is smaller i.e. if the position of Fermi level is above the charge neutrality level, electron transfer takes place from the metal to the MIGS, an upward dipole barrier at the metal-organic interface i.e. the vacuum level shifts upward from the metal to the organics. The concepts of MIGS and charge neutrality level as developed by Vazquez et al. (98) are applicable only to weakly interacting organic-metal interfaces. In most cases its bonding and electronic defects formed at the interfaces control the Fermi level position.

## **1.8 Investigation methods:**

The common methods used to investigate the energetics of interfaces are direct (PES) and inverse (IPES) photoemission spectroscopies. Direct photoemission work involves a specific type of PES, Ultraviolet Photoemission Spectroscopy (UPS), which has been successfully used for mapping the frontier orbital states (85, 86) i.e. the highest occupied molecular orbital (HOMO) of the molecule at the interface. While not as widely used, Inverse photoemission spectroscopy (IPES) permits measurement of the empty frontier orbitals, in particular the lowest unoccupied molecular orbital (LUMO) of the molecules at the interface (87, 88).

### **1.8.1 Photoelectron spectroscopy:**

When the molecule is in the ground electronic state, the LUMO is empty of electrons, while the HOMO is filled with electrons. The HOMO and LUMO energy levels are generally set as negative values (absolute energy levels) relative to the vacuum level ( $E_{\text{vac}}$ ), whose energy level is zero. The energy difference between the HOMO and LUMO of a molecule is called the HOMO-LUMO gap.

XPS and UPS are similar in their instrumentation, but different in incident light source. The core-level photoemission work is usually done with standard mono-chromatized X-ray sources providing two different radiation lines- Al K $\alpha$ ,  $h\nu=1486.6$  eV and Mg K $\alpha$ ,  $h\nu=1253.6$  eV, and the energy resolution of the XPS measurement is typically 800 meV (69). The energy resolution of XPS and UPS largely depend on the line width of the incident photon source, which are a few meV for the discharge lamps of UPS and 1.0 eV for the X-ray anodes of UPS. Using synchrotron radiation sources can effectively improve the resolution of UPS to 0.02 eV, although with very high cost of operation. XPS is more useful for obtaining the information of core-level states at higher binding energies of the sample material, and UPS is excellent in providing the fine structure of the valence band.

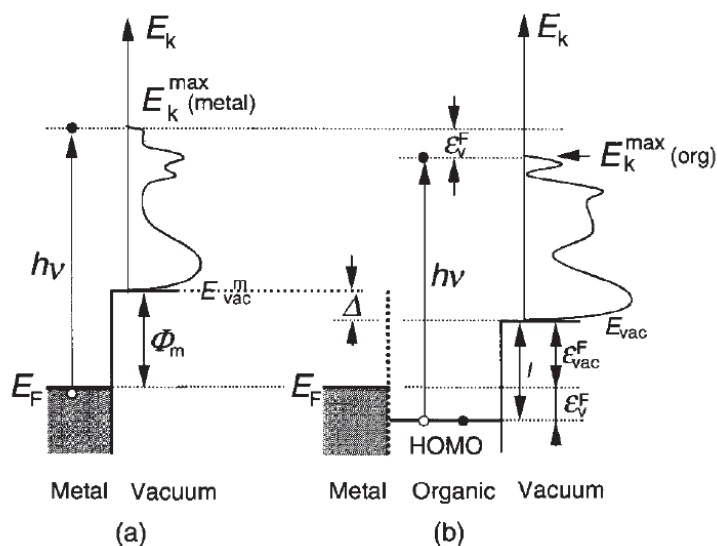
The fundamental principle of UPS is the “photoelectric effect” which was described by Albert Einstein in the early 20<sup>th</sup> century. When a light of particular wavelength and energy is shined on the surface of metal, it can lead to the emission of electrons. If the energy of the photons absorbed by the electrons in the metal is large enough to overcome the ionization energy then the electron escapes from the surface of the metal. The photoelectric spectrum consists of two principal components (see figure 1.9): (1) primary electrons which do not suffer inelastic collisions, and (2) secondary electrons, which are primary electrons which lost varying amount of energy before escaping. The primary peaks allow the determination of the binding energies of the electronic states in the sample, while the secondary states are used for the measurement of the work function of the sample. The kinetic energy ( $E_{Kin}$ ) of the photoelectron upon the absorption of a photon with adequate energy is given by

(Eqn 1.8)

$$E_{Kin} = h\nu - E_b - \phi_s$$

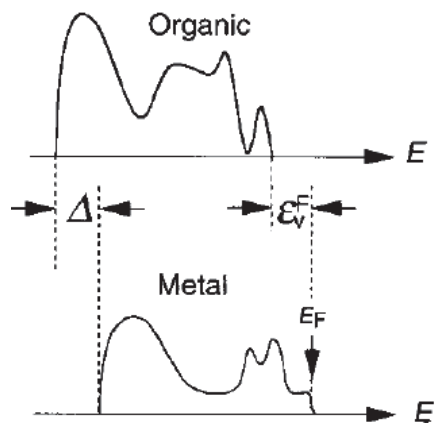
where ‘ $h$ ’ is the Planck constant, ‘ $\nu$ ’ is the frequency of the incident photon, ‘ $\phi_s$ ’ is the work function of the sample and ‘ $E_b$ ’ is the binding energy of the excited electron. The fastest electron of this spectrum will be primary electrons emitted directly from the Fermi edge ( $E_b = 0$ ) having  $E_{Kin} = h\nu - \phi_s$ . The energy of the absorbed photon needs to be greater than the work function of the material to allow the emission of photoelectron. For valence photoemission work, UPS utilizes helium discharge lamps with specific radiation lines: He1  $h\nu = 21.22$  eV. The photoexcited electrons are then passed through a kinetic energy analyzer into the detector. The energy resolution of the UPS measurement is 100-150 meV.

The sample for UPS is usually a thin film with tens of nanometers thickness; thicker samples may cause charging due to the accumulation of positive charge at the sample surface, which is left by the emission of negatively charged electrons. Figure 1.13 shows the principle of UPS and its application to determine the interfacial electronic state (73).



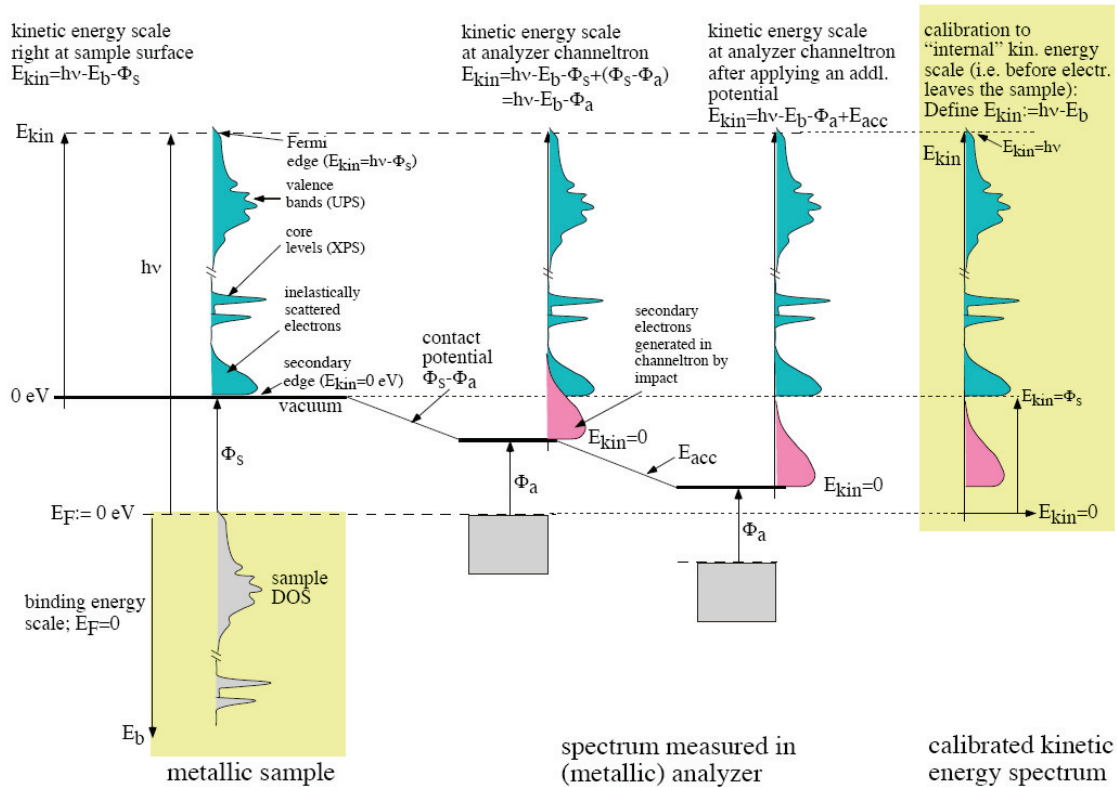
**Figure 1.13:** Principle of UPS study of an organic/metal interface. a) Photoemission from the metal. b) Photoemission from the organic layer deposited on the metal surface. Picture adopted from reference (5)

Figure 1.13(a) shows the electronic structure of a metal substrate sample and its photoemission process. The electrons in the occupied state are shown at the top of the Fermi level  $E_F$ , excited by the incident light of photon energy  $h\nu$ . The electrons with energy above the vacuum level (VL)  $E_{Vac}^m$  can escape from the surface. The electrons which escaped from the surface are then passed through the kinetic energy analyzer into the detector where they get counted. Figure 1.13(b) shows the situation when a thin organic layer is deposited on the metal surface. The spectrum becomes dominated by photoelectrons from the organic layer with increasing thickness. The electrons with maximum kinetic energy correspond to the electrons excited from the HOMO. The energy of the vacuum level shifts compared to that of the bare metal substrate. This shift is observed as ' $\Delta$ ' for the low energy cut-off of the photoelectron spectra. Thus the origin of the kinetic energy is also changed by the shift of the VL to the vacuum level of the organic layer  $E_{vac}$  (see figure 1.14). The energy difference of the fastest electron between the metal and the organic layer gives the energy of the top of the valence state of the organic layer  $\epsilon_V^F$  relative to the Fermi level of the metal. From the above figure 1.14 the shift of the right-hand edge gives  $\epsilon_V^F$ , while the shift of the left hand edge gives ' $\Delta$ '.



**Figure 1.14:** Shows the UPS spectra of metal and organic material with the energy of an emitted electron with an arbitrary origin as the abscissa. Picture adopted from reference (5).

More detailed explanation on the calibration of photoemission spectra refer Rudy Schalf tutorial lesson titled calibration of photoemission spectra and work function determination. (<http://rsl.eng.usf.edu/Documents/Tutorials/PEscalibration.pdf>).



**Figure 1.15:** Schematic of photoemission spectroscopy (PES) process on metallic sample. Picture adapted from Rudy Schalf tutorial lesson.

### 1.8.2 Inverse photoelectron spectroscopy:

Inverse Photoelectron spectroscopy (IPES) (88, 89) is considered as a complementary technique to photoemission spectroscopy (PES). As explained in section 1.5.1, PES probes the occupied density of states in a sample through the photoelectric effect, whereas IPES does the reverse, i.e. the sample is exposed to an electron beam and the emitted photons are collected. The detailed explanation regarding IPES is given in Dr. Rudy Schalf's tutor lessons. (<http://rsl.eng.usf.edu/Documents/Tutorials/TutorialsIPES.pdf>).

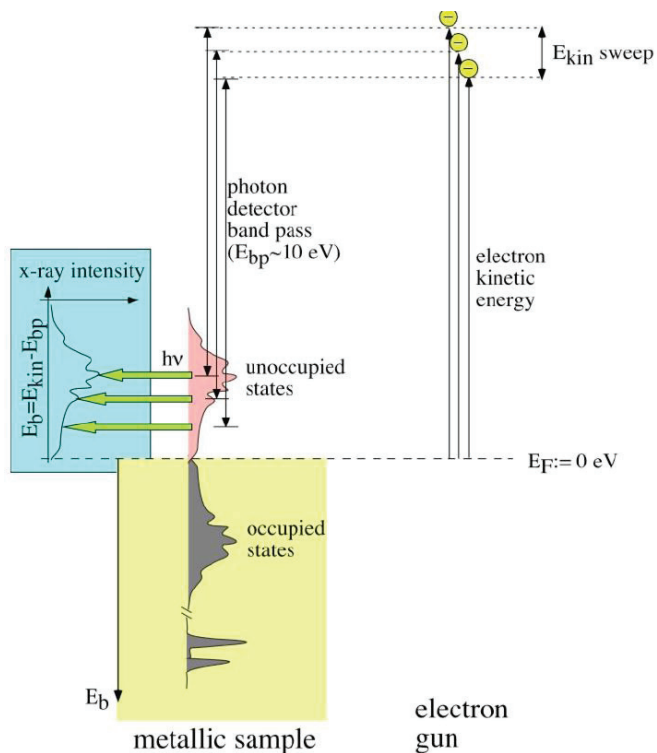


**Figure 1.16:** Schematic of IPES in “Isochromat” mode. Electrons with particular kinetic energy are emitted from the electron gun. At the sample surface they recombine into empty states above the Fermi level and photons are emitted. A detector with a narrow (0.6 eV) fixed energy window (10 eV) counts emitted photons. Variation of the electron kinetic energy allows scanning through the unoccupied states, resulting in IPES spectrum. (Figure adopted from Dr. Rudy Schalf’s tutorial lessons).

### 1.8.3 Other spectroscopic investigation methods:

The other major spectroscopic techniques include two-photon photoemission (2PPE) (90), and near-edge X-ray absorption fine structure (NEXAFS or XANES). These two techniques have proven to be powerful tools for investigating the energetics of organic molecule interfaces. 2PPE provides information on the transport gap ( $E_t$ ) or optical gap ( $E_{opt}$ ) of the molecular material, depending on whether the first of the two excitations is either inter or intramolecular (91, 92). In the intermolecular case, the hole state is measured by a two-photon excitation of an electron from the HOMO to the vacuum. The electron state is measured by first populating the LUMO with an external electron, eg. from the metal substrate, followed by a photoemission from the LUMO. In

the case of intramolecular excitation the first photon excites an electron from the HOMO to the LUMO, forming an exciton on the neutral molecule and populating the empty states across  $E_{opt}$  and the second photon breaks the electron-hole pair (71). 2PPE is very powerful and versatile tool for investigating the energetics of metal/molecule systems and if used in the time resolved mode, 2PPE becomes a powerful tool for probing the dynamics of charge exchange and excitation on organic systems (92). The HOMO-LUMO gap measured from the 2PPE measurement is the optical one i.e. the gap for onsite excitation of the neutral molecule, whereas for the PES/IPES it is the cation-anion gap that is measured, generally known as transport gap (71). It is often assumed that the transport gap controls the charge transfer from substrates to molecules, or transport measurement through organics.

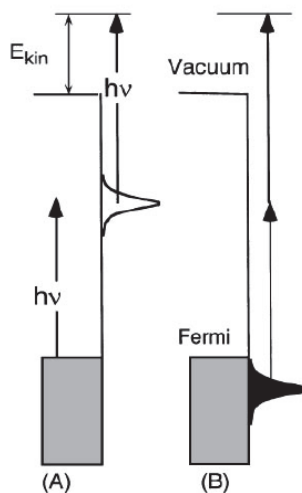


**Figure 1.17:** Schematic illustration of possibilities in two photon photoemission involving (A) unoccupied states below the vacuum level (B) and an occupied state below the Fermi level.

NEXAFS involves the excitation of an electron from a core level into unoccupied orbitals. Hence it provides information about the chemical state of the molecule and enables the exact determination of the LUMO energy (93). NEXAFS has much higher resolution and much higher sensitivity than IPES. NEXAFS seems preferable for the determination of unoccupied orbitals.

## 1.9 Research Objectives:

The ultimate goal of molecular electronics is to make molecule based functional devices. Progress in the field has been inhibited by the difficulty in determining the energy levels of molecules after being perturbed by interaction with the conducting contacts. A complete understanding of a molecular junction would require considering the junction structure as one electronic system, rather than attributing device characteristics only to isolated molecules or contacts. The overall objective of the research work described in this thesis is to investigate the interaction of light with carbon-based molecular electronic junctions. The mechanism(s) underlying the observed photoeffects were identified and used to determine the interfacial transport barriers in molecular tunnel junctions.

Following the introductory chapter, Chapter 2 describes how bonding the molecule to a substrate results in electronic inductive effects which modulate the energy levels of the system and modifies the tunneling barrier. This finding indicates that the entire system must be considered to understand the impact of a variety of electronic factors that act to determine the tunnel barriers.

Chapter 3 describes the experimental procedures and instrumental apparatus used to obtain photocurrent from carbon based molecular junction. We measured the photocurrent spectra for large-area aliphatic and aromatic molecular tunnel junctions with partially transparent copper top contacts.

In chapter 4 we describe the different methods used to differentiate the “photo-effects” of IPE mechanism from the secondary molecular absorption “MA” mechanism. The photocurrent measurement is correlated with the absorption spectra for all the molecules used in this study. A mechanism is proposed for the photocurrent generation at IPE regime. IPE mechanism contains

information regarding energy level alignment within a complete, working molecular junction and its sign indicates whether transport is through the occupied or unoccupied molecular orbitals.

Chapter 5 describes about the possible mechanism(s) to explain the observed photoeffects when the molecular layer starts absorbing light. In addition a comparison of photocurrent yield for aromatic junctions with partially transparent carbon/copper top contacts with Cu only top contact has been carried out.

Finally, this thesis is ended with conclusions of all the work presented herein and outlook on future work and directions of molecular electronics.

## 1.10 References:

1. Feynman R (1960) There's Plenty of Room at the Bottom. *Engineering and Science*. 23(5):22-36.
2. Aviram A & Ratner MA (1974) Molecular Rectifiers. *Chem. Phys. Lett.* 29(2):277-283.
3. Carroll RL & Gorman CB (2002) The Genesis of Molecular Electronics. *Angew. Chem. Int. Ed.* 41:4378-4400.
4. Binnig G & Rohrer H (1983) Scanning Tunneling Microscopy. *Surf. Sci.* 126:236-244.
5. Murray RW & Elliot CM (1976) Chemically Modified Electrodes. *Anal. Chem.* 48(8):1247-1254.
6. Murray RW (1980) Chemically Modified Electrodes. *Acc. Chem. Res.* 13:135-141.
7. Allara D & Nuzzo RG (1985) Spontaneously Organized Molecular Assemblies. 2. Quantitative Infrared Spectroscopic Determination of Equilibrium Structures of Solution-Adsorbed n-alkanoic Acids on an Oxidized Aluminum Surface. *Langmuir*. 1:52-66.
8. Porter MD, Bright TB, Allara DL, & Chidsey CED (1987) Spontaneously Organized Molecular Assemblies. 4. Structural Characterization of n-alkyl Thiol Monolayers on

- Gold by Optical Ellipsometry, Infrared Spectroscopy, and Electrochemistry. *J. Am. Chem. Soc.* 109(12):3559-3568.
9. McCreery RL & Bergren AJ (2009) Progress with Molecular Electronic Junctions: Meeting Experimental Challenges in Design and Fabrication. *Adv. Mater.* 21:4303-4322.
  10. Cahen D, Haick H, Niitsoo O, & Ghabboun J (2007) Electrical Contacts to Organic Molecular Films by Metal Evaporation: Effect of Contacting Details. *J. Phys. Chem. C.* 111:2318-2329.
  11. Wold DJ & Frisbie CD (2001) Fabrication and Characterization of Metal-Molecule-Metal Junctions by Conducting Probe Atomic Force Microscopy. *J. Am. Chem. Soc.* 123:5549.
  12. Bumm LA, Arnold JJ, Dunbar TD, Allara DL, & Weiss PS (1999) Electron Transfer through Organic Molecules. *J. Phys. Chem.* 103(38):8122-8127.
  13. Fan F-RF, Yang J, Cai I, Price DW, Dirk SM, Kosynkin DV, Yao Y, Rawlett AM, Tour JM & Bard AJ (2002) Charge Transport through Self-Assembled Monolayers of Compounds of Interest in Molecular Electronics. *J. Am. Chem. Soc.* 124(19):5550-5560.
  14. Holmlin RE, Haag R, Chabinyc ML, Ismagilov RF, Cohen AE & Whitesides GM (2001) Electron Transport through Thin Organic Films in Metal-Insulator-Metal Junctions Based on Self-Assembled Monolayers. *J. Am. Chem. Soc.* 123:5075-5085.
  15. Chabinyc ML, Holmlin RE, Jacobs H, Skulason H, Frisbie CD, Mujica V, Ratner MA, Rampi MA, Whitesides GM (2002) Molecular Rectification in a Metal-Insulator-Metal Junction Based on Self-Assembled Monolayers. *J. Am. Chem. Soc.* 124 11730-11736.

16. Chang S-C, Li Z, Lau CN, Larade B, & Williams RS (2003) Investigation of a Model Molecular-Electronic Rectifier with an Evaporated Ti-Metal Top Contact. *App. Phys. Lett.* 83(15):3198-3200.
17. Stewart DR, Ohlberg DAA, Beck PA, Stoddart JF (2004) Molecule-Independent Electrical Switching in Pt/Organic Monolayer/Ti Devices. *Nano Lett.* 4(1):133-136.
18. Ranganathan S, Steidel I, Anariba F, & McCreery RL (2001) Covalently Bonded Organic Monolayers on a Carbon Substrate: A New Paradigm for Molecular Electronics. *Nano Lett.* 1:491-494.
19. Anariba F & McCreery RL (2002) Electronic Conductance Behavior of Carbon-Based Molecular Junctions with Conjugated Structures. *J. Phys. Chem. B.* 106:10355-10362.
20. Ohtani H, Wilson RJ, Chiang S, & Mate CM (1988) Scanning Tunneling Microscopy Observations of Benzene Molecules on the Rh(111)-(3x3)(C<sub>6</sub>H<sub>6</sub>+2CO) Surface. *Phys. Rev. Lett.* 60(23):2398-2401.
21. Bain CD & Troughton EB (1989) Formation of Monolayers Films by Spontaneous Assembly of Organic Thiols from Solution onto Gold. *J. Am. Chem. Soc.* 111:321-335.
22. Laibinis PE, Whiteside GM, Parikh AN & Nuzzo R (1991) Comparison of the Structures and Wetting Properties of Self-assembled Monolayers of n-alkanethiols on the Coinage Metal Surfaces, Copper, Silver, and Gold. *J. Am. Chem. Soc.* 113(19):7152-7167.
23. Laibinis PE & Whitesides GM (1991) Attenuation of Photoelectrons in Monolayers of n-Alkanethiols Adsorbed on Copper, Silver and Gold. *J. Phys. Chem.* 95:7017-7021.
24. Li Z, Chang S-C, & Williams RS (2003) Self-Assembly of Alkanethiol Molecules onto Platinum and Platinum Oxide Surfaces. *Langmuir.* 19(17):6744-6749.

25. Love JC, Wolfe DB, Haasch R, Chabynyc ML, Paul KE, Whitesides GM & Nuzzo RG (2003) Formation and Structure of Self-Assembled Monolayers of Alkanethiolates on Palladium. *J. Am. Chem. Soc.* 125:2597-2609.
26. Magnussen OM, Ocko BM, Deutsch M, Regan MJ, Pershan PS, Abernathy D & Legrand JF (1996) Self-Assembly of Organic Films on a Liquid Metal. *Nature.* 384:6606.
27. Baum T, Ye S, & Uosaki K (1999) Formation of Self-Assembled Monolayers of Alkanethiols on GaAs Surface with in Situ Surface Activation by Ammonium Hydroxide. *Langmuir.* 15(25):8577-8579.
28. Schwartzman M, Sidorov V, Ritter D, & Paz Y (2003) Passivation of InP Surfaces of Electronic Devices by Organothiolated Self-Assembled Monolayers. *J Vac Sci Technol B: Microelectron Nanometer Struct Process Meas Phenom.* 21(1):148-155.
29. Nuzzo RG & Allara DL (1983) Adsorption of Bifunctional Organic Disulfides on Gold Surfaces. *J. Am. Chem. Soc.* 105:4481-4483.
30. Ulman A (1991) *An Introduction to Ultrathin Organic Films From Langmuir-Blodgett to Self-Assembly* (Academic Press, San Diego, CA) 1st Ed.
31. Schreiber F, Eberhardt A, Schwartz LP, Wetterer SM, Lavrich DJ, Berman L & Scholes G (1998) Adsorption Mechanisms, Structures, and Growth Regimes of an Archetypal Self-Assembling System: Decanethiol on Au(111). *Phys. Rev. B.* 57(19):12476-12481.
32. Nitzan A & Ratner MA (2003) Electron Transport in Molecular Wire Junctions. *Science.* 300:1384-1389.
33. Xue Y, Datta S, & Ratner MA (2001) Charge Transfer and 'Band Lineup' in Molecular Electronic Devices: A Chemical and Numerical Interpretation. *J. Chem. Phys.* 115:4292-4299.

34. Love JC, Estroff LA, Kriebel JK, Nuzzo RG, & Whitesides GM (2005) Self-Assembled Monolayers of Thiolates on Metals as a Form of Nanotechnology. *Chem. Rev.* 105:1103-1170.
35. Fisher GL, Walker AV, Hooper AE, Opila RL & Allara DL (2002) Bond Insertion, Complexation, and Penetration Pathways of Vapor-Deposited Aluminum Atoms HO- and CH<sub>3</sub>O-Terminated Organic Monolayers. *J. Am. Chem. Soc.* 124:5528-5541.
36. Walker AV, Tighe TB, Cabarcos OM, Reinard MD, Brendan C, Uppili Sundararajan & Allara DL (2004) The Dynamics of Noble Metal Atom Penetration through Methoxy-Terminated Alkanethiolate Monolayers. *J. Am. Chem. Soc.* 126(12):3954-3963.
37. Silerova R & Gyepi-Garbrah SH (2001) Probing Temperature-Dependent Behavior in Self-Assembled Monolayers by AC-Impedance Spectroscopy. *Phys. Chem. Chem. Phys.* 3:2117-2123.
38. McCreery RL (2008) Advanced Carbon Electrode Materials for Molecular Electrochemistry. *Chem. Rev.* 108(7):2646-2687.
39. Delamar M, Hitmi R, Pinson J, & Saveant JM (1992) Covalent Modification of Carbon Surfaces by Grafting of Functionalized Aryl Radicals Produced from Electrochemical Reduction of Diazonium Salts. *J. Am. Chem. Soc.* 114: 5883-5884.
40. Barbier B, Pinson J, Desarmot G, & Sanchez M (1990) Electrochemical Bonding of Amines to Carbon Fiber Surfaces Toward Improved Carbon-Epoxy Composites. *J. Electrochem. Soc.* 137(6):1757.
41. Knickerbocker T, Strother T, Schwartz MP, Russell, Smith LM & Hamers RJ (2003) DNA-Modified Diamond Surfaces. *Langmuir.* 19(6):1938-1942.

42. Ranganathan S, McCreery RL, Majji SM, & Madou M (2000) Photoresist-Derived Carbon for Microelectrochemical Applications. *J. Electrochem. Soc.* 147:277 - 282.
43. Bergren AJ, Harris KD, Deng F, & McCreery R (2008) Molecular Electronics using Diazonium-Derived Adlayers on Carbon with Cu Top Contacts: Critical Analysis of Metal Oxides and Filaments. *J. Phys. Condens. Matter.* 20:374117.
44. Mahmoud AM, Bergren AJ, Pekas N, & McCreery RL (2011) Towards Integrated Molecular Electronic Devices: Characterization of Molecular Layer Integrity During Fabrication Processes. *Adv. Funct. Mater.* 21(12):2273-2281.
45. Mahmoud AM, Bergren AJ, & McCreery RL (2009) Derivatization of Optically Transparent Materials with Diazonium Reagents for Spectroscopy of Buried Interfaces. *Anal. Chem.* 81(16):6972-6980.
46. Kumar R, Yan H, McCreery RL, & Bergren AJ (2011) Electron-beam Evaporated Silicon as a Top Contact for Molecular Electronic Device Fabrication. *Phys. Chem. Chem. Phys.* 13:14318-14324.
47. Yan H, Bergren AJ, & McCreery RL (2011) All-Carbon Molecular Tunnel Junctions. *J. Am. Chem. Soc.* 133(47):19168-19177.
48. Bergren AJ, McCreery RL, Stoyanov SR, Gusarov S, & Kovalenko A (2010) Electronic Characteristics and Charge Transport Mechanisms for Large Area Aromatic Molecular Junctions. *J. Phys. Chem. C.* 114:15806-15815.
49. Hamers RJ, Coulter SK, Ellison MD, Hovis JS, Padowitz DF & Schwartz MP (2000) Cycloaddition Chemistry of Organic Molecules with Semiconductor Surfaces. *Acc. Chem. Res.* 33(9):617-624.

50. Reed MA, Zhou C, Muller CJ, Burgin TP, & Tour JM (1997) Conductance of a Molecular Junction. *Science*. 278:252.
51. Salomon A, Cahen D, Lindsay S, Tomfohr J, Engelkes VB, Frisbie CD (2003) Comparison of Electronic Transport Measurements on Organic Molecules. *Adv. Mater.* 15(22):1881-1890.
52. Kim B, Beebe JM, Olivier C, Rigaut S, Touchard D, Kushmerick JG, Zhu XY and Frisbie CD (2007) Temperature and Length Dependence of Charge Transport in Redox-Active Molecular Wires Incorporating Ruthenium(II) Bis(s-arylacetylide) Complexes. *J. Phys. Chem. C*. 111:7521-7526.
53. Haiss W, Zalinge HV, Higgins SJ, Bethell D, Hobenreich H, Cahen D & Nichols RJ (2003) Redox State Dependence of Single Molecule Conductivity. *J. Am. Chem. Soc.* 125(50):15294-15295.
54. Sedghi G, Sawada K, Esdaile LJ, Hoffmann M, Anderson HL, Bethell D, Haiss W, Higgins SJ & Nichols RJ (2008) Single Molecule Conductance of Porphyrin Wires with Ultralow Attenuation. *J. Am. Chem. Soc.* 130(27):8582-8583.
55. Cui XD, Primak A, Zarate X, Tomhofr J, Sankey OF, Moore AL, Gust D, harris G, Lindsay SM (2001) Reproducible Measurement of Single-Molecule Conductivity. *Science*. 294:571-574.
56. Kim, Beebe JM, Jun Y, Zhu XY, & Frisbie CD (2006) Correlation between HOMO Alignment and Contact Resistance in Molecular Junctions: Aromatic Thiols versus Aromatic Isocyanides. *J. Am. Chem. Soc.* 128(15):4970-4971.
57. McCreery RL (2009) Electron Transport and Redox Reactions in Molecular Electronic Junctions. *ChemPhysChem*. 10(14):2387-2391.

58. McCreery RL (2004) Molecular Electronic Junctions. *Chem. Mater.* 16:4477-4496.
59. Simmons JG (1971) *DC Conduction in Thin Films* (Mills and Boon Ltd., London).
60. Yamamoto H & Waldeck DH (2002) Effect of Tilt-Angle on Electron Tunneling through Organic Monolayer Films. *J. Phys. Chem. B.* 106(30):7469-7473.
61. Skourtis SS, Archontis G, & Xie Q (2001) Electron Transfer Through Fluctuating Bridges: On the Validity of the Superexchange Mechanism and time-Dependent Tunneling Matrix Elements. *J. Chem. Phys.* 115(20):9444-9462.
62. Galperin M, Segal D, & Nitzan A (1999) Perturbation Theory Approach to Tunneling: Direct and Resonance Transmission in Superexchange Models. *J. Chem. Phys.* 111(4):1569-1579.
63. Mujica V & Ratner MA (2001) Current-Voltage Characteristics of Tunneling Molecular Junctions for Off-Resonance Injection. *Chem. Phys.* 264(3):365-370.
64. Mujica V, Roitberg AE, & Ratner M (2000) Molecular Wire Conductance: Electrostatic Potential Spatial Profile. *J. Chem. Phys.* 112(15):6834-6839.
65. Meggers E, Michel-Beyerle ME, & Giese B (1998) Sequence Dependent Long Range Hole Transport in DNA. *J. Am. Chem. Soc.* 120:12950-12955.
66. Cordes M & Giese B (2009) Electron Transfer in Peptides and Proteins. *Chem. Soc. Rev.* 38:892-901.
67. Segal D, Nitzan A, Davis WB, Wasielewski MR, & Ratner MA (2000) Electron Transfer Rates in Bridged Molecular Systems 2. A Steady-State Analysis of Coherent Tunneling and Thermal Transitions. *J. Phys. Chem. B.* 104(16):3817-3829.
68. Buttiker M & Landauer R (1982) Traversal Time for Tunneling. *Phys. Rev. Lett.* 49:1739.

69. Hwang J, Wan A, & Kahn A (2009) Energetics of Metal-Organic Interfaces: New Experiments and Assessment of the Field. *Mater. Sci. Eng. R-Rep.* 64:1-31.
70. Cahen D & Kahn A (2003) Electron Energetics at Surfaces and Interfaces: Concepts and Experiments. *Adv. Mater.* 15(4):271-277.
71. Cahen D, Kahn A, & Umbach E (2005) Energetic of molecular interfaces. *Mater. Today.* 8(7):32-41.
72. Salomon A, Bocking T, Gooding JJ, & Cahen D (2006) How Important Is the Interfacial Chemical Bond for Electron Transport through Alkyl Chain Monolayers? *Nano Lett.* 6(12):2873-2876.
73. Ishii H, Sugiyama K, Ito E, & Seki K (1999) Energy Level Alignment and Interfacial Electronic Structures at Organic/Metal and Organic/Organic Interfaces. *Adv. Mater.* 11(8):605-625.
74. Seki K & Ishii H (1998) Photoemission Studies of Functional Organic Materials and their Interfaces. *J. Electron. Spectros. Rel. Phenom.* 88-91:821-830.
75. Ishii H & Seki K (1997) Energy Level Alignment at Organic/Metal Interfaces Studied by UV Photoemission: Breakdown of Traditional Assumption of a Common Vacuum Level at the Interface. *IEEE. Electr. Device. L.* 44(8):1295-1301.
76. Hill IG & Kahn A (1998) Energy level Alignment at Interfaces of Organic Semiconductor Heterostructures. *J. Appl. Phys.* 84(10):5583-5586.
77. Rhoderick EA & Williams RH (1998) *Metal-Semiconductor contacts.* (2nd edition, Clarendon, Oxford).
78. Shen C & Kahn A (2001) The Role of Interface States in Controlling the Electronic Structure of Alq3/Reactive Metals Contacts. *Org. Electron.* 2:89-95.

79. Wan AS-C (2006) *Electrical engineering, vol. Ph.D.*, (Princeton University, Princeton).
80. Schalf R( <http://rsl.eng.usf.edu/Documents/Tutorials/TutorialsWorkFunction.pdf>).
81. Woodruff DP & Delchar TA (1986) *Modern Techniques of Surface Science* (Cambridge University Press, Cambridge 1986).
82. Wandelt K (1987) *Thin Metal Films and Gas Chemisorption* (Elsevier, Amsterdam 1987).
83. Lang N & Kohn W (1970) Theory of Metal Surfaces: Charge Density and Surface Energy. *Phys. Rev. B.* 1(12):4555-4568.
84. Lang ND & Kohn W (1971) Theory of Metal Surfaces: Work Function. *Phys. Rev. B.* 3(4):1215-1223.
85. William R, Seki K, Kahn A & Pireaux JJ (2001) *Conjugated Polymer and Molecular Interfaces* (Marcel Dekker, Inc).
86. Hoffman R (1989) *Solids and Surfaces* (VCH NewYork, Inc).
87. Gensterblum G, Pireaux JJ, Thiry PA, Caudano R, Vigneron JP, Lambin PH & Lucas AA (1991) High-Resolution Electron-Energy-Loss Spectroscopy of thin Films of C60 on Si(100). *Phy. Rev. Lett.* 67(16):2171-2174.
88. Wu CI, Hirose Y, Sirringhaus H, & Kahn A (1997) Electron-Hole Interaction Energy in the Organic Molecular Semiconductor PTCDA. *Chem. Phys. Lett.* 272(1-2):43-47.
89. Weaver JH & Poirier DM (1994) *Solid State Physics* (Academic, NewYork).
90. Zhu XY (2002) Electron Transfer at Molecule-Metal Interfaces: A Two-Photon Photoemission Study. *Annu. Rev. Phys. Chem.* 53:221-247.
91. Probst M & Haight R (1997) Unoccupied Molecular Orbital States of tris (8-hydroxy quinoline) Aluminum: Observation and Dynamics. *Appl. Phys. Lett.* 71(2):202-204.

92. Zhu XY (2004) Electronic Structure and Electron Dynamics at Molecule–Metal Interfaces: Implications for Molecule-based Electronics. *Surf. Sci. Rep.* 56(1-2):1-83.
93. Taborski J, Vaterlein P, Deitz H, Zimmermann U, & Umbach E (1995) NEXAFS Investigation on Ordered Adsorbate Layers of Large Aromatic Molecules. *J. Electron. Spectrosc. Relat. Phenom.* 75:129-147.
94. Spicer WE, Lindau I, Gregory PE, Garner CM, Pianetta P & Chye PW (1976) Synchrotron Radiation Studies of Electronic Structure and Surface Chemistry of GaAs, GaSb, and InP. *J. Vac. Sci. Technol. A* 13(4):780-785.
95. Choong VE, Mason MG, Tang CW, & Gao Y (1998) Investigation of the Interface Formation Between Calcium and tris-(8-hydroxy quinoline) Aluminum. *Appl. Phys. Lett.* 72(21):2689-2691.
96. Heine V (1965) Theory of Surface States. *Phys. Rev.* 138(6A):A1689-A1696.
97. Louie SG & Cohen H (1976) Electronic Structure of a Metal-Semiconductor Interface. *Phys. Rev. B* 13(6):2461-2469.
98. Vazquez H, Oszwaldowski R, Pou P, Ortega J, Perez R, Flores F & Kahn A (2004) Dipole Formation at metal/PTCDA Interfaces: Role of the Charge Neutrality Level. *EuroPhys. Lett* 65(6):802.
99. Vazquez H, Flores F, Oszwaldowski R, Ortega J, Perez R & Kahn A (2004) Barrier Formation at Metal–Organic Interfaces: Dipole Formation and the Charge Neutrality Level. *Applied Surface Science* 234(1):107-112.

# Chapter-2

## Charge Transport in Molecular Electronic Junctions: Compression of the Molecular Tunnel Barrier in the Strong Coupling Regime.

### 2.1 Introduction:

Molecular junctions are essentially modified electrodes which are familiar to electrochemists, in which the electrolyte is replaced by a conducting “contact.” It is generally hypothesized that changing molecular structure will alter system energy levels, leading to a change in the transport barrier. The conductance of electrical charge through and across molecular entities is the basis of molecular and organic electronics (1, 2). Understanding, controlling, and designing electronic circuits using organic molecules as components is a major goal of molecular electronics (3). However, it has been a challenge to identify all of the factors that govern the conductance of a molecular junction. Rather than being a simple property of the molecule itself, many circumstances contribute to the measured electronic properties of the junction. Some important features that contribute to the junction property includes the nature of the molecule-contact bonding (4), the properties of the contact materials (5, 6), the orientation of the molecules relative to the contacts (7), and the structure of the molecule (5, 8, 9). While there is no general consensus on exactly how each of these features affects the conductance of the junction, it is generally agreed that the alignment of the molecular energy level vs. the contact energy levels is an important factor (10-13). The offset between the substrate Fermi energy ( $E_f$ ) and the molecular orbital closest in energy to  $E_f$  is often used to estimate charge transport barriers in the

context of tunneling or charge injection models. However, it is increasingly clear that the situation is complex and that there is no simple method for measuring these energy levels in a completed junction. The actual energy barrier in a molecular tunnel junction is a function of the way the molecule interacts with the contacts in the completed device, a function that in turn depends on a number of factors such as bond type, electronegativity and orbital energies.

There are numerous paradigms for studying charge transport in molecular electronics (3) which use different techniques to make electrical contacts between the conductors and the molecular components. While each method for studying charge transport in molecular electronics has certain advantages and disadvantages, it is clear that the entire system i.e. two contact electrodes along with molecules must be considered in order to delineate the main factors influencing molecular conduction. While many groups employ thiolate-based self-assembled monolayers (SAMs) on metallic substrates as a base system, we have taken an alternative approach using carbon electrodes (6, 14-19). The foundation of this paradigm is a flat carbon electrode, composed of pyrolyzed photo-resist films (PPF), with covalently bonded nanoscopic molecular layers deposited using the electrochemical reduction of diazonium reagents. The covalent bonds formed between the molecules and the substrate lead to strong electronic coupling (20, 21), remarkable stability (6, 19, 22), and the ability to vapour deposit top contact materials without degrading the layer integrity (22, 23). As a consequence, large area ( $\sim 0.0013 \text{ cm}^2$ ) molecular junctions with the general structure of carbon/molecule/Cu can be made in high yield (typically  $>90\%$ ), with good reproducibility, and are robust under potential cycling (i.e., the electronic properties of the devices do not change after more than  $10^9$  cycles to  $\pm 1 \text{ V}$ ) and temperature excursions in the range of 5 K to  $350^\circ\text{C}$  (18, 19). Due to these properties, the

carbon/molecule/Cu system is a good candidate for systematic studies into the factors that control charge transport, especially in the strong coupling regime.

We extend our investigations to include a variety of molecular structures in order to determine how energy level alignment is affected. After selecting molecules that have calculated gas-phase molecular orbital energies (i.e., HOMOs and LUMOs) that vary by  $>2$  eV, we examined the factors that control energy level alignment after the molecules bonded to the surface. We also examined the junction conductance and attenuation factors for these structures and correlated the electronic properties with electronic structure measurements. We also used ultraviolet photoelectron spectroscopy (UPS) to probe the energy levels of modified carbon electrodes to determine a model that explains how and why the molecule-surface energy levels change upon molecule-surface bonding. UPS provides an estimate of the molecular HOMO onset energy which can be compared to tunneling barrier values obtained from electronic measurements. These studies reveal some of the important factors that control the conductance of molecular junctions relative to energy level alignment, and may lead to promising strategies for designing molecular junctions with targeted electronic properties.

## **2.2 Junction fabrication and electrical characterization:**

### **2.2.1 Junction fabrication :**

Polished silicon wafers (Technical Glass Products, <http://www.technicalglass.com/>) were diced into 1.2 x 1.5 cm chips to serve as substrates. Acetonitrile, acetone and isopropanol (HPLC grade, Fischer Scientific) were used as received. Water was purified by a Millipore system (18M $\Omega$ ,  $< 3$  ppb TOC). The substrates were initially cleaned by sonication in acetone, isopropanol and finally ultrapure water for 10 mins in each solvent. The substrates were then

dried in a directed stream of nitrogen gas. Conductive carbon in the form of pyrolyzed photoresist films (PPF) were produced by first spin-coating commercially available photoresist (AZ-P4330-RS, AZ Electronic materials, Somerville, NJ) onto pre-cleaned silicon chips (24, 25) at 6000 rpm for 40 seconds (two coats) followed by a soft baking at 90° C for 15 mins. Next, the photoresist was patterned using photolithography to yield four parallel 0.5 mm wide lines. Finally, the photoresist was converted to conductive carbon by heating to 1100° C (held for 60 min) in a tube furnace with a constant flow of forming gas (5% H<sub>2</sub>, balance N<sub>2</sub> at 100 mL·min<sup>-1</sup>). PPF is a flat (RMS roughness <0.5 nm measured by AFM) and electrically conductive (resistivity ~0.005 Ω cm) substrate upon which molecules are bonded (see figure 2.1) (24).

Formation of molecular layers ranging from 1-5 nm thickness (measured using AFM) was carried out by electrochemical reduction of diazonium salts in solution (see step-6 in figure 2.1). For this step, PPF was used as the working electrode in a three-electrode electrochemical cell with a 1 mM solution of the diazonium precursor with 0.1 M tetrabutylammonium tetrafluoroborate (TBABF<sub>4</sub>) as the supporting electrolyte in acetonitrile. To deposit the molecular layer, cyclic voltammetric sweeps starting from +0.4 V versus Ag/Ag<sup>+</sup>, to a desired negative potential as described below. The switching potential and the number of sweeps depend on the molecule used and the desired thickness. The switching potential for a given diazonium salt is selected by finding out the reduction potential value of that diazonium molecule. In order to get complete reduction of diazonium salts, the switching potential was set to be 0.2-0.4 V negative of the reduction peak potential. After modification, the sample was rinsed with acetonitrile and dried using a stream of nitrogen. The dried substrates were then transferred to an electron-beam evaporator (Kurt J. Lesker PVD75), where various metals were deposited directly onto the surface of the molecular layer. The chamber was evacuated to 3.0 x 10<sup>-6</sup> Torr before beginning

the deposition. For junction fabrication metals were deposited through a shadow mask (0.6 mm) oriented perpendicular to PPF strips to result in a cross-bar junction. The deposition rate was  $1 \text{ \AA s}^{-1}$  and the metal thickness was measured by a quartz crystal microbalance (QCM). Junctions are designated by the various layers from bottom to top with the top contact metal layer thickness indicated in parentheses, and measured in nm. For example, PPF/AB/Cu (20) indicates AB layer on 1-2  $\mu\text{m}$  thick PPF with copper top contact 20 nm thick. In all the cases where the current-voltage behaviour was determined, the junction area was  $3.0 \times 10^{-3} \text{ cm}^2$ .

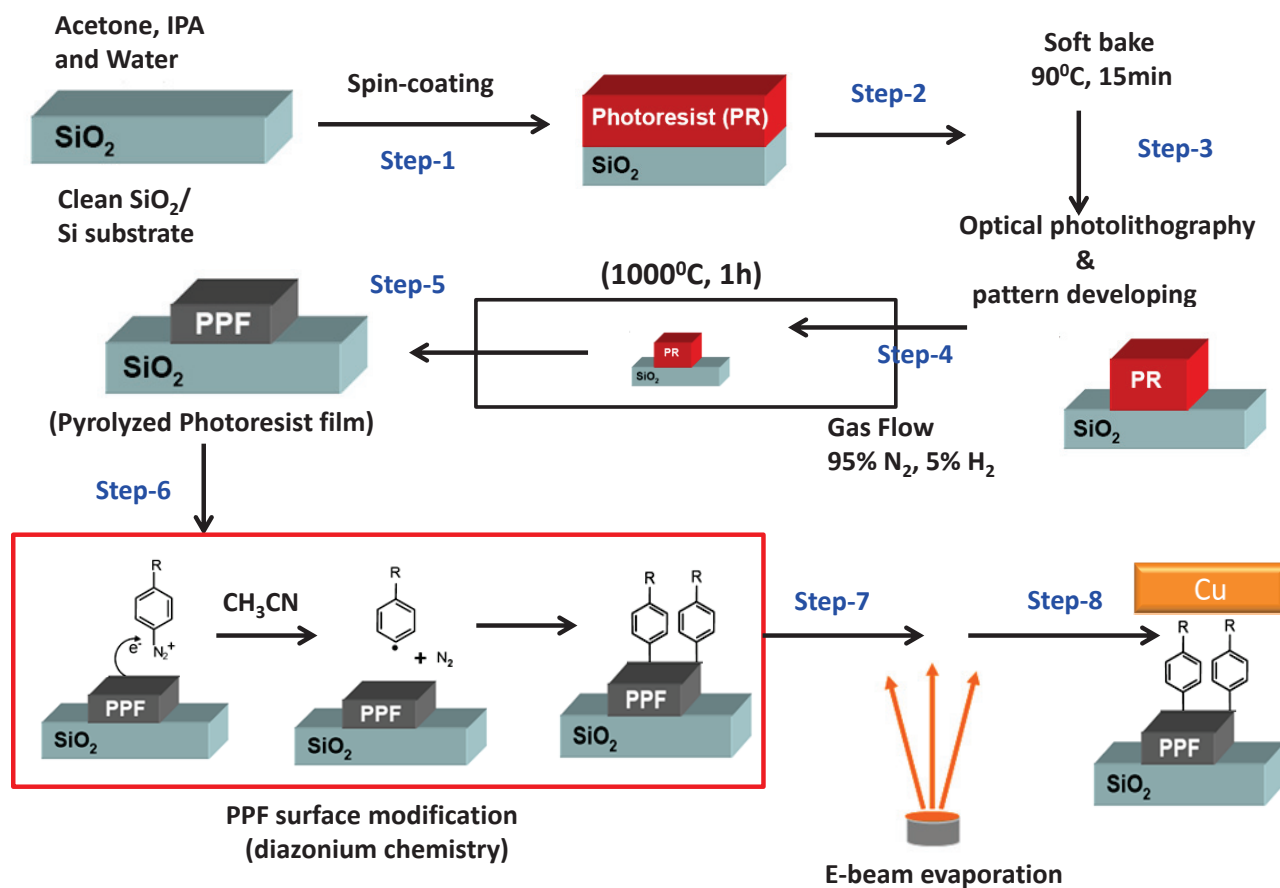


**Figure 2.1:** Flow chart for fabrication of carbon based molecular junction.

### 2.2.2 Molecular structures used in this study:

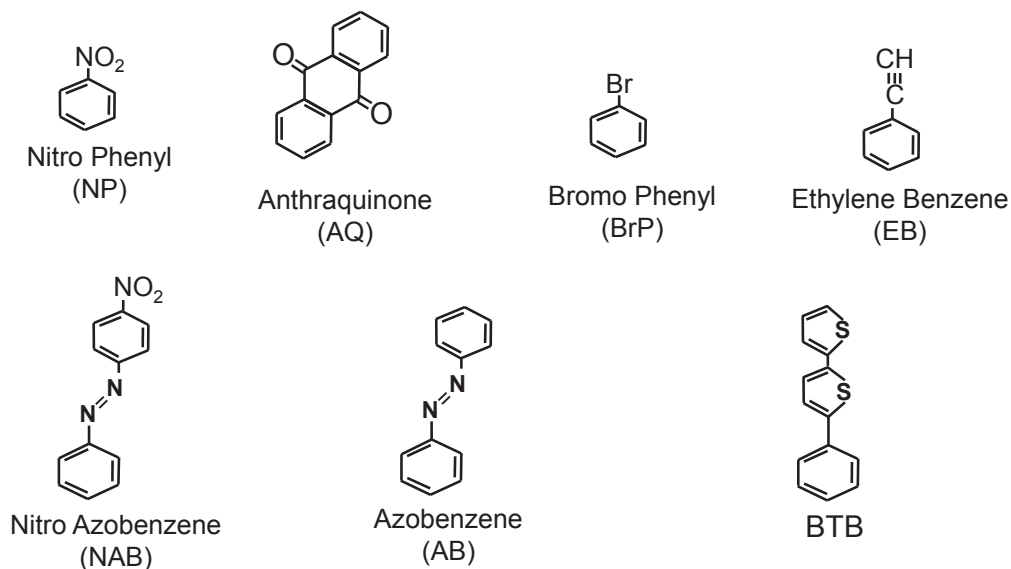


**Figure 2.2:** Molecular structures used in this study. NP = Nitrophenyl, AQ = Anthraquinone, NAB = Nitroazobenzene, BrP = Bromophenyl, EB = Ethynylbenzene, AB = Azobenzene, and BTB = Bisthienylbenzene.

### 2.2.3 Conditions for film growth:

The general procedure for molecular layer growth used in our study is given in this section. Derivatization of PPF surfaces was performed by the reduction of the corresponding diazonium salt in acetonitrile (Aldrich) with *n*-tetrabutylammonium tetrafluoroborate (0.1 M; Aldrich) as the supporting electrolyte. Tetrafluoroborate diazonium salts of all the molecules were prepared using existing procedures(26, 27). The diazonium salt solutions were freshly prepared, degassed thoroughly (up to 20 mins) by purging with argon gas to ensure low oxygen content before derivatization.

In all cases except BTB, the carbon surface (PPF) was used as the working electrode in a three-electrode electrochemical cell in a dilute solution (1.0 mM) of diazonium precursor (2.0 mM for both 1-AQ, and 2-AQ) in acetonitrile (with 0.1 M tetrabutylammonium tetrafluoroborate as supporting electrolyte). External contact to the PPF electrode was made with an alligator clip

connected to the top portion of PPF. Electrografting was performed by sweeping the electrode potential at a rate of 0.1 or 0.2 V s<sup>-1</sup> from a potential where no reduction occurs (+0.4 V vs. Ag/Ag<sup>+</sup>) to a negative potential of -0.6 V for (AB, NAB), -0.8V for (1AQ,2AQ), NP (-1.1 V) and BrP(-1.2 V), respectively (see figure 2.3). In the case of EB, potential sweep was done from 0.3 to -0.8 V. The numbers of cycles were also varied from 1 to 10, and also a higher negative potential was used for all molecules to yield different thickness (see figure 2.4).

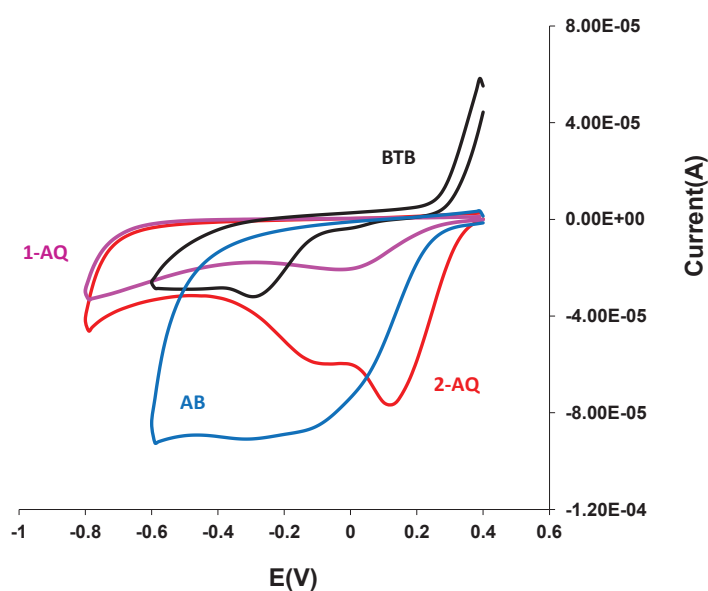


**Figure 2.3:** Cyclic voltammograms of (1AQ, BTB, 2AQ, AB) diazonium ions on carbon (PPF) in 0.1 M TBABF<sub>4</sub> in acetonitrile. Single scan was used for all the molecules with a scan rate of 200 mV/s.

**In situ diazonium formation of BTB:** An acetonitrile (ACN) solution (20 mL) containing 4-amino-1-bisthiénylbenzene (5mM, ~2.6 mg) and tetrabutylammonium tetrafluoroborate (TBABF<sub>4</sub>, 0.1M, ~0.66 g) as supporting electrolyte was prepared and degassed with high purity Ar for ~30 mins. Tert-butyl nitrite (18 µL) was then added to the above solution and was stirred for 15 mins before electrografting was started. The diazonium salt concentration may vary with time, so the time elapsed before surface derivatization was kept constant. After surface modification, samples

were thoroughly rinsed with copious ACN and dried with Ar. After derivatization, PPF samples were immediately rinsed with 30 ml of acetonitrile and then dried using Ar gas.

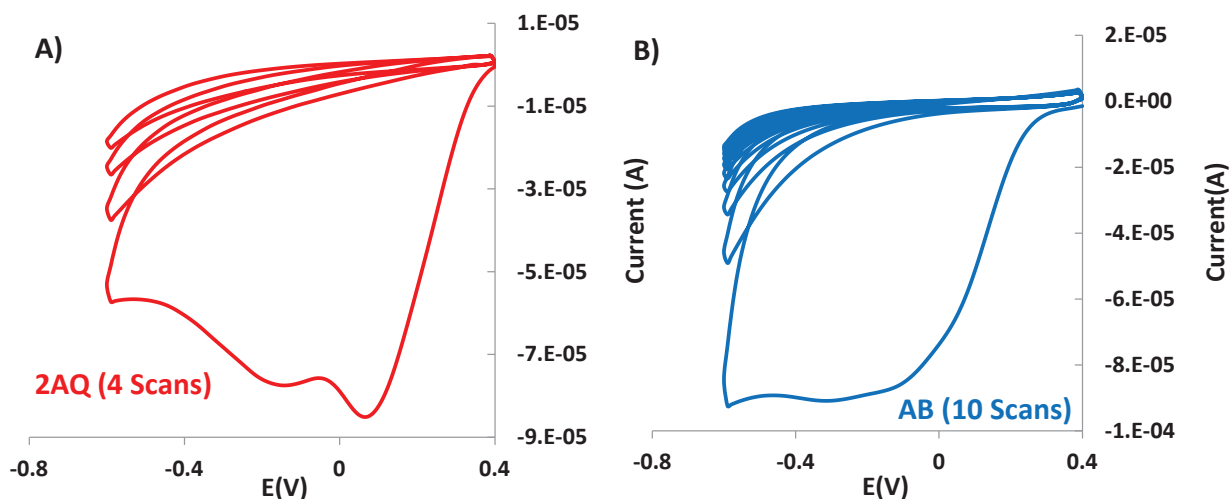


**Figure 2.4:** Cyclic voltammograms of 2AQ (4 scans) (a), AB (10 scans) (b) diazonium ions on carbon (PPF) in 0.1 M TBABF<sub>4</sub> in acetonitrile. The largest voltammetric current was observed on the first scan, and then decreased with successive scans, as shown.

#### 2.2.4 Electrical characterization:

Electronic characterization methods such as monitoring  $i$ - $v$  behaviour are similar to those used in electrochemistry and semiconductor-device characterization. In any electronic measurement of a molecular junction, precautions should be taken to ensure that the programmed voltage is applied across the molecular layer (28). Although this process appears trivial, the conductors used for top contacts are often very thin (20-35nm), and the probes used to make contact with the conductors cannot always be placed close to the junction. These factors can render the resistance of the leads and contact probes significant enough to cause ohmic potential errors (i.e., an  $iR$  drop) that interfere with the electrical measurement. Electrical characterization of molecular junctions utilized a four-wire configuration (28, 29) where the top contact is virtual ground, with the drive voltage ( $V_{\text{drive}}$ ) applied to PPF (thus, all voltages reported herein indicate the voltage of

the PPF relative to the top contact). The wiring schematics for a four-wire configuration are given in figure 2.5. The third and the fourth probes are used to sense voltages on the PPF and top contact to compensate for ohmic losses ( $iR$  drop) due to resistances of the leads. The active four-wire mode uses an operational amplifier to compensate for ohmic loss by increasing the drive voltage- a technique commonly employed in electrochemistry in three-electrode potentiostats. This mode controls the applied voltage to the desired value and corrects for both ohmic losses in both the top and bottom leads of the molecular junction (30). Obtaining an accurate correction for such losses depends on the use of high-impedance voltage monitors and assumes that there is a negligible potential gradient across the lateral dimension of the junction itself. Data collection was carried out using a National Instruments 6111 or 6120 DAQ board controlled by Labview software to execute voltage sweeps and record the resulting current after amplification by an SRS 570 current amplifier (30). The  $\ln J$ - $V$  curves and the  $J$ - $V$  curves obtained for different molecules as a function of thickness is given in figure 2.6 and figure 2.7.

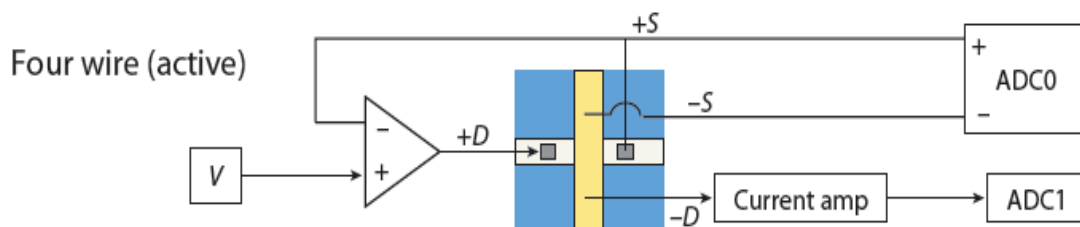


**Figure 2.5:** Wiring schematics for four-wire measurements of current-voltage ( $i$ - $V$ ) behavior of molecular junctions.  $V$  refers to the bias voltage from a digital-to-analog converter, and ADC1 stands for the analog-to-digital channel for current. ADC0 monitors the voltage and has a differential input in the case of a four-wire arrangement.  $D$  and  $S$  denote drive and sense, respectively;  $S$  leads correspond to high-impedance voltage monitors. Picture adopted from reference (30).

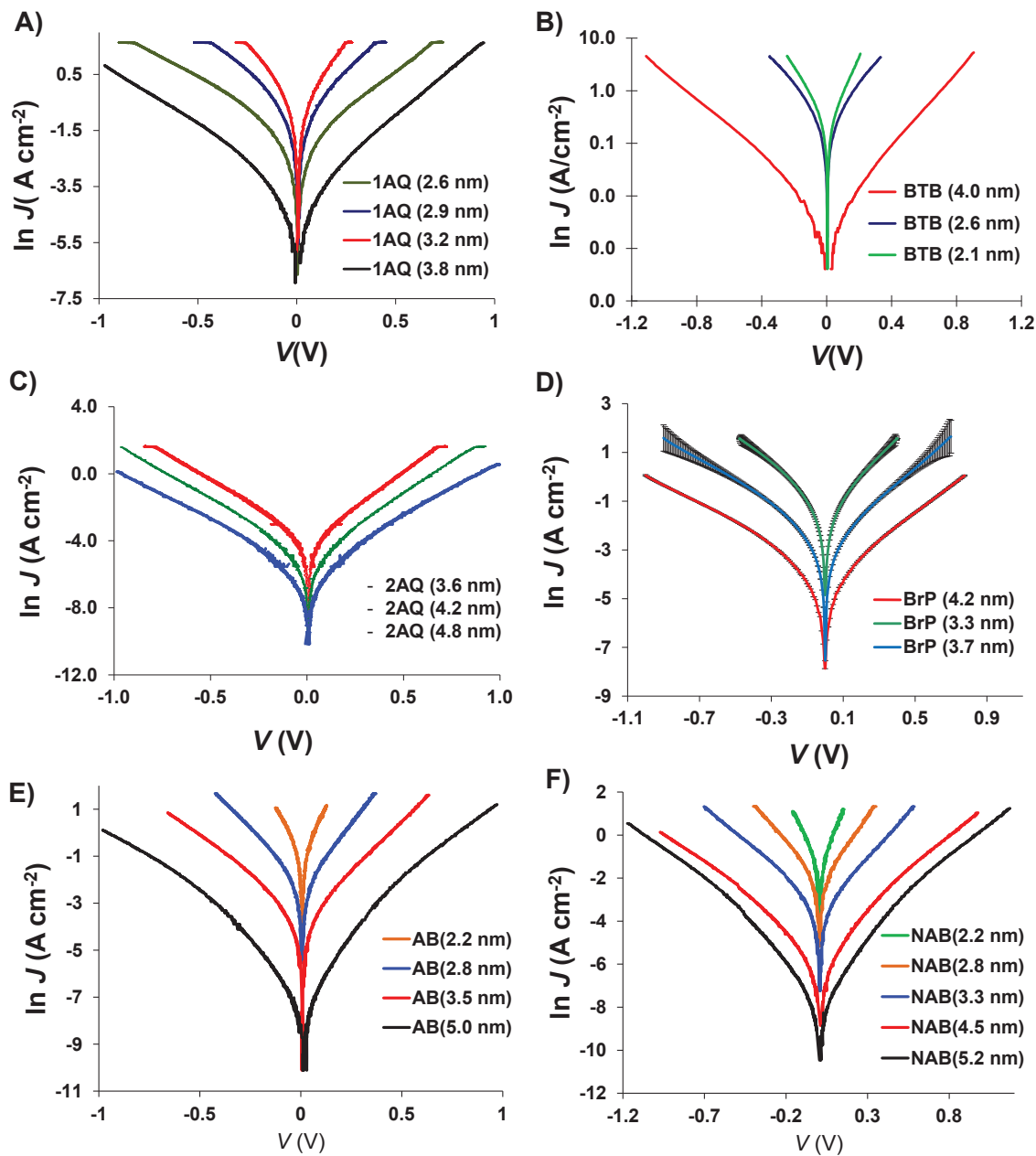


**Figure 2.6:**  $\ln J$ - $V$  curves for 1AQ (A), BTB (B), 2AQ (C), BrP (D), AB (E) and NAB (F) as a function of thickness. Error bars for  $\ln J$  ( $\pm \sigma$ ) are included, but are smaller than the width of the lines for all molecules except BrP. Data for AB and NAB are adopted from reference (31).  $J$  values represents averages of typically 3 or 4 junctions on a given sample.

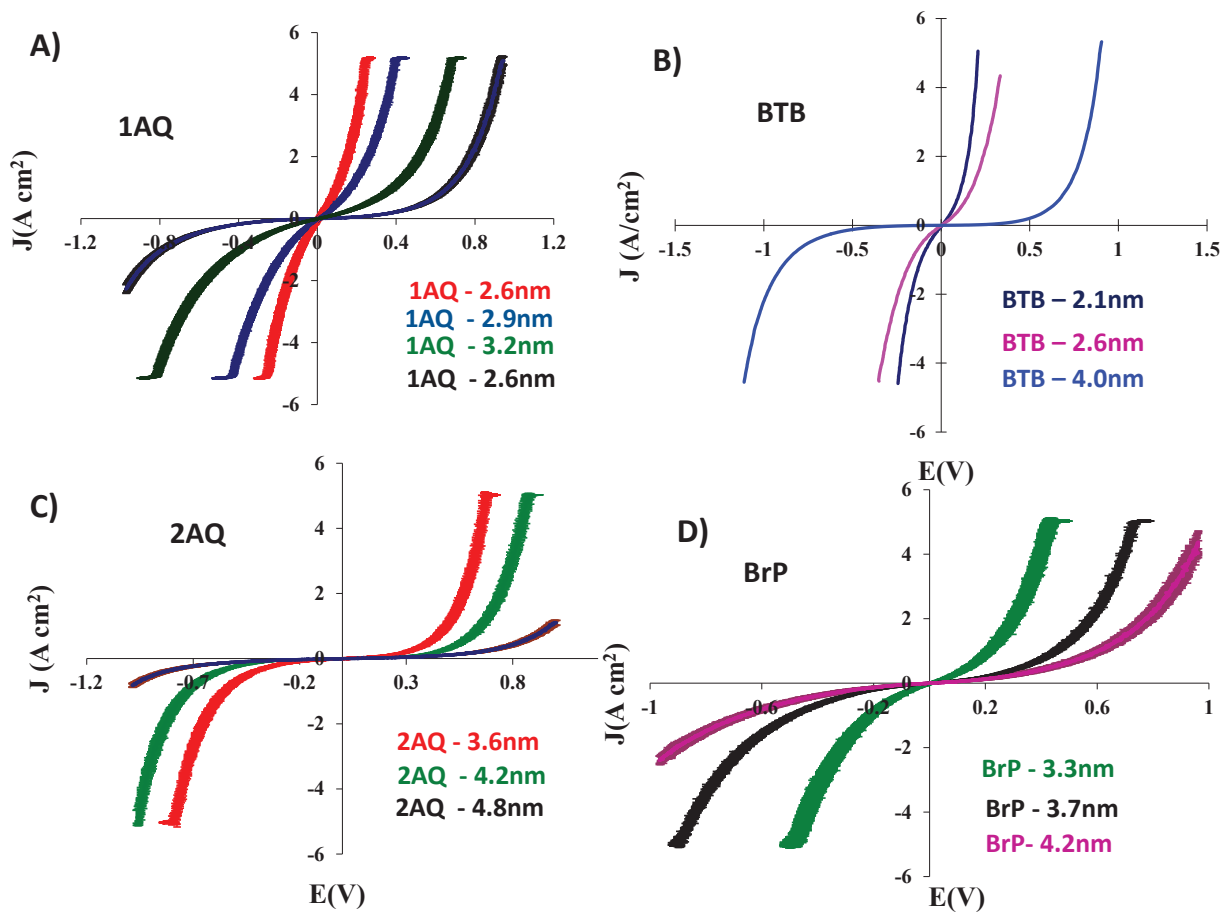


**Figure 2.7:** J-V curves for 1AQ (A), BTB (B), 2AQ (C), BrP (D), as a function of thickness. Error bars for  $J$  ( $\pm \sigma$ ) are included, except for BTB.  $J$  values represents averages of typically 3 or 4 junctions on a given sample.

## 2.3 AFM and UPS measurements:

### 2.3.1 AFM measurements:

Atomic Force Microscopy (AFM) measurements were carried out in air with a Nanoscope IIIa multimode instrument (Digital Instruments, Santa Barbara, CA), Rotated Tapping mode Etched Silicon Probes (RTESP) with resonant frequencies of  $\sim 300$  kHz were purchased from Veeco (Sunnyvale, CA). The AFM tip was replaced after several scratches and its resonant frequency was checked frequently to test for tip damage or possible residue adhering to the tip. The Z-axis of the AFM was calibrated with a standard grid provided by Digital Instruments. The force used

for scratching was determined to be  $\sim 1 \mu\text{N}$ , which was sufficient enough to remove the molecular layer without visible damage to the underlying PPF. Height measurements were made in tapping mode and scratches were made in contact mode. The images were acquired with a scan rate of either 0.5 or 1.0 Hz and were flattened with a first order polynomial before analysis.

Figure 2.8 shows a  $5 \times 5 \mu\text{m}$  tapping mode image including the trench and the surrounding area. Figure 2.9 shows the histogram generated from the height data fit by two different Gaussian functions. The molecular layer thickness stated here is the difference of the centers of the Gaussian distribution, with the uncertainty in thickness stated as the quadrature addition of the two best-fit  $\sigma$  values. The overall average uncertainty in for thickness measurements carried out in this way was  $\sim 0.55 \text{ nm}$ .

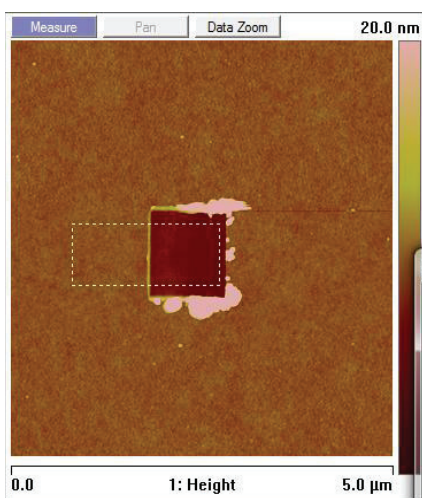


**Figure 2.8:** AFM image of a trench made in a molecular layer of nitro phenyl on carbon (PPF).

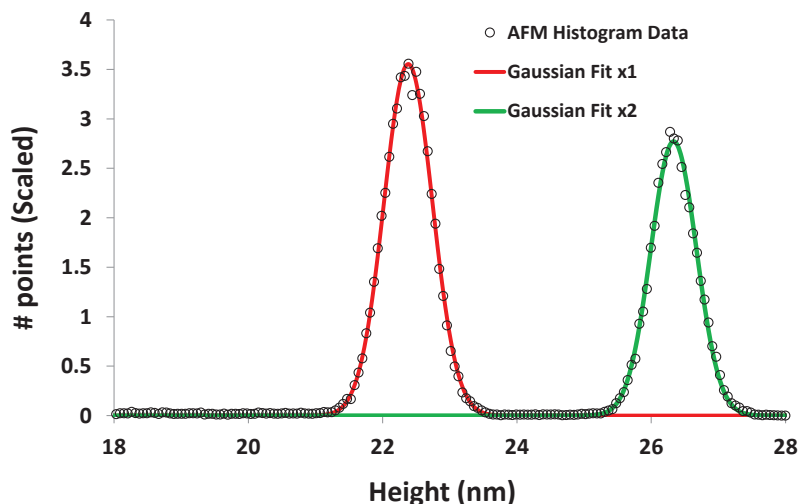


**Figure 2.9:** Fitting of the data generated as a histogram from the AFM data shown in figure 2.7.

### 2.3.2 UPS measurements:

Electronic structure measurements via UPS in ultrahigh vacuum have been used to correlate molecular conductance with energy level alignment (4, 32). The UPS spectrum can be used to determine the work function ( $WF$ ) of the sample using the high binding energy cut-off (HBEC), where  $WF = 21.21 - \text{HBEC}$  ( $21.21 \text{ eV} = h\nu$  of the incident He I light), as shown in figure 2.10.

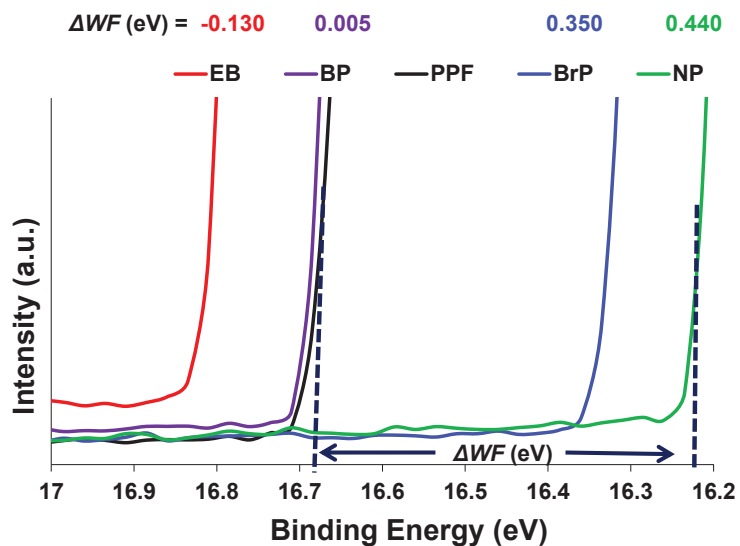


**Figure 2.10:** (A) Close-up of the HBEC region for unmodified PPF and four samples modified with different molecular structures.

Figure 2.11 shows the low binding energy region, where the onset of photoemission can be used to determine  $E_{\text{HOMO, onset}}$  as shown (4). Since  $E_{\text{HOMO, onset}}$  represents the low-lying occupied states, it is a good estimate of the hole tunneling barrier (4).

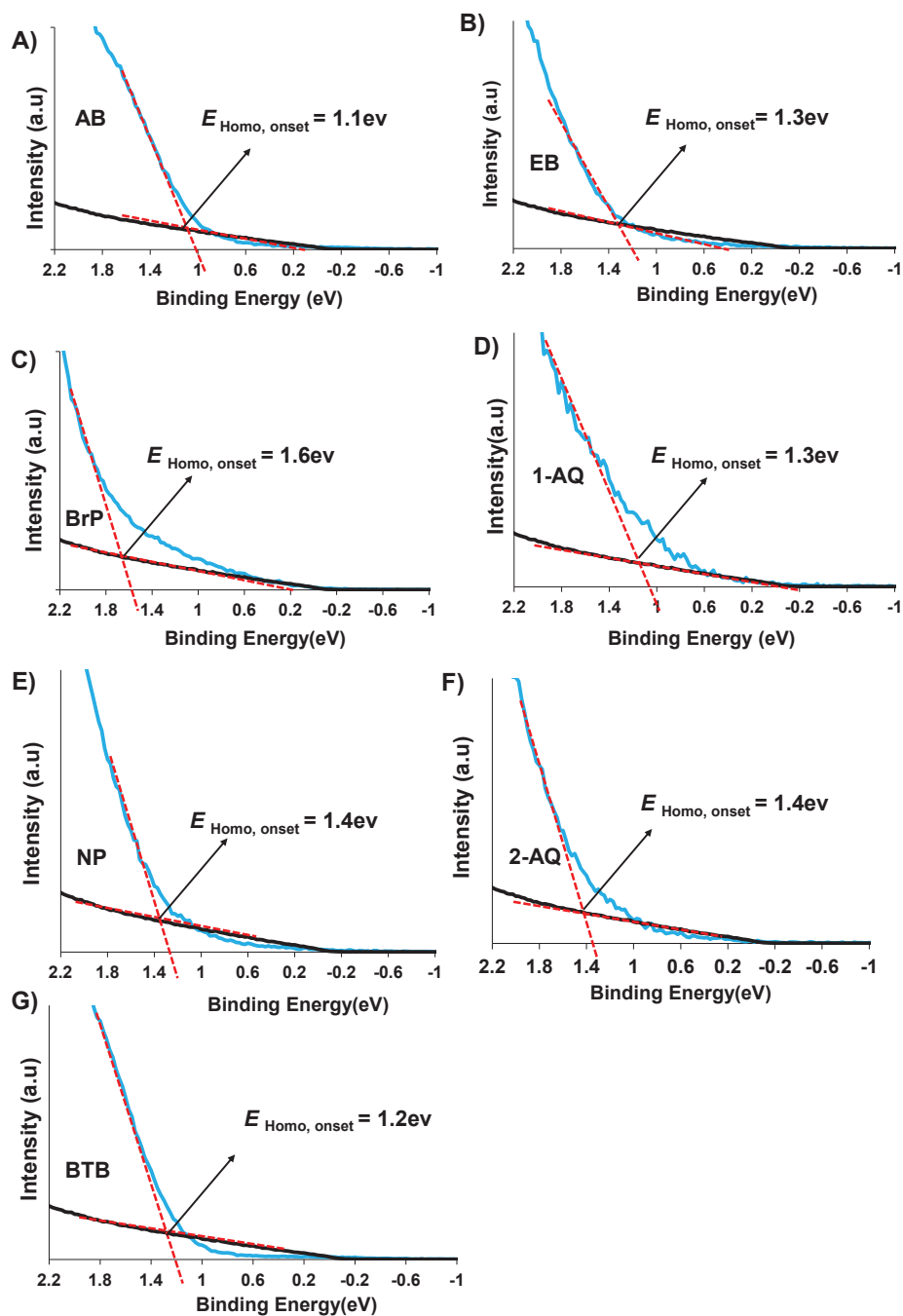


**Figure 2.11:** UPS spectra used for the determination of  $E_{\text{HOMO, onset}}$  values for different molecules: AB, EB, BrP, 1-AQ, 2-AQ, NP and BTB.

## 2.4 Experimental results and discussion:

Figure 2.12 shows a schematic of a molecular junction (2.12A) and a corresponding generic energy level diagram (2.12B). An offset between the Fermi level ( $E_f$ ) of the contact(s) and the molecular levels is generally considered the energy barrier ( $\phi$ ) to charge transport, for hole tunneling in the case shown. Depending on the total distance between the two contacts, transport may proceed through a variety of mechanisms, including quantum mechanical tunneling when this distance is small (i.e. less than  $\sim 5$  nm).

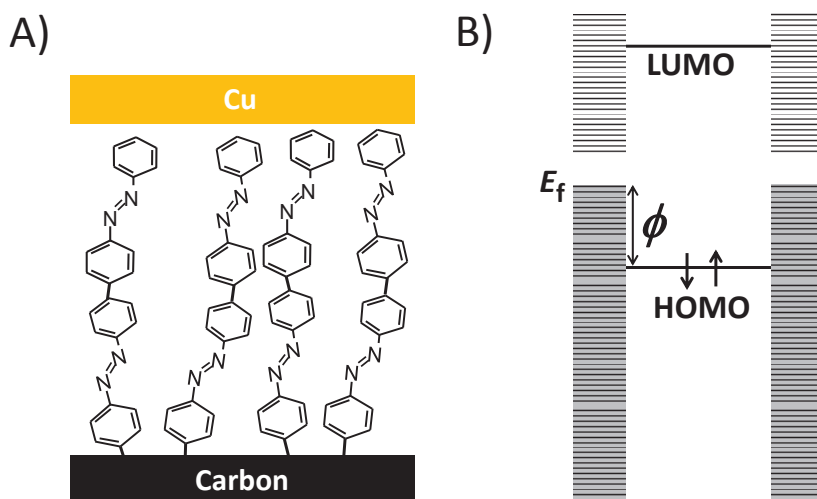


**Figure 2.12:** (A) Schematic of a carbon/molecule/Cu molecular junction with a multilayer of azobenzene sandwiched between carbon and Cu. (B) Corresponding energy level diagram showing the Fermi level of the contacts offset from the molecular energy levels, where the closest occupied level (in this case the HOMO) represents a barrier for hole tunneling ( $\phi$ ). Filled orbitals in the contacts are indicated by shading. A parallel situation can be drawn for electron tunneling through a barrier determined by the LUMO.

While any molecular energy level can represent a charge transport pathway, usually only the frontier orbitals are considered since they typically are the smallest barriers for electron (LUMO) or hole (HOMO) transport. In some cases, the sign of the majority carrier can be assessed experimentally (33, 34). Often, the frontier orbital energies are estimated from experimental data or theoretical calculations and the Fermi level of the contacts are taken from literature or

experimental work function data (e.g. UPS, Kelvin probe). While such estimates of the tunneling barrier are common, it is recognized they represent only one of many possibilities (35). Here, we consider several factors discussed in the relevant literature of organic electronics regarding energy level alignment (11, 36) in order to determine how changing the molecule in the carbon/molecule/Cu system affects junction conductance.

The chemical structures of seven different aromatic molecules used in this study (see figure 2.2), which were chosen since: a) they are readily adapted to diazonium surface modification schemes and b) they provide a 2.3 eV range in calculated gas-phase HOMO energy (the LUMO energies also vary by 2.7 eV), as listed in table 2.1. It has been shown that there is a linear free energy relationship between the binding energy of electrons in benzene derivatives and the substituents that are attached to the benzene ring (37). Thus, electron withdrawing groups, as assessed using the Hammett  $\sigma$  constant, lead to measured shifts of the  $C_{1s}$  electrons to higher binding energies (37). This shift serves as one indication that the molecular HOMO energy shifts to deeper levels when electronegative groups are present, as reflected in figure 2.10. When the given molecules are covalently bonded to a carbon surface, the resulting electronic coupling perturbs the energy levels of the system, as discussed below.

Molecules	NP	AQ	NAB	BrP	EB	AB	BTB
HOMO <sub>free</sub>	-7.59	-7	-6.66	-6.58	-6.29	-6.12	-5.29
LUMO <sub>free</sub>	-2.43	-2.77	-3.04	-0.34	-0.78	-2.17	-1.48
$\phi_{est}^+$ ( $E_f = 4.6$ )	2.99	2.4	2.06	1.98	1.69	1.52	0.69
$\phi_{est}^-$ ( $E_f = 4.6$ )	2.17	1.83	1.56	4.26	3.82	2.43	3.12

**Table 2.1:** Calculated HOMO energies for the free, gas phase molecule (Gaussian, B3LYP-631G (d)).  $\phi_{est}^+ = E_f - E_{HOMO}$ , and  $\phi_{est}^- = E_{LUMO} - E_f$ . NP = nitrophenyl, AQ = anthraquinone, NAB = nitroazobenzene, BrB = Bromophenyl, EB = Ethynylbenzene, AB = azobenzene, and BTB = bisthienylbenzene.

Using the simple model outlined in figure 2.12, the values of the predicted hole and electron tunneling barriers are given in table 2.1. By analogy, these values correspond to the Schottky-Mott limit in semiconductors, where there is no electronic interaction between the molecule and contact. Assuming that the smaller of the hole and electron tunneling barriers determines the observed tunneling rate, the predicted tunneling barriers range from 2.17 eV for NP to 0.69 eV for BTB, a range of 1.48 eV (a constant value of  $E_f = -4.6$  eV is assumed for the carbon electrode). In order to investigate if this range of barrier heights is realized in carbon/molecule devices, large area PPF/molecule/Cu molecular junctions were constructed from these molecular structures using previously described techniques (see section 2.2.1). In all cases, the value of the attenuation factor ( $\beta$ ) was measured by variation of the molecular layer thickness. Current density-voltage ( $J$ - $V$ ) curves shown are averages of four to eight junctions for a given molecule and thickness, from a total of ~300 fabricated and tested junctions.

Figure 2.13 shows  $\ln J$ - $V$  curves for two molecules: nitrophenyl (NP, figure 2.9A) and ethynylphenyl (EB, figure 2.13B). The  $\ln J$ - $V$  curves for the five other molecules used in this study were given in the figure 2.6. As described previously, diazonium reduction generally results in multilayers, with covalent and usually conjugated bonding between molecular subunits (19, 38, 39). The results in figure 2.13 are important for several reasons: two molecules represented here have free molecular HOMO energies that differ by more than 1 eV (see table 2.1). These two molecules are also part of a series of phenyl species with different functional groups in the *para* position (relative to the diazonium group which is eliminated before bonding the molecules to the carbon surface). However, as apparent in figures 2.13C, the slopes of the attenuation plots (“ $\beta$ ” values, see below) are similar, and the conductance of NP and EB junctions with similar thicknesses are not significantly different (i.e. given a 0.6 nm uncertainty

in the thickness of each sample, the null hypothesis is confirmed in a student's t-test with 95% certainty).

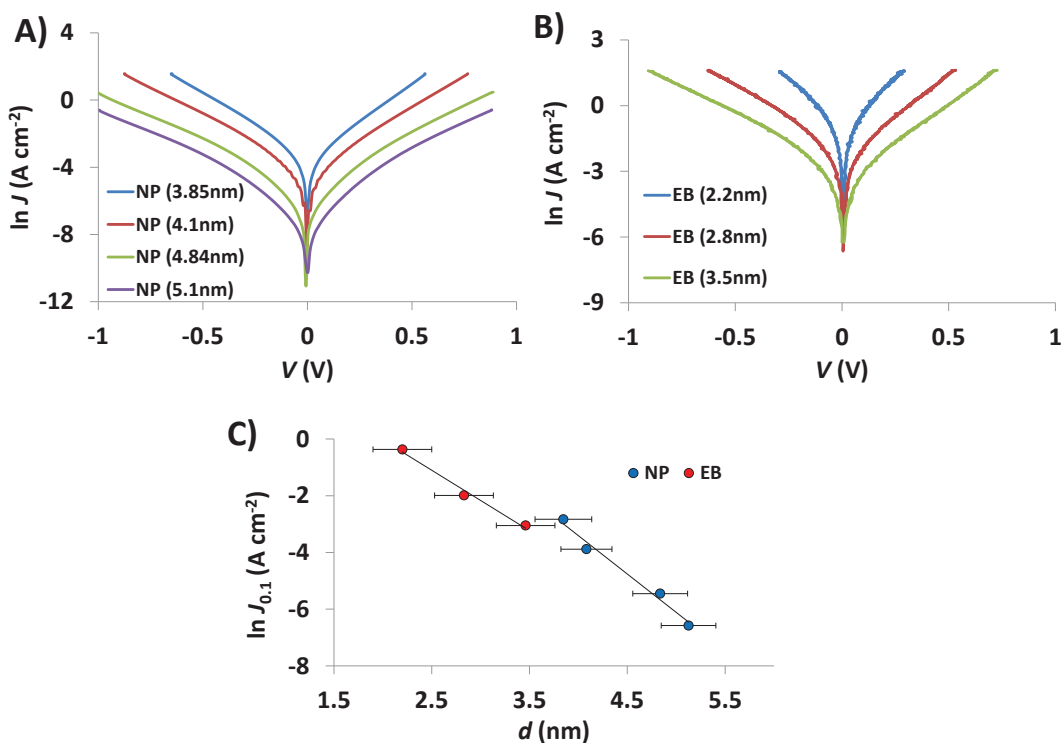


**Figure 2.13:** Representative examples of J-V curves on a semi-logarithmic scale for two molecules, NP (A) and EB (B). (C) The corresponding attenuation plots show conductance values at 0.1 V, Junction area = 0.0013 cm<sup>2</sup>.

One of the most often reported values in molecular junction measurements is the attenuation factor ( $\beta$ ) since it captures many of the relevant system properties. First, an exponential decay of the current density with molecular layer thickness serves as one indication that quantum mechanical tunneling is operative. Additional support for tunneling is the temperature dependence, which we have extensively shown is consistent with tunneling for the carbon/molecule/Cu junctions (6, 8, 18, 19). Second, the value of  $\beta$  is generally sensitive to the electronic structure of the molecular bridge, where aliphatic molecules display higher  $\beta$  values than aromatic species (40). Even for different aromatic species, it has been hypothesized that the way in which conjugation is extended or even the nature of the molecule-substrate bonding can

affect the value of  $\beta$  (41, 42). Finally, according to theoretical descriptions (43, 44) of tunneling, the value of  $\beta$  is proportional to the square root of the barrier height ( $\phi$ ) (45):

(Eqn 2.1)

$$\beta = 2\sqrt{\frac{2m\phi}{\hbar^2}}$$

where  $m$  is the effective carrier mass and  $\hbar$  is the reduced Plank's constant. Therefore,  $\beta$  represents an indirect but convenient indicator of  $\phi$ . Thus, determination of  $\beta$  for the range of structures (figure 2.14) provides a basis for comparison of the impact of structure on barrier heights. In particular, we see that for a 1.5 eV spread of  $\phi$  (from 0.8 to 2.3, as an example),  $\beta$  is expected to vary by a factor of  $2\sqrt{1.5} = 2.45$ .

The analysis described above was carried out on all of the molecular structures shown in figure 2.2. For comparison, we have included data for a series of aliphatic molecular junctions measured using a soft contact method (8). Figure 2.14 shows an overlay of  $\ln J_{0.1V}$  vs. molecular layer thickness for the aromatic structures and the alkane series along with error bars for the thickness (the error bars for the  $y$ -axis are smaller than the data points and can be safely ignored in the statistical analysis). It is clear from figure 2.10 and table 2.1 that there are two groupings: aromatic and aliphatic molecules. After carrying out a full statistical analysis (explained later, section 2.5), we reach the conclusion that  $\beta$  for the alkane series is statistically different from that for all of the aromatic molecules. The average  $\beta$  for the aromatic molecules is  $2.7 \pm 0.6 \text{ nm}^{-1}$ , where the error in layer thickness results in the uncertainty. A detailed statistical test (section 2.5) revealed that we cannot claim that differences in  $\beta$  for any two different aromatic molecules are statistically significant. Furthermore, equation (2.1) predicts that the experimental range of  $\beta$

we observe is consistent with a  $<0.5$  eV variation in barrier height, much smaller than the 1.48 eV implied by the free-molecule energies of table 2.1.

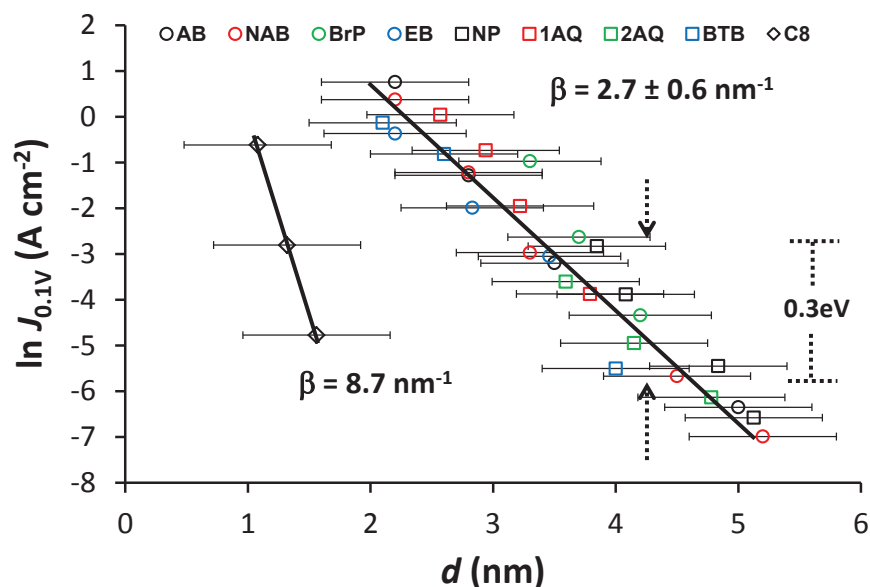


**Figure 2.14:** (A) Overlay of attenuation plots for eight different molecules constructed from J-V curves with different thicknesses of each structure. The lines are least squares regression lines for aliphatic ( $\beta = 8.7 \text{ nm}^{-1}$ ) and all aromatic ( $2.7 \text{ nm}^{-1}$ ) molecules. ‘ $\beta$ ’ determined by least squares for each aromatic molecule are listed in table 2.1. Data for AB (19), NAB (19), and alkanes (8) are taken from previous work. J-V curves for all of the molecules represented here can be found in figure 2.3.

When comparing the conductance values of different molecules in figure 2.2 for a given thickness, small variations in conductance may be obscured by the experimental error in thickness, but large differences (more than  $\sim$ one power of  $e$ ) can be ruled out. More importantly, however, we can determine that a 1.48 eV spread of tunneling barrier heights (as estimated above using the simple model in Figure 2.12) for the structures shown in figure 2.2 is not consistent with the results in figure 2.14 and table 2.1. Based on a modified Simmons model (19), we predict that changing the barrier height by 0.5 eV should result in a variation in  $J$  of 6 powers of  $e$  (note that the plot in figure 2.14 spans a total of 10 powers of  $e$ ). We can determine from figure 2.14 that the differences in barrier heights among the aromatic molecules are less

than  $\sim 0.3$  eV (i.e. a 0.3 eV change in  $\phi$  causes  $J$  to vary by at most 3 powers of  $e$ , as illustrated on the plot). These observations clearly indicate that the tunneling barrier is significantly compressed compared to the 1.48 eV predicted from free molecule energy levels. This compression is a key result of this study: the molecular tunnel barrier appears to be pinned within a far narrower range than that predicted by the Schottky-Mott limit. In order to determine the origin of this apparent compression, we probed the electronic structure of bare and modified PPF samples by determining the work functions and HOMO onset energies with UPS, as described above in section 2.3.2.

Electronic structure measurements via UPS in ultrahigh vacuum have been used to correlate molecular junction conductance with energy level alignment (4, 34). When substrates are modified, the observed UPS work function is sensitive to a local vacuum level shift induced by the (new) chemical composition of the surface, including any dipoles present (11, 36). In addition, analysis of UPS spectra can provide an estimate of the interfacial barrier height by analysing the onset of photoemission near the Fermi level (4, 6). Thus, UPS enables a reasonable estimate of the occupied energy levels in carbon/molecule samples lacking the Cu top contact.

Figure 2.10 shows a detailed view of the HBEC region for unmodified PPF and four samples modified with nanoscopic layers of BP, EB, BrP, and NP, respectively. It is apparent that modification of PPF with a molecule lacking a dipole (BP) has a minor effect on the observed HBEC, while molecules with dipoles and electron donating or withdrawing substituents cause significant shifts in the HBEC. Surface bonded molecules with electron-withdrawing groups such as nitro- or bromo- cause a shift of the apparent work function to higher energies, while bonding of EB shifts it to lower energy. This change in work function is most often interpreted as a shift of the local vacuum level (11, 35, 36) due to the presence of the molecular layer. These

shifts in the work function and local vacuum level due to the bonded molecules illustrates that the energy levels in a molecular junction as depicted in figure 2.12 cannot be adequately predicted by measuring (or calculating) the substrate and molecule energies of the isolated components. Although the molecular layers used herein are dimers and trimers of the molecules in figure 2.2, the  $WF$  is still affected by the donating or withdrawing properties of the substituents, as is the case for thick ( $>50$  nm) films in organic electronics (35).

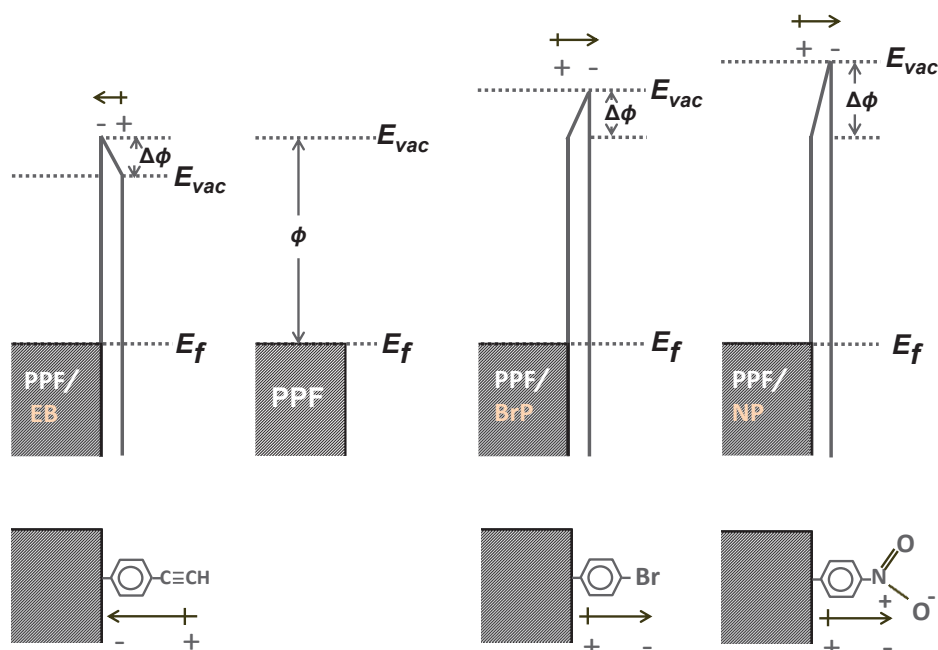


**Figure 2.15:** Energy level diagram showing the vacuum level shift induced by the molecular dipole for the molecules.

The experimental values of the sample work function, the shift in work function relative to an unmodified PPF substrate,  $E_{HOMO, onset}$  and the barrier values obtained from fitting the  $J$ - $V$  curves to a modified Simmons model are compiled in table 2.2.  $E_{HOMO, onset}$  and  $\phi_{Simmons}$  agree to within 0.2 eV of each other, but more importantly, the aromatic molecules have UPS-determined barriers that span a range of 0.5 eV for the seven aromatic molecules examined. Recalling that figure 2.13 indicates a range of tunneling barriers of at most 0.3 eV for the aromatic molecules, it

is clear that the Schottky-Mott rule fails. The compression of the interfacial barrier from the 1.48 eV predicted by Schottky-Mott to the maximum of 0.3-0.5 eV observed experimentally is attributable to an interaction between the molecules and the surface, as discussed in more detail below.

Sample	$WF$ (eV)	$\Delta WF$	$E_{\text{HOMO, onset}}$	$\phi_{\text{Simmons}}$ (eV)
PPF	4.53	-	-	-
PPF/EB	4.40	-0.13	$1.4 \pm 0.1$	1.4
PPF/BP	4.53	0	$1.7 \pm 0.1$	-
PPF/ BrB	4.88	+0.35	$1.5 \pm 0.3$	1.5
PPF/ NP	4.97	+0.44	$1.4 \pm 0.2$	1.0
PPF/AB	4.66	+0.13	$1.0 \pm 0.1$	1.0
PPF/BTB	4.41	-0.12	$1.2 \pm 0.1$	1.1
PPF/1AQ	4.56	+0.03	$1.3 \pm 0.1$	1.4
PPF/2AQ	4.43	-0.1	$1.4 \pm 0.1$	1.25
PPF(2)(6)	4.71	-	-	-
PPF(2)/NAB(6)	5.04	+0.33	$1.2 \pm 0.1$	1.1
PPF(2)/FL(6)	4.65	-0.06	$1.5 \pm 0.1$	1.3
PPF(2)/Alkane(6)	4.93	+0.22	$2.0 \pm 0.1$	1.8
PPF/NAB	5.07			
Au/NAB	5.1			
Pt/NAB	5.2			

**Table 2.2:** Values of apparent work function, work function shift, the onset of the molecular HOMO energy measured using UPS, and the barrier obtained from fitting the data to a modified (19) form of the Simmons tunneling model.

Measurement of the apparent work function of different metals after modification with a molecular layer is a useful way to probe energy levels in studies of interfacial barriers between metals, semiconductors and molecules (46-48). In these studies, a parameter  $S$  is often defined to describe the electronic interactions between the substrate and the modification layer.  $S$  is defined as the slope of the observed  $WF$  for the modified surface (i.e., the HBEC) versus the work function of the unmodified substrate. In the Schottky-Mott limit, weak or negligible interactions

between the substrate and the molecular layer retain the energy levels of the isolated components and  $S \sim 1$  (35). However, in the case where strong electronic interactions between the substrate and the molecular layer are present,  $S \sim 0$ , in which case Fermi level-pinning occurs. Intermediate cases where  $S$  is between zero and one also exist, depending on the initial energy levels of the substrate and molecular layer and the level of interaction between them. We measured the work function of carbon (PPF) (4.8eV), gold (5.1eV) and platinum (6.35eV) using kelvin probe experiment. We then measured the factor  $S$  for one molecule (NAB) by modifying samples of carbon (PPF), gold, and platinum (see last three entries in table 2.2), which yields a constant observed  $WF$  close to -5.1 eV despite a difference in substrate work function of  $\sim 1.5$  eV, meaning that the value of  $S$  is 0.069 and therefore close to 0. This pinning of the observed  $WF$  confirms that for NAB on carbon, gold, and platinum, the Schottky-Mott rule fails. Thus, the main consequence of the strong electronic coupling between the molecule and the substrate is the significant alteration of energy levels from those of the free molecules and unmodified substrate.

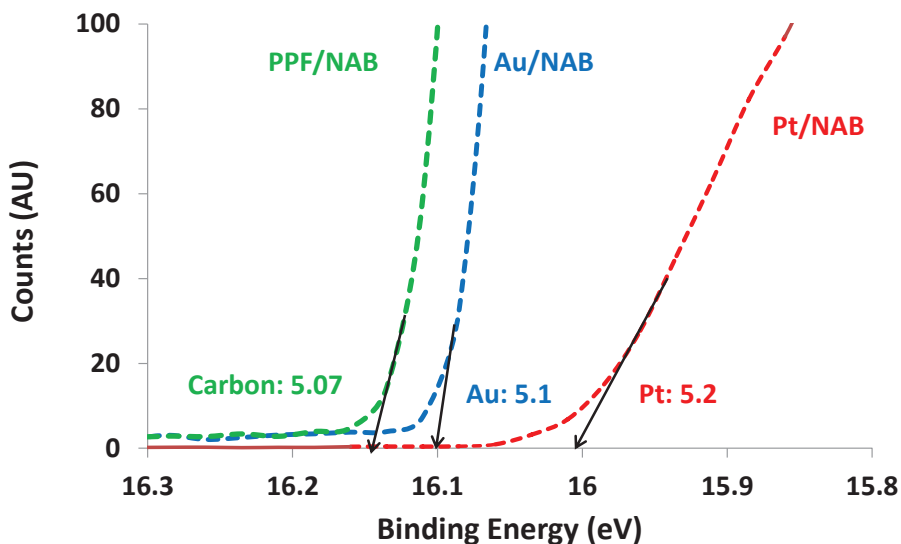


**Figure 2.16:** UPS spectra in the HBEC region for NAB on three different metals.

Figure 2.17 compares energy level diagrams for the Mott-Schottky limit with those indicated by the UPS results. We focus here only on the HOMO to simplify the discussion and since UPS probes occupied levels (i.e., we cannot construct a corresponding diagram for LUMO-mediated transport from UPS). The Schottky-Mott limit (figure 2.17A) predicts a hole tunneling barrier range from 0.69 to 2.99, a span of 2.3 eV. Figure 2.17B shows the energy level diagram constructed from the experimental UPS data in table 2.2, where the observed value of the  $E_{\text{HOMO, onset}}$  varies from 1.0 to 1.5 eV relative to  $E_{\text{f}}$ , indicating that the expected range for the hole tunneling barrier is 0.5 eV based on UPS. We note that the experimental error in the UPS determined  $E_{\text{HOMO, onset}}$  values is 0.1 to 0.2 eV, and these measurements do not include any effect of the top contact. The small range of tunneling barriers predicted from UPS is consistent with figure 2.14, where the range of current densities for seven different aromatic molecules corresponds to a variation in barrier height of  $< 0.3$  eV. From the UPS results of figure 2.17B, the average tunneling barrier is  $1.3 \pm 0.2$  eV for the aromatic molecules. The near constant barriers determined from both UPS and  $J$ - $V$  characteristics despite a much larger variation in free-molecule HOMO energies is a consequence of the strong electronic coupling between the carbon surface and the molecules. Electron-withdrawing molecules shift both the substrate and molecular orbitals to lower energy after partial charge transfer between the substrate and molecule. This phenomenon is similar to that observed for thick molecular layers on metals, in which the offset between metal and molecule energy levels at equilibrium is established by charge transfer between the two layers, to result in a common Fermi energy at equilibrium (49).

The addition of the Cu top contact to the PPF/molecule system depicted in figure 2.17 and studied with UPS would be expected to perturb the energy levels somewhat, although the change should be similar for all seven aromatic molecules. Since the work functions of unmodified PPF

and Cu are similar ( $\sim 4.9$  eV), a significant built-in field is not expected in the completed junction. Furthermore, the tunneling barriers derived from the  $J$ - $V$  curves using a modified Simmons analysis (19) ( $\phi_{\text{Simmons}}$  in table 2.2) exhibit an average value of  $1.2 \pm 0.2$  eV, quite close to the  $1.3 \pm 0.2$  eV estimated from UPS. The slightly lower value is consistent with the findings of others (4, 50-52) where a second metal lowers the barrier height slightly due to image charge effects.

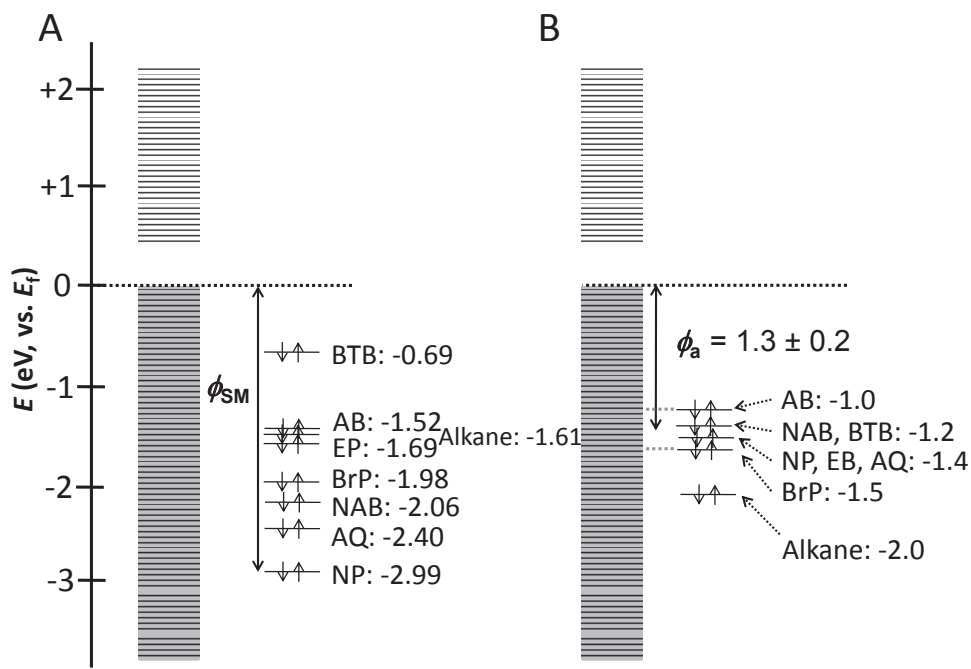


**Figure 2.17:** (A) Energy levels before bonding the molecules to the carbon substrate, where the hole transport barrier is defined by the Schottky-Mott rule ( $\phi_{\text{SM}}$ ), and spans a 2.3 eV range. (B)  $E_{\text{HOMO, onset}}$  energy, measured using UPS for molecules bonded to PPF. The numbers next to each molecule are the estimated tunneling barriers based on the indicated orbital energies.

Given that electronic coupling between the PPF substrate and a range of aromatic molecules suppresses the effects of electron donating or withdrawing substituents on the tunneling barrier, the question arises of what other factors can be used to modulate junction conductance, and ultimately lead to rational design of junction electronic behaviour. At the least, the type of molecule (alkane vs. aromatic) and the degree of electronic coupling between the contacts and

molecules have major effects. The conjugation between carbon substrate and aromatic molecule inherent in the diazonium chemistry used herein promotes strong coupling, but we expect alternative surface modification paths to more closely approximate the Schottky-Mott limit. Similarly, breaking conjugation within the molecular layer should permit “insulation” of orbitals and molecular fragments from the effects of electronic coupling. It should also be noted that the experimental error in the UPS results and the molecular thicknesses may obscure differences in  $J$ - $V$  response resulting from 0.2-0.3 eV variations in barrier height. Since the results show clearly that the energetics of both substrate and molecular layer must be considered to understand transport, rational design is ultimately likely to depend on quantum mechanical modeling of large molecules bonded to conducting contacts. Our preliminary effort to model such systems using DFT-based methods has shown promise, and it is likely that insights from computations of the entire system will help to design systems with targeted properties.

## 2.5 Statistical analysis:

For each molecule the number of points used to obtain the beta value ( $n_i$ ) is noted and then the standard deviation for each  $\beta$  value ( $\sigma_\beta$ ) is determined, with only the layer thickness error contributing significantly to  $\sigma_\beta$ . The uncertainty in the thickness from AFM measurements is typically 0.6 nm (see below), and so this value was used in all cases. Using 0.6nm for the uncertainty in thickness yields the values listed in table 2.2 and table 2.3 below for the  $\sigma_\beta$  in  $\beta$  via the equation (from the 2nd edition of [An Introduction to Error Analysis](#) by John R. Taylor, pages 184-190):

(Eqn 2.2)

$$\sigma_\beta = 0.6 \sqrt{\frac{n}{n \sum d_i^2 - (\sum d_i)^2}}$$

where  $n$  is the number of data points in the attenuation plot and  $d_i$  is the thickness of each molecular layer used to generate the attenuation plot.

In order to determine if two  $\beta$  values are significantly different from each other given the values of  $\sigma_\beta$ , a Student's-t analysis is carried out at 95% confidence level. To begin, the equation to determine  $\sigma_{\text{pooled}}$  for the two data sets being compared is given below (from the 4th edition of Quantitative Chemical Analysis by Daniel C. Harris, page 67):

(Eqn 2.3)

$$\sigma_{\text{pooled}} = \sqrt{\frac{\sigma_1^2(n_1 - 1) + \sigma_2^2(n_2 - 1)}{n_1 + n_2 - 2}}$$

where  $\sigma_i$  is the standard deviation for beta as calculated above for a given molecule and  $n_i$  is the number of data points in each attenuation plot. The values obtained for  $\sigma_{\text{pooled}}$  are given in table 2.4. The value for the student's-t value ( $t_{\text{calc}}$ ) is determined using the formula given below (from the 4th edition of Quantitative Chemical Analysis by Daniel C. Harris, page 67):

(Eqn 2.4)

$$t_{\text{calc}} = \frac{\bar{x}_1 - \bar{x}_2}{\sigma_{\text{pooled}}} \sqrt{\frac{n_1 n_2}{n_1 + n_2}}$$

where  $\bar{\beta}_i$  is the average value for  $\beta$  for a given molecule, and the other parameters have been defined previously. The value calculated ( $t_{\text{calc}}$ ) from Equation 2.4 are then compared with the  $t_{95\%}$  value for a given degree of freedom ( $n_1 + n_2 - 2$ ) listed on page 63 of the 4th edition of Quantitative Chemical Analysis by Daniel C. Harris. These comparison results are given in table 2.5, where red highlighting indicates a statistical difference in  $\beta$  values at the 95% confidence level. Here, a clear difference is seen between the  $\beta$  values for aromatic series with that of aliphatic series. However, we do not have sufficient evidence here to claim any differences between the aromatic molecules. A possible difference is indicated in 3 out of 36 comparisons,

but these differences are not robust enough to make any claims. That is,  $t_{95\%} = 2.447$  and  $2.365$  for 6 and 7 degrees of freedom respectively. For one of these comparisons, the value of  $t_{\text{calc}}$  is 2.53 (6 dof), and 2.47 and 2.94 (7 dof) in the other two cases.

npts	molecule	$\beta$	$\sigma_{\beta}$
3	EtBen	2.1	0.7
4	NP	2.7	0.6
4	BrP	3.7	0.9
4	1AQ	3.3	0.7
3	2AQ	2.1	0.7
3	BTB	2.9	0.4
4	AB	2.5	0.3
5	NAB	2.5	0.2
3	C8	8.7	1.8

**Table 2.3:** Summary of the number of points in the attenuation plot for each molecule, the average value of  $\beta$ , and the resulting standard deviation in  $\beta$  calculated using eqn 2.2.

$\sigma_{\text{pooled}}$									
	EtBen	NP	BrP	1AQ	2AQ	BTB	AB	NAB	C8
EtBen									
NP	0.641872								
BrP	0.825833	0.764853							
1AQ	0.7	0.65192	0.806226						
2AQ	0.7	0.641872	0.825833	0.7					
BTB	0.570088	0.52915	0.74162	0.598331	0.570088				
AB	0.5	0.474342	0.67082	0.538516	0.5	0.343511			
NAB	0.43589	0.420883	0.608276	0.482553	0.43589	0.282843	0.247848		
C8	1.36565	1.229634	1.334916	1.260952	1.36565	1.30384	1.161895	1.051982	

**Table 2.4:** calculated values for  $\sigma_{\text{pooled}}$ .

$t_{calc}$									
	EtBen	NP	BrP	1AQ	2AQ	BTB	AB	NAB	C8
EtBen									
NP	1.22389								
BrP	2.53670	1.84900							
1AQ	2.24452	1.30158	0.70164						
2AQ	0	1.22389	2.53670	2.24452					
BTB	1.71867	0.49487	1.41237	0.87530	1.71867				
AB	1.04744	0.59628	2.52982	2.10090	1.04744	1.52461			
NAB	1.25656	0.70837	2.94085	2.47137	1.25656	1.93649	0		
C8	5.91905	6.38876	4.90408	5.60708	5.91905	5.44815	6.98660	8.07019	

**Table 2.5:** Student's t-values for comparison of  $\beta$  values for different molecules. Those that are greater than  $t_{95\%}$  are highlighted.

### Number of Junctions

Molecule	No: of Junctions tested
EB	24
NP	64
BrP	64
BrP	32
1AQ	96
2AQ	72
BTB	24
AB	32
NAB	40
Alkanes	24

**Table 2.6:** Summary of the number of junctions made for each molecule. We note that AB (19), NAB (19), and the alkane (8) data were previously published.

Molecule	$\beta$ (nm <sup>-1</sup> )	$\sigma_\beta$
EB	2.1	0.7
NP	2.7	0.6
BrP	3.7	0.9
1AQ	3.3	0.7
2AQ	2.1	0.7
BTB	2.9	0.4
AB	2.5	0.3
NAB	2.5	0.2
Alkanes	8.7	1.8

**Table 2.7:** Measured values of  $\beta$  for each molecule and the uncertainty due to the standard deviation of the molecular layer thickness measurements.

## 2.6 Conclusions:

This chapter describes how the tunneling barrier in carbon/molecule/metal molecular junctions is compressed relative to that predicted from the HOMO or LUMO energies in the Schottky-Mott limit. The similarity of current/voltage behaviour for seven aromatic molecules is consistent with independent UPS measurements of the tunneling barrier, with both indicating barriers with a range of  $(1.2-1.3) \pm 0.2$  eV despite a 1.5 eV range of free molecule HOMO energies. The origin of this effect is rooted in the interaction between the molecular layer and the substrate. Thus, changing the energy level of the molecular species leads to a partial transfer of charge, which leads to a molecular tunneling barrier that is defined by the equilibrium position of the contact and molecular energy levels in the system. UPS measurements show that molecular layers derived from diazonium reduction gives a value near zero for the interface parameter (S),

indicating that strong electronic coupling leads to the failure of the Schottky-Mott rule for this system. As is observed for other metal/organic systems, this partial charge transfer is correlated with an interfacial dipole, the magnitude of which stems from the relative values of the isolated system energy levels and how the molecular layer and substrate interact.

## 2.7 References:

1. Lua L, Choi SH, & Frisbie CD (2011) Probing Hopping Conduction in Conjugated Molecular Wires Connected to Metal Electrodes. *Chem Mater.* 23(3):631-645.
2. Siebbeles LDA & Grozema FC eds (2011) *Charge and Exciton Transport through Molecular Wires* (Wiley-VCH, Weinheim, Germany).
3. McCreery RL & Bergren AJ (2009) Progress with Molecular Electronic Junctions: Meeting Experimental Challenges in Design and Fabrication. *Adv. Mater.* 21:4303-4322.
4. Kim B, Choi SH, X.-Y.Zhu, & Frisbie CD (2011) Molecular Tunnel Junctions Based on  $\pi$ -Conjugated Oligoacene Thiols and Dithiols between Ag, Au, and Pt Contacts: Effect of Surface Linking Group and Metal Work Function. *J. Am. Chem. Soc.* 133(49):19864-19877.
5. Kumar R, Yan H, McCreery RL, & Bergren AJ (2011) Electron-beam Evaporated Silicon as a Top Contact for Molecular Electronic Device Fabrication. *Phys. Chem. Chem. Phys.* 13:14318-14324.
6. Yan H, Bergren AJ, & McCreery RL (2011) All Carbon Molecular Tunnel Junctions. *J. Am. Chem. Soc.* 133(47):19168-19177.
7. Venkataraman L, Klare JE, Nuckolls CD, Hybertsen MS, & Steigerwald ML (2006) Dependence of Single-Molecule Junction Conductance on Molecular Conformation. *Nature.* 442(24):904-907.

8. Bonifas AP & McCreery RL (2010) "Soft" Au, Pt and Cu Contacts for Molecular Junctions through Surface-Diffusion-Mediated Deposition. *Nat. Nanotechnol.* 5(8):612-617.
9. Bonifas AP & McCreery RL (2011) Assembling Molecular Electronic Junctions One Molecule at a Time. *Nano Lett.* 11(11):4725-4729.
10. Dell'Angela M, Kladnik G, Cossaro A, Verdini A, kamenetska M, Tamblyn I, Neaton JB, Cvetko d, Morgante A & Venkatraman L (2010) Relating Energy Level Alignment and Amine-Linked Single Molecule Junction Conductance. *Nano Lett.* 10:2470-2474.
11. Ishii H, Sugiyama K, Ito E, & Seki K (1999) Energy Level Alignment and Interfacial Electronic Structures at Organic/Metal and Organic/Organic Interfaces. *Adv. Mater.* 11(8):605-625.
12. Neshar G, Vilan A, Cohen H, Cahen D, Amy F, Chan C, Hwang J & Kahn A (2006) Energy Level and Band Alignment for GaAs-Alkylthiol Monolayer-Hg Junctions from Electrical Transport and Photoemission Experiments. *J. Phys. Chem. B.* 110:14363-14371.
13. Yan H & McCreery RL (2009) Anomalous Tunneling in Carbon/Alkane/TiO<sub>2</sub>/Gold Molecular Electronic Junctions: Energy Level Alignment at the Metal/Semiconductor Interface. *ACS Appl. Mater. Interfaces.* 1(2):443-451.
14. Anariba F & McCreery RL (2002) Electronic Conductance Behavior of Carbon-Based Molecular Junctions with Conjugated Structures. *J. Phys. Chem. B* 106:10355-10362.
15. Anariba F, Steach JK, & McCreery RL (2005) Strong Effects of Molecular Structure on Electron Transport in Carbon/Molecule/Copper Electronic Junctions. *J. Phys. Chem. B* 109(22):11163-11172.

16. McGovern WR, Anariba F, & McCreery RL (2005) Importance of Oxides in Carbon/Molecule/Metal Molecular Junctions with Titanium and Copper Top Contacts. *J. Electrochem. Soc.* 152(5):E176-E183.
17. Ranganathan S, Steidel I, Anariba F, & McCreery RL (2001) Covalently Bonded Organic Monolayers on a Carbon Substrate: A New Paradigm for Molecular Electronics. *Nano Lett.* 1(9):491-494.
18. Bergren AJ, Harris KD, Deng F, & McCreery RL (2008) Molecular Electronics using Diazonium-Derived Adlayers on Carbon with Cu Top Contacts: Critical Analysis of Metal Oxides and Filaments. *J. Phys.: Condens. Matter.* 20(37):374117.
19. Bergren AJ, McCreery RL, Stoyanov SR, Gusarov S, & Kovalenko A (2010) Electronic Characteristics and Charge Transport Mechanisms for Large Area Aromatic Molecular Junctions. *J. Phys. Chem. C.* 114(37):15806-15815.
20. Itoh T & McCreery RL (2002) In Situ Raman Spectroelectrochemistry of Electron Transfer between Glassy Carbon and a Chemisorbed Nitroazobenzene Monolayer. *J. Am. Chem. Soc.* 124:10894-10902.
21. Tian H, Bergren AJ, & McCreery RL (2007) Ultraviolet-Visible Spectroelectrochemistry of Chemisorbed Molecular Layers on Optically Transparent Carbon Electrodes. *Appl. Spectrosc.* 61(11):1246-1253.
22. Mahmoud AM, Bergren AJ, Pekas N, & McCreery RL (2011) Towards Integrated Molecular Electronic Devices: Characterization of Molecular Layer Integrity during Fabrication Processes. *Adv. Funct. Mater.* 21:2273-2281.

23. Mahmoud AM, Bergren AJ, & McCreery RL (2009) Derivatization of Optically Transparent Materials with Diazonium Reagents for Spectroscopy of Buried Interfaces. *Anal. Chem.* 81(16):6972-6980.
24. Ranganathan S, McCreery RL, Majji SM, & Madou M (2000) Photoresist-Derived Carbon for Microelectrochemical Applications. *J. Electrochem. Soc.* 147:277 - 282.
25. Ranganathan S & McCreery RL (2001) Electroanalytical Performance of Carbon Films with Near-Atomic Flatness. *Anal. Chem.* 73:893-900.
26. Liu Y-C & McCreery RL (1997) Raman Spectroscopic Determination of the Structure and Orientation of Organic Monolayers Chemisorbed on Carbon Electrode Surfaces. *Anal. Chem.* 69:2091.
27. Solak AO, Eichorst LR, Clark WJ, & McCreery RL (2003) Modified Carbon Surfaces as "Organic Electrodes" that Exhibit Conductance Switching. *Anal. Chem.* 75:296-305.
28. Bergren AJ, Harris KD, Deng F, & McCreery R (2008) Molecular Electronics using Diazonium-Derived Adlayers on Carbon with Cu Top Contacts: Critical Analysis of Metal Oxides and Filaments. *J. Phys. Condens. Matter.* 20:374117.
29. Anariba F, Steach J, & McCreery R (2005) Strong Effects of Molecular Structure on Electron Transport in Carbon/molecule/Copper Electronic Junctions. *J. Phys. Chem B.* 109:11163-11172.
30. Bergren AJ & McCreery RL (2011) Analytical Chemistry in Molecular Electronics. *Annu. Rev. Anal. Chem.* 4(1):173-195.
31. Bergren AJ, McCreery RL, Stoyanov SR, Gusarov S, & Kovalenko A (2010) Electronic Characteristics and Charge Transport Mechanisms for Large Area Aromatic Molecular Junctions. *J. Phys. Chem. C* 114:15806-15815.

32. Qi Y, Yaffe O, Tirosh E, Vilan A, Cahen D & Kahn A (2011) Filled and empty states of alkanethiol monolayer on Au (111): Fermi level Asymmetry and Implications for Electron Transport. *Chem. Phys. Lett.* 511(4-6):344-347.
33. Majumdar A, Reddy P, Jang S-Y, & Segalman RA (2007) Thermoelectricity in Molecular Junctions. *Science.* 315:1568-1571.
34. Qi Y, Yaffe O, Tirosh E, Vilan A, Cahen D & Kahn A (2011) Filled and Empty States of Alkanethiol Monolayer on Au(111): Fermi Level Asymmetry and Implications for Electron Transport. *Chem. Phys. Lett.* 511:344-347.
35. Kahn A, Koch N, & Gao W (2003) Electronic Structure and Electrical Properties of Interfaces between Metals and  $\pi$ -Conjugated Molecular Films. *J. Polymer Sci.: Part B: Polymer Phys.* 41:2529-2948.
36. Cahen D & Kahn A (2003) Electron Energetics at Surfaces and Interfaces: Concepts and Experiments. *Adv. Mater.* 15(4):271-277.
37. Lindberg B, Svensson S, malmquist PA, Basilier E, Gelius U & Siegbahn K (1976) Correlation of ESCA Shifts and Hammett Substituent Constants in Substituted Benzene Derivatives. *Chem. Phys. Lett.* 40(2):175-179.
38. Anariba F, DuVall SH, & McCreery RL (2003) Mono- and Multilayer Formation by Diazonium Reduction on Carbon Surfaces Monitored with Atomic Force Microscopy "Scratching". *Anal. Chem.* 75:3837-3844.
39. Anariba F, Viswanathan U, Bocian DF, & McCreery RL (2006) Determination of the Structure and Orientation of Organic Molecules Tethered to Flat Graphitic Carbon by ATR-FT-IR and Raman Spectroscopy. *Anal. Chem.* 78:3104-3112.

40. Salomon A, Cahen D, Lindsay S, Tomfohr J, Engelkes VB & Frisbie CD (2003) Comparison of Electronic Transport Measurement on Organic Molecules. *Adv. Mater.* 15(22):1881-1890.
41. Choi SH, Kim B, & Frisbie CD (2008) Electrical Resistance of Long Conjugated Molecular Wires. *Science.* 320:1482-1486.
42. Liu H, Wang N, Zhao J, Guo Y, Yin X, Boey FY & Zhang H (2008) Length-Dependent Conductance of Molecular Wires and Contact Resistance in Metal-Molecule-Metal Junctions. *ChemPhysChem.* 9:1416-1424.
43. Simmons JG (1963) Generalized Formula for the Electric Tunnel Effect between Similar Electrodes Separated by a Thin Insulating Film. *J. Appl. Phys.* 34(6):1793-1803.
44. Huisman EH, Guedon CM, Wees BJV, & Molen SJvd (2009) Interpretation of Transition Voltage Spectroscopy. *Nano Lett.* 9(11):3909-3913.
45. Engelkes VB, Beebe JM, & Frisbie CD (2004) Length-Dependent Transport in Molecular Junctions Based on SAMs of Alkanethiols and Alkanedithiols: Effect of Metal Work Function and Applied Bias on Tunneling Efficiency and Contact Resistance. *J. Am. Chem. Soc.* 126:14287-14296.
46. Kock N & Vollmer A (2006) Electrode-molecular Semiconductor Contacts: Work-Function-Dependent Hole Injection Barriers versus Fermi-Level Pinning. *Appl. Phys. Lett.* 89:162107.
47. Ivanko J, Netzer FP, & Ramsey MG (2007) On Validity of the Schottky-Mott Rule in Organic Semiconductors: Sexithiophene on Various Substrates. *J. Appl. Phys.* 101:103712.

48. Yan L, Watkins NJ, Zorba S, Gao Y, & Tang CW (2001) Direct Observation of Fermi-Level Pinning in Cs-doped CuPc Film. *Appl. Phys. Lett.* 79(25):4148-4150.
49. Yan L, Watkins NJ, Zorba S, Gao Y, & Tang CW (2002) Thermodynamic Equilibrium and Metal-Organic Interface Dipole. *Appl. Phys. Lett.* 81(15):2752-2754.
50. Chen J, Markussen T, & Thygesen KS (2010) Quantifying Transition Voltage Spectroscopy of Molecular Junctions: Ab initio Calculations. *Phys. Rev. B.* 82:121412(R).
51. Heimel G, Romaner L, Bredas J-L, & Zojer E (2008) Odd-Even Effects in Self-Assembled Monolayers of w-(Biphenyl-4-yl)alkanethiols: A First-Principles Study. *Langmuir.* 24:474-482.
52. Garcia-Lastra JM, Rostgaard C, Rubio A, & Thygesen KS (2009) Polarization-Induced Renormalization of Molecular Levels at Metallic and Semiconducting Surfaces. *Phys. Rev. B.* 80:245427.

## Chapter-3

### Direct Optical Determination of Interfacial Transport barriers in Molecular Tunnel Junctions:

#### 3.1 Introduction:

In addition to possibly representing an important size limit for miniaturization of electronic components (1), circuit elements incorporating molecules may provide new functions or better performance than current devices (2). The ability to make the advanced function/performance molecular components that have been envisioned requires specific tailoring of electronic energy levels (3-5), which generally differ significantly from those of the isolated molecules and contact materials (6), as noted in the chapter-2. It is therefore critical to determine these energy levels in functioning devices in order to fully understand the factors that control the electronic properties of molecular devices.

Photocurrent measurements have been used to probe the height of interfacial barriers in classical oxide-containing tunnel junctions, many of which are based on aluminum oxide films (7-12). In these cases, non-equilibrium carriers generated from the decay of photoexcited surface plasmons in a metal contact (13) produce photocurrent when the incident photons have energy in excess than the interfacial barrier height. For example, photocurrent cut-off energies can directly yield the barrier for electron or hole tunneling (10). The generation of photocurrent in molecular devices has been considered theoretically (14) and a few measurements of a range of photoeffects have been reported (15-17). These have generally shown a persistent, non-

bolometric photocurrent, but the observed effects have not been correlated with device energy levels.

Charge transport in molecular junctions is governed by the height of the interfacial energy barriers, as well as the total distance between the conductors. For small distances (i.e., less than  $\sim 5$  nm (18, 19)), coherent tunneling dominates transport. Previously it is shown that transport in PPF(carbon)/molecule/Cu molecular junctions with thickness of less than  $\sim 5$  nm is consistent with coherent tunneling, with very weak temperature dependence (6, 20, 21). Figure 3.1 shows an energy level diagram of the molecular junction. Here, the offset between the Fermi level ( $E_f$ ) of the contacts and the molecular orbital energies defines the tunneling barrier for electrons ( $\phi_{e-}$ , for LUMO-mediated transport) and holes ( $\phi_{h+}$ , for HOMO-mediated transport).

While the energy level diagram seems straight-forward, the energy levels of the isolated components often cannot be used to determine the tunneling barrier in a completed device (6, 22). As concluded in chapter 2, failure of the Schottky-Mott rule (5, 23) in carbon/molecule/Cu devices results from strong electronic coupling between the substrate and molecule, which perturbs the energy levels such that the local vacuum levels of the substrate and molecular layer are not aligned. While *ex-situ* measurements using ultraviolet photoelectron spectroscopy (UPS) can be used to estimate hole barriers (6, 24), and correlated to transport measurements, such methods do not include the effect of the top contact. Because the entire system needs to be considered together, it is clear that a technique for direct measurement of the tunnel barrier in a completed, working molecular junction is highly desirable.

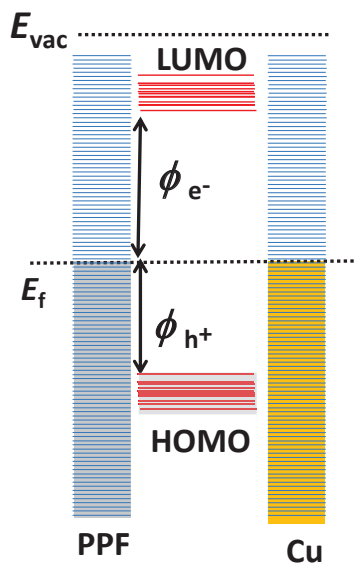


**Figure 3.1:** Energy level diagram showing a non-resonant tunnel barrier for holes (HOMO-mediated transport) and electrons (LUMO-mediated transport).

### 3.1.1 Internal photoemission (IPE) vs. external photoemission:

External photoemission, which is often referred to as the photoelectric effect, is a well-known phenomenon where the light interacts with solid matter. According to the classical theory it is attributed mainly to the transfer of energy from the light to an electron in the metal. Electrons are only dislodged from the metals if light reaches or exceeds a threshold frequency below which no electron can be emitted from the metals regardless of the intensity of the light and the length of the exposure.

Figure 3.2 shows a schematic representation of the Potassium metal surface, with the work function ( $\phi_{\text{work}}$ ) of 2 eV. When a photon of particular energy 1.77 eV (shown in red line) hits the surface of metal the electrons are not ejected from the metal surface because the energy of the incident light is less than the work function of the metal. Whereas, when photons with energy greater than 2.0 eV are incident on the metal surface, the electrons are ejected out with a particular kinetic energy (shown by the green and the violet lines in figure 3.2).

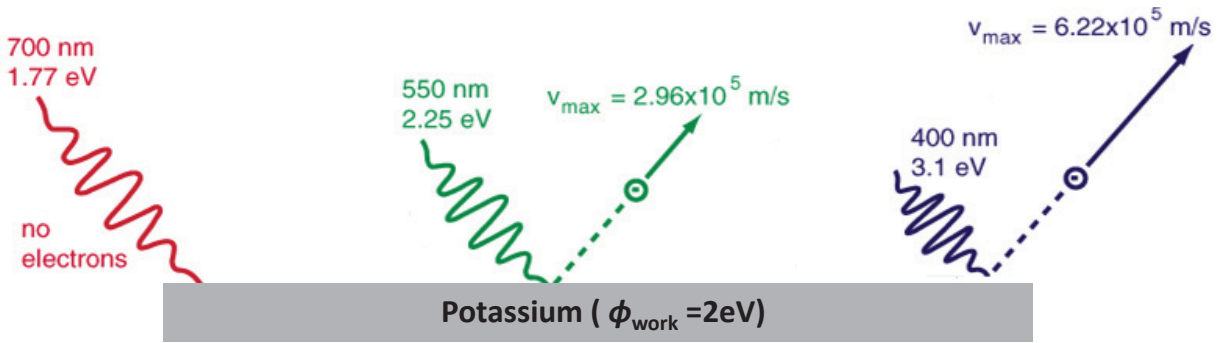


**Figure 3.2:** Light of different energy (wavelength), incident on the surface of the metal (potassium, work function  $\phi_{\text{work}} = 2 \text{ eV}$ ). Only photons of energy greater than the work function of the metal eject electrons from surface of metal.

Einstein proposed mathematical equations to explain the photoelectric effect built upon Planck's photon hypothesis.

$$\text{(Eqn 3.1)} \quad E = h\nu$$

where  $E$  is the energy,  $h$  is the Planck's constant and  $\nu$  is the frequency. When a photon hits the surface of the metal they could donate their energy to the electrons. A certain amount of energy will always be required to remove electrons from their bonds. The remaining energy appears as the kinetic energy of the released electrons. The maximum kinetic energy that the electrons could have is given by

$$\text{(Eqn 3.2)} \quad E_{\text{kin}} = h\nu - \phi_{\text{work}}$$

by plotting equation (3.2), figure 3.3 shows that, by measuring the kinetic energy of the ejected electron and knowing the frequency of the incident light it is possible to determine the work function of the given metal. Figure 3.4 shows the idealized representation of the energy level diagram of Potassium metal, with the given work function of 2 eV. Work function is the energy difference between the vacuum level and the Fermi level. When a photon of energy greater than 2 eV hits the surface of the metals, then the electrons are ejected out from the surface of the metal to above the vacuum level, where the electrons can be detected.

$E_{kin}$  = Kinetic energy of emitted electrons

$h\nu$  = Energy of incident light

$\phi_{work}$  = Work function of the metal

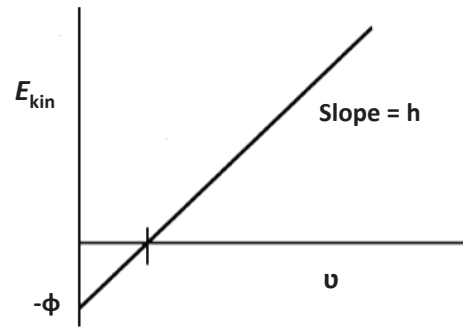


**Figure 3.3:** Plot of Kinetic energy of the ejected electrons vs. the frequency of the incident photons.

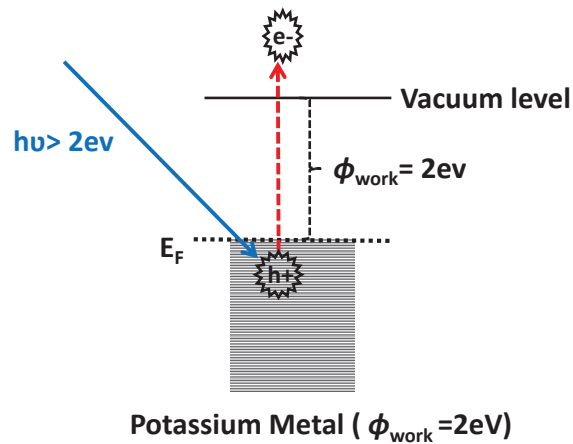


**Figure 3.4:** Idealized cartoon representation of potassium metal (energy level) showing external photoemission (photoelectric effect).

Internal Photoemission (IPE), on the other hand, has been described as a sub-work function photoelectric effect, where the charge carriers are excited from one conductor into another across a solid state barrier material rather than into a vacuum (which would require a higher energy than barrier crossing) (25).

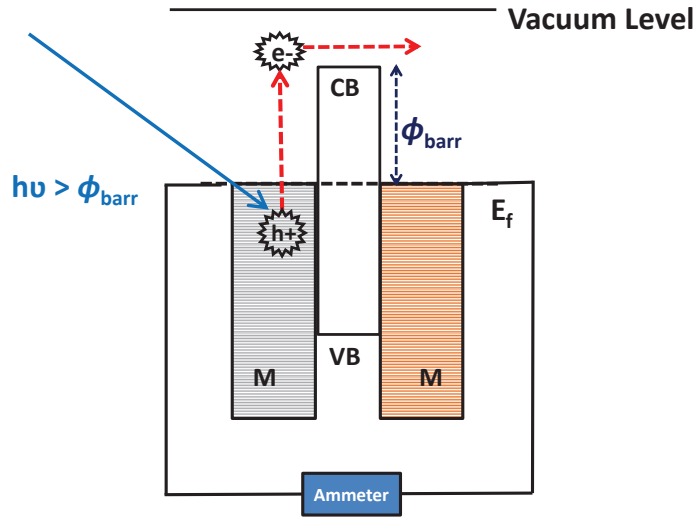


**Figure 3.5:** Idealized cartoon representation of energy level diagram showing internal photoemission (IPE) process, where  $\phi_{\text{barr}}$  denotes the interfacial barrier height.

Figure 3.5 shows the cartoon representation of the energy level diagram of a Metal-Insulator-Metal (MIM) system. Where  $E_f$  represents the Fermi energy level, VB and CB represent the valence band and the conduction band of the insulator, respectively.  $\phi_{\text{barr}}$  denotes the interfacial barrier height as shown in the diagram. If a photon of energy greater than that of the interfacial barrier height is incident on the surface of the metals hot charge carriers were generated, (e.g. electrons if figure 3.5), and they have enough energy to cross the interfacial barrier and move into the other conductor. The term “hot charge carrier” is used here to mean a non-equilibrium carrier such as an electron with energy higher than the Fermi energy. The key difference between IPE and external photoemission is that in the case of IPE the generated hot electrons lack enough energy to exceed the vacuum level and therefore, cannot be experimentally detected by an external detector. In most IPE experiments, the photocurrent is detected by an ammeter completing an electronic circuit between the two conductors, as shown in figure 3.5.

### 3.1.2 Fowler theory:

Generally, internal photoemission yield (Y) is governed by Fowler theory. The barrier height for a metal-insulator, metal-semiconductors or semiconductor-insulator interfaces is generally determined from the spectral dependence of the photocurrent (7, 26). The principle of internal photoemission is explained using a Fowler model, which involves three different steps (8). The first step involves the measurement of photocurrent as a function of incident energy given by the equation

(Eqn 3.3)

$$I = A(h\nu)(h\nu - \phi_{barr})^2$$

where, I is the measured photocurrent, A (hν) is the pre-factor, hν is the photon energy and  $\phi_{barr}$  is the interfacial barrier height. The second step involves the measurement of quantum yield from the measured photocurrent in the first step.

(Eqn 3.4)

$$Y(h\nu) = \text{Photocurrent} / \text{incident flux} = \frac{I(h\nu)}{qF}$$

where I= measured photocurrent in amperes, q= electronic charge in coulombs and F= photon flux in photons/sec. The final step is construction a Fowler plot of the square root of the quantum yield vs. the photon energy. From equations 3.3 and 3.4,  $Y^{1/2}$  is a linear function of incident photon energy(8), and the interfacial barrier height can be extracted from the X-axis intercept of the Fowler plot.

Considering the example of an Al/Al<sub>2</sub>O<sub>3</sub>/Al junction (8), Figure 3.6A shows the idealized representation of energy level alignment of Al<sub>Top</sub>(100 nm)/Al<sub>2</sub>O<sub>3</sub>/Al<sub>Bottom</sub>(17 nm) sandwich structure, where a photon of particular energy is incident from the bottom side (green arrow). A

previous investigation shows that the zero-bias barrier is nearly trapezoidal with the greater barrier height at the top electrode(27). Figure 3.6B shows the Fowler plot for the Al/Al<sub>2</sub>O<sub>3</sub>/Al junction, linear relation fall in accordance with the mathematical equation and the X intercept value (2 eV), is considered to be the interfacial barrier heights for the Al/Al<sub>2</sub>O<sub>3</sub> junctions. (The value reported for barrier height (2 eV), is shown in the energy level diagram as red double sided arrows in figure 3.6A).

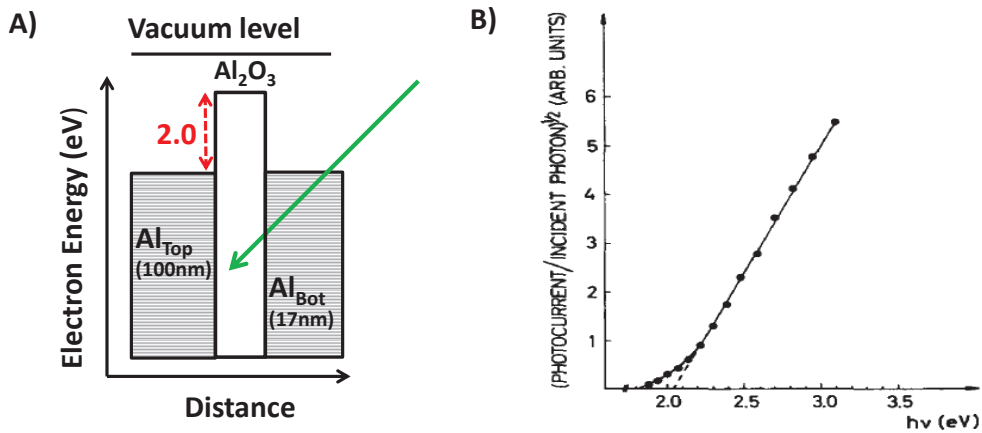


**Figure 3.6:** (A) Idealized energy level alignment diagram of Al/Al<sub>2</sub>O<sub>3</sub>/Al sandwich structure (reference 8). (B) Fowler intercept for the Al/Al<sub>2</sub>O<sub>3</sub> junction previously reported Gundlach et al (reference 8).

### 3.1.2.1 Determination of barrier heights using Fowler method:

To illustrate experimental determination of barrier heights, consider a related example used by Goodman, et al. (10), Figure 3.7A shows the experimental apparatus, in which one contact (the base electrode) to the Al<sub>2</sub>O<sub>3</sub> layer is the Al from which it was grown. The counter electrode (contact on the opposite side of the Al<sub>2</sub>O<sub>3</sub> layer) is distilled de-ionized water. The water is contained in a plastic box and a strip of Pt was used to make contact with water. The light passes through the water on its way to the sample, as shown. The advantage of using the water counter electrode is that the water is transparent in the wavelength region of interest. Figure 3.7B shows the energy level representation of the system.

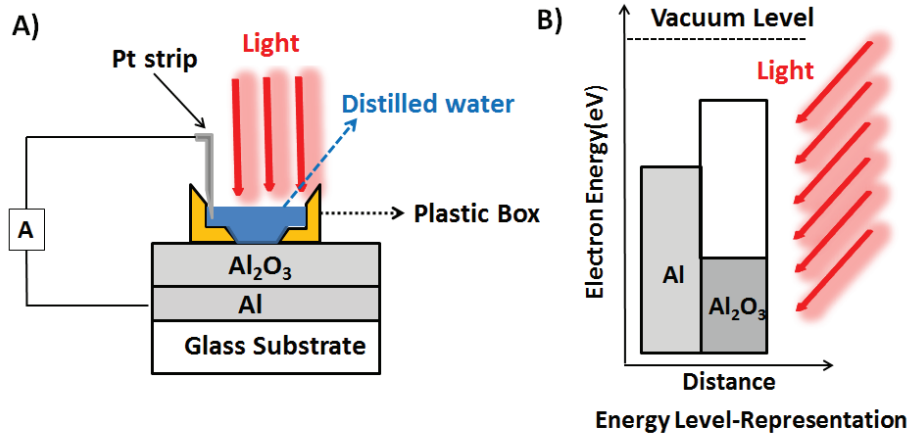


**Figure 3.7:** (A) Experimental apparatus used for Al/Al<sub>2</sub>O<sub>3</sub> junction by Goodman and co-workers (reference 10). (B) Energy level diagram for the Al/Al<sub>2</sub>O<sub>3</sub> junction (reference 10).

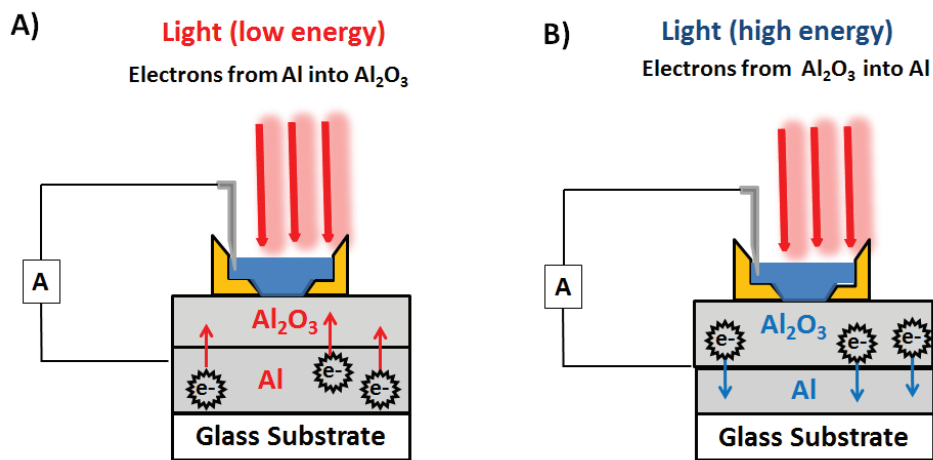


**Figure 3.8:** (A) Experimental apparatus used for Al/Al<sub>2</sub>O<sub>3</sub> junction by Goodman and co-workers showing the direction of flow of electrons at low energy (B) direction of flow of electrons at high energy.

Figure 3.8A shows the photocurrent yield spectrum obtained from the above experiment. The spectrum shows that with no voltage applied in the external circuit, the photocurrent is in the direction of the electron emission at low photon energy and in the direction of hole emission at high photon energy (see figure 3.8A and 3.8B). Figure 3.9B and 3.9C shows the Fowler plot for both the hole and the electron emission regime respectively, The Fowler intercept value reported

for the photoemission of electrons is  $2.0 \pm 0.2$  eV, in reasonable agreement with the value of  $2.0 \text{ eV} \pm .02$  eV reported by Gundlach et al. (which agrees with the value of the Fowler intercept for the higher energy light corresponding to hole emission was  $3.1 \pm 0.2$  eV).

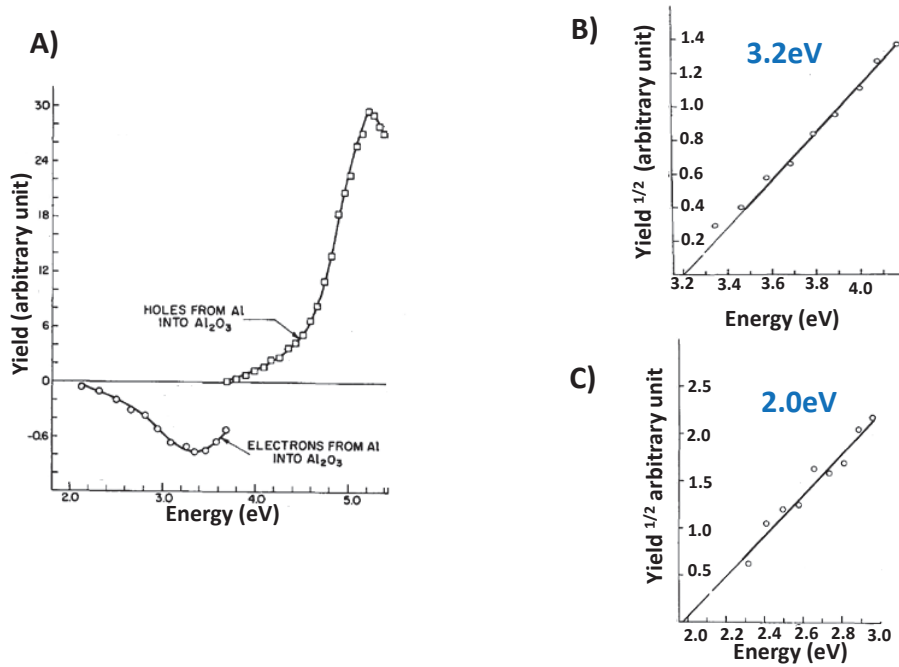


**Figure 3.9:** (A) Photocurrent yield spectrum reported for Al/Al<sub>2</sub>O<sub>3</sub> junction (B) Fowler plot obtained from the positive regime of the photocurrent spectrum (C) Fowler plot obtained from negative regime of the photocurrent spectrum (reference10).

Goodman and co-workers also proposed an approximate band diagram based on the value obtained from the Fowler intercept and by the known work function of Alumina. Figure 3.10 shows the completed band diagram for Al/Al<sub>2</sub>O<sub>3</sub> oxide junctions, with the hole and the tunneling barrier values obtained from the Fowler plots (figure 3.9B & 3.9C).

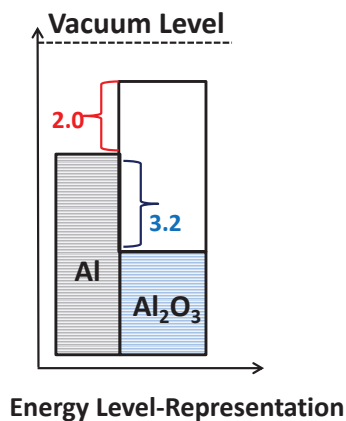


**Figure 3.10:** Idealized Energy level representation of Al/Al<sub>2</sub>O<sub>3</sub> junction with barrier values obtained from Fowler plot (reported by Goodman and coworkers, reference 10).

## 3.2 Junction fabrication and electrical characterization:

### 3.2.1 Junction fabrication:

In order to ensure against photocurrents resulting from silicon, polished fused quartz wafers (Technical Glass Products, <http://www.technicalglass.com/>) were diced into 1.2 x 1.5 cm chips to serve as substrates. Conductive carbon in the form of pyrolyzed photoresist films (PPF) were produced exactly by the same method described in the previous chapter under junction fabrication, section 2.2.1. No bulk silicon or silicon wafers were involved in junction fabrication. Formation of molecular layers ranging from 1-5 nm thickness was carried out by electrochemical reduction of diazonium salts in solution (see section 2.2.3 for details). Briefly, PPF was used as the working electrode in a three-electrode electrochemical cell with a 1 mM solution of the diazonium precursor with 0.1 M tetrabutylammonium tetrafluoroborate (TBABF<sub>4</sub>) as the supporting electrolyte in acetonitrile. To deposit the molecular layer, cyclic voltammetric sweeps starting from +0.4 V versus Ag/Ag<sup>+</sup>, to a negative potential were carried out. The switching potential and the number of sweeps depend on the molecule used and the desired thickness. After modification, the sample is rinsed with acetonitrile (ACN) and dried using a stream of nitrogen.

The derivatization of PPF with aminododecane (C12) was performed by amine oxidation. First, a solution of 5 mM aminododecane in acetonitrile with 0.1 M TBABF<sub>4</sub> was stirred for 1 hour. Next, using the PPF as a working electrode, +1.4 V vs. Ag/Ag<sup>+</sup> was applied for 12 min (28) to obtain a thickness of 2.3 (standard deviation) nm. Initial and final scans were swept from 0 to +1.4 respectively, before and after CPE to check for the passivation of the PPF surface(28, 29). Finally, top contact deposition was carried out via electron beam evaporation through a shadow mask with 0.25 mm wide openings oriented perpendicular to the PPF lines, which results in a cross bar junction of ~0.00125 cm<sup>2</sup> area.

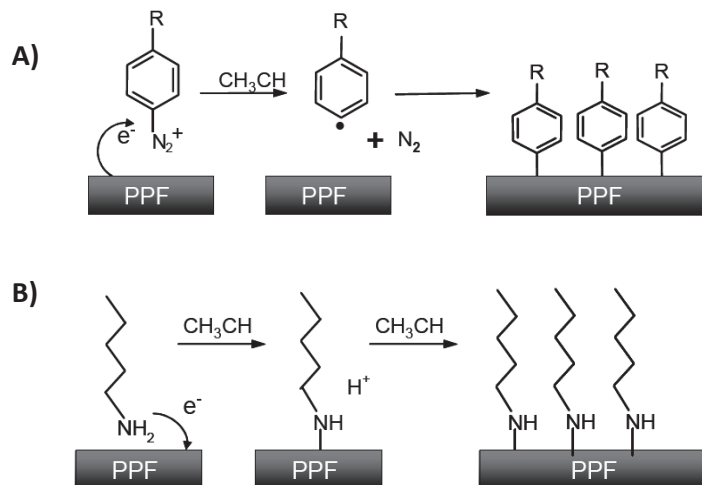


**Figure 3.11:** (A) Schematic of molecular attachment through diazonium reduction, where aryl radical formation is through one-electron electrochemical reduction. (B) Schematic of molecular attachment through oxidation of a primary amine, where radical formation is through one-electron electrochemical oxidation.

For UV absorption measurements a Perkin Elmer 900 spectrometer and optically transparent PPF on quartz was utilized (30, 31). Fabrication follows the same procedure outlined at section 2.2.1, but employs photoresist diluted to a concentration of 5% (v/v) with propylene glycol methyl ether acetate as the solvent, without a photolithography step. These electrodes maintained sufficient conductivity for electrochemistry, enabling modification of the surface via diazonium

ion reduction (31), with derivatization carried out as outlined above. Measurement of molecular layer thickness was done using AFM, using the same procedure described in the previous chapter-2, section 2.3.1.

### 3.2.2 Molecular structures used in this study:

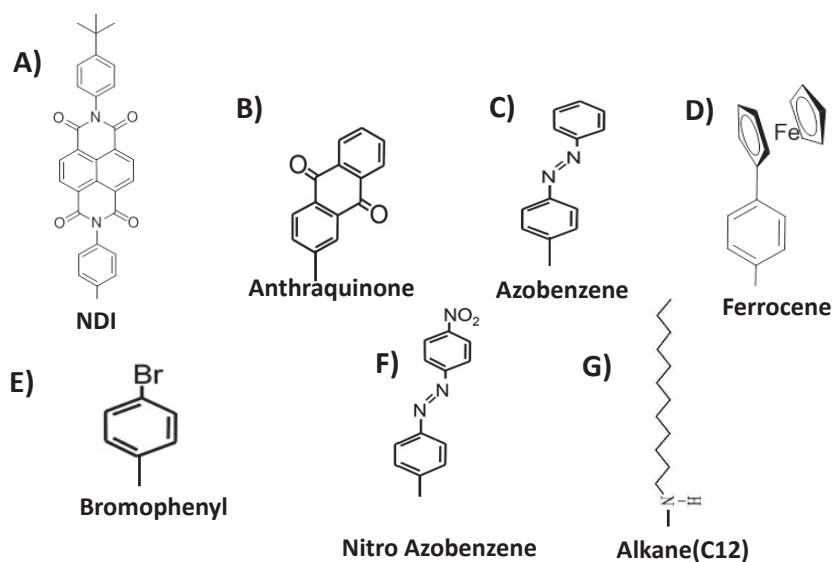


**Figure 3.12:** The structures of all the molecules used in this study. (A) NDI; (B) Anthraquinone; (C) Azobenzene; (D) Ferrocene; (E) Bromophenyl; (F) Nitroazobenzene; (G) Alkane (C<sub>12</sub>H<sub>25</sub>N). In most cases, molecular layers were multilayers of several molecules.

### 3.2.3 Electrical characterization:

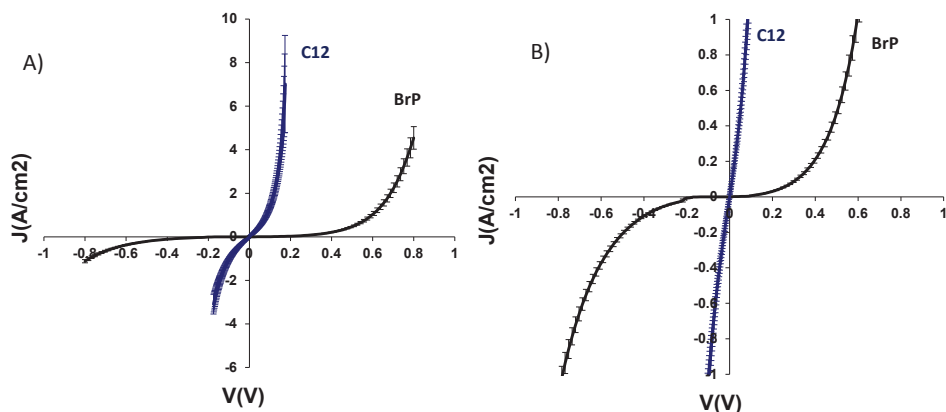


**Figure 3.13:** (A) J-V curves for a series of BrP and C12 junctions with two different Y axis scales. Error bars represent one standard deviation of current density for four junctions on one sample.

The electronic characteristics of the molecular junctions were measured by using the same procedure explained in chapter 2 section 2.2.4. These results indicate that the molecular junctions are not short circuits, which result in linear  $J-V$  curves, but instead result from tunneling across the molecular layer. We note that when “shorted” junctions exhibiting linear  $J-V$  curves are illuminated, the photocurrent signal is indistinguishable from zero.

### 3.3 AFM and UPS measurements:

#### 3.3.1 AFM measurements:

Atomic force microscopy (AFM) was carried out in air with a NanoscopeIIIa Multimode instrument (Digital Instruments, Santa Barbara, CA), using the same procedure as explained in chapter 2 section 2.2.4. Rotated tapping mode etched silicon probes (RTESP) with resonant frequencies of  $\sim 300$  kHz were purchased from Veeco (Sunnyvale, CA). Table-3.1 lists the thicknesses determined for the alkane (C12) and aromatic (bromophenyl) as examples, along with the standard deviation.

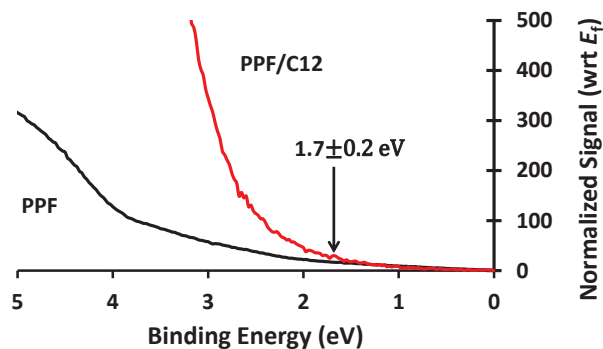
Molecule	Thickness(nm)	Standard Deviation(nm)
Alkane (C12)	2.26	0.79
Bromophenyl(BrP)	2.99	0.37

**Table-3.1:** Summary of the different type of molecules used, and their measured thickness and standard deviation data from the AFM measurements.

#### 3.3.2 UPS measurements:

Electronic structure measurements via UPS in ultrahigh vacuum have been used to correlate molecular conductance with energy level alignment (32, 33). The UPS spectrum can be used to determine the work function (WF) of the sample using the high binding energy cut-off (HBEC), where  $WF = 21.21 - HBEC$  (21.21 eV =  $h\nu$  of the incident He I light). In order to verify the hole barrier for the C12 junction, UPS was carried out to determine the HOMO onset energy (6, 24).

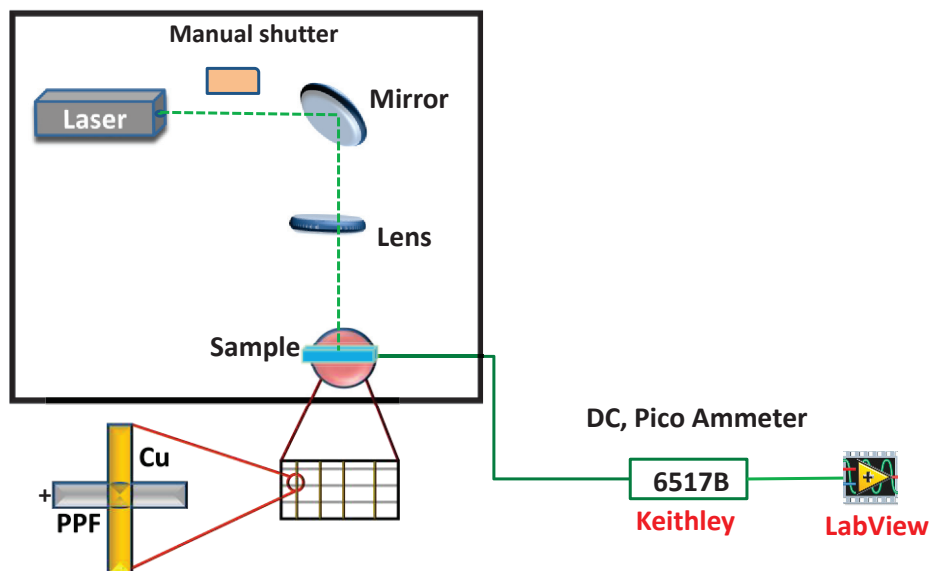
The onset of photoemission for a surface modified with a molecular layer above that for an unmodified substrate in the low binding energy portion of the spectra indicates the presence of occupied states in the modification layer. The onset of this emission has been reported to correspond to the hole tunneling barrier (24). Using the method described by Frisbie et.al (24), an analysis of UPS data for C12 gives the hole barrier height of  $1.7 \pm 0.2$  eV.



**Figure 3.14:** UPS measurement of the HOMO onset energy for C12 on PPF.

### 3.4 Experimental apparatus:

#### 3.4.1 Laser experimental apparatus:



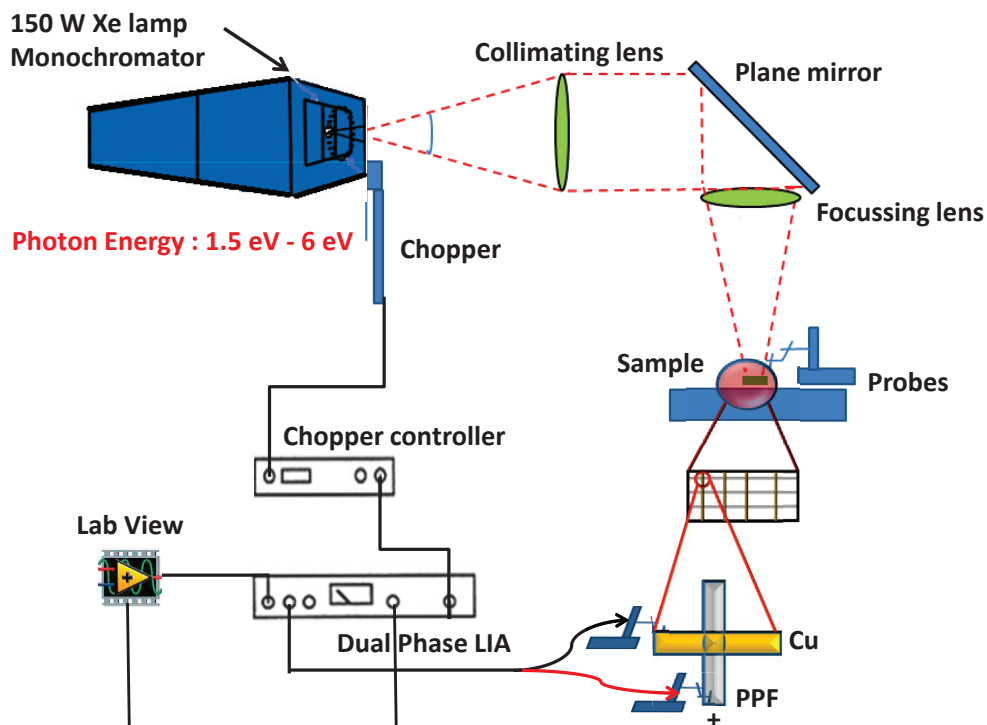
**Figure 3.15:** Experimental apparatus for DC laser illumination and photocurrent measurement.

Figure 3.15 shows the diagram of the experimental apparatus for DC photocurrent measurements, using different lasers argon ion (458 nm/2.7 eV, and 514 nm/2.4 eV), krypton ion (675 nm/1.8 eV), and a diode laser (780 nm/1.58 eV) as different sources of illumination. The wavelength of the monochromatic laser source before each experiment was verified using an Ocean Optics spectrometer (USB-4000). The power from the laser beam at the junction was measured using a Newport power meter (Model 1936-R) before and after each experiment. For all the experiments carried out in this study, the intensity of the laser beam was varied between 1 and 50 mW at the sample. A manual shutter was used to control the exposure time. The PPF contact was connected via a tungsten probe and connected to the input of a DC picoammeter (Kiethley 6517B), where the photocurrent measurements (including polarity) were obtained. The output from the DC Pico ammeter was recorded using a Labview data acquisition program. Laser diodes (808 nm and 852 nm Fabry-Perot laser diodes) were purchased from Thorlabs, each capable of 100 mW maximum output. The power from the laser diode at the junction was also measured using a Newport power meter (Model 1936-R), A Thorlabs LDC 210C laser diode controller and a TED 200C thermoelectric temperature controller were also used to drive and control the laser output.

### **3.4.2 Lock-In Amplifier experimental apparatus:**

Figure 3.16 shows the Xe arc apparatus diagram using a 150 W Xenon arc lamp (Newport model 6256) as the source of illumination. After passing through a model 74004 Cornerstone 130 1/8 m motorized monochromator (band pass = 13 nm), the selected wavelength was chopped at frequency  $\omega$  (typically 400 Hz). The chopped light was then directed through a series of lenses and mirrors for focusing. The PPF contact was connected via a tungsten probe and shielded cable to the AC-coupled current input of a dual phase lock-in amplifier (LIA, Stanford-830), and the

shield (ground) was connected to the Cu contact of the molecular junction. The output from the LIA was recorded using a Labview data acquisition program. In all cases, the PPF was considered the positive terminal.



**Figure 3.16:** Apparatus with Xe arc continuum source, modulation by an optical chopper and detection with Lock-In -Amplifier (LIA).

### 3.5 Calibration of experimental apparatus:

Direct DC photocurrent measurement for BrP junction at 458 nm was carried out using (argon ion laser), with the experimental apparatus shown in figure 3.15. Laser experiments as described previously in section 3.4.1, always give you direct DC measurement. Here in the case of Bromophenyl at 458 nm the photocurrent obtained was positive (see figure 3.17).

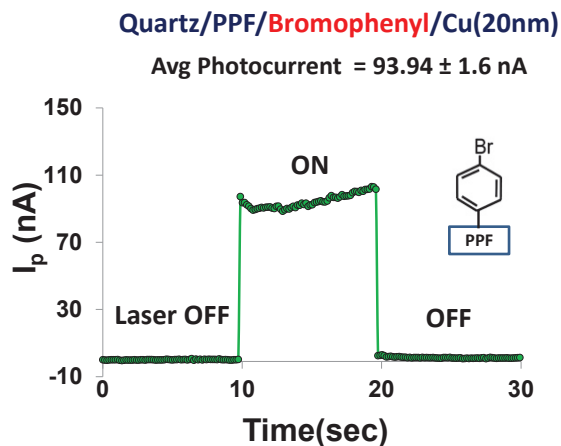


**Figure 3.17:** Direct DC measurement of photocurrent for a BrP junction using 458 nm laser illumination. Positive photocurrent corresponds to electrons flowing from the Cu to PPF electrode in the external circuit.

The main advantage of laser illumination is the direct determination of the sign of the photocurrent at a given energy. The output power of laser can be varied within a wide range, usually from 1 mW-100 mW. However, the selection of wavelengths is limited to one or two values for a given laser. Whereas, for Xe arc lamp with a monochromator different desired wavelength can be obtained and studied using lock in amplifier (LIA). The dual phase lock in amplifier measures both the magnitude and phase of the photocurrent but gives no direct indication of the photocurrent sign unlike the laser experiment. The maximum power obtained from Xe arc source is also significantly lower than that of the lasers, generally <10 mW over the 13 nm bandpass.

### 3.5.1 Oscilloscope calibration apparatus:

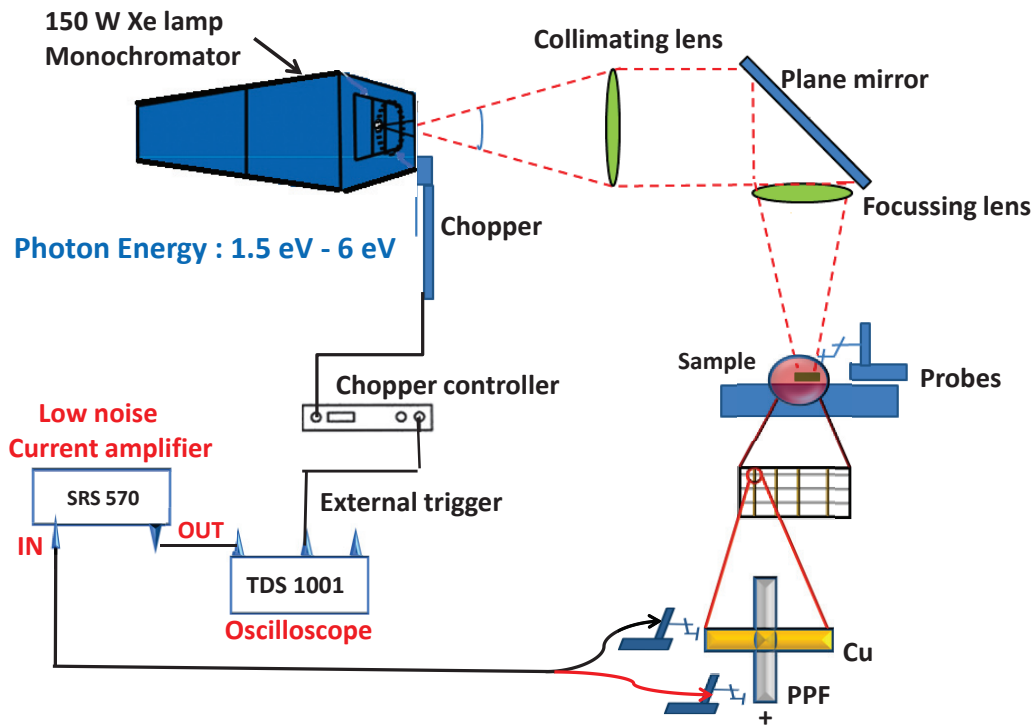


**Figure 3.18:** Apparatus with Xe arc continuum source, modulation by an optical chopper and calibration using an Oscilloscope.

The experimental apparatus using oscilloscope is very similar to that of the lock in amplifier, and was used to verify the photocurrent sign. Here the signal from the junction was directed to an SRS amplifier which in turn is wired to an Oscilloscope. Since the chopper phase relative to the light intensity is determined mechanically and is variable, it must be calibrated with a known photoactive detector. Initially a readily available photodiode (Advanced Photonix P/N: PDB-C613-2, response time 50 ns) was used for phase calibration with the oscilloscope. Figure 3.18A shows the synchronization signal from the chopper, with a given chopper frequency of 400Hz and the illumination from the arc source kept at 400 nm wavelength. From the figure it's quite clear that the response time for the photodiode is much faster than the chopping frequency. The photodiode polarity was selected to positive photocurrent output, meaning that electrons flowed

toward the positive lead of the photodiode when it was illuminated. The photodiode was then replaced with a molecular junction (Azobenzene (AB) junction), with the PPF lead replacing the positive lead of the photodiode, as shown in figure 3.16. The AB junction gives a negative photocurrent at 400 nm when the light is ON, as shown in figure 3.19-B. This result indicates that a direct, modulated response from a molecular junction can be obtained using the Xe arc, without using the LIA. Furthermore, it directly indicates that electrons flow from PPF to Cu of the AB junction in the external circuit when illuminated.

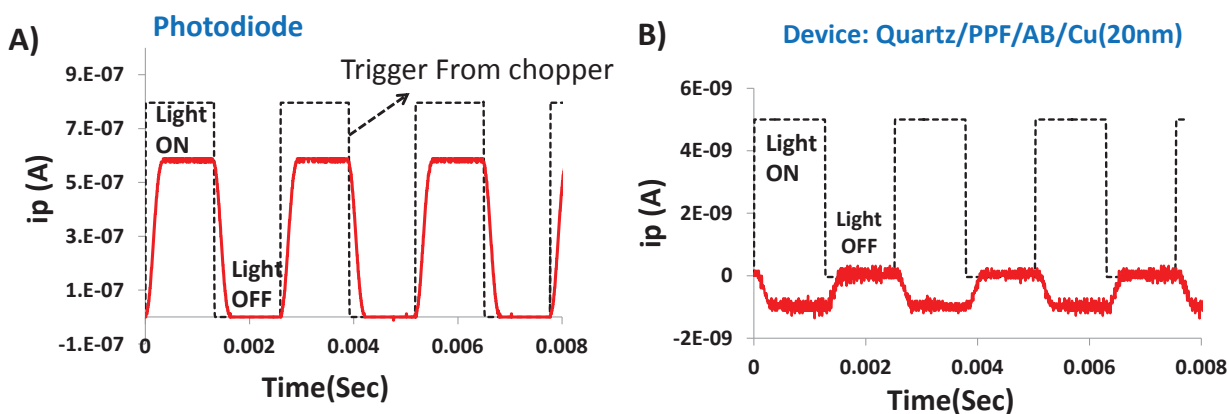


**Figure 3.19:** (A) Photoresponse of the photodiode (ON and OFF) overlaid with trigger from the chopper. (B) Photoresponse of AB junction overlaid with the trigger from chopper, indicating a real response from molecular junction.

### 3.5.2 Phase calibration using photodiode:

The photocurrent measured using the apparatus given in Figure 3.16 with a lock-in amplifier (LIA) gives only the magnitude of the current, the sign has to be determined through phase. For calibrating the phase, we employed a photodiode (Advanced Photonix P/N: PDB-C613-2, response time 50 ns), wired so that a positive photocurrent resulted from illumination (see Figure 3.19). Figure 3.20A & 3.20B shows the spectrum for the photocurrent and the phase obtained directly from the dual lock-in amplifier (LIA). The chopper frequency was 400Hz. The output phase was then adjusted at LIA to read zero degrees (figure 3.20C). While keeping the geometry

and all other variables (including the wiring) constant, the photodiode was replaced with a molecular junction. The sign of the photocurrent can then be determined from the phase value obtained from Lock-In-Amplifier (LIA), as described below

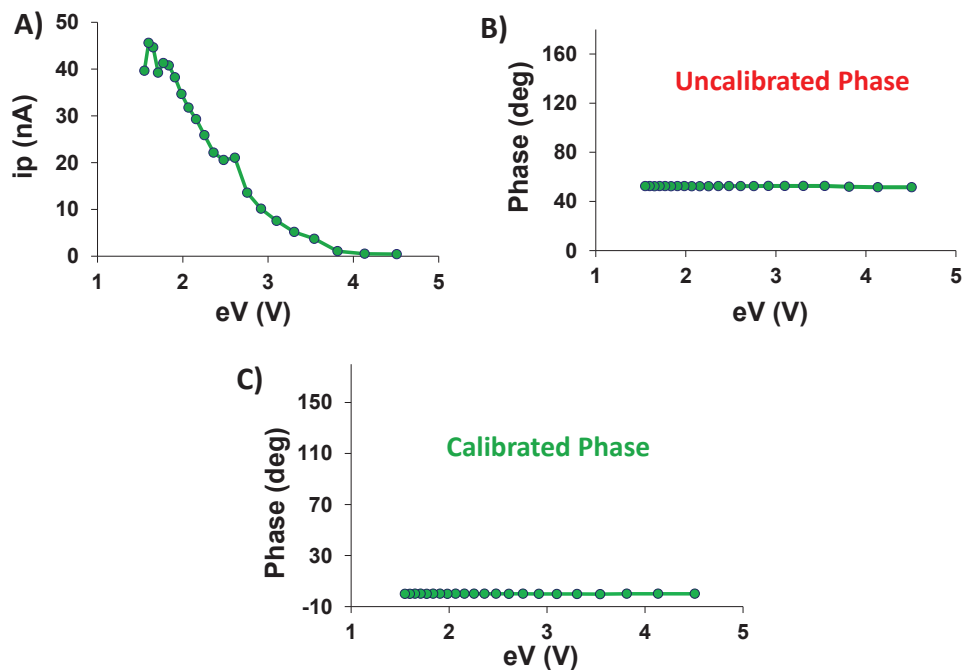


**Figure 3.20:** (A) Photocurrent spectrum of the photodiode obtained from LIA experimental apparatus (B) the phase spectrum obtained from the LIA for the photodiode. (C) Zero-phase adjusted spectrum for photodiode.

### 3.5.3 Dependence of phase & photocurrent on chopper frequency:

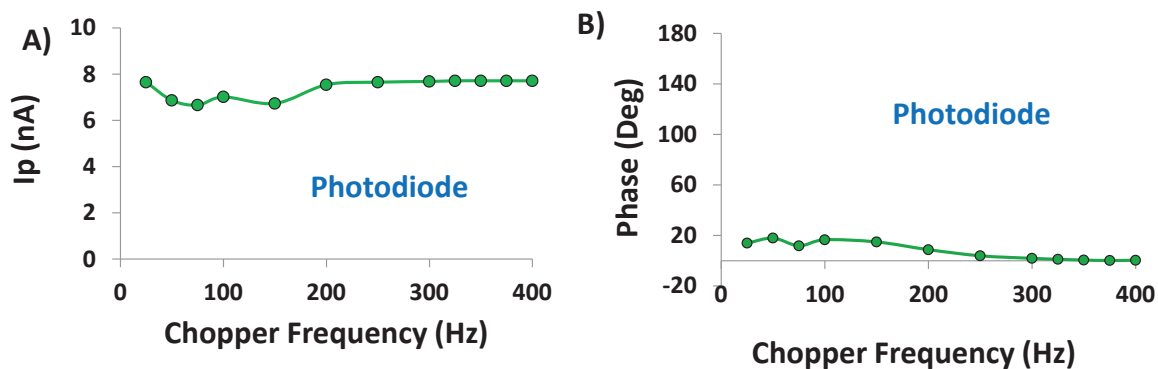


**Figure 3.21:** (A) Photoresponse of photodiode vs. chopper frequency. (B) Photodiode phase as a function of chopper frequency.

Figure 3.20A shows the response of the photodiode while varying the chopper frequency. The photoresponse is independent of the chopper frequency, and the small changes observed in the photocurrent as a function of chopping frequency are likely due to mechanical and geometrical factors in the experimental arrangement. Figure 3.20B shows photodiode phase as a function of chopper frequency. The phase remains very close to zero in the entire range of chopping frequency studied. By keeping the geometry and other variables constant and replacing the photodiode with a molecular junction, the dependence of phase and photocurrent for a molecular junction was also studied. Figure 3.22 shows the results of these studies, where the phase and the photocurrent remain independent of the chopper frequency. The phase of the molecular junction is  $180^\circ$  different from that of the photodiode, indicating that the photocurrent is negative for the example shown. As noted earlier, a negative photocurrent indicates electrons flowing from the Cu contact to the PPF contact through the external circuit when the junction is illuminated.

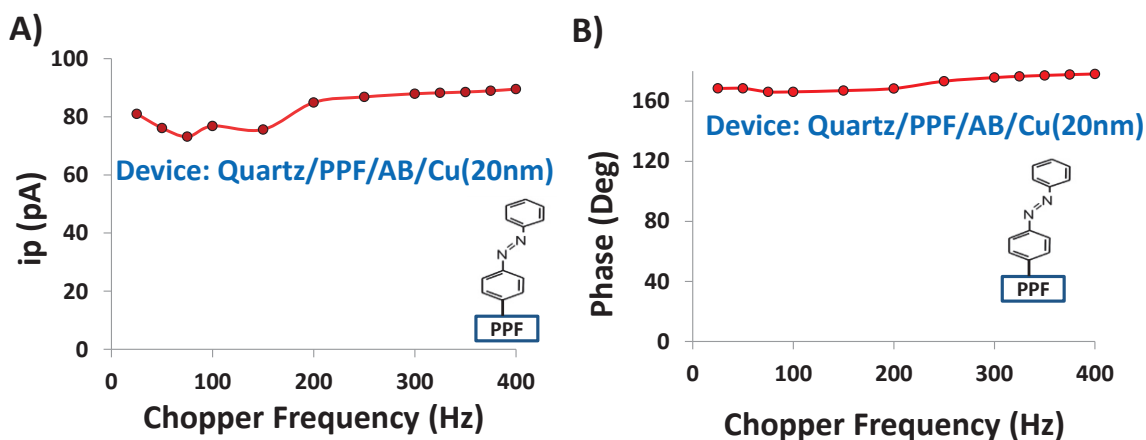


**Figure 3.22:** (A) Photoresponse of an AB junction vs. chopper frequency. (B) Phase of the AB junction as a function of chopper frequency.

### 3.5.4 Assigning photocurrent sign for molecular junctions:

By keeping the geometry and other variables constant and replacing the photodiode with a molecular junction, the sign of the photocurrent can be determined from the phase output of the LIA. For example, when the phase remains near zero, the photocurrent is positive, with the molecular junctions exhibiting the same polarity as the photodiode. Conversely, a phase output of  $180^\circ$  indicates negative photocurrent. We have defined a negative photocurrent for cases where the phase is between  $-90^\circ$  and  $-180^\circ$ , while positive photocurrent is taken for  $0^\circ$  to  $-90^\circ$ .

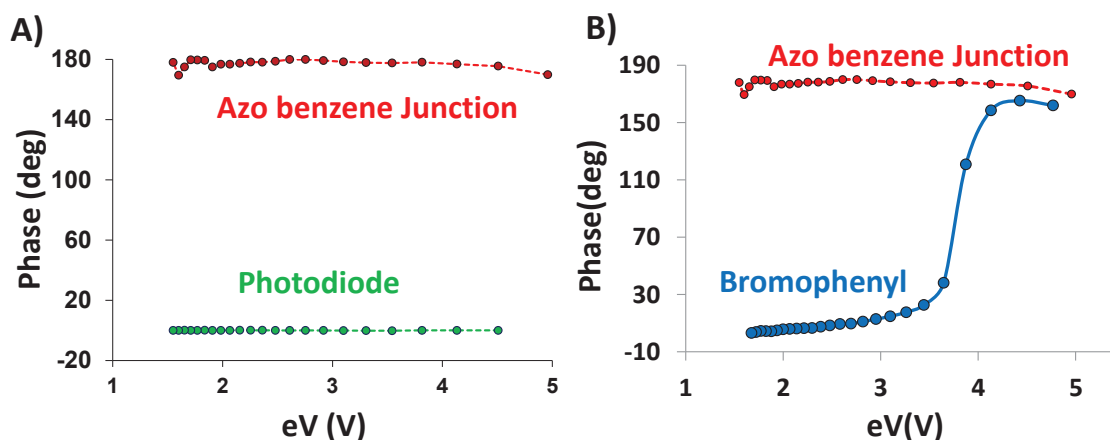


**Figure 3.23:** (A) Overlay of phase spectrum of AB junction and photodiode. (B) Overlay of phase spectrum of AB and Bromophenyl junctions obtained from the LIA apparatus.

### 3.5.5 Verification of phase using laser experiment:

The phase output for the AB junction for all energies studies is near  $180^\circ$  (see figure 3.23A), indicating a negative photocurrent. Whereas for the Bromophenyl junction the phase output remains near zero below 3.8 eV, indicating a positive photocurrent with the same polarity as the photodiode. At energy greater than 3.8 eV the phase value indicates a photocurrent sign change for the BrP molecule i.e. from positive to negative. We used the Direct DC laser experiment to verify the phase.

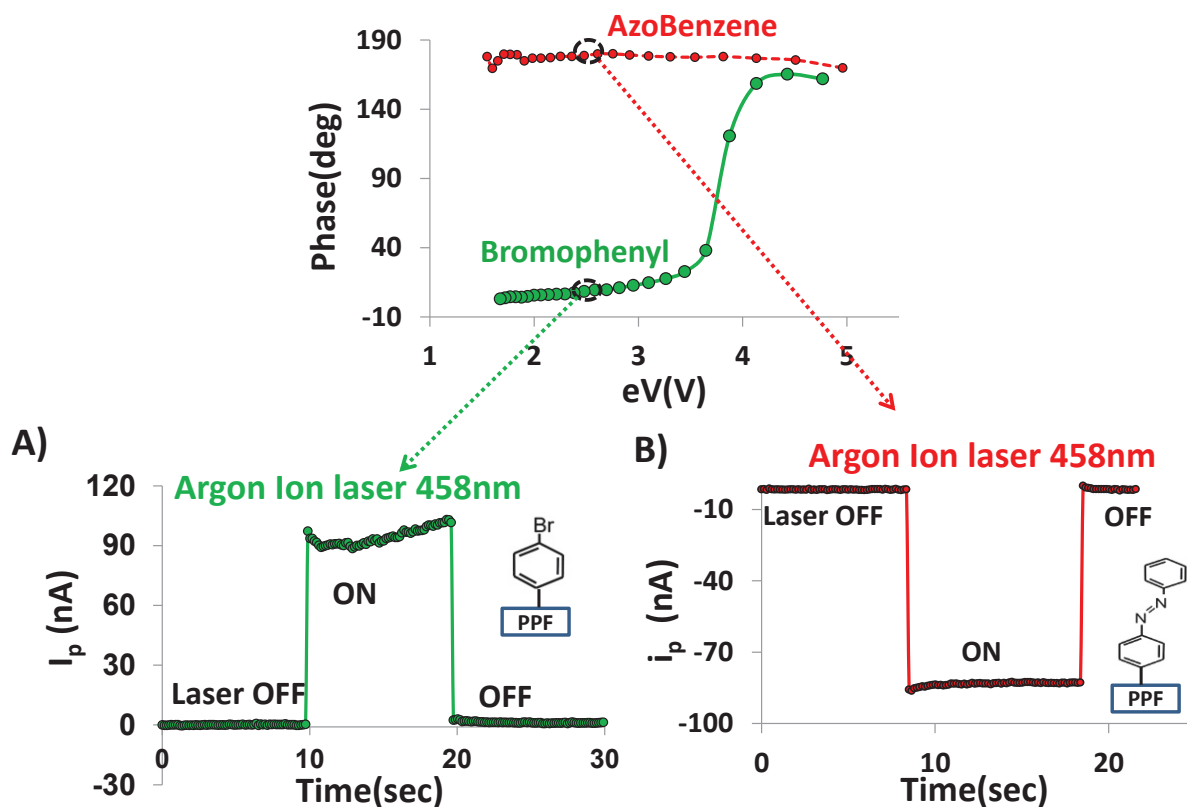


**Figure 3.24:** (A) Direct DC measurement of photocurrent for a BrP junction using 458nm laser illumination, showing positive photocurrent. (B) Direct DC measurement of photocurrent for a BrP junction using 458nm laser illumination, showing negative photocurrent.

The laser experimental apparatus used was explained previously in section 3.4.1, Argon ion laser at 458 nm (2.7eV) with 20 mW power at sample was used for illumination. From the phase spectrum 3.22B it was expected that at 458nm (2.7 eV), AB molecules will exhibit a negative photocurrent whereas BrP should be positive. Results obtained from direct DC measurements (Figure 3.24A and 3.24B), indicates that the photocurrent sign from phase calibration with the photodiode is correct, and the same procedure was used to determine the sign of the photocurrent for other molecules.

### 3.5.6 Analysis of bolometric mechanism:

We carried out various tests to assess the possibility of heat-induced currents in molecular junctions. Initially, we observed excellent stability and the response time was faster than the mechanical limit imposed by the chopper. As shown in Figure 3.25, a response time faster than  $250\ \mu\text{s}$  was observed.

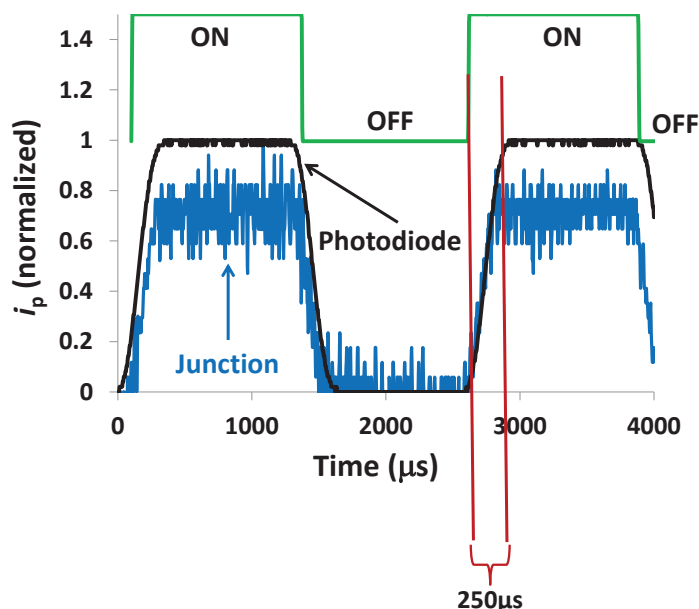


**Figure 3.25:** Oscilloscope trace of photocurrent versus time for 400 nm wavelength at 400 Hz for a photodiode (black curve) and a molecular junction (blue curve), showing that the response time of the molecular junction is faster than  $250\ \mu\text{s}$ . This lag time is due to the mechanical limit of the chopper wheel in the experimental setup, shown by the overlay of the photodiode response. Although the electronic response time of the photodiode is 50 ns, it shows a similar rise time to the molecular junction.

An additional test for heat-induced currents is the dependence of the photocurrent on chopping frequency. According to literature (34), heat-related photocurrent is expected to decrease with increasing chopping frequency, by the factor  $f_{\text{chop}}^{-1.5}$ . As shown in Figure 3.25, this is clearly not the case for the molecular junctions studied here. In addition, the overlay of the response for the photodiode (response time 50 ns) indicates that the small changes observed in the photocurrent

as a function of chopping frequency are likely due to mechanical and geometrical factors in the experimental apparatus. Therefore the possibility of heat-induced photocurrent, if any, is much smaller than the observed junction photocurrents.

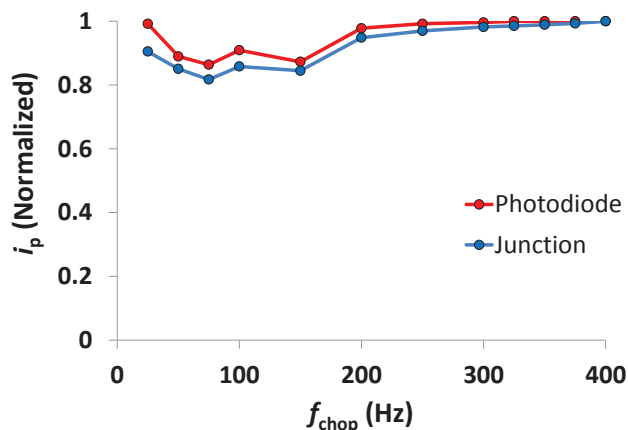


**Figure 3.26:** Variation of the measured photocurrent for a molecular junction (red curve) and photodiode (blue curve).

### 3.6 Conversion of photocurrent to yield:

In order to determine the quantum yield for photocurrent generation, the power incident onto the junction was determined at each wavelength using a Newport power meter (Model 1936-R). The power density as a function of wavelength is given in Figure 3.26, and was periodically verified. The beam power density ( $P_b$ , in  $\text{W cm}^{-2}$ ) was then calculated by dividing the observed power by the beam area ( $0.0576 \text{ cm}^2$ ). Since the beam area is much larger than the junction area ( $A_j = 0.0012 \text{ cm}^2$ ), the total power incident onto the junction was  $P_b \times A_j$ , with visual inspection (a magnified camera view) and micrometer-controlled stage used to ensure proper junction positioning. Photon flux (pf, photons per second incident onto the junction) is given by

$$\text{(Eqn 3.5)} \quad \text{pf} = \frac{P_b A_j}{h\nu}$$

where  $h$  is Planck's constant ( $6.62607 \times 10^{-34}$  J s) and  $\nu$  is the frequency of the incident light ( $c/\lambda$ ). The measured photocurrent was converted to electron flux,  $ef$  (e- per second):

$$(Eqn 3.6) \quad ef = \frac{i_p}{q}$$

where  $q$  is the elementary charge ( $1.60218 \times 10^{-19}$  C/e). Finally, yield ( $Y$ , in e- per photon incident on the junction) is calculated by

$$(Eqn 3.7) \quad Y = \frac{ef}{pf}$$

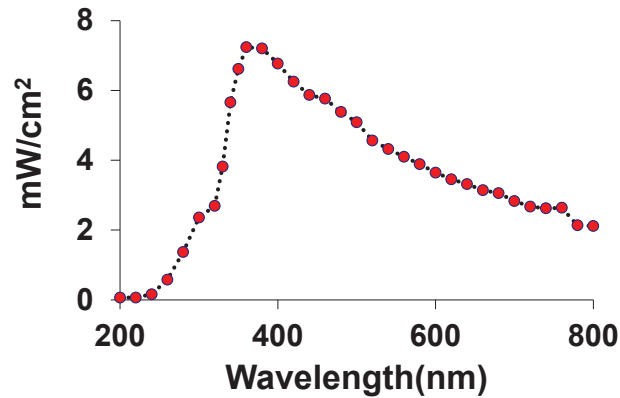


**Figure 3.27:** Power density of Xe arc/monochromator with bandpass of 13 nm, measured at the sample position.

### 3.7 Background correction & noise level:

With the experimental apparatus as shown in figure-3.16, the photocurrent measured in the molecular junction was in the range of 1-1000 pA. Therefore, it is important to measure the background noise level of the system. In order to measure the background level we kept the illumination source ON and chopper ON, the probes were then connected to the molecular junctions which in turn was connected to the Lock-in amplifier using a BNC cable but the shutter was kept closed i.e. all the conditions were kept exactly the same except the shutter closed so no source photons reached the junction. Then the background noise was measured continuously for

28 hrs. The average background noise was measured to be 3.1pA and its time course is shown in figure 3.27. Background responses at various other conditions were also tested with illumination source ON, probes disconnected, varying the BNC connection cables etc., but in all other cases the background noise was found to be less than 3pA.

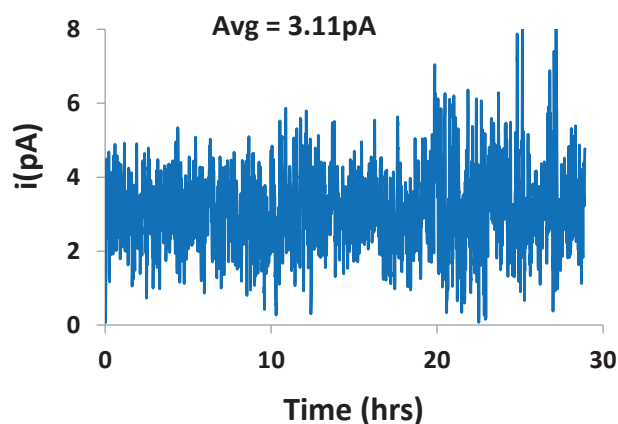


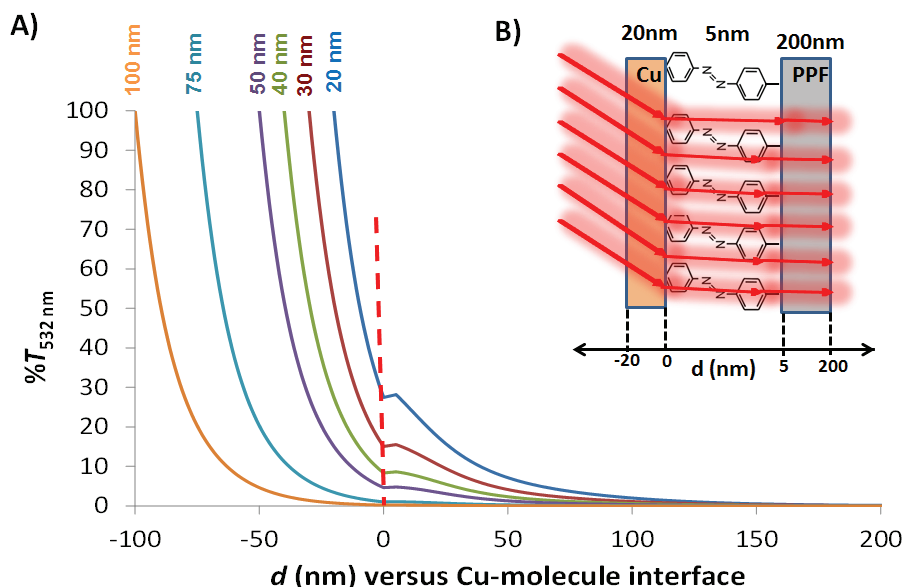
**Figure 3.28:** Background noise continuously measured for 28 hrs.

In-order to obtain a background corrected photocurrent spectrum from a particular junction, the photocurrent spectrum of that junction with the given energy range was taken and then another photocurrent measurement (background) was made with the same experimental conditions except the shutter remained closed so that no source photons reach the junction. The background response spectrum obtained was then subtracted from the initial photocurrent measurement to obtain a background corrected photocurrent spectrum, which was then used to calculate the yield of the photocurrent.

### **3.8 Thin film optical property calculation:**

Optical thin film calculations were performed with “Filmstar” software on the PPF/molecule/Cu system to understand how transmission occurs through the junction stack, i.e. how much of light is transmitted through each layer of the molecular junction. Figure 3.29A

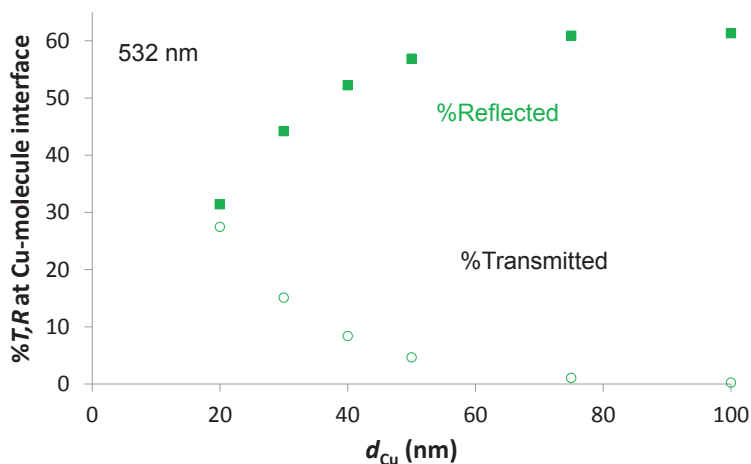
shows the predicted transmission of Cu/molecule (5 nm)/PPF system where the thickness of the top contact (Cu) is varied. In this model (figure 3.29B) light was incident perpendicular to the copper surface so that a certain amount of light is transmitted through the copper to the molecule and finally to the carbon (PPF). For the calculated spectrum given below in figure 3.29A the wavelength used was 532 nm and the point '0' on the x axis was considered to be Cu/molecule interface also shown in figure 3.29B for better understanding. The optical constants ( $n$ = refractive index and  $K$ = di-electric constant) used for Filmstar calculation in each layer was Cu ( $n=1.03$ ,  $K= 2.59$ ), molecule ( $n=1.2$ ,  $K=0$ ) and PPF ( $n=2.37$ ,  $K= 1.09$ ).



**Figure 3.29:** (A) Film star calculation carried out on PPF/molecule/Cu system. %T at 532 nm is plotted as a function of thickness, where Cu/molecule interface is defined as  $X=0$  (B) Model showing the light transmission through different layers such as Cu (20 nm), molecular layer (5 nm) and PPF (200 nm). Molecular layers are multilayers but for simplicity shown as monolayers.

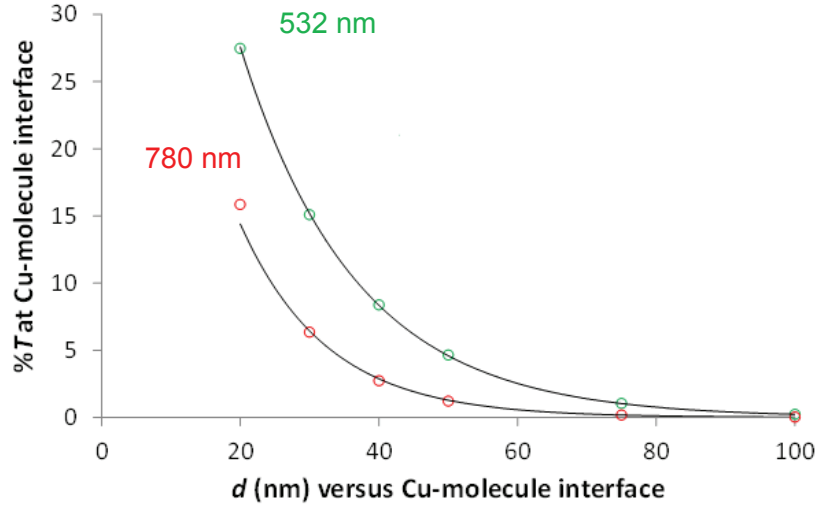
The figure 3.29A shows that for 20 nm Cu layer (blue line on figure 3.29A-indicating 20 nm) as the top contact, at 532 nm  $\sim 30\%$  of the light incident on the Cu surface will reach the Cu/molecule interface and less than 1% of the light is absorbed by the molecules (5 nm thick) and the remaining amount of light will be transmitted into the PPF(200 nm thick). Whereas, for 50 nm copper (violet line) top contact only  $\sim 5\%$  of the light reaches the Cu/molecule interface

and the rest of the light has been reflected by the copper top contact (see figure 3-29A). The top contact thickness for all the experiments described in this chapter was fixed at 20 nm unless otherwise noted.



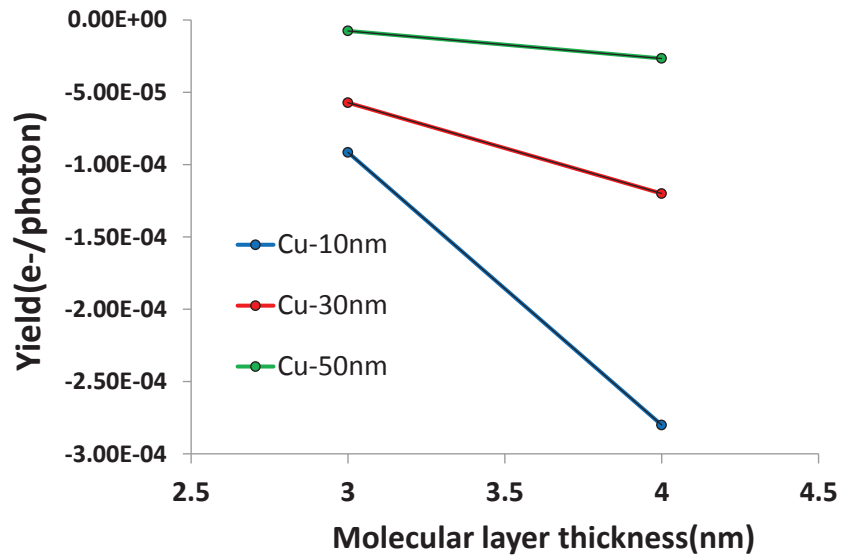
**Figure 3.30:** Film star calculation showing the % of reflected & transmitted light at 532 nm vs. the thickness of copper interface.

Figure 3.30 shows the Filmstar calculation at 532 nm, it predicts about the percentage of light reflected and transmitted at the Cu-molecule interface with respect to copper thickness. Figure 3.31 shows the Filmstar calculation for Cu/AB (5 nm)/PPF system at two different wavelengths. The overlay of the %T with varying Cu thickness shows that the wavelength studied are also important because at 532 nm  $\sim 30\%$  of the light is transmitted through Cu whereas, at 780 nm its  $\sim 15\%$  keeping all other conditions the same. The calculation shows that at different wavelengths different amounts of light are transmitted through Cu top contact.



**Figure 3.31:** Film star calculation showing the overlay of % of transmitted light at 532 & 780 nm vs. the thickness of copper interface.

- **Experimental verification of film star calculation:**



**Figure 3.32:** The photocurrent yield obtained by varying the molecular layer thickness with three different copper top contact thicknesses.

In order to verify the Film star calculation experimentally, we determined the photocurrent yield for carbon/AB/Cu junctions with different Cu thicknesses (10, 30 and 50 nm). Keeping the thickness of AB molecule approximately the same (~3.0 nm), the thickness of the copper top

contact was varied between 10 and 50 nm. The photocurrent spectrum for each thickness was obtained and then the photocurrent yield at 3 eV photon energy was determined and plotted (see figure 3.32). Anyone will predict from the filmstar calculation (see figure 3.29), for the sample with minimum top contact thickness to obtain maximum yield since the amount of light reflected from the top contact is minimum and allows maximum amount of light to reach the copper/molecule interface. The photocurrent yield measured for 3 nm molecular film is maximum for the sample with 10nm top contact (Cu) thickness, and low for 50 nm thickness (see figure 3.32). The same experiment was repeated for molecular film with 4 nm thickness. These results shows that with increase in the top contact thickness for the same molecular thickness more amount of light gets reflected at the top contact and the percentage of light transmitted to the molecular layer reduces considerably which falls in agreement with the Filmstar calculation.

### **3.9 UV-Vis absorption spectra of chemisorbed molecules:**

#### **3.9.1 Method for determining the absorption spectra of molecular layers on PPF:**

Polished quartz wafers (Technical Glass Products, Inc.) were diced in to 1.2 x 1.5 cm chips to serve as substrates. The substrates were initially cleaned by sonication in acetone, IPA, and water for 10 minutes each (35, 36). After sonication, the cleaned quartz substrates were dried using a stream of N<sub>2</sub> gas. The absorption spectra of quartz substrate (with an air reference) were taken using a Perkin Elmer 900 spectrometer. The red curve in figure 3.33-A shows the absorption spectrum of a bare quartz substrate. After obtaining the absorption spectrum of the quartz substrate, a commercially available photoresist (AZ-P4330-RS) was diluted (5% by volume) using propylene glycol methyl ether acetate. This solution was spin coated onto quartz slides at

6000 rpm for 60 sec (31). After soft baking at 90° C for 10 min, samples were transferred to a tube furnace (2.5cm in diameter) for pyrolysis. A 5% H<sub>2</sub> in N<sub>2</sub> gas was kept flowing at 100sccm throughout pyrolysis, where the temperature was ramped at 10° C min<sup>-1</sup> up to 1025 °C for 1 hour, as reported elsewhere (36), resulting in an optically transparent pyrolyzed photoresist film (OTPPF). The absorption spectrum of this OTPPF was acquired with an air reference, with a typical result shown in figure 3.33-A, blue curve. Finally the OTPPF substrate was modified with molecular layers ranging from 1 to 5 nm in thickness using electrochemical reduction of diazonium salts in solution as reported in chapter 2 section 2.2.3. Figure 3-33A shows the absorption spectrum of quartz (red), quartz/OTPPF (blue) and quartz/OTPPF/molecule (green) taken at different times during fabrication, all with an air reference. Figure 3.33-B shows the schematic of a completed OTPPF/AB sample.

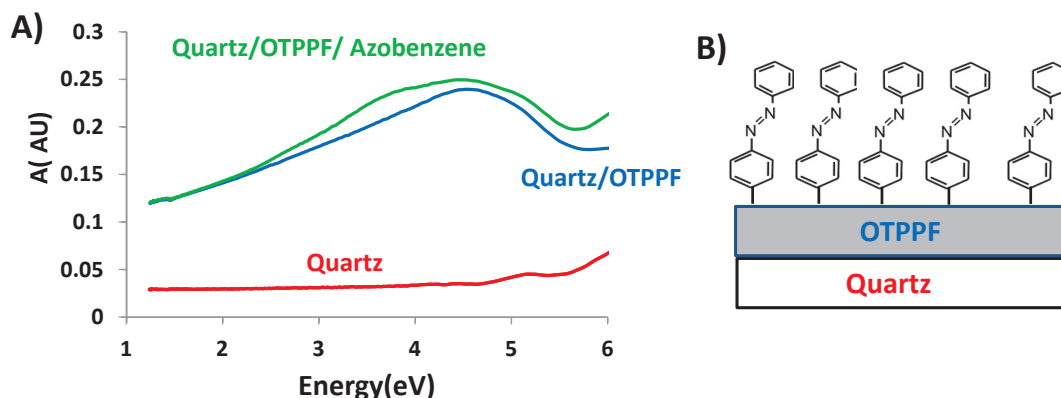


**Figure 3.33:** (A) Absorption spectra of quartz (red) only, Quartz with optically transparent photoresist film (OTPPF-blue) and finally the Quartz/OTPPF surface modified with azobenzene to make Quartz/OTPPF/Azobenzene (green). (B): Schematic representation of the sample.

In order to obtain the absorption spectrum of the molecular layer, the absorbance obtained from an unmodified quartz/OTPPF substrate (blue line) was subtracted from the absorption spectra of the same sample modified with molecules (quartz/OTPPF/AB). The absorption spectrum of the molecular layer obtained after the final subtraction is given in figure 3.34.

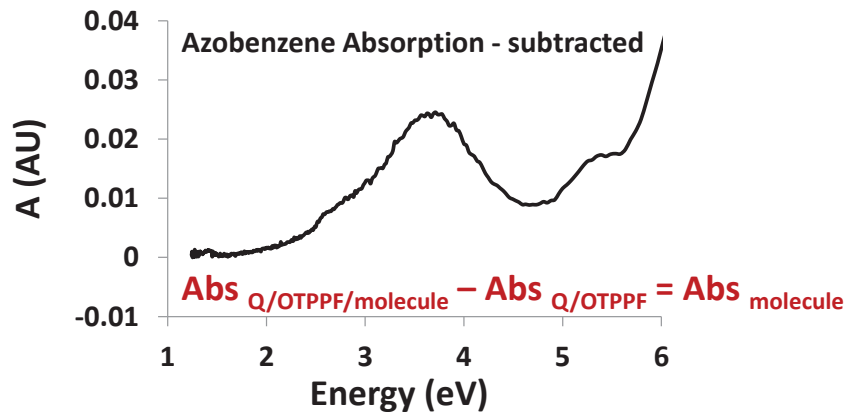


**Figure 3.34:** Absorption spectrum of azobenzene (3.4 nm) obtained from figure 3.33.

### 3.9.2 Optical absorption spectra of different molecules used in the study:

Figure 3.35 shows the optical absorption spectra of all the molecules used in this study (Azobenzene-AB (red), Anthraquinone- AQ (green), Nitro Azobenzene- NAB (violet), Bromophenyl- BrP (Blue) & alkane-C12 (black) . Here the response of the molecular components were obtained by similar method explained above in section 3.9.1 (31). Alkane (C12) shows no sign of absorbance throughout the whole spectral range. The small shift in baseline observed for the absorption spectra of all the molecules due to the reflectivity changes from refractive index variation has been corrected.

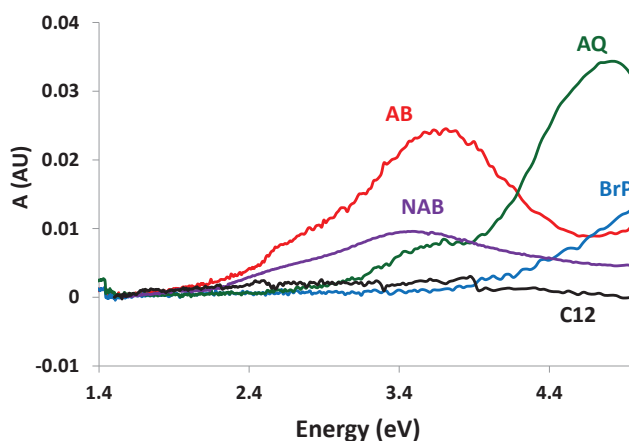


**Figure 3.35:** Optical absorption spectra C12, AQ, AB, NAB, and BrP following subtraction of OTPPF spectrum.

- **UV - Vis absorption spectra of free and adsorbed molecules:**

We also measured the absorption spectra of aromatic molecules in solution. Calculated concentration of each molecules (given in table: 3.2) was dissolved in cyclohexane to obtain the solution absorption spectra given in figure: 3.36, cyclohexane was used as the reference.

Molecules	Conc used (mM)
Azobenzene(AB)	0.31
NitroAzobenzene(NAB)	0.14
Nitrophenyl(NP)	0.71
Nitrobiphenyl(NBP)	0.56
Biphenyl(BP)	0.66

**Table 3.2:** Different molecules used for UV-Vis solution absorption studies and their concentration used for this study.

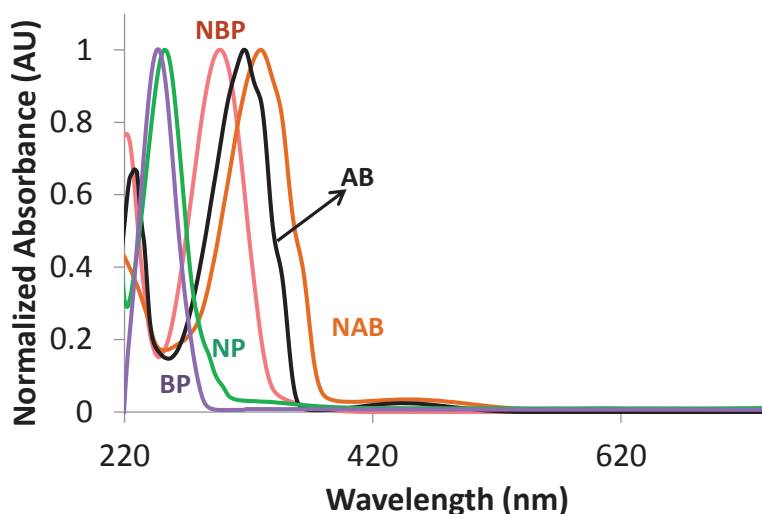


**Figure 3.36:** Normalized absorption solution spectra of different molecules (BP, NP, NAB, AB and NBP) used in this study.

### 3.9.3 Yield vs. Energy photocurrent spectrum:

Figure 3.36 shows the plot of yield (Y) vs. energy (eV) for two molecular junctions (in all cases, a carbon substrate is used with a 20 nm thick Cu top contact): bromophenyl (BrP, 3.0 nm thick multilayer) and aminododecane (C12, 2.3 nm). Differences were observed in the shape of the spectra for two molecules and also at the energy where the photocurrents sign changes. This

is a preliminary indication that the response is dependent on molecular structure (and the associated energy levels) and is not due to heating effects or other artifacts.

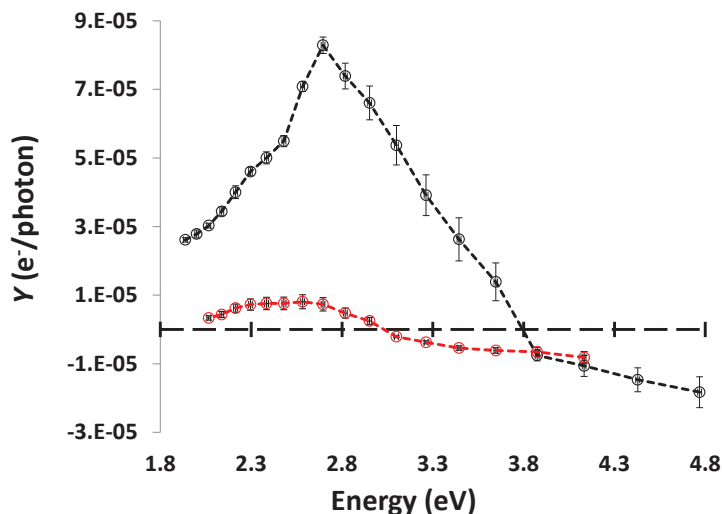


**Figure 3.37:** Photocurrent yield as a function of energy for molecular junctions containing alkane (red triangles) and bromophenyl (black circles) molecular layers. The y-axis error bars are  $\pm$  one standard deviation for three (BrP) or six (C12) junctions, while the overall length of the x-axis error bars represent the band pass of the spectrometer (13 nm).

The response obtained from these junctions is consistent with internal photoemission (IPE), due to the fact that at the given energy regime these two molecules are weakly absorbing (see figure 3.35) and most of the absorption takes place at the Cu top contacts. In the carbon/molecule/Cu devices employed here, IPE might involve optically-generated carriers in the top Cu metal crossing the molecular layer and passing into the underlying PPF(carbon) substrate to generate photocurrent. Generally, internal photoemission yield (Y) is governed by Fowler theory such that under the conditions employed (25, 37). Considering equation 3.3, a plot of  $Y^{1/2}$  versus photon energy (i.e., a Fowler plot) is expected to be linear if IPE is the only process involved in photocurrent generation. Linear extrapolation of the Fowler plot to the x-axis can be used to estimate the value of the interfacial barrier height. The generation of charge carriers in Cu follows excitation and decay of surface plasmons, generating both electrons and

holes with excess energy. These hot carriers can therefore cross both electron and hole tunneling barriers (25), resulting in either positive or negative photocurrents and serving as an indication of the position of both occupied and unoccupied states in the barrier region.

### **3.10 Conclusion:**

This chapter has shown that reliable photocurrent measurements can be made from (carbon/molecule/Cu) large area molecular junctions with partially transparent copper as the top contact. This chapter also gives detail information on different experimental apparatus used for the photocurrent measurements. Photocurrent yield vs. energy results shows that the photocurrent depends on the nature and type of the molecules used in the junction, indicating that the observed photocurrent is not due to heating effects or other artifacts. We anticipate significant information regarding the system energy levels to be gained by analysis of IPE portion of the photocurrent spectrum. The photocurrent spectrum of a completed molecular junction may establish it as a unique platform for investigating primary photoeffects and interfacial transport phenomenon in devices related to energy conversion, optical detection, and charge carrier dynamics.

### **3.11 References:**

1. Carroll RL & Gorman CB (2002) The Genesis of Molecular Electronics. *Angew. Chem. Int. Ed.* 41:4378-4400.
2. McCreery RL & Bergren AJ (2009) Progress with Molecular Electronic Junctions: Meeting Experimental Challenges in Design and Fabrication. *Adv. Mater.* 21:4303-4322.
3. Ishii H, Sugiyama K, Ito E, & Seki K (1999) Energy Level Alignment and Interfacial Electronic Structures at Organic/Metal and Organic/Organic Interfaces. *Adv. Mater.* 11(8):605-625.

4. Zhong S, Zhong JQ, Mao HY, Zhang JL, Lin JD & Chen W (2012) The Role of Gap States in the Energy Level Alignment at the Organic-Organic Heterojunction Interfaces. *Phys. Chem. Chem. Phys.* 14:14127-14141.
5. Braun S, Salaneck WR, & Fahlman M (2009) Energy-Level Alignment at Organic/Metal and Organic/Organic Interfaces. *Adv. Mater.* 21(14-15):1450-1472.
6. Sayed SY, Fereiro JA, Yan H, McCreery RL, & Bergren AJ (2012) Charge Transport in Molecular Electronic Junctions: Compression of the Molecular Tunnel Barrier in the Strong Coupling Regime. *Proc. Natl. Acad. Sci. U.S.A.* 109(29):11498-11503.
7. Powell R (1970) Interface Barrier Energy Determination from Voltage Dependence of Photoinjected Currents. *J. Appl. Phys.* 41(6):2424.
8. Gundlach KH & Kadlec J (1975) Interfacial Barrier Height Measurement from Voltage Dependence of Photocurrent. *J. Appl. Phys.* 46(12):5286-5287.
9. DiMaria DJ & Arnett PC (1975) Hole Injection into Silicon Nitride: Interface Barrier Energies by Internal Photoemission. *Appl. Phys. Lett.* 26(12):711-713.
10. Goodman AM (1970) Photoemission of Holes and Electrons from Aluminum into Aluminum Oxide. *J. Appl. Phys.* 41(5):2176-2179.
11. Deal BE & Snow EH (1966) Barrier Energies in Metal-Silicon Dioxide-Silicon Structures. *J. Phys. Chem. Solids.* 27:1873-1879.
12. Kovacs DA, Winter J, Meyer S, Wucher A, & Diesing D (2007) Photo and Particle Induced Transport of Excited Carriers in Thin Film Tunnel Junctions. *Phys. Rev. B.* 76(23):235408.
13. Campbell IH & Smith DL (2002) Metal-Organic Schottky Energy Barriers: Measurements and Device Implications. *Conjugated Polymer and Molecular Interfaces: Science and*

- Technology for Photonic and Optoelectronic Applications*, eds Salaneck WR, Seki K, Kahn A, & Pireaux J-J (Marcel Dekker, New York), pp 693-732.
14. Galperin M & Nitzan A (2012) Molecular Optoelectronics: The Interactions of Molecular Conduction Junctions with Light. *Phys. Chem. Chem. Phys.* 14:9421-9438.
  15. Mangold MA, Calame M, Mayor M, & Holleitner AW (2011) Resonant Photoconductance of Molecular Junctions Formed in Gold Nanoparticle Arrays. *J. Am. Chem. Soc.* 133:12185-12191.
  16. Huang W, Masuda G, Maeda S, Tanaka H, & Ogawa T (2006) Molecular Junctions Composed of Oligothiophene Dithiol-Bridged Gold Nanoparticles Exhibiting Photoresponsive Properties. *Chem. Eur. J.* 12:607-619.
  17. Battacharyya S, Kibel A, Kodis G, Liddell PA, Gervado M, Gust D & Lindsay S (2011) Optical Modulation of Molecular Conductance. *Nano Lett.* 11:2709-2714.
  18. Choi SH, Kim B, & Frisbie CD (2008) Electrical Resistance of Long Conjugated Molecular Wires. *Science.* 320(5882):1482-1486.
  19. Choi SH, Risko C, Delgado CR, Kim BS, Bredas JL & Frisbie CD (2010) Transition from Tunneling to Hopping Transport in Long, Conjugated Oligo-imine Wires Connected to Metals. *J. Am. Chem. Soc.* 132(12):4358-4368.
  20. Bergren AJ, McCreery RL, Stoyanov SR, Gusarov S, & Kovalenko A (2010) Electronic Characteristics and Charge Transport Mechanisms for Large Area Aromatic Molecular Junctions. *J. Phys. Chem. C.* 114:15806-15815.
  21. Yan H, Bergren AJ, & McCreery RL (2011) All-Carbon Molecular Tunnel Junctions. *J. Am. Chem. Soc.* 133(47):19168-19177.

22. Salomon A, Boecking T, Seitz O, Markus T, Amy F, Chan C, Cahen D & Kahn A (2007) What is the Barrier for Tunneling Through Alky Monolayers? Results from n- and p--Si-Alkyl/Hg Junctions. *Adv. Mater.* 19:445-450.
23. McCreery RL, Yan H, & Bergren AJ (2013) A Critical Perspective on Molecular Electronic Junctions: There is Plenty of Room in the Middle. *Phys. Chem. Chem. Phys.* 15(4):1065-1081.
24. Kim B, Choi SH, Zhu XY, & Frisbie CD (2011) Molecular Tunnel Junctions Based on pi-Conjugated Oligoacene Thiols and Dithiols between Ag, Au, and Pt Contacts: Effect of Surface Linking Group and Metal Work Function. *J. Am. Chem. Soc.* 133(49):19864-19877.
25. Afanas'ev VV (2008) Internal Photoemission Spectroscopy: Principles and Applications (Elsevier, London).
26. Goodman AM (1966) Photoemission of Holes from Silicon into Silicon Dioxide. *Phys. Rev.* 152(2):780-784.
27. Gundlach KH (1971) Logarithmic Conductivity of Al/Al<sub>2</sub>O<sub>3</sub>/Al Tunneling Junctions Produced by Plasma and by Thermal Oxidation. *Surf. Sci.* 27(1):125-141.
28. Yan H & McCreery RL (2009) Anomalous Tunneling in Carbon/Alkane/TiO<sub>2</sub>/Gold Molecular Electronic Junctions: Energy Level Alignment at the Metal/Semiconductor Interface. *ACS Appl. Mater. Interfaces.* 1(2):443-451.
29. Deinhammer RS, Ho M, Anderegg JW, & Porter MD (1994) Electrochemical Oxidation of Amine-Containing Compounds: A Route to the Surface Modification Glassy Carbon Electrodes. *Langmuir.* 10:1306-1313.

30. Donner S, Li HW, Yeung ES, & Porter MD (2006) Fabrication of Optically Transparent Carbon Electrodes by the Pyrolysis of Photoresist Films: Approach to Single-Molecule Spectroelectrochemistry. *Anal. Chem.* 78(8):2816-2822.
31. Tian H, Bergren AJ, & McCreery RL (2007) Ultraviolet-Visible Spectroelectrochemistry of Chemisorbed Molecular Layers on Optically Transparent Carbon Electrodes. *Appl. Spectrosc.* 61(11):1246-1253.
32. Kim B, Choi SH, X.-Y.Zhu, & Frisbie CD (2011) Molecular Tunnel Junctions Based on  $\pi$ -Conjugated Oligoacene Thiols and Dithiols between Ag, Au, and Pt Contacts: Effect of Surface Linking Group and Metal Work Function. *J. Am. Chem. Soc.* 133(49):19864-19877.
33. Qi Y, Yaffe O, Vilan A, Cahen D & Kahn Antoine (2011) Filled and Empty States of Alkanethiol Monolayer on Au (111): Fermi level Asymmetry and Implications for Electron Transport. *Chem. Phys. Lett.* 511(4-6):344-347.
34. Lee CH, Yu G, & Heeger AJ (1993) Persistent Photoconductivity in poly(p-phenylenevinylene): Spectral Response and Slow Relaxation. *Phys. Rev. B.* 47(23):15543-15553.
35. Ranganathan S & McCreery RL (2001) Electroanalytical Performance of Carbon Films with Near-Atomic Flatness. *Anal. Chem.* 73:893-900.
36. Ranganathan S, McCreery RL, Majji SM, & Madou M (2000) Photoresist-Derived Carbon for Microelectrochemical Applications. *J. Electrochem. Soc.* 147:277 - 282.
37. Sze SM (1981) *Physics of Semiconductor Devices* (Wiley, New York) 2nd Edition Ed.

## Chapter-4

# Internal Photoemission in Molecular Junctions: Parameters for Interfacial Barrier Determinations.

### 4.1 Introduction:

Internal Photoemission (IPE) has been used to measure barrier heights in various M-I-M junctions (where “I” is an insulator typically an oxide tunneling barrier), notably across aluminum oxide tunnel junctions (1-4). In chapter 3 we indicated that IPE might be useful to characterize the interfacial barrier of molecular junctions consisting of carbon/molecule/Cu, with the energy threshold for photocurrent indicating the  $E_f - E_{\text{HOMO}}$  or  $E_{\text{LUMO}} - E_f$  interfacial barriers (where  $E_f$  is the system Fermi level). We also anticipated that the sign of the photocurrent can provide information regarding the involvement of the HOMO or LUMO in mediating tunneling across the molecular junction.

In this chapter, we show that photocurrent observed in large-area carbon/molecule/Cu tunnel junctions can be used to determine transport parameters, including the relative alignment of molecular energy levels and the height(s) of the tunnel barrier(s). The results reported here establish a method for directly measuring the energy levels in working molecular junctions and may be used to design more advanced molecular electronic circuitry. We extend our previous results to a wider range of molecular structures, and explore the use of IPE to characterize energetics in molecular junctions. Through systematic correlation of the photocurrent spectrum with that of the absorbance spectrum of different molecules, plus variation of the molecular layer

thickness, source intensity, and photon energy, we differentiated photocurrents resulting from photon absorption in the contacts with those induced by photon absorption in the molecular layer. The results permit formulation of criteria for determining the origin of the photocurrent, and the relationship to the position of system energy levels. For molecular junctions that show only IPE-based photocurrent, an analysis through construction of a Fowler plot can yield a measurement of the interfacial barrier, where the photocurrent sign can be used to determine whether electron or hole transport is dominant. IPE was characterized and illustrated with molecular junctions made with seven different aromatic and aliphatic molecular junction structures (see figure 3.11, chapter 3), which exhibit conduction mediated by both occupied and unoccupied system orbitals.

#### 4.1.1 Optical absorption spectra for different molecules:

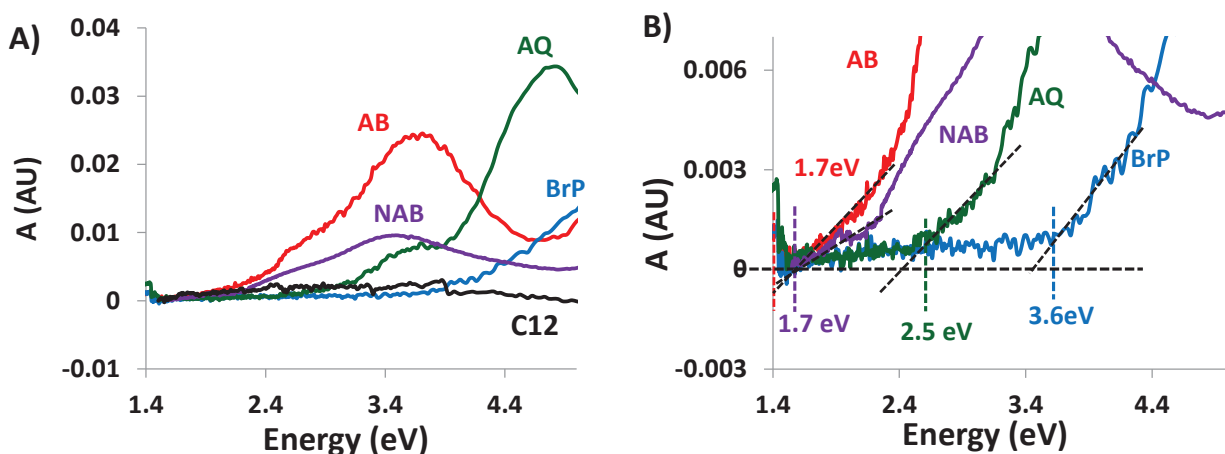


**Figure 4.1:** (A): Optical absorption spectra C12, AQ, AB, NAB, and BrP following subtraction of OTPPF spectrum. (B): Method for determining onset of optical absorption.

Figure 4.1(A) shows the overlay of optical absorption spectra for different molecules used in this study and are derived using the procedure explained previously in chapter 3, section 3.9. The onset of absorption by molecular layer is taken as the intersection of two linear regions of the

corrected spectrum as shown in figure 4.1(B). The optical absorption onset thus determined was 1.7 eV for AB and NAB, 2.5 eV for AQ and 3.6 eV for BrP (see figure 4.1(B)).

#### 4.1.2 Structure and absorption spectra for NDI and ferrocene molecular layers:

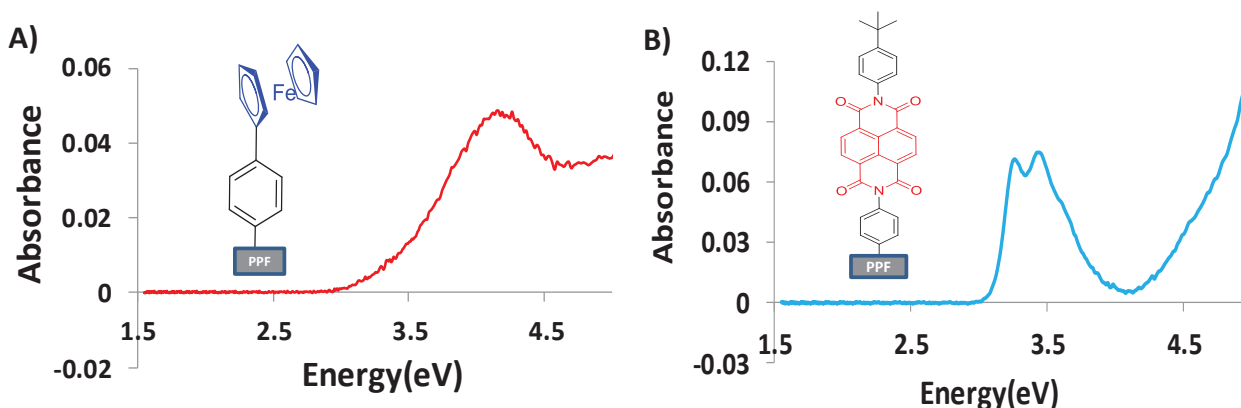


**Figure 4.2:** Absorption spectra of Fc (A) and NDI (B) films on OTPPF (both NDI & Fc are 3-4nm thick), after subtraction of the OTPPF spectrum. Multilayers of molecules are formed; however monolayers are shown for simplicity.

Figure 4.2(A) shows the optical absorption spectrum for Ferrocene (Fc) with an inset showing schematic structure of a phenyl-Fc molecule on carbon surface (PPF) & figure 4.2(B) shows the optical absorption spectrum of NDI with inset showing its structure. The optical absorption spectrum for each molecule was obtained from the procedure explained in section 3.9, chapter 3.

## 4.2 Experimental section:

Figure 4.3 shows the schematic of the junction structure used in this study. Details of junction fabrication (5) and the photocurrent measurement was previously explained under section 3.2, chapter 3. Briefly, a narrow band ( $\Delta\lambda=13$  nm) of light from a Xe arc source (Newport model 6256) passes through an optical chopper before incidence onto the top of a molecular junction. A dual phase LIA is used to measure both the phase and the magnitude of the photocurrent simultaneously.

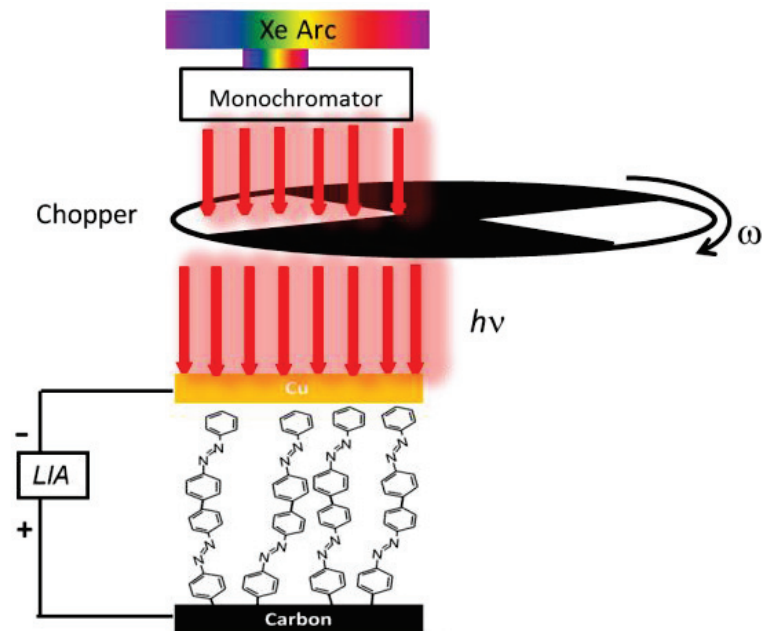


**Figure 4.3:** Schematic representation of the junction structure:

The absorption spectra in Figures 4.1 and 4.2 include molecular layers such as azobenzene (AB), anthraquinone (AQ), bromophenyl (BrP), nitroazobenzene (NAB), phenyl ferrocene (Fc), dodecylamine (C12), and naphthalene di-imide (NDI), all of which were multilayers on pyrolyzed photoresist film (PPF) substrates with their thicknesses determined using AFM (in nm) indicated as follows: AB (3.4 nm), BrP (3.0 nm). The fabrication of molecular junctions has been described in detail previously (6-11), and utilizes the electrochemical reduction of diazonium reagents on flat carbon surfaces (12) and vapour deposition of metallic (6) or carbon (13) top contacts. However, rather than silicon substrates with an insulating layer of thermal oxide, polished fused quartz substrates (from Technical Glass Products, Inc) were used as the substrate in the current study to avoid the possibility of stray photocurrent from crystalline silicon.

For the Al/Al<sub>2</sub>O<sub>3</sub>/Cu junctions, polished borosilicate glass was first cleaned by sonication in acetone followed by IPA and water for 10 minutes each, and then 60 nm of Al was deposited via

e-beam evaporation through a shadow mask with a 3 nm Cr adhesion layer. Next, the samples were heated in air to a temperature of 175° C (verified using an IR thermometer) for 10 minutes. Finally, 20 nm Cu was deposited using a shadow mask oriented perpendicular to the Al/Al<sub>2</sub>O<sub>3</sub> lines.

As illustrated in the schematic representation of the optical apparatus (10) in Figure 4.3, photocurrent spectra was measured by passing a small band ( $\Delta\lambda= 13$  nm) of light from a Xe arc source and monochromator through an optical chopper and onto the junction. A Lock-in detection apparatus (see figure 3.14, section 3.4.2) was used to measure the resulting photocurrent. The optical power incident on the junction was measured using a Newport 1936-R power meter, and then the external quantum efficiency (EQE) (10) was determined. EQE is defined as the number of photoelectrons in the external circuit divided by the number of photons incident on the junction. The sign of the photocurrent was determined by calibrating the phase of the lock-in detection using a photodiode as the reference, as described previously (section 3.5.2, chapter 3) where a positive photocurrent indicates electrons flowing from the Cu to PPF in the external circuit. Laser diodes operating at 808 nm (1.53 eV) and 852 nm (1.46 eV) from Thorlabs were used to extend the photocurrent measurements beyond the useful range of Xe arc source.

The photocurrent sign was then verified using laser illumination and DC current measurements in several cases (see section 3.4.1, chapter 3) to avoid any ambiguity resulting from phase sensitive detection. In order to measure photocurrent as a function of incident power, laser light from an Ar-ion laser was directed onto the junction, which permitted the use of direct current measurements and a wider range of incident power than that available with the Xe arc source. The optical power delivered to the junction was determined immediately above the

sample with the Newport power meter and the focussed spot size was determined visually. The power density at the junction varied from  $0.6 - 7 \text{ mW/cm}^2$  for Xe arc illumination and up to  $50 \text{ mW/cm}^2$  for laser illumination, with the resulting photocurrents remaining stable for many hours. In all cases, at least four junctions on a given chip were studied in order to determine the standard deviation of the photocurrent.

### 4.3 Results and discussion:

Figure 4.4 shows the schematic energy level diagram for a molecular junction. This model is based on the availability of electronic states, represented by horizontal lines, where shading represents occupied states in the conducting contacts. The Fermi level ( $E_f$ ) of the contacts (defined as the energy level where the probability of finding an electron is 0.5) therefore represents the demarcation between filled and empty states for the conductors, while the molecular component has filled (HOMO) and empty (LUMO) orbitals. The gap between the frontier orbitals in the molecular region (i.e., the HOMO-LUMO gap,  $E_g$ ) creates a region where electrons are not allowed so that when these orbitals are separated from  $E_f$  by an energy greater than  $kT$ , carriers cannot pass freely from one contact into the other, resulting in an interfacial barrier for electrons ( $\phi_e^-$ ; LUMO-mediated transport) and holes ( $\phi_h^+$ ; HOMO-mediated transport). In cases where the distance between the two conductors is small,  $\phi$  is a non-resonant quantum mechanical tunneling barrier. Multiple values of molecular orbitals are shown to represent inhomogeneous broadening by various orientations and environments of molecules in the molecular multilayer.

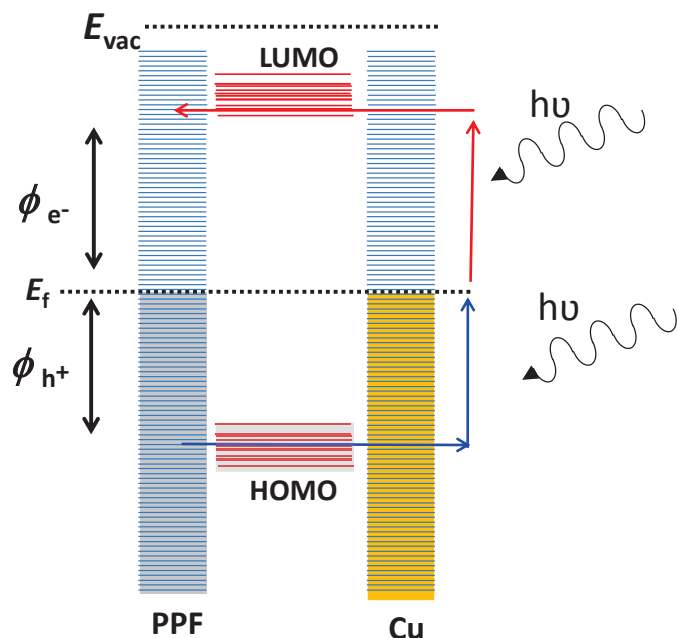


**Figure 4.4:** Energy level diagram showing a non-resonant tunnel barrier for holes (HOMO-mediated transport, blue arrows) and electrons (LUMO-mediated transport, red arrows).

While the model in Figure 4.4 has been used in numerous descriptions of molecular junctions, there are several issues that are not readily apparent in this diagram. For example, strong electronic coupling between the contacts and molecular layer can result in a dipole across the interface that can be important in determining the actual system barrier (i.e., an electrostatic dipole barrier results from partial charge transfer between the molecule and contact) (11, 14, 15). Moreover, interactions between the molecule and contacts can lead to hybridization, creating orbitals that span both the molecule and the contact(s). These effects can result in a distribution of occupied (OSOs) and unoccupied (USOs) system orbitals with significantly different energies from free-molecule HOMO or LUMO levels, as well as shifts in the local vacuum level over the molecular layer (15, 16). As will be discussed below, the orbital energy levels relevant to transport in the junction are not those for isolated molecules but instead are the occupied system orbitals (OSOs) and unoccupied system orbitals (USOs) which incorporate electronic changes

during fabrication. For all of these reasons, methods that provide energy level alignment and barrier height information in-intact complete junctions are highly valuable.

#### 4.3.1 Photocurrent Yield spectrum for Alkane and BrP junctions.

Figure 4.5(A) shows the optical absorption spectra for multilayers of the two molecules: C12 (blue curve) and BrP (black curve). The absorbance in Figure 4.5(A) was obtained by subtracting the absorbance of an unmodified quartz/carbon substrate (described in section 3.9.1) from that of a similar substrate modified with the molecular layer (17). It is clear that C12 sample shows no significant optical absorbance over the entire range tested. The shift in the baseline absorbance is due to reflectance changes between the reference (unmodified transparent carbon) and the sample with the thin molecular layer, which has a refractive index different from air.

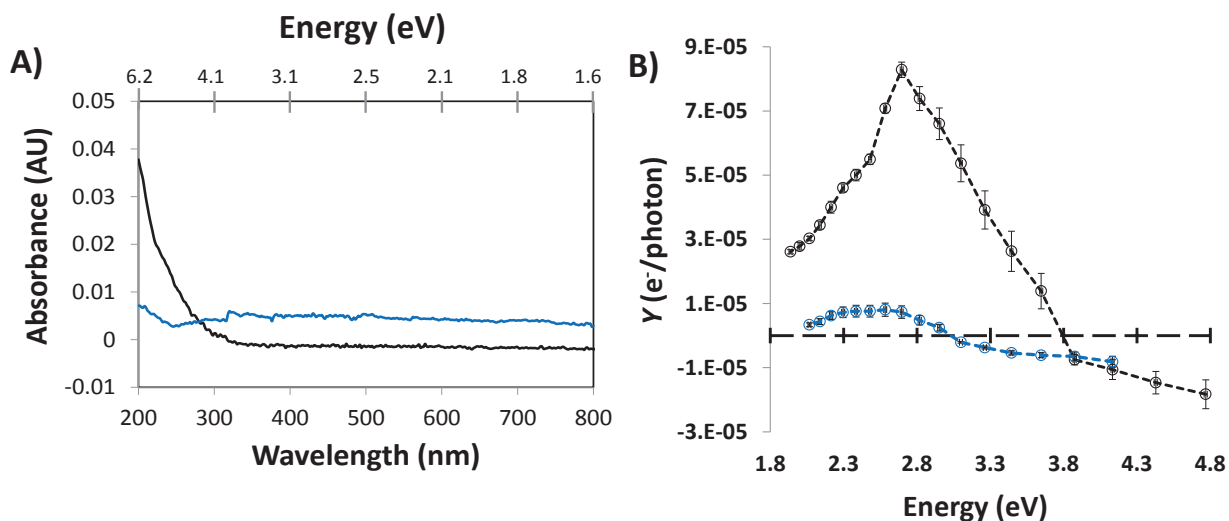


**Figure 4.5:** (A) Overlay of the optical absorption spectra for the alkane (C12, blue curve) and bromophenyl (BrP, black curve) on optically transparent carbon. (B) Photocurrent yield as a function of energy for molecular junctions containing alkane (red triangles) and bromophenyl (black circles) molecular layers. The y-axis error bars are  $\pm$  one standard deviation for three (BrP) or six (C12) junctions, while the overall length of the x-axis error bars represent the band pass of the spectrometer (13 nm).

Figure 4.5(B) shows the plot of yield (Y) vs. energy (eV) for two molecular junctions (in all cases, a carbon substrate was used with a 20 nm thick Cu top contact): bromophenyl (BrP, 3.0

nm thick multilayer, black curve) and aminododecane (C12, 2.3 nm, blue curve). Differences were observed in the shape of the spectra for two molecules and also in the energy where the photocurrents sign changes. This is a preliminary indication that the response is dependent on molecular structure (and the associated energy levels) and is not due to heating effects or other artifacts. The response obtained from these junctions is consistent with internal photoemission (IPE), where hot carriers generated in the Cu top contact can cross the interfacial tunneling barrier.

#### 4.3.2 Fowler plots for alkane and BrP junctions:

IPE has been described as a sub-work function photoelectric effect, where the charge carriers are excited from one conductor into another across a solid state barrier material rather than into a vacuum (18). In the carbon/molecule/Cu devices employed here, IPE might involve optically-generated carriers in the top Cu metal crossing the molecular layer and passing into the underlying carbon substrate to generate a photocurrent. Generally, internal photoemission yield (Y) is governed by Fowler theory such that under the conditions employed (18, 19).

$$Y \propto (E - \phi_{barr})^2 \quad (\text{Eqn 4.1})$$

where E is the incident photon energy ( $E = h\nu$ , where h is Planck's constant and  $\nu$  is frequency), and  $\phi_{barr}$  is the interfacial barrier (here, a tunneling barrier). Considering equation 4.1, a plot of  $Y^{1/2}$  versus photon energy (i.e., a Fowler plot) is expected to be linear if IPE is the only process involved in photocurrent generation. Linear extrapolation of the Fowler plot to the x-axis can be used to estimate the value of the interfacial barrier height. The generation of charge carriers in the Cu follows excitation and decay of surface plasmons, generating both electrons and holes with excess energy. These hot carriers can therefore cross both electron and hole tunneling

barriers (18), resulting in either positive or negative photocurrents and serving as an indication of the position of both occupied and unoccupied states in the barrier region.

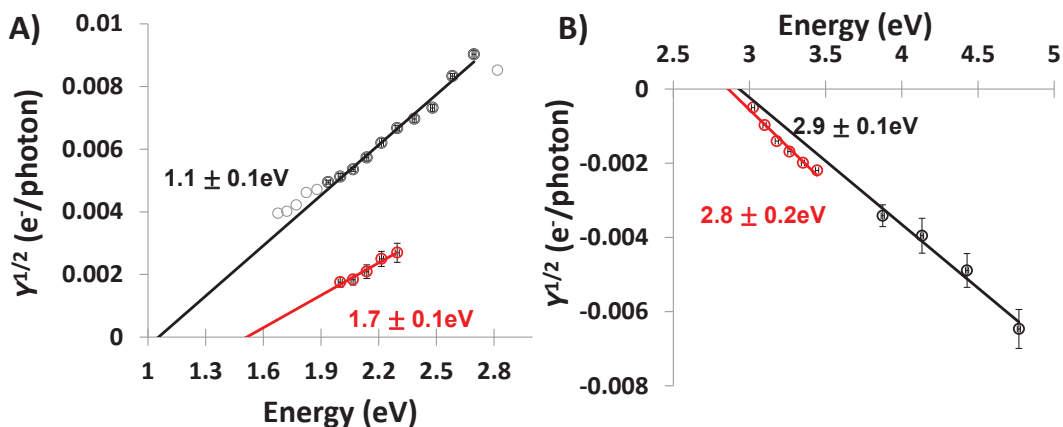


**Figure 4.6:** (A) Fowler plots for two different junctions where positive photocurrent is observed at PPF. (B) Fowler plots for negative photocurrent for the same two junctions. Extrapolated thresholds for each case are given.

Figure 4.6(A) shows Fowler plots for the positive photocurrent region. From figure 4.4, a positive photocurrent in the external circuit is observed when an electron is transferred from the carbon to a photogenerated hole in the top Cu contact via the molecular HOMO. Both Fowler plots display good linearity, indicating that an IPE model fits well with the experimental data. In addition, the slopes of these plots are similar, indicating that the energetic distribution of optically generated charge carriers is similar. Finally, the extrapolated barrier heights for holes ( $\phi_{h+}$ ) obtained from the Fowler plots in figure 4.6(A) are 1.1 eV for BrP and 1.7 eV for C12, respectively. Given the error in the measurements ( $\pm 0.1$  eV), these values are clearly statically different from each other, demonstrating a structural effect on the barrier for hole tunneling in molecular junctions. In addition, these results are consistent with measurements of  $E_{\text{HOMO, onset}}$  energies determined using ultraviolet photoelectron spectroscopy (UPS) and J-V curve fitting (13), where  $E_{\text{HOMO, onset}}$  for C12 is 1.7 eV (See figure 3.13) and for BrP is  $1.5 \pm 0.3$  eV (13). Thus,

the optical method used here indicates that the changes in the barrier height resulting from differences in molecular structure can be determined using photocurrent measurements. However, the optical method is conducted in-situ, resulting in a barrier value for a functioning molecular junction with a top contact, while UPS can probe only the occupied states of a carbon/molecule system in vacuum.

While UPS can only determine the energy onset of the occupied states, IPE can be sensitive to both electron and hole barriers(18). Determination of the sign of the dominant tunneling carrier has been a long-standing issue in molecular electronics. A few studies have reported values either through ex-situ photoelectron measurements (20, 21) or observation of the thermoelectric effect (22, 23). However, in some cases, IPE can yield the dominant carrier sign as well as the values of tunneling barriers for both carrier types.

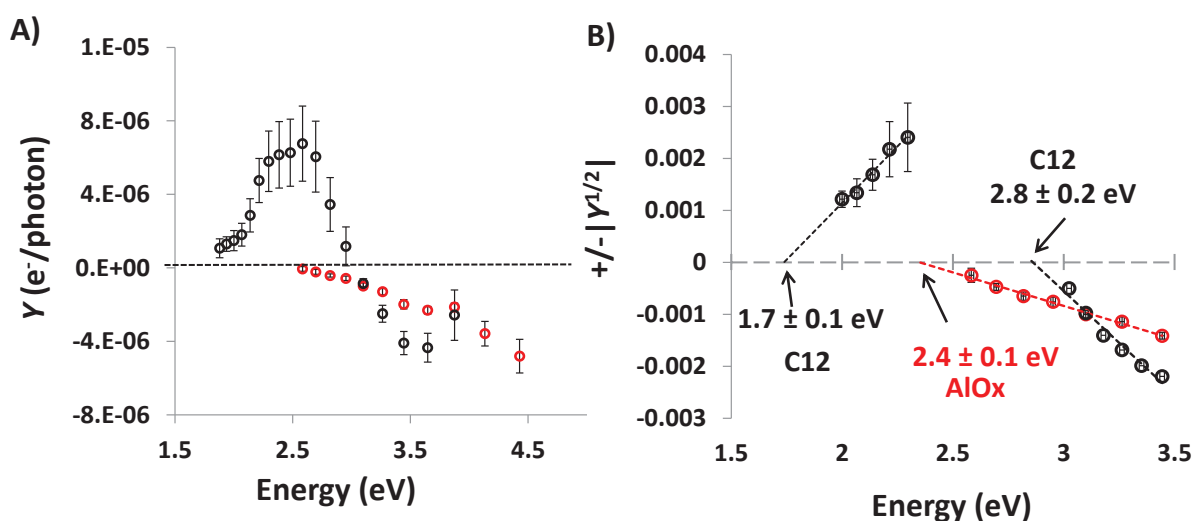
Figure 4.6(B) shows the Fowler plot at the high energy region where the measured photocurrent is negative (here, the y-axis is given as  $-[|Y|^{1/2}]$ ). These plots show good linearity and yield electron tunneling barriers of 2.9 and 2.8 eV for C12 and BrP, respectively. While the interpretation of these data may be used to construct energy-level diagrams (discussed later), we first comment on the mechanism involved in photocurrent generation and the implicit assumptions in the model.

### **4.3.3 Alumina junctions:**

In order to provide a baseline that is free from molecular absorbance, we used the photocurrent spectrum of Al/AlO<sub>x</sub>/Cu junctions and compared it with Carbon/C12/Cu junctions (C12 and AlO<sub>x</sub> do not absorb light in this 200-800 nm spectral range). The measured photocurrent yield (i.e., the number of electrons per incident photon after calibration of the light intensity) as a function of photon energy for both junctions is shown in Figure 4.7(A). The negative

photocurrent measured for the AlOx junction indicates that the Al substrate becomes negative when illuminated, such that photoexcited electrons in the copper traverse the oxide through its conduction band. The opposite sign for the case of the alkane junctions (black curve) at low energy results from electron transport through the HOMO into photogenerated holes in the Cu contact, as reported previously (10, 11).

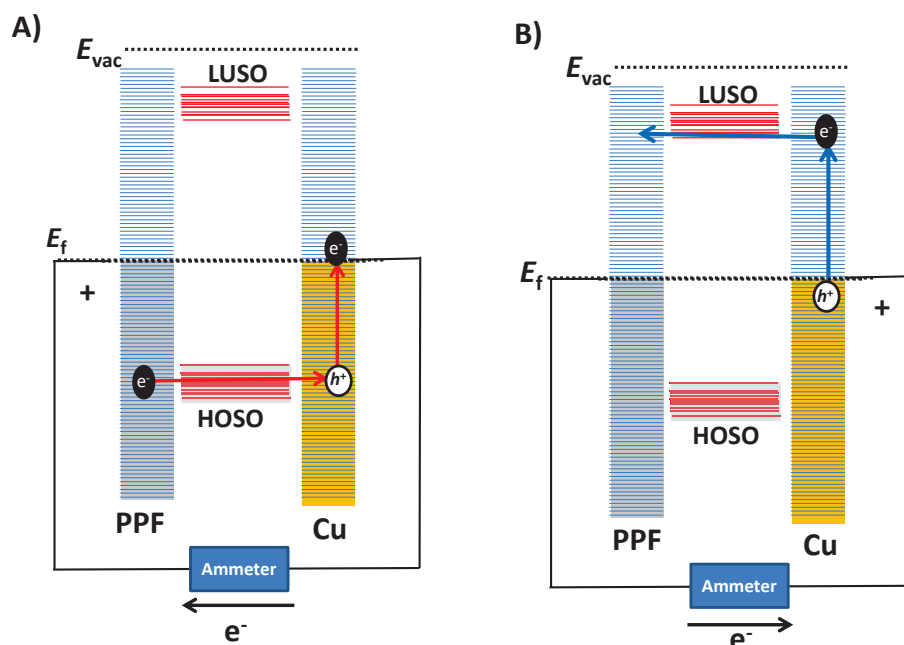
Figure 4.7(B) shows the Fowler plot for an Al/AlOx/Cu (20 nm) junction, where the extrapolated value of the electron tunneling barrier is determined to be  $2.4(\pm 0.1)$  eV. Although a range of 0.9 to 3 eV; e.g. has been reported, Goodman reported a value of  $2.0 \pm 0.2$  eV for electrons in AlOx exposed to liquid water(4). As reported previously, and is apparent in Figure 4.6, the hole tunneling barrier ( $E_f - E_{OSO}$ ) for a PPF/alkane/Cu junction is  $1.7(\pm 0.1)$  eV and  $E_f - E_{USO}$  is  $2.8(\pm 0.2)$  eV respectively, both based on the Fowler plot intercept. In the cases shown in Figure 4.7(A), absorbance by the molecular portion of the junction is avoided by the choice of materials. However, molecular electronics involves the use of a wide range of structures with varied optical absorption characteristics, and the consequences of molecular absorption are considered later.



**Figure 4.7:** (A) Photocurrent yield spectra for two junctions (Al/AlOx/Cu, red curve and carbon /C12 / Cu, black curve). (B): Corresponding Fowler plots with extrapolated barrier values.

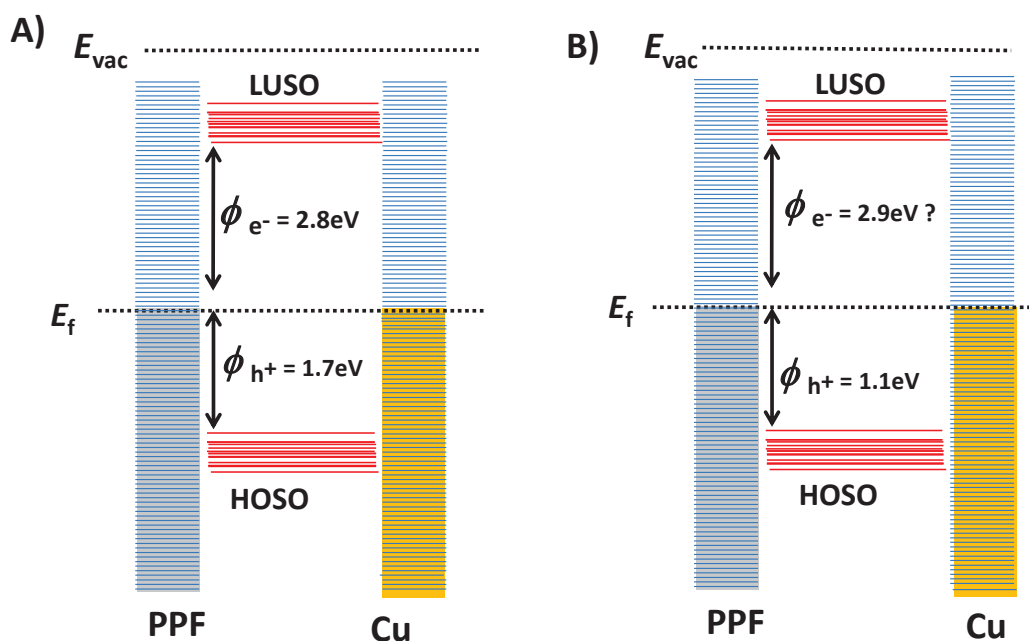
#### 4.4 Proposed mechanism for Alkane and BrP:

Figure 4.8 shows the idealized schematic diagram of IPE for hole and electron current. As shown in figure 4.8(A), low energy light incident onto the Cu top contact creates electron-hole pairs with an energy defined by the photon energy. Thus, the deepest hole has an energy ( $E_f - hv$ ), and when this is larger than the hole tunneling barrier, HOSO-mediated transport of an electron from the bottom carbon contact into the hole created in the Cu can lead to a positive photocurrent in the external circuit. As shown in Figure 4.8(B), higher energy excitation may lead to LUSO-mediated transport when the value ( $E_f + hv$ ) exceeds the LUSO level, leading to negative photocurrent. In this model, it is implicit that excitons are generated in the Cu only, and not the carbon. In addition, it is assumed that there is no light-induced excitation of the molecular component.



**Figure 4.8:** (A) Diagram of the IPE mechanism for excitation of holes from Cu to carbon. (B) Diagram for electron transport from Cu to carbon. The alignment of the occupied system orbitals (OSOs) and unoccupied system orbitals (USOs) relative to the contact Fermi levels determines the sign of the observed photocurrent and the energy threshold for onset.

In order to determine the potential impact of molecular absorption on the photocurrent, the absorption spectra of the molecules bonded to a transparent carbon support were obtained (see figure 4.1(A) & 4.5(A)). These results show that the alkane molecules are non-absorbing throughout the entire energy range tested, while the BrP molecular layer shows no significant absorbance below  $\sim 3.8$  eV. Thus, the value for both hole-tunneling barriers and that for the C12 electron barrier are unlikely to be affected by excitation involving molecular orbitals. However, we cannot be certain this is the case for the BrP electron tunneling barrier. In fact, the response of photocurrent at higher energy may be due to “MA” currents generated by a mechanism involving Molecular Absorption(18). In this case the interpretation of the threshold exhibited in the Fowler plot at high energy may need to be modified.



**Figure 4.9:** Energy level diagrams constructed based on IPE characterization (A) Alkane (B) BrP molecule.

Figure 4.9 shows the energy-level diagrams constructed for two different molecules alkane (A) and BrP (B) assuming that only IPE generates photocurrent. While this diagram provides a complete picture of the energy barriers that determine tunneling, we note that the HOMO and LUMO levels are not isolated, but instead represented by occupied system orbitals (OSOs) and unoccupied system orbitals (USOs). Accordingly, these (OSOs & USOs) are drawn as a distribution of states below and above  $E_f$ , where the onset of photoemission represents the edges of these states becoming energetically accessible. For this reason, the HOSO-LUSO gap determined using IPE does not directly reflect the HOMO-LUMO gap of the isolated molecule used in the junction, but rather the transport gap relevant in determining the interfacial barriers. This distinction is important, as the IPE observed here yields information regarding a completed junction, including the results of any interactions between the molecules and contacts, which tends to decrease the energy gap(14).

Turning to the comparison of these results, we noted that the alkane-based junction has a larger energy gap than the aromatic junction (4.5 vs. 4.0 eV), consistent with the decreased conductivity in previous measurements (24). The absolute value for the transport gap of the alkane junction as assessed here is smaller than other reported values (21), which range from 7 to 8 eV, where the barrier values obtained are 3 to 4 eV. However, as recently summarized (25), the barrier heights reported for alkane-containing junctions using other paradigms is often less than 2 eV (26-28), suggesting that the details of the system (i.e., contact materials and interactions between the contacts and molecules) impact the transport barrier. Given that the system studied here has strong electronic coupling between the molecules and substrate, the reduced gap may be due to an induced density of interface states (29, 30), sometimes referred to as gap states (31),

which are transport states lying within the HOMO-LUMO gap of the molecular species. A distribution of such gap states may be sufficient to cause a lowering of the transport gap.

From the analysis carried out on alkane and BrP junctions, we can conclude that an IPE mechanism is useful for determining both electron and hole tunneling barriers for a complete and operational carbon/alkane/Cu molecular junction. The values of the hole-tunneling barriers obtained from BrP junctions agree well with recent measurements of  $E_{\text{HOMO, onset}}$  values obtained with UPS. Pseudo-IPE current may complicate the interpretation of the data at higher energies for molecules that show optical absorbance. This additional mechanism is related to the molecular component, and we anticipate significant information to be gained by analysis of both IPE and pseudo-IPE portions of the photocurrent spectrum.

#### **4.5 Differentiating IPE from other photocurrent generating mechanism:**

After determining the photocurrents for C12 and BrP molecules, we broadened our study to a range of molecules, including some which may absorb light. In order to provide a test-bed for investigating IPE, we have identified several molecules that have different absorption spectra (see figure 4.1), and have tested the dependence of the photocurrent on several parameters, including molecular structure, molecular layer thickness, source intensity and energy, as discussed below. The main aim of these experiments is to determine possible ways to distinguish IPE from other photocurrent-generating mechanisms and thereby use IPE to characterize energy level alignment and barrier heights in molecular junctions.

#### 4.5.1 Relationship between absorption spectrum and photocurrent spectrum:

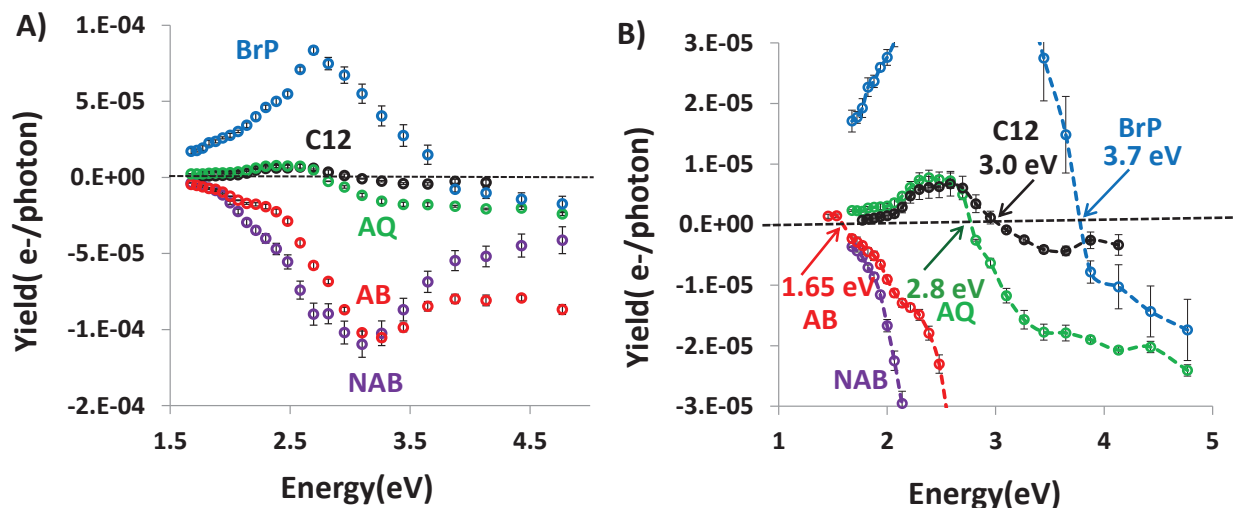


**Figure 4.10(A):** Photocurrent yield spectrum for five different junctions (BrP (Blue curve), C12 (black), AQ (green), AB (red) and NAB (violet)). (B): Shows the same data on an expanded Y axis, with the photon energies indicated where the curves cross the X axis.

The structures of seven different organic molecules (AB, NAB, AQ, BrP, C12, NDI & Fc) were given in figure 3.12 chapter-3, and have all been used previously to construct molecular junctions of the structure carbon/molecule/Cu (20nm)(11). Figure 4.10(A) shows a plot of the photocurrent yield as a function of photon energy for five different molecular structures with approximately equal molecular layer thicknesses, as follows: C12 (2.3 nm, black curve)(10), BrP (3.0 nm, blue curve)(10), AQ (2.5 nm, green curve), AB (3.4 nm, red curve) and NAB (4.0 nm, violet curve). Notable observations from Figure 4.10(A) include a similar photo-response for C12 and AQ at low energy (<2.8eV), while a larger and negative photocurrent is observed for AQ junction above 3 eV. The magnitude of the yield for junctions containing AB and NAB molecules at low energy (<2 eV) is comparable to that of C12 and AQ, but at higher energies the yield for these two molecules increases significantly and is negative. In the previous section 4.4 we proposed(10) that the change in sign for the C12 junction was indicative of the smaller interfacial barrier defined by the HOSO being more energetically accessible from the contact

Fermi level than the LUSO. Thus, the photocurrent at low energies is positive, but becomes negative when the electron-tunneling barrier becomes accessible. This enables the energy level alignment of electron and hole barriers for the C12 junction to be determined(10).

Note that in Figure 4.10(A) the energy where the photocurrent sign changes [i.e. the “crossing point” of the plot in Figure 4.10(B)] depends on the structure of the molecule: the crossing points are 3.7 eV for BrP, 2.8 eV for AQ and 1.65 eV for AB, while NAB remains negative in the spectral range studied and does not cross the abscissa. In order to determine if the absorbance of the molecule correlates with these crossing points, the photocurrent yield spectra were overlaid with the absorbance spectra for each of the aromatic molecules studied.

#### **4.5.2 Overlay of photocurrent yield, absorption vs. energy spectrum:**

A striking relationship between optical absorbance (black curves) and the measured photocurrent yield spectra (coloured data points) implies that absorption by the molecular component plays a role in determining the photocurrent spectrum characteristics, notably the abscissa crossing energy and the onset of negative photocurrent. In Figure 4.11(A), it is apparent that the magnitude of the photocurrent for AQ is similar to that of the alkane junction (see Figure 4.10(A)) in the energy range where little or no absorption by AQ takes place (below ~2.5 eV). However, at higher energies, when the AQ photocurrent crosses the abscissa and becomes progressively more negative, the AQ photocurrent significantly exceeds that of the alkane. One possible explanation is that when the molecule does not absorb incident light, IPE is the main mechanism contributing to the photocurrent, and so the positive photocurrent indicates that the OSO mediates the tunneling process for both molecules (i.e. it is more energetically accessible). When the molecule absorbs light, a secondary mechanism contributes additional negative current to the photo-response.

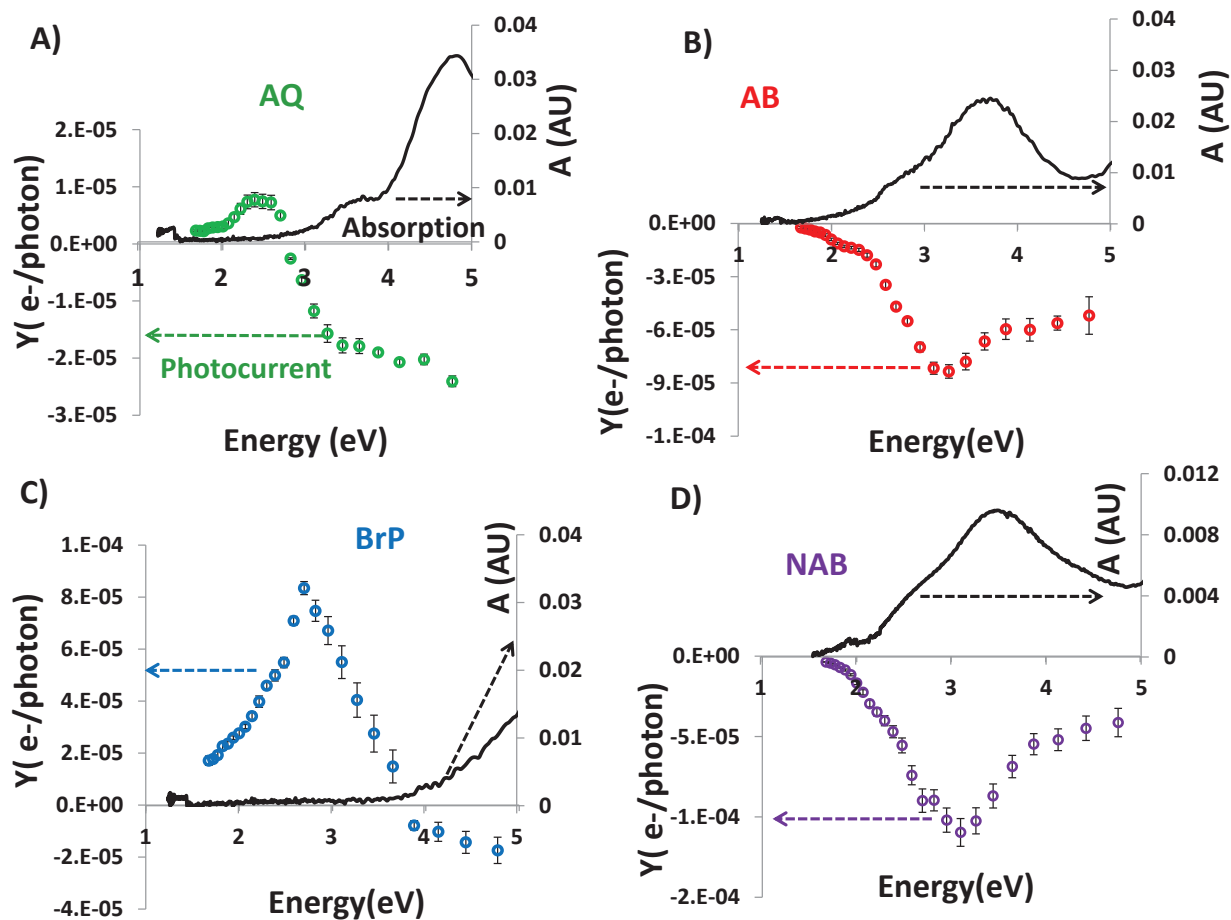


**Figure 4.11:** An overlay of photocurrent yield and absorption spectra for four different junctions; black line indicates the optical absorption spectra of the molecular layer corrected for PPF absorption and the coloured line indicates the measured photocurrent spectrum of a particular molecular junction (A) AQ, (B) AB, (C) BrP, and (D) NAB.

Recalling that the AQ molecule photocurrent crossing point was 2.8 eV (figure 4.10(B), we note that the onset for optical absorption for AQ chemisorbed to a transparent carbon surface is 2.5 eV (see figure 4.1(B)). A similar analysis of absorption and abscissa crossing energy was done for all the molecules studied here including C12, and is summarized in Table 4.1.

<b>Energy (eV)</b>	<b>BrP</b>	<b>AQ</b>	<b>AB</b>	<b>NAB</b>	<b>C12</b>
<b>Free molecule, DFT (HOMO-LUMO)</b>	<b>6.2</b>	<b>4.2</b>	<b>3.9</b>	<b>3.6</b>	<b>7.8</b>
<b>UV-Vis peak, solution</b>	<b>&gt;6</b>	<b>~ 4</b>	<b>3.9/2.7s<sup>a</sup></b>	<b>3.7/2.7s</b>	<b>&gt;6</b>
<b>UV-Vis absorption onset</b>	<b>5.2</b>	<b>3.6</b>	<b>3.4/2.4s</b>	<b>3.2/2.3s</b>	<b>-</b>
<b>PPF-bonded peak</b>	<b>&gt;6</b>	<b>4.8/3.6s</b>	<b>3.6/2.5s</b>	<b>3.4/2.5s</b>	<b>&gt;6</b>
<b>PPF-bonded onset</b>	<b>3.6</b>	<b>2.5</b>	<b>1.7</b>	<b>1.7</b>	<b>&gt;6</b>
<b>PC Crossing point</b>	<b>3.7</b>	<b>2.8</b>	<b>1.6</b>	<b>&lt;1.46</b>	<b>3.0</b>

**Table 4.1:** Summary of optical absorption data for molecular layers:

a. “s” indicates shoulder on main UV-Vis absorption peak.

In the case of AB and NAB, where significant optical absorption occurs even at low energy, the photocurrent measured using the continuum light source remains negative throughout the entire spectral range accessible with the Xe arc (See figure 4.11(B) and 4.11(D)). Either there is no photocurrent crossing point for these molecules, or it cannot be observed using the continuum source, due to its limited power. However, laser diodes provide sufficient power to enable the measurement of the photocurrent at lower photon energies. The two points (808 nm and 852 nm, or 1.54 and 1.46 eV) obtained from these measurements both resulted in positive photocurrent for AB junction, and are included in the AB photocurrent spectrum in Figure 4.10(B), showing that the crossing point for AB is ~1.6 eV (also see figure 4.12). Analysis of the compiled data in Table 4.1 clearly shows that the photocurrent crossing point correlates with the onset of optical absorbance for the four molecules. This result indicates that a two-regime model is needed to explain the entire photocurrent spectrum for certain molecules: an IPE regime at low energies where molecular absorption is negligible, and a second photocurrent mechanism involving molecular absorption (MA) at higher energies, with the particular crossing point dictated by molecular structure. The conclusion from analysis of Table 4.1 is that in order to use IPE to

characterize energy levels while avoiding interference by a molecular absorption photocurrent the analysis must be done in a region where the observed photocurrent is dominated by IPE. In order to provide additional tests of the contribution of molecular absorption, we examined the dependence of the photocurrent on excitation intensity and the molecular layer thickness.

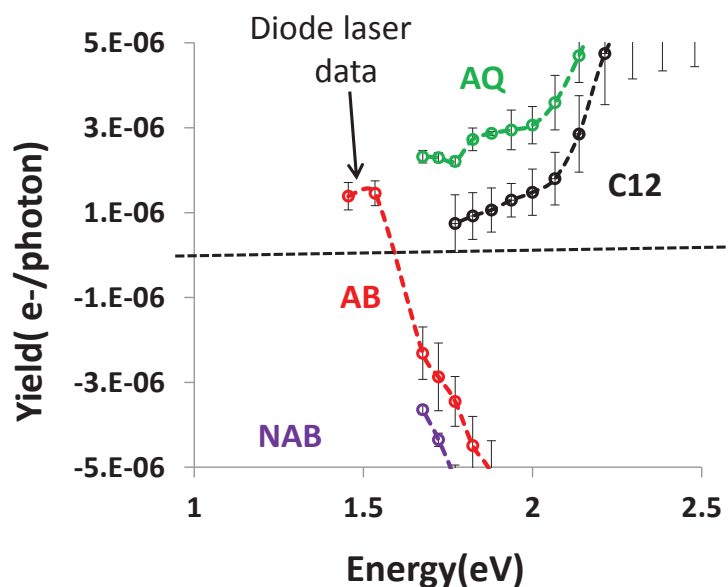


**Figure 4.12:** Expanded view of figure 4.10(B), showing positive photocurrent for AB junction (red curve) obtained from diode laser at two different energies (1.46 eV and 1.54 eV).

### 4.5.3 Photocurrent vs. excitation intensity:

IPE current is presumed to be originated by the excitation of surface plasmons in the contacts, which decay into hot electron-hole pairs, with subsequent transport across internal system barriers at appropriate energies(18). Because conductors have very high carrier concentrations, the excitation of hot carriers is linearly dependent on the excitation source intensity as long as the number of the excited carriers is small compared to the total number of carriers present. Thus, the IPE photocurrent is expected to increase linearly with excitation intensity over a wide range of intensity. However, exciton formation in molecular materials can show non-linearity for at least two reasons. First, the density of molecular ground states may be depleted faster than they

can refill at high excitation levels. Second, various models of exciton generation include a non-linear term due to recombination effects. In particular, bimolecular and/or surface recombination is expected to result in proportionality between the square of the photocurrent and the excitation intensity (32-34). Following a previously-reported derivation for exciton generation(33), the number of excitons ( $n$ ) and the resulting photocurrent is linearly dependent on the illumination intensity ( $I$ , in photons/sec), given by equation (2),

$$n = \alpha I \quad (\text{Eqn 4.2})$$

where  $\alpha$  is a constant representing optical absorption in the material. Next, we define the rate constant for monomolecular recombination ( $k_m$ ) as being inversely related to the lifetime of the mobile charge carrier optically generated in the material. In the case of IPE, an optically-generated hot electron in Cu crosses the barrier and undergoes recombination with a non-mobile hole in the carbon contact. Here, the process of a ‘single mobile charge carrier’ annihilating a localized positive charge in the carbon contact makes the carbon more negative and represents a monomolecular process, since a single mobile charge carrier is eliminated. For the case of two mobile charges (bound or not) recombining, we define a rate constant  $k_b$ , the bimolecular<sup>a</sup> recombination rate constant. (<sup>a</sup> The recombination can occur in one molecule or between two molecules, but the literature convention is to call both “bimolecular”). Since the steady-state condition gives the rate of change of  $n$  with respect to time as zero, we have

$$\alpha I - mn - bn^2 = 0 \quad (\text{Eqn 4.3})$$

such that for small  $n$ :

$$n = \frac{\alpha}{m} I \quad (\text{Eqn 4.4})$$

and for large  $n$

$$n = \sqrt{\frac{\alpha I}{b}} \quad (\text{Eqn 4.5})$$

eqn (4.4) shows that when the photocurrent is controlled by monomolecular recombination, such as a hot carrier crossing a barrier and being collected by a second electrode(33), then the photocurrent will be a linear function of intensity. Eqn (4.5), on the other hand, shows that bimolecular recombination is expected to exhibit a photocurrent that is proportional to the square root of intensity. These considerations imply that a good test of photocurrent generation mechanism is the relationship between photocurrent and excitation intensity.

Given the mechanistic inferences from Figure 4.11, the response to a particular incident wavelength can be predicted to be linear or quadratic. For example, at photon energies below 3.0 eV, AlOx, BrP, and AQ junctions are expected to show linear photocurrent vs. intensity plots, since the molecules do not absorb light and the dominant mechanism is IPE. By contrast, AB absorbs light over the range of 1.7 to 3 eV, and is expected to show a non-linear dependence on intensity. Figure 4.13 shows plots of the photocurrent ( $i_p$ ) as a function of the incident power for several different junctions under constant (i.e. unmodulated) laser illumination at selected optical energies. First, Figure 4.13A shows a plot for the Al/Al<sub>2</sub>O<sub>3</sub>/Cu (20) sample, for which a negative DC photocurrent was recorded using a picoammeter and Ar-ion laser illumination at 475 nm (2.65 eV). The photocurrent response is linear with excitation intensity, as expected for a pure-IPE derived photocurrent and monomolecular recombination. Since AlOx does not have any optical transitions within the energy region tested, it provides an excellent control experiment and confirms the linearity of IPE current with intensity. Second, figure 4.13(B) shows a similar plot for an AQ junction which exhibits linear response for both 514 nm (2.41 eV) and 689 nm

(1.80 eV), as predicted from figure 4.11(A) given the weak absorbance of AQ at these wavelengths.

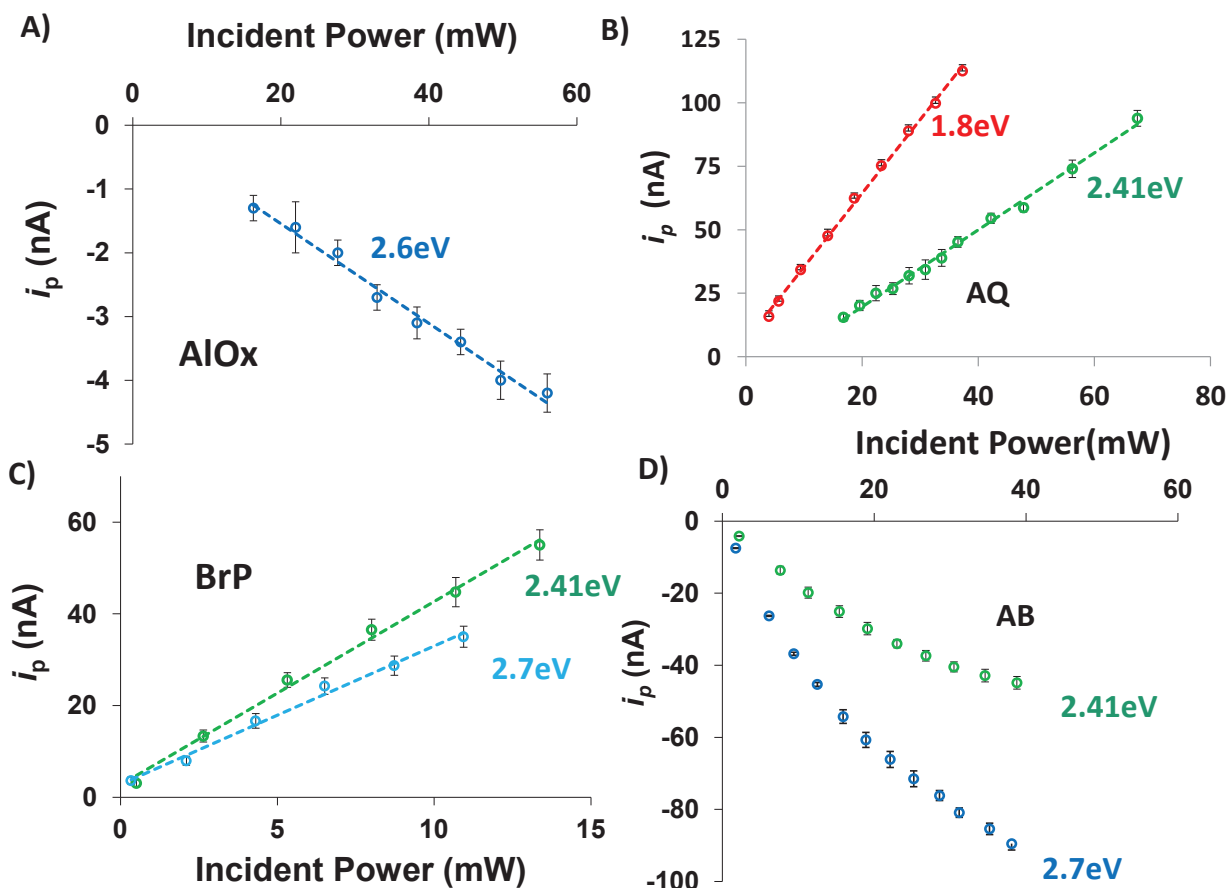


**Figure 4.13:** Photocurrent vs. light intensity curves for (A) Al/AIOx/Cu, blue curve at 2.6 eV (476nm) (B) Carbon/AQ/Cu at 1.8 eV (688 nm), red curve and 2.4eV (516 nm), green curve (C) Carbon/BrP/Cu at 2.4 eV (516 nm), green curve and 2.7eV (458 nm), blue curve (D) carbon/AB/Cu at 2.4 eV (516 nm), green curve and 2.7 eV (458 nm), blue curve.

Third, figure 4.13(C) shows the analogous plots for BrP at 2.4 eV and 2.7 eV, again displaying a linear increase with intensity as expected from Figure 4.11(C). It is also important to note that the sign of the photocurrents from figure 4.11 and 4.13 match, such that in cases where no absorption takes place, the photocurrent is negative, indicating USO mediated transport ( $\text{Al}_2\text{O}_3$ ) or positive indicating OSO transport (AQ and BrP) where expected. Taken together, the results for AlOx, AQ, and BrP in Figures 4.13A(C) indicate that the observed photocurrent is dominated

by IPE, with negligible contribution from photon absorption in the molecular layer. Finally, the AB molecular layer does show significant absorbance below 3 eV, and plots of  $i_p$  versus excitation intensity for two wavelengths (458nm, or 2.7 eV; and 514 nm or 2.4 eV) where AB absorbs light is shown in Figure 4.13(D). Here, the photocurrent is negative and displays a clear non-linear trend. This sub-linear increase of photocurrent with intensity is consistent with a simple quadratic function, showing that when molecule absorbs a significant amount of the incident light, the photocurrent is governed by a bimolecular recombination mechanism (eqn 4.5) which is distinct from IPE. To confirm this hypothesis, photocurrent vs. intensity for alkane junctions at 2.4 and 2.7 eV (see figure 4.14) were monitored and in both cases the plots were found to be linear. Overall, the dependence of photocurrent on excitation intensity enables us to determine which photocurrent generating mechanism (IPE or molecular absorption) is dominant at a given energy.

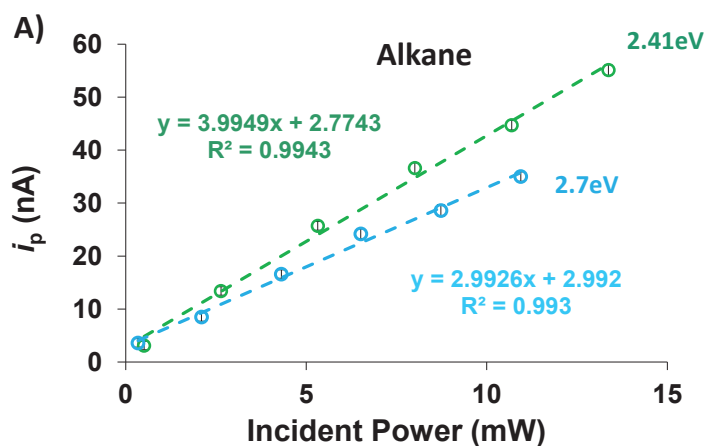


**Figure 4.14:** Photocurrent vs. intensity plot for an alkane junction at 2.4 eV (458 nm) and 2.7 eV (516 nm).

#### 4.5.4 NDI and Ferrocene molecular junctions:

In order to obtain further insight into the IPE regime of the photocurrent spectra, molecular junctions containing ferrocene and NDI molecular layers were examined. These molecules exhibit very weak optical absorption below 3 eV (figures 4.15(A) and 4.15(B), solid lines and right ordinate), which leads to the expectation that IPE should dominate the photocurrent spectra for these molecules below 3 eV. Figures 4.15(A) and 4.15(B) show overlays of the absorption and photocurrent spectra as functions of photon energy for molecular junctions containing ferrocene and NDI, respectively. Figure 4.15(A) shows that the photocurrent measured for Fc junction is positive throughout the entire spectral range, indicating that the OSOs mediate transport for the IPE mechanism. However, at energies above 3 eV, the photocurrent yield decreases in magnitude. One possible explanation for this observation is that above 3 eV the secondary mechanism (i.e. MA) might significantly exceed the primary IPE mechanism. A second possibility is that USO-mediated IPE begins contributing to the overall current, acting to decrease the overall yield. Figure 4.15(B) shows the photocurrent spectrum for an NDI junction, where the photocurrent remains negative throughout the whole spectral energy range studied. The lack of molecular absorbance at low energy (<3 eV) implies that for both the molecules (Fc and NDI), photocurrents are due to IPE, and that they are OSO and USO mediated, respectively. To test this hypothesis the dependence of photocurrent on excitation intensity for both Fc and NDI at two different energies were monitored. In all the cases below 3 eV, the photocurrent was linear with intensity, and expected to have IPE mechanism without significant molecular absorption.

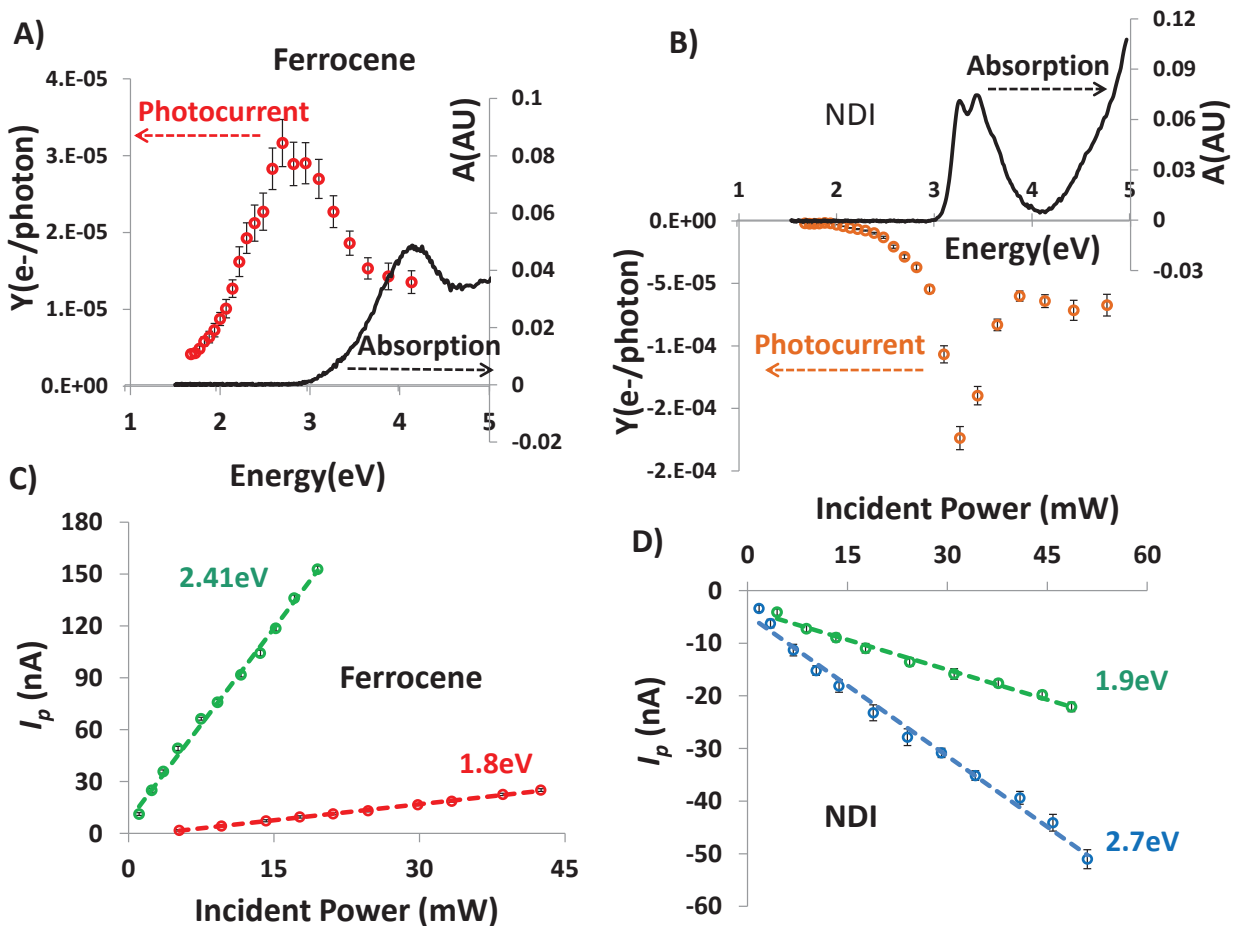


**Figure 4.15:** Overlay of Photocurrent yield (colored lines) and absorbance spectra (black lines), for Fc (A) and NDI (B). (C) Photocurrent vs. Intensity for PPF/Fc/Cu at 2.4 eV (green line), and 1.8 eV (red) (D) Photocurrent vs. intensity for PPF/NDI/Cu at 2.7 eV (blue) and 1.9 eV (green).

Table 4.2 lists the correlation coefficient ( $R^2$ ) determined from linear ( $I_{\text{photo}}$  vs. intensity) or quadratic [ $(I_{\text{photo}})^2$  vs. intensity] plots of photocurrent vs. incident light intensity in Watts. NDI, Fc, BrP, AQ and alkane junctions more closely fit a linear function of intensity at 2.7 and 2.4 eV, while AB has a better fit to a quadratic function at either 2.4 or 1.9 eV.

NDI			Fc		
Graph	R <sup>2</sup> fitting value (2.7eV)	R <sup>2</sup> fitting Value (2.4eV)	Graph	R <sup>2</sup> fitting value (2.4eV)	R <sup>2</sup> fitting Value (1.9eV)
I <sub>photo</sub> vs. incident power	0.9899	0.9893	I <sub>photo</sub> vs. incident power	0.9966	0.9967
(I <sub>photo</sub> ) <sup>2</sup> vs. incident power	0.9552	0.9819	(I <sub>photo</sub> ) <sup>2</sup> vs. incident power	0.944	0.9073

BrP			AB		
Graph	R <sup>2</sup> fitting value (2.4eV)	R <sup>2</sup> fitting Value (2.7eV)	Graph	R <sup>2</sup> fitting value (2.4eV)	R <sup>2</sup> fitting Value (1.9eV)
I <sub>photo</sub> vs. incident power	0.9917	0.9946	I <sub>photo</sub> vs. incident power	0.9638	0.9653
(I <sub>photo</sub> ) <sup>2</sup> vs. incident power	0.9646	0.9696	(I <sub>photo</sub> ) <sup>2</sup> vs. incident power	0.998	0.9937

AQ			Alkane		
Graph	R <sup>2</sup> fitting value (2.4eV)	R <sup>2</sup> fitting value (1.8eV)	Graph	R <sup>2</sup> fitting value (2.4eV)	R <sup>2</sup> fitting Value (2.7eV)
I <sub>photo</sub> vs. incident power	0.9952	0.9981	I <sub>photo</sub> vs. incident power	0.9943	0.993
(I <sub>photo</sub> ) <sup>2</sup> vs. incident power	0.9314	0.9728	(I <sub>photo</sub> ) <sup>2</sup> vs. incident power	0.9646	0.9692

**Table 4.2:** R<sup>2</sup> correlation coefficient for both I<sub>photo</sub> vs. incident power and the (I<sub>photo</sub>)<sup>2</sup> vs. incident power for all the molecules used in this study at different energies.

#### 4.5.5 Thickness test:

An additional mechanistic test for a MA contribution is the variation of the photocurrent with the thickness of the molecular layer. The IPE mechanism should show a weak dependence on the thickness of the molecular layer, at least up to the scattering length of electrons in the molecular layer. Any mechanism involving optical absorption by the molecular layer should increase linearly with layer thickness. Figures 4.16(A) and 4.16(B) shows the photocurrent yield spectrum for junctions with molecular layer thicknesses varied in the range of 3-5 nm for Fc, NDI, AB and NAB. For ferrocene junctions within the IPE regime (i.e., at energies less than 3 eV), the photocurrent yield is independent of molecular layer thickness (within experimental error),

indicating that a greater path length available for optical absorption has no significant effect on photocurrent. Figure 4.16B shows a slightly different behaviour for junctions containing NDI: the yield remains almost independent of molecular thickness at low energy, whereas at energies above 3 eV, yield increases considerably with molecular layer thickness. Figure 4.16 also shows photocurrent yield spectra for increasing thicknesses of AB (4.16(C)) and NAB (4.16(D)) junctions in the range of 2-5 nm, showing a significant dependence of yield on molecular layer thickness.

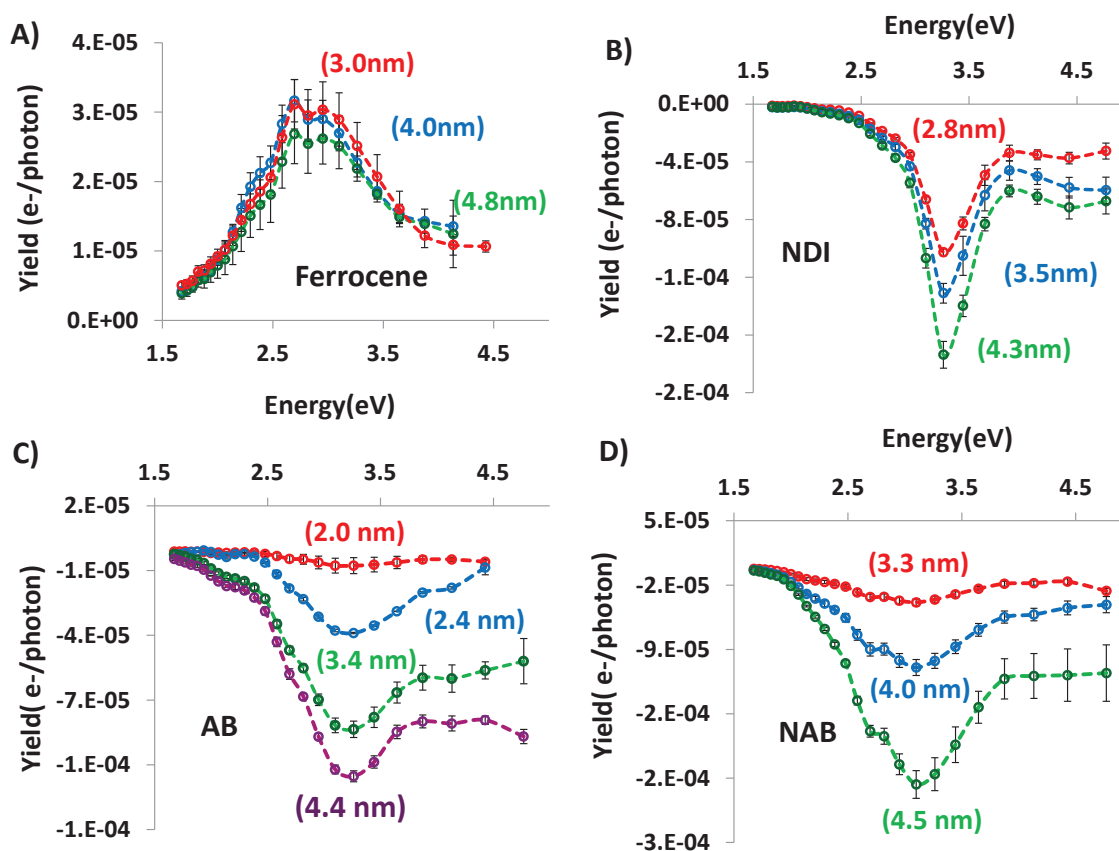


**Figure 4.16:** Photocurrent yield spectra for increasing molecular layer thicknesses, as indicated. (A) Ferrocene (B) NDI (C) AB (D) NAB.

Comparison of plots of yield vs. thickness for all four molecules (see figure 4.17) reveals two distinct behaviours. For cases where the absorption by the molecular layer is small (Fc, 1.82 and

3.26 eV; NDI, AB, and NAB at 1.82 eV), the yield depends weakly on thickness. When molecular absorption is significant, there is a pronounced increase in photocurrent with increasing molecular layer thickness.

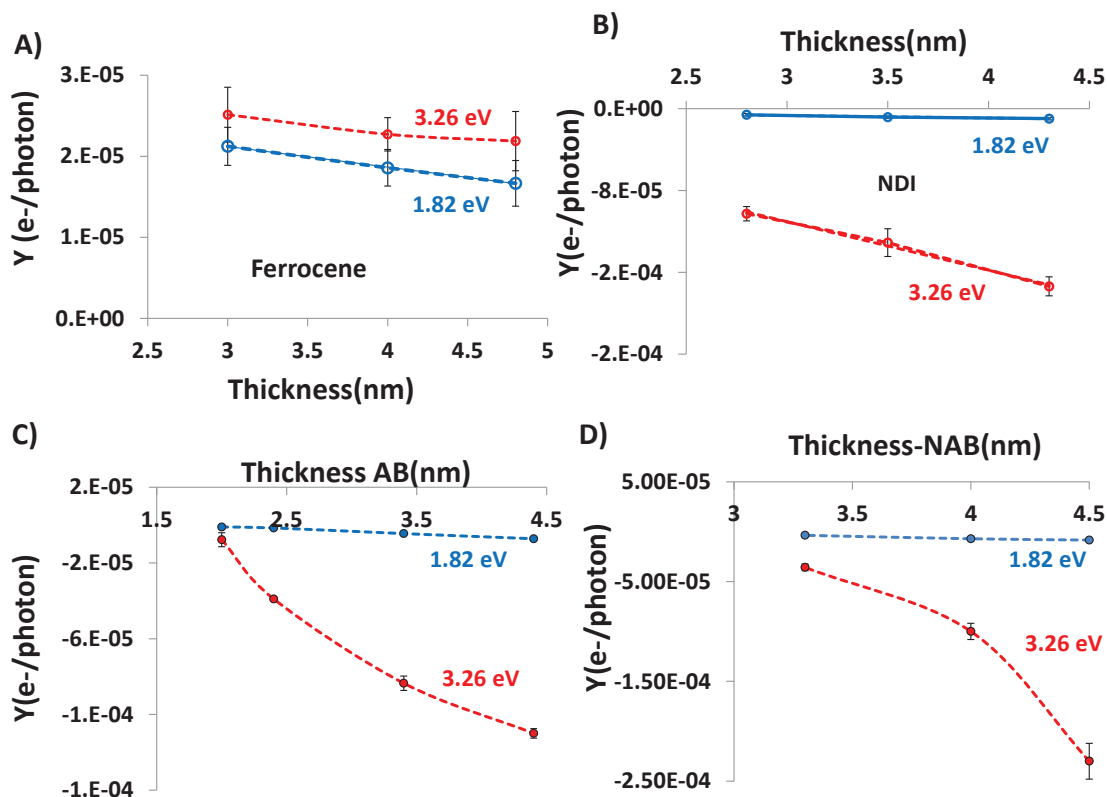


**Figure 4.17:** Yield vs. thickness plots of (A) Fc, (B) NDI, (C) AB and (D) NAB junctions.

Considering the results from figures 4.16 and 4.17 together, we conclude that two different mechanisms are responsible for generating photocurrent in molecular junctions, which can be distinguished by the site of optical absorption. In IPE, hot carriers generated by light absorption in one contact cross the internal system tunneling barrier, as long as they have sufficient energy, and are then collected by the second contact. In the second mechanism, carriers are generated by absorption in the molecular layer and may be collected or undergo bimolecular recombination. It is important to note that IPE is operative to some extent in all cases, although the yield for this

process is small compared to the MA process for AB and NAB for most of the spectral range examined.

#### 4.5.6 Fowler plots:

Having established how to distinguish the two different regimes, we move on to an analysis of junction energy-level characterizations using IPE by avoiding photon energies where molecular absorption contributes significantly. Fowler plots for all of the molecules which meet the requirement of negligible molecular absorption appear in figure 4.18(A), and their intercepts are listed in table 4.3. Table 4.3 also includes  $E_f - E_{\text{HOMO}}$  offsets determined with UPS and the barrier height determined from a detailed Simmons analysis of current-voltage response of completed junctions. Table 4.3 shows that the value obtained for barrier heights using three different methods agrees within a reasonable margin given the experimental errors inherent in each technique. It is important to note that the experimental UPS measurements were obtained from incomplete devices without top contacts, i.e. molecular layers on carbon substrates in vacuum, whereas the Fowler intercepts were obtained from complete, working devices. In addition, the meaning of the abscissa intercept of  $Y^{1/2}$  vs. photon energy for the case of photon absorption within the molecular layer is not necessarily equal to an interfacial barrier, and should not be confused with the Fowler intercept for non-absorbing molecules.

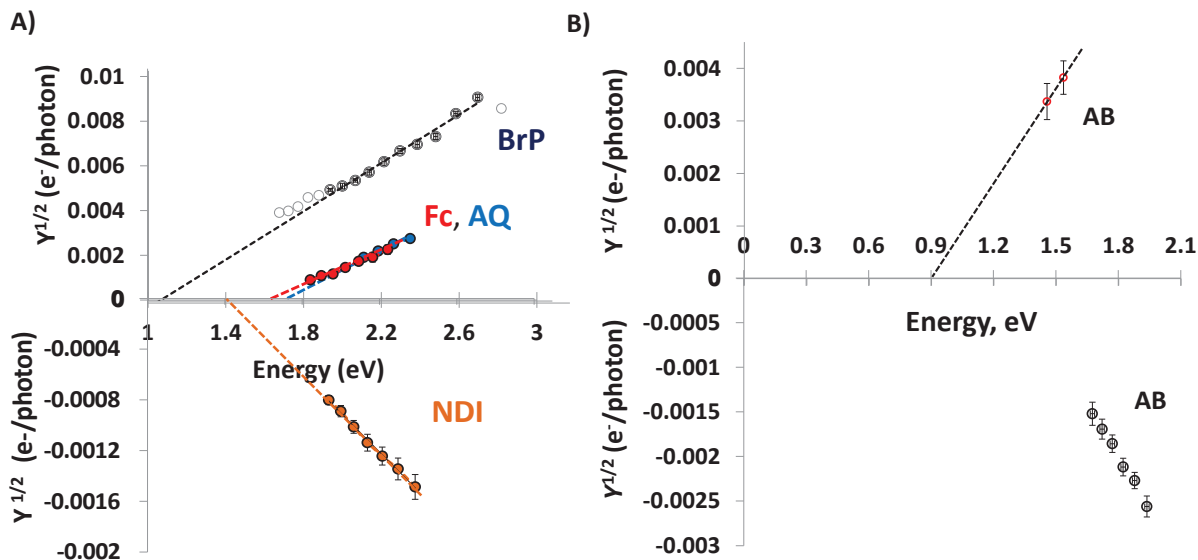


**Figure 4.18:** (A) Fowler plots for BrP, NDI, Fc and AQ (B) shows the Fowler plot of AB.

Note that the Fowler intercept for AB is approximate due to insufficient data outside the molecular absorbance regime.

Junction	IPE/Fowler <sup>a</sup>	UPS <sup>b</sup>	Simmons Fit <sup>b</sup>
BrP(3nm)	$1.1 \pm 0.1$	$1.5 \pm 0.15$	$1.5 \pm 0.3$
AQ(3.3nm)	$1.5 \pm 0.1$	$1.4 \pm 0.1$	$1.4 \pm 0.2$
AB(3.4nm)	$0.9^c$	$1.0 \pm 0.1$	$1.1 \pm 0.2$
NAB(3.3nm)	$< 1.4$	$1.2 \pm 0.15$	$1.3 \pm 0.2$
Fc(4.0nm)	$1.4 \pm 0.15$	-	-
NDI(3.5nm)	$1.35 \pm 0.30^d$	-	-

**Table 4.3:** Summary of barrier heights obtained using three different methods.

a. Fowler intercept from figure 4.17(A)

b. UPS ( $E_f - E_{HOMO, offset}$ ) and Simmons barriers from reference (11)

c. Approximate, based on two points (808 and 852 nm)

d. Photocurrent for Fowler plot was negative, all others were positive.

The error bars in figure 4.18 shows the standard deviation of photocurrent for four different junctions on the same sample. Table 4.4 shows the value of Fowler intercepts obtained from the Fowler plots, and are provided in table 4.3. The intercepts and their errors were determined statistically using standard methods (35) as follows. Let  $x_i$  represent photon energy  $y_i$  represent  $Y^{1/2}$ ,  $A$  the Fowler intercept,  $B$  the associated slope, and  $\sigma_A$  the error on the intercept on the ordinate.

$$A = \frac{\sum x^2 \sum y - \sum x \sum xy}{\Delta} \quad (\text{Eqn 4.6})$$

$$B = \frac{N \sum xy - \sum x \sum y}{\Delta} \quad (\text{Eqn 4.7})$$

$$\Delta = N \sum x^2 - (\sum x)^2 \quad (\text{Eqn 4.8})$$

$$\sigma_y = \sqrt{\frac{1}{N-2} \sum_{i=1}^N (y_i - A - Bx_i)^2} \quad (\text{Eqn 4.9})$$

$$\sigma_A = \sigma_y \sqrt{\frac{\sum x^2}{\Delta}} \quad (\text{Eqn 4.10})$$

$$\sigma_B = \sigma_y \sqrt{\frac{N}{\Delta}} \quad (\text{Eqn 4.11})$$

The Fowler intercept on the photon-energy axis is the absolute value of A/B, and the error on this intercept ( $\sigma_{Fowler}$ ) is determined by equation 4.12.

$$\sigma_{Fowler} = \left| \frac{A}{B} \right| \left( \frac{\sigma_B}{|B|} + \frac{\sigma_A}{|A|} \right) \quad (\text{Eqn 4.12})$$

The value obtained from this equation is given in table 4.4:

Junction	Fowler intercept	$\sigma$ Fowler
BrP (3.0nm)	1.10 eV	0.11 eV
AQ (3.3nm)	1.65 eV	0.10 eV
AB <sup>a</sup> (3.4nm)	0.9eV	-
NAB <sup>b</sup> (3.3nm)	<1.4eV	-
Fc (4.0nm)	1.60eV	0.15 eV
NDI (3.5nm)	1.40eV	0.30 eV

**Table 4.4:** Fowler intercepts for each molecule along with their errors.

a- Approximate, based on two points (808 and 852 nm), insufficient data points to calculate the error for intercept.

b- NAB does not meet the criteria for IPE; therefore the Fowler intercept is not relevant.

Although the Fc and NDI intercepts are similar, they clearly differ in the sign of the photocurrent, with NDI exhibiting negative photocurrent near the intercept and Fc, AQ, BrP and AB all having positive photocurrent in the same region. Since all the cases except NAB listed in table 4.3 meet the criteria for IPE, the sign of the photocurrent provides unambiguous determination of the system energies responsible for the tunneling barrier. The onset of IPE occurs at the energy closest to the system Fermi level, and represents the barrier for electron or hole-tunneling.

## 4.6 Proposed Mechanism for Fc and NDI:

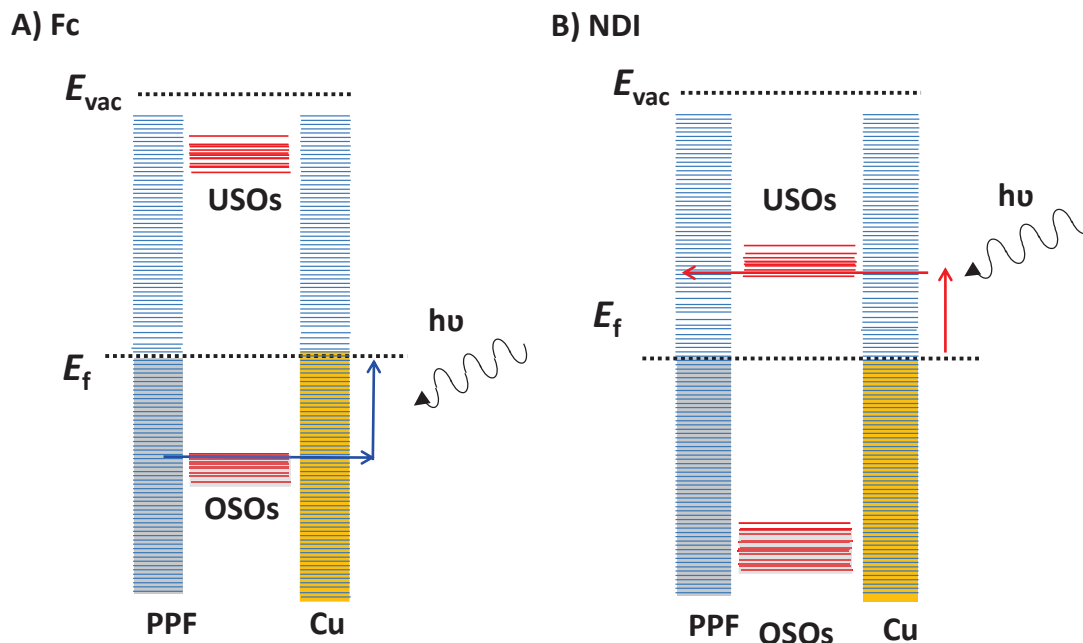


**Figure 4.19:** (A) Proposed diagram of the IPE mechanism for OSO mediated transport of electrons from PPF to Cu for the ferrocene molecule. (B): Diagram for electron transfer from Cu to carbon through the USO for the NDI molecule. The alignment of the occupied system orbitals (OSOs) and the unoccupied orbitals (USOs) relative to the contact Fermi levels determines the sign of the observed photocurrent and the energy threshold for onset.

Based on the model of IPE in figure 4.4, positive photocurrent corresponds to transport mediated by the nearest OSO, while negative photocurrent is mediated by the nearest USO. Therefore, NDI is a case of electron tunneling while AQ, AB, BrP, Fc, and C12 undergo hole-tunneling near the Fowler threshold. Figure 4.19(A) shows the resulting energy-level diagram for the Fc junction, where a positive photocurrent was measured in the IPE wavelength regime. Along with the energy level diagram, a schematic representation of IPE is shown, in which an excited hole in the Cu is filled by an electron from the carbon via a OSO. Figure 4.19(B) provides a contrasting IPE mechanism and energy-level diagram for NDI-containing molecular junction, in which electron transport from Cu to carbon takes place internally through a USO. The transport in the IPE mechanism is through a molecular orbital, and therefore ‘resonant’,

meaning it can proceed over significant molecular layer thickness, limited by the scattering length. These results show that IPE may be used to obtain information from working molecular junctions about the alignment of occupied and unoccupied molecular orbitals relative to the system Fermi level, for either USO-mediated (electron) tunneling or OSO-mediated (hole) tunneling. In this model it is implicit that photoexcitation occurs predominantly in the Cu, and that IPE is the dominant mechanism, with negligible contribution from absorption by the molecular layer or the carbon substrate.

The average tunneling barrier obtained from UPS results was  $1.3 \pm 0.2$  eV for the aromatic molecules, quite close to the  $1.2 \pm 0.2$  eV estimated from the J-V curves using modified Simmons analysis (7). The average tunnelling barriers obtained for the aromatic molecules by the Fowler analysis is  $1.2 \pm 0.2$  eV, in good agreement with the previous determinations. We have previously reported the compression of interfacial barriers in our junctions (11) due to the strong electronic coupling between the molecule and the substrate causes a significant alteration of energy levels from those of the free molecules and unmodified substrate. Upon bonding, electronic-inductive effects result in local changes in electrostatic potential and compression of the tunnelling barrier from values predicted from the free molecule energy levels. This compression has been attributed to an induced density of interface states (29, 30), sometimes referred to as the gap states (31), which are transport states lying within the HOMO-LUMO gap of the molecular species. Such effects are a consequence of the interaction between the molecules and the contacts, and reinforce the conclusion that the entire system must be considered when predicting interfacial barriers. Therefore, direct determination of energy levels in complete, intact devices using photocurrent measurements can provide valuable information

about energy level alignment, and can assist in the larger problem of understanding the structural factors that determine the electronic behaviour of molecular junctions.

#### **4.7 Conclusion:**

This chapter has shown that photocurrent measurements of completed carbon/molecule/Cu junctions can yield valuable information about energy level alignment. An IPE mechanism was shown to be useful in determining both electron and hole tunneling barriers for a complete and operational carbon/alkane/Cu molecular junction. This chapter also demonstrates that the observed photocurrent spectrum of a molecular tunnel junction is often composed of two types of photocurrent: one involving an IPE process, which can be useful for determining energy level alignment and interfacial energy barriers, and one that involves optical absorption by the molecular layer. IPE occurs when the molecular layer absorption is weak, and IPE photocurrent is linear with light intensity and weakly dependent on molecular layer thickness. The Fowler plot for IPE is linear, with its intercept on the abscissa equal to the energy offset between the system Fermi level and the nearest orbital, with positive photocurrent indicated USO-mediated transport and negative photocurrent indicating OSO mediation. Chemisorbed molecules which absorb photons within the molecular layer lead to additional photocurrent, which is nonlinear with light intensity and dependent on molecular layer thickness. Although the additional photocurrent can complicate the IPE analysis, it is likely directly relevant to photovoltaic devices with much thicker molecular layers than those studied here. We anticipate significant new information like exciton diffusion, bilayer photocurrent relation to molecular structure etc., from these photoeffects, beyond the tunneling barriers and transport orbitals determined with IPE.

## 4.8 References:

1. Powell R (1970) Interface Barrier Energy Determination from Voltage Dependence of Photoinjected Currents. *J. Appl. Phys.* 41(6):2424.
2. Gundlach KH & Kadlec J (1975) Interfacial Barrier Height Measurement from Voltage Dependence of Photocurrent. *J. Appl. Phys.* 46(12):5286-5287.
3. DiMaria DJ & Arnett PC (1975) Hole Injection into Silicon Nitride: Interface Barrier Energies by Internal Photoemission. *Appl. Phys. Lett.* 26(12):711-713.
4. Goodman AM (1970) Photoemission of Holes and Electrons from Aluminum into Aluminum Oxide. *J. Appl. Phys.* 41(5):2176-2179.
5. Ranganathan S & McCreery RL (2001) Electroanalytical Performance of Carbon Films with Near-Atomic Flatness. *Anal. Chem.* 73:893-900.
6. Bergren AJ, Harris KD, Deng F, & McCreery R (2008) Molecular Electronics using Diazonium-Derived Adlayers on Carbon with Cu Top Contacts: Critical Analysis of Metal Oxides and Filaments. *J. Phys. Condens. Matter.* 20:374117.
7. Bergren AJ, McCreery RL, Stoyanov SR, Gusarov S, & Kovalenko A (2010) Electronic Characteristics and Charge Transport Mechanisms for Large Area Aromatic Molecular Junctions. *J. Phys. Chem. C.* 114:15806-15815.
8. Anariba F & McCreery RL (2002) Electronic Conductance Behavior of Carbon-Based Molecular Junctions with Conjugated Structures. *J. Phys. Chem. B.* 106:10355-10362.
9. McGovern WR, Anariba F, & McCreery RL (2005) Importance of Oxides in Carbon/Molecule/Metal Molecular Junctions with Titanium and Copper Top Contacts. *J. Electrochem. Soc.* 152(5):E176-E183.

10. Fereiro JA, McCreery RL, & Bergren AJ (2013) Direct Optical Determination of Interfacial Transport Barriers in Molecular Tunnel Junctions. *J. Chem. Soc.* 135(26):9584-9587.
11. Sayed SY, Fereiro JA, Yan H, McCreery RL, & Bergren AJ (2012) Charge Transport in Molecular Electronic Junctions: Compression of the Molecular Tunnel Barrier in the Strong Coupling Regime. *Proc. Natl. Acad. Sci. U.S.A.* 109(29):11498-11503.
12. Ranganathan S, McCreery RL, Majji SM, & Madou M (2000) Photoresist-Derived Carbon for Microelectrochemical Applications. *J. Electrochem. Soc.* 147:277 - 282.
13. Yan H, Bergren AJ, & McCreery RL (2011) All-Carbon Molecular Tunnel Junctions. *J. Am. Chem. Soc.* 133(47):19168-19177.
14. Braun S, Salaneck WR, & Fahlman M (2009) Energy-Level Alignment at Organic/Metal and Organic/Organic Interfaces. *Adv. Mater.* 21(14-15):1450-1472.
15. Cahen D & Kahn A (2003) Electron Energetics at Surfaces and Interfaces: Concepts and Experiments. *Adv. Mater.* 15(4):271-277.
16. Ishii H, Sugiyama K, Ito E, & Seki K (1999) Energy Level Alignment and Interfacial Electronic Structures at Organic/Metal and Organic/Organic Interfaces. *Adv. Mater.* 11(8):605-625.
17. Tian H, Bergren AJ, & McCreery RL (2007) Ultraviolet-Visible Spectroelectrochemistry of Chemisorbed Molecular Layers on Optically Transparent Carbon Electrodes. *Appl. Spectrosc.* 61(11):1246-1253.
18. Afanas'ev VV (2008) *Internal Photoemission Spectroscopy: Principles and Applications* (Elsevier, London).
19. Sze SM (1981) *Physics of Semiconductor Devices* (Wiley, New York) 2nd Edition Ed.

20. Yaffe O, Qi Y, Scheres L, Reddy S, Segev L, Ely T, Haick H, Vilan A, Kronik L, Kahn A & Cahen D. (2012) Charge Transport Across Metal/Molecular (alkyl) Monolayer-Si Junctions is Dominated by the LUMO Level. *Phys. Rev. B.* 85:045433.
21. Qi Y, Yaffe O, Tirosh E, Vilan A, Cahen D & Kahn A (2011) Filled and Empty States of Alkanethiol Monolayer on Au (111): Fermi level Asymmetry and Implications for Electron Transport. *Chem. Phys. Lett.* 511(4-6):344-347.
22. Reddy P, Jang S-Y, Segalman RA, & Majumdar A (2007) Thermoelectricity in Molecular Junctions. *Science.* 315(5818):1568-1571.
23. Malen JA, Doak P, Baheti K, Tilley TD, Segalman RA & Majumdar A (2009) Identifying the Length Dependence of Orbital Alignment and Contact Coupling in Molecular Heterojunctions. *Nano Lett.* 9(3):1164-1169.
24. Salomon A, Cahen D, Lindsay S, Tomfohr J, Engelkes VB & Frisbie CD (2003) Comparison of Electronic Transport Measurements on Organic Molecules. *Adv. Mater.* 15(22):1881-1890.
25. Niskala JR, Rice WC, Bruce RC, Merkel TJ, Tsui F & You W (2012) Tunneling Characteristics of Au–Alkanedithiol–Au Junctions formed via Nanotransfer Printing (nTP). *J. Am. Chem. Soc.* 134:12072-12082.
26. Wang G, Kim T-W, Jo G, & Lee T (2009) Enhancement of Field Emission Transport by Molecular Tilt Configuration in Metal-Molecule-Metal Junctions. *J. Am. Chem. Soc.* 131:5980-5985.
27. Li X, He J, Hihath J, Xu B, Lindsay SM & Tao NJ(2006) Conductance of Single Alkanedithiols: Conduction Mechanism and Effect of Molecule-Electrode Contacts. *J. Am. Chem. Soc.* 128:2135-2141.

28. Engelkes VB, Beebe JM, & Frisbie CD (2004) Length-Dependent Transport in Molecular Junctions Based on SAMs of Alkanethiols and Alkanedithiols: Effect of Metal Work Function and Applied Bias on Tunneling Efficiency and Contact Resistance. *J. Am. Chem. Soc.* 126:14287-14296.
29. Shen C & Kahn A (2001) The Role of Interface States in Controlling the Electronic Structure of Alq3/Reactive Metals Contacts. *Org Electron.* 2:89-95.
30. Segev L, Salomon A, Natan A, Cahen D, & Kronik L (2006) Electronic Structure of Si(111)-bound Alkyl Monolayers: Theory and Experiment. *Phys. Rev. B.* 74:165323.
31. Zhong S, Zhong QJ, Mao HY, Zhang JL, Jin JD & Chen W(2012) The Role of Gap States in the Energy Level Alignment at the Organic-Organic Heterojunction Interfaces. *Phys. Chem. Chem. Phys.* 14:14127-14141.
32. Martijn L, Mauro, Morana., Christoph, J, Brabec., Paul, W, M, Blom (2009) Recombination-Limited Photocurrents in Low Band Gap Polymer/Fullerene Solar Cells. *Adv. Funct. Mater.* (19):1106-1111.
33. Huynh WU, Dittmer JJ, Tecler N, Milliron DJ, & Alivisatos AP (2003) Charge Transport in Hybrid Nanorod-Polymer Composite Photovoltaic Cells. *Phys. Rev. B.* 67:115326.
34. Schillinsky P, Waldauf, C., Brabec, C, J. (2002) Recombination and Loss Analysis in Polythiophene Based Bulk Heterojunction Photodetectors. *App. Phys. Lett.* 81:3885.
35. Taylor JR (1997) *An Introduction to Error Analysis: The Study of Uncertainties in Physical Measurements* (University Science Books, Sausalito, California) 2nd Ed.

## Chapter-5

### Photoresponse of Aromatic Molecules in Molecular Tunnel

#### Junctions: Converting Photons to Charge Carriers

##### 5.1 Introduction:

Organic molecules have found an important place in electronics as organic light-emitting diodes and in molecule-based photovoltaics. These applications are generally not considered molecular junctions because the molecular film is much thicker than the molecular dimensions (typically >100 nm). An understanding of the factors that govern how molecular structure is related to charge transport mechanisms in molecular junctions has been a topic of great interest, stimulated by the goal of designing molecules for specific electronic functions (1-4).

The interaction of light with molecular tunnel junctions is an increasingly popular area of research because of its possible potential applications. Two independent groups, Ward et al. and Liu et al. have demonstrated simultaneous optical and electrical measurements on molecular junctions that provide structural information (5, 6). The generation of photocurrent in molecular junctions has been considered theoretically by Galperin and Nitzan (7) and some experimental measurements of a range of photoeffects have also been previously reported (8-10). However, most of the previous work in this area has been focused on optical methods such as Raman and infrared spectroscopy (11, 12) as characterization tools, and have not considered the direct conversion of photons into current. Chapters 3 and 4 explained that for large- area aliphatic and aromatic molecular tunnel junctions, the photocurrent was dominated by internal photoemission mechanism (IPE) for incident photon energies where molecular absorption is weak (i.e. there is

no light induced excitation of the molecular component) (13). In this chapter, the study of photoeffects is extended to a set of aromatic molecules that absorbs light in the energy regime examined. The large body of research on organic photovoltaic devices (OPVs) deals almost exclusively with absorption in molecular layers, but the molecular layer thicknesses are typically much greater than those in molecular junctions.

The total distance between the conductors and the interfacial barrier heights plays a key role in the charge transport mechanism in molecular junctions. Some similar concepts are involved in OPV approaches, but the much shorter transport distance in molecular junctions has major consequences to the transport mechanism. Because we have kept all other parameters like the type of top contacts (Cu), the thickness of the top contact (Cu 20nm), light intensity, etc., constant, the results in this chapter indicate that at energies where molecular absorption takes place in a completed junction the photocurrent spectrum depends on the nature, type, and thickness of the layers of molecules used in this study. In addition, developing an understanding of photoeffects in molecular junctions also illustrates the possibility of chemically tailoring the energy levels for advanced optoelectronic functions.

## **5.2 Single layer organic photovoltaic devices compared to Carbon molecular junctions:**

The conventional single-layer photovoltaic devices (e.g. ITO/organic/Al) (14) are qualitatively similar to carbon molecular junctions (carbon/molecule/Cu) in that they consist of an organic layer sandwiched between two dissimilar electrodes. In carbon devices a thin layer (2-6 nm) of aromatic molecule is covalently bonded to a carbon substrate using diazonium chemistry(15), whereas for the single layer photovoltaic devices the polymer/organic molecules ( >100 nm thick) are vapour deposited or spin coated onto the substrate. In single-layer photovoltaic devices the difference in the work function between the two contacts creates a built-in potential in the

organic layer which helps to split excitons and separate charges (16-19). For example, a layer of ITO (Indium Tin Oxide) with a high work function of  $-4.8$  eV, and a metal such as Al (aluminum) with a lower work function of  $-4.3$  eV, are often used to fabricate the device. In this single layer photovoltaic cells the electrode/organic interface plays the major role for the photo generation of free charge carriers(20, 21).

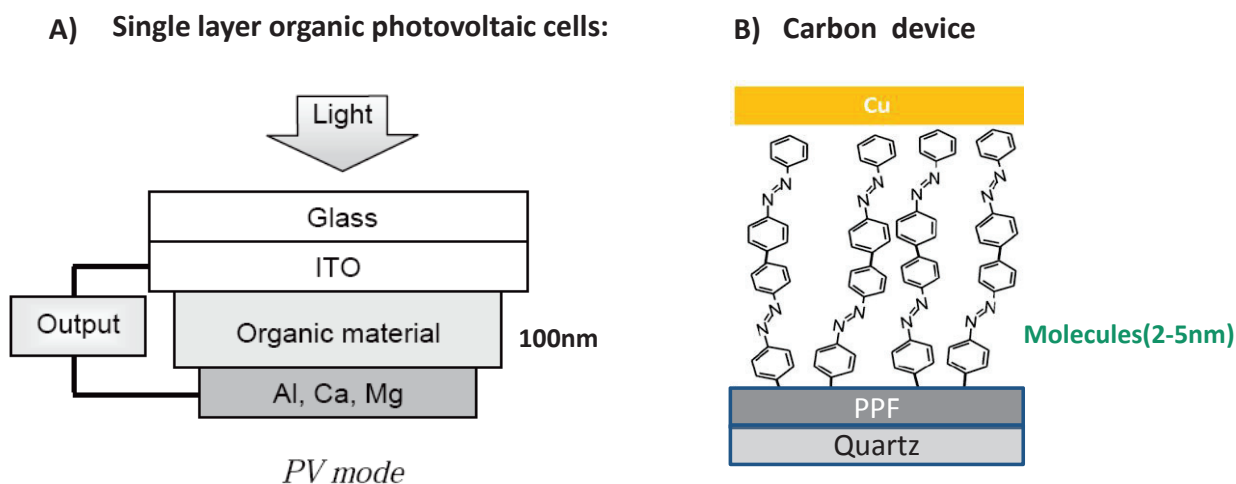


**Figure 5.1:** (A) Single layer photovoltaic cell, in which indium tin oxide (ITO) serves as a transparent high work-function electrode and Al serves as a low work-function electrode (picture adopted from reference(21)). (B) carbon/molecule/Cu device.

Figure 5.1(A) shows the configuration of typical single-layer organic photovoltaic cell compared to the carbon-based molecular junction described in chapters 3 and 4. The photocurrent-generation process in single layer organic/polymer cells has been studied in detail by different groups (22, 23). When these devices are excited using photons, excitons are created in the active organic/polymer layer, which can diffuse in the bulk of the films. Since the work function is different for the two conducting contacts, electrons will flow in the external circuit from the conductor with highest energy (low work function, Al) to that with the lowest energy (high work function, ITO) creating a negative potential at the conductor with high work function (ITO) (21, 24). The excitons created as a result of photon absorption can then diffuse

through the polymer layer to reach the conductor/organic interface to create free charges. The built in electric field pulls electrons in the molecular layer to the positive electrode (Al) and holes to the negative electrode (ITO) (see figure 5.2).

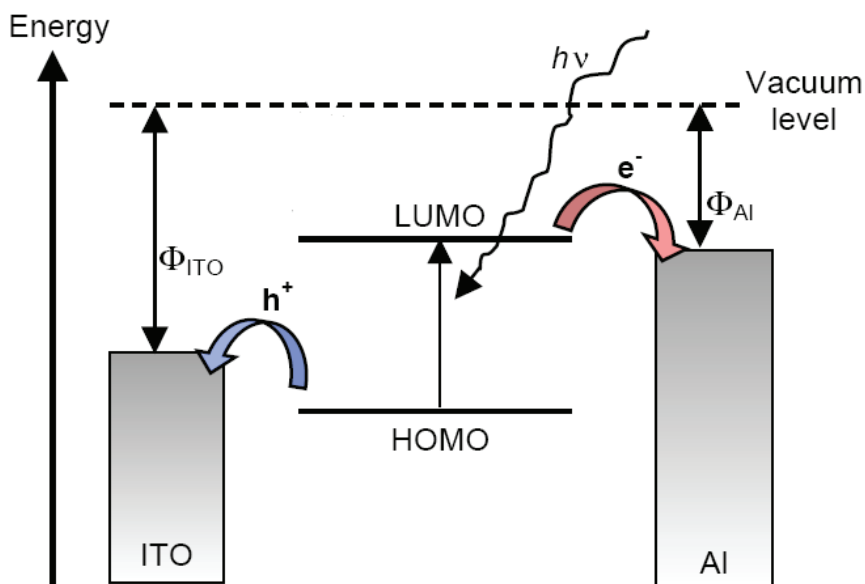


**Figure 5.2:** Single-layer photovoltaic cell, in which indium tin oxide (ITO) serves as a transparent high work-function electrode and Al serves as low work-function electrode. Figure adopted from reference (21).

The quantum and power-conversion efficiencies of single-layer photovoltaic devices are very low due to the fact that the excitons created are charge-neutral. They do not drift in an electric field to reach an electrode to separate into independent charges and more often the electron recombines with the hole instead of being collected by the electrodes (24). The single-layer photovoltaic device is usually thick enough to absorb most of the light and create excitons, however most of the excitons created cannot diffuse across the thick film to find the interface. The built in electric field is not sufficient to pull the excitons to the organic/electrode interface to generate free charges (20). The length over which excitons can propagate prior to the decay of the exciton population to  $1/e$  (roughly 35%) of its initial value is the exciton diffusion length. The reported values for exciton diffusion length in organic/polymers varies from 6-10 nm (20,

22, 23). For organic photovoltaic devices there is a trade-off involved between thin layers for good exciton diffusion and thick layers for maximum light absorption, charge mobility etc.

### **5.3 Experimental section:**

The schematic of the junction structure used in this study was given in chapter 4 (figure 4.3). The details regarding the junction fabrication with the diagram of optical and electronic apparatus was also explained in chapter 3. Briefly, a small band ( $\Delta\lambda=13$  nm) of light from the Xe arc source passes through an optical chopper before incidence onto the junction. Dual-phase sensitive LIA detection is used to measure the resulting photocurrent, which is converted to yield by calibration of the incident power. Using this apparatus, the photocurrent response carbon/molecule/Cu (20 nm) was measured under ambient conditions at room temperature.

The fabrication of molecular junctions has been described in numerous past reports(13, 25-29), and utilizes the electrochemical reduction of diazonium reagents on flat carbon surfaces(30) and vapour deposition of metallic(25) or carbon(31) top contacts. Polished fused-quartz substrates are used as a support in order to insure no stray photocurrents are generated from a silicon substrate.

### **5.4 Results and discussion:**

In chapter 4 we concluded that two different mechanisms namely internal photoemission (IPE) and molecular absorption (MA) are responsible for generating photocurrent in molecular junctions, and they can be distinguished by the site of optical absorption. To understand the mechanism(s) of photocurrent generation in carbon/molecule/copper junctions in an energy region where excitation of molecules takes place, we measured both the chemisorbed (chapter 3, figure 3.34) and solution spectra (chapter 3, figure 3.35) of six different aromatic molecules used

in this study. It is important to note that IPE is operative to some extent in all cases, although the yield for this process is small compared to the MA process for AB and NAB for most of the spectral range examined.

#### **5.4.1 IPE to molecular absorption(MA) mechanism:**

Figure 5.3(A) shows the overlaid photocurrent spectra of AQ (green) and C12 (black) molecular junctions. A change in photocurrent sign was observed for AQ and C12 junctions at 2.8 eV and 3.0 eV respectively. The shapes of the photocurrent spectrum of AQ and C12 junctions look very similar but their absorption spectra are quite different (see figure 5.3B). A detailed explanation regarding the change in sign for C12 junction was given in chapter 4, section 4.3.1. For junctions containing AQ molecules, one possible explanation for the change in sign is that when the molecule does not absorb incident light ( $<3$  eV) IPE is the main mechanism contributing to the photocurrent. A positive photocurrent for AQ junction at low energy indicates that its OSO mediated tunneling since it is closer in energy to the contact Fermi level, similar to the case of alkanes at low energies. At higher energies the photocurrent generation mechanism for the AQ junction is quite different from that of C12 junction. For AQ junctions at higher energies ( $>3$  eV) when the molecule starts absorbing a secondary photocurrent generating mechanism starts contributing and then dominates the process. Whereas for C12 junctions, even at high energies molecular absorption is absent and IPE remains the major mechanism contributing to the photocurrent. Negative photocurrent at high energies for the C12 junction indicates that its USO mediate transport (for more explanation see chapter 4, section 4.3.3).

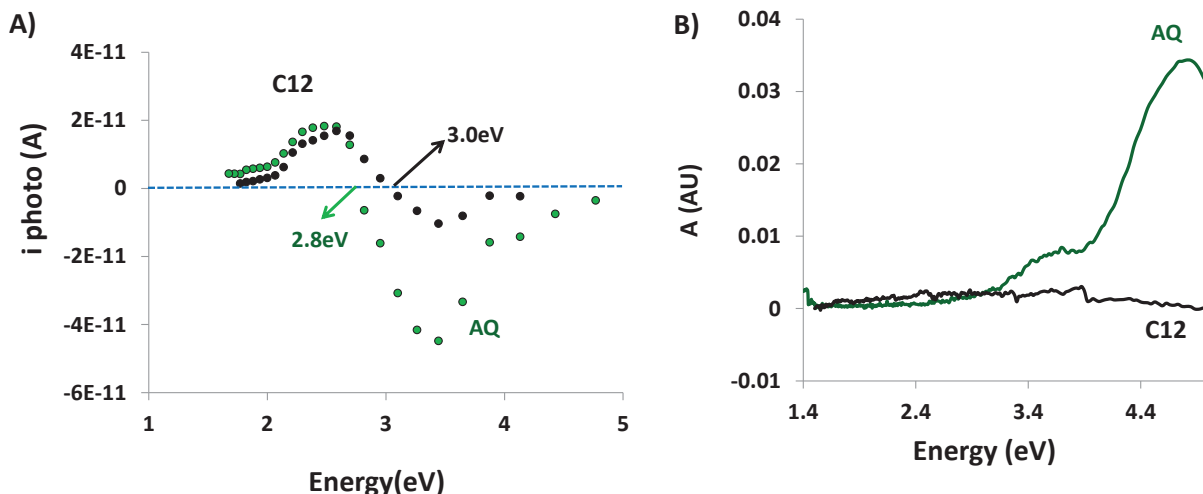


**Figure 5.3:** (A) Overlay of photocurrent spectrum of AQ (green) and C12 (Black) junctions (B) Overlay of absorption spectrum of AQ (green) and C12 (black) molecules.

To understand the molecular absorption process in detail we overlaid the photocurrent and absorption spectra as functions of energy for all the molecules used in this study. The results are given in chapter 4, figure 4.11 and summarized in table 4.1. For BrP & AQ the photocurrent sign becomes negative at the energy region where optical absorption of the molecules takes place 3.8 eV for BrP and 2.7 for AQ respectively. These results indicate that the change in photocurrent sign at higher energies might be due to the light-induced excitation of the molecular components in the junction. For NAB and AB, molecular absorption takes place even at low energies, and the photocurrent sign remains negative throughout the spectral range examined. All these observations add to our assumption that when light induced excitation of the molecules take place negative photocurrents result.

As shown in table 4.1(chapter 4), the optical-absorption edge is correlated with the onset of the negative photocurrent. In general, the optical-absorption edge is  $\sim 0.2$  eV below the onset of the negative photocurrent for all the aromatic molecules, although a precise determination of the

onset of this regime is hindered somewhat by the convolution of IPE and molecular-absorption photocurrent simultaneously contributing to photocurrent over this portion of the spectra.

As has been discussed previously(32), the generation of free carriers from excitons following absorption of light requires a total energy ( $E_t$ ) that is composed of the energy required for the optical transition ( $E_{opt}$ ) and the binding energy ( $E_{xb}$ ) resulting from the creation of a Coulombic attraction between the excited negative electron and the hole that is left behind such that

$$E_t = E_{xb} + E_{opt} \quad (\text{eqn 5.1})$$

equation (5.1) indicates that  $E_t$  cannot be any smaller than the onset energy for optical absorption. This provides one indication that the OSO-USO gap of a molecular junction determines the onset of molecular-absorption photocurrent, and that the IPE current can add to the photocurrent at lower energies that are still larger than the interfacial transport barrier ( $\phi_{barr}$ ). We have seen that the offset between the system orbital energies and  $E_f$  defines this barrier in terms of the junction electronic properties (i.e. the tunneling barrier height is  $\phi_{barr}$ ). However, we cannot correlate the optical-absorption event with what drives interfacial charge transport driven by voltage, as these processes may involve different states.

If one considers our previous measurements (see chapter 2), where hole-tunneling barriers were observed to be pinned at  $\sim 1.3$  eV, then a calculation of the electron-tunneling barrier using the optical onset results in very low values for the electron tunneling barrier if we assume that the optical and transport gaps are directly related. For example, a molecular junction containing NAB would have a calculated electron-tunneling barrier of  $\sim 0.5$  eV given that a hole -tunneling barrier of 1.3 eV was measured and the optical onset is  $\sim 1.8$  eV. However, we do not observe conductance that is consistent with these observations. Stated another way, the electronic conductance of molecular junctions containing a variety of aromatic molecules does not correlate

in any obvious way to the measured optical gaps. On the other hand, the optoelectronic properties do show a molecule-dependent photocurrent that correlates with the measured optical gap. These facts indicate that while the electronic gap may be related in some way to the optical gap, it is not a direct relationship. Instead, the electronic gap appears to be larger than the optical gap, possibly due to the fact that the voltage-driven tunneling process requires wave function overlap and is mediated purely by electronic states. The optical process does not involve wave function overlap, but rather involves exciton generation based on optically active states. Some of these optically active states may reside within the electronic OSO-USO gap, but in effect are not active in determining the electronic tunnel barrier.

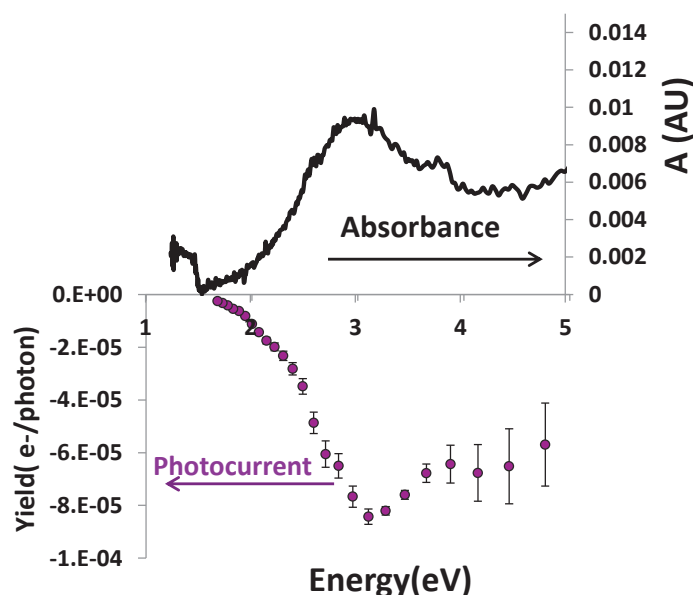


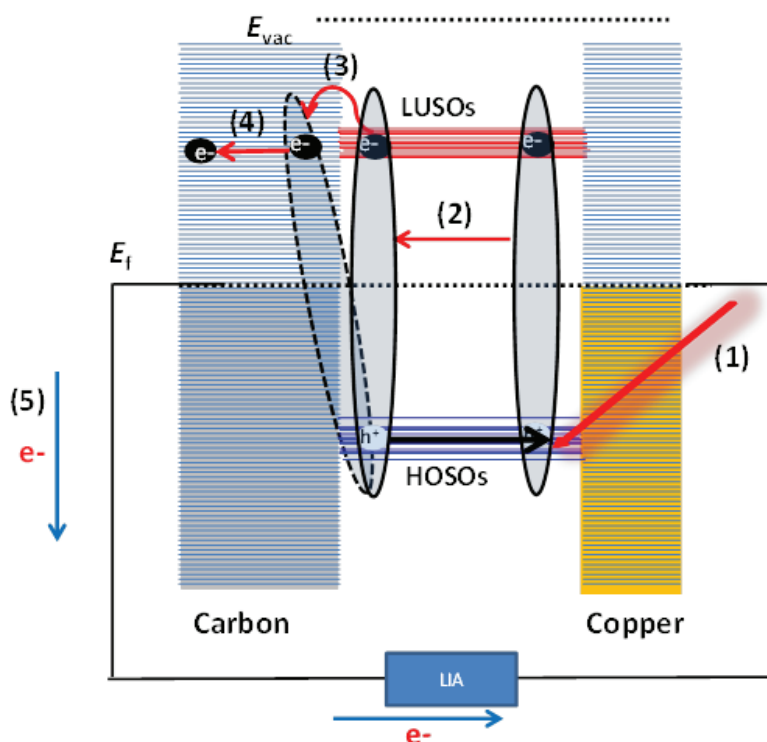
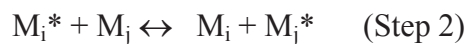
**Figure 5.4:** An overlay of photocurrent yield and absorption spectra for DAB junctions; black line indicates the optical absorption spectra of the molecular layer corrected for PPF absorption and the coloured line indicates the measured photocurrent spectrum of a particular molecule.

To further strengthen our hypothesis of a negative photocurrent response correlates with the spectral region where the molecular absorption takes place, we chose an additional aromatic molecule Diaminobenzidine (DAB) whose molecular absorption starts at low energy (see figure 5.4) similar to that of AB and NAB molecule. From the previous results shown in figure 4.11, we

expect a negative photocurrent for DAB junction throughout the spectral range examined. The photocurrent obtained for DAB junction is shown in figure 5.4 and supports our hypothesis. By examining the photocurrent results obtained from five different aromatic molecules (AQ, BrP, AB, NAB, and DAB), we conclude that for the energy region where optical absorption by the molecules takes place correlates with a negative photocurrent.

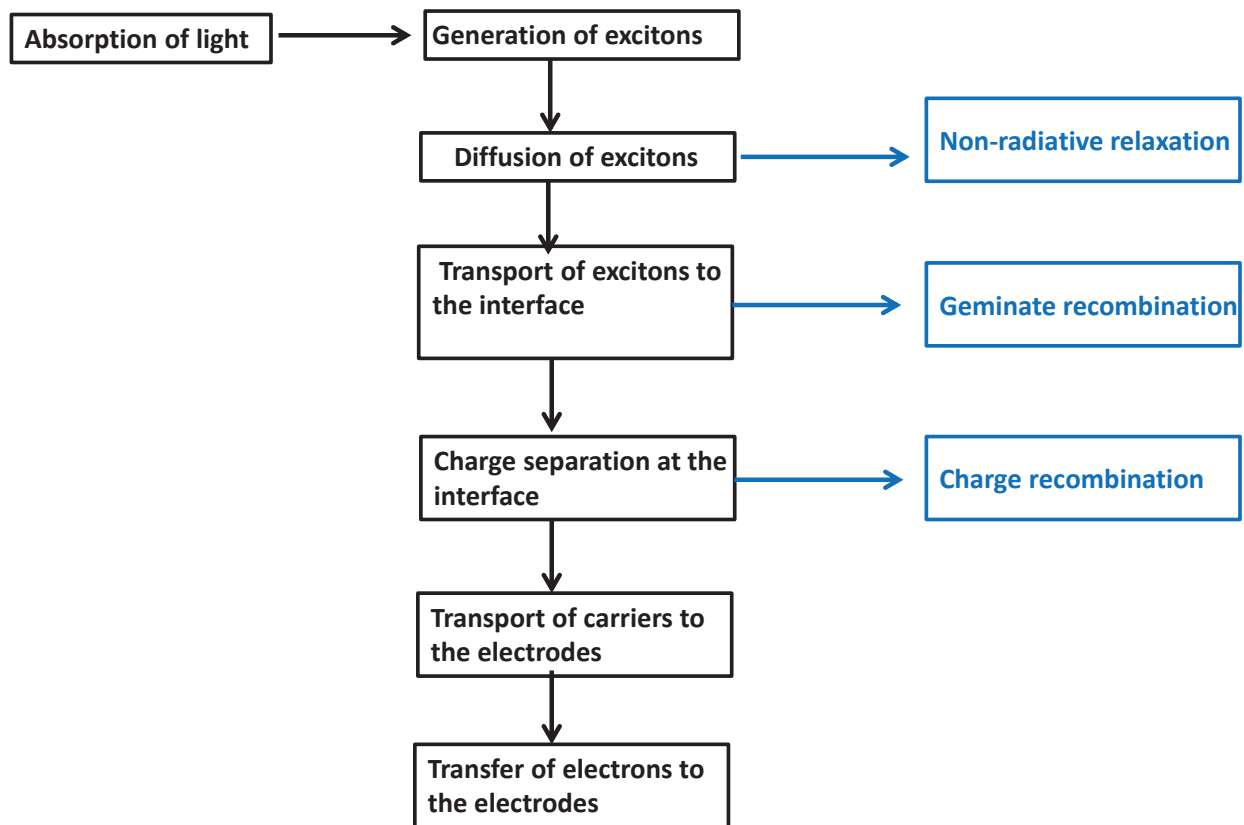
## 5.5 Proposed Model:

Figure 5.5 shows the schematic representation of one of the possible process leading to photocurrent generation in the molecular-absorption regime. This mechanism is separated into five parts for convenience: (1) the optical excitation occurs in the molecular layer from a distribution of occupied system orbitals (OSOs) to an unoccupied system orbital (USOs) which includes both the molecule and substrate. The optically-generated exciton is a bound pair. (2) The generated excitons interact with the neighbouring molecule by transferring its extra energy and returning to the ground state. For efficient charge transfer to occur there should be direct electronic coupling between the molecules and the bottom electrode meaning that the energy absorbed by a molecule not intimately coupled or adjacent to the substrate by direct orbital overlap must be transferred through the medium to the interface to contribute to the photocurrent (20). This energy-transfer process where no net transport of charge or mass occurs is called exciton diffusion. (3) Next step involves the formation of charge transfer (CT) exciton or the geminate exciton. The thermodynamic requirements to form the geminate CT state species at the electrode-molecule interface can be understood by considering the change in enthalpy for the photo-induced charge transfer reaction. Previous studies show that the coulombic stabilization of the CT state is roughly 10 times greater than  $kT$  at room temperature (20). The three steps described above can be represented by equations the given below.



**Figure 5.5:** Proposed idealized schematic representation leading to photocurrent generation and different steps involved with the process: (1) exciton generation (2) exciton diffusion (3) charge transfer state generation (4) charge separation (5) charge collection.

Next, (4) charge separation can be accomplished as long as the excitation energy is sufficient to overcome  $E_{xb}$ . Here, we have now generated an unbound exciton. The last step (5) is the charge collection step, where the electron acceptor states in the carbon substrates accept the electron, followed by refilling of the hole from an electron in the Cu metal. The result is a net flow of current, measured as negative at the PPF (see figure 5.5).



**Figure 5.6:** The steps and loss mechanisms of converting light power into electric power. Light which is not converted to electricity is converted to heat.

In principle, the likelihood of excitation from an OSO to carbon is same as that to Cu substrate. However, our results indicate that excitation of all the aromatic molecular layers studied here occurs exclusively into carbon substrate making it more negative. This observation may be accounted for in several ways, but here we consider three factors: electronic coupling, a built-in field, and excitation profiles. First, the physical location of the OSO and USO states may be distributed across the molecule and one or both contacts in such a way that the main electron acceptor/donor states span the carbon/molecule interface. In effect, the extent of delocalization of the donor and acceptor states across the molecular layer and each electrode reflects the way in which the molecular layer interacts with each contact. Second, a built-in field, due to the

different nature of the two contact materials may favour electron transport toward carbon. Third, the excitation profile through the molecule may result in more direct exciton formation near the carbon substrate, either because the optically-active states reside at this interface or because the transmission and reflection of light through the material layers in the junction results in the enhanced possibility of absorption near the carbon/molecule interface. Finally, these effects are not mutually exclusive, and all of them may act in concert or in opposition with each other.

The molecular layer here is thus envisioned as the electron donor, with a distribution of empty states in the carbon substrate as the electron acceptor. The molecular absorption mechanism proposed in Figure 5.5 essentially involves optical excitation of the molecule as an initial step. After charge separation, it is important to note that as long as refilling from the Cu metal is rapid relative to nuclear motion (i.e., if the Born-Oppenheimer approximation applies), then chemical oxidation will not result from this process. This is an important point, as it will indicate that as long as this condition holds, the potential for parasitic side reactions resulting in decomposition of the molecular layer is small. This is in contrast to studies that have shown that the use of low band-gap organics in solar cells, for example, suffer from stability problems due to such reactions. Using a nanoscale charge-transport junction may therefore add value in the design of organic photovoltaics.

## **5.6 Thickness Dependence:**

In chapter 4, section 4.5.5 we showed that a diagnostic test for the MA mechanism is the variation of the photocurrent with the thickness of the molecular layer. Any mechanism involving optical absorption by the molecular layer is expected to increase linearly with molecular layer thickness. The IPE mechanism should show a weak dependence on the thickness of the molecular layer, at least up to the scattering length of the electrons in the molecular layer.

The photocurrent yield vs. thickness plot of Ferrocene (Fc) and NDI junctions (2-5nm) was shown in chapter 4, figure 4.16. Here we extend our investigation to junctions of NDI and Fc above 5nm, as shown in figure 5.7(A) and 5.7(B). Previously obtained 2-5nm thickness data is included with these results for comparison.

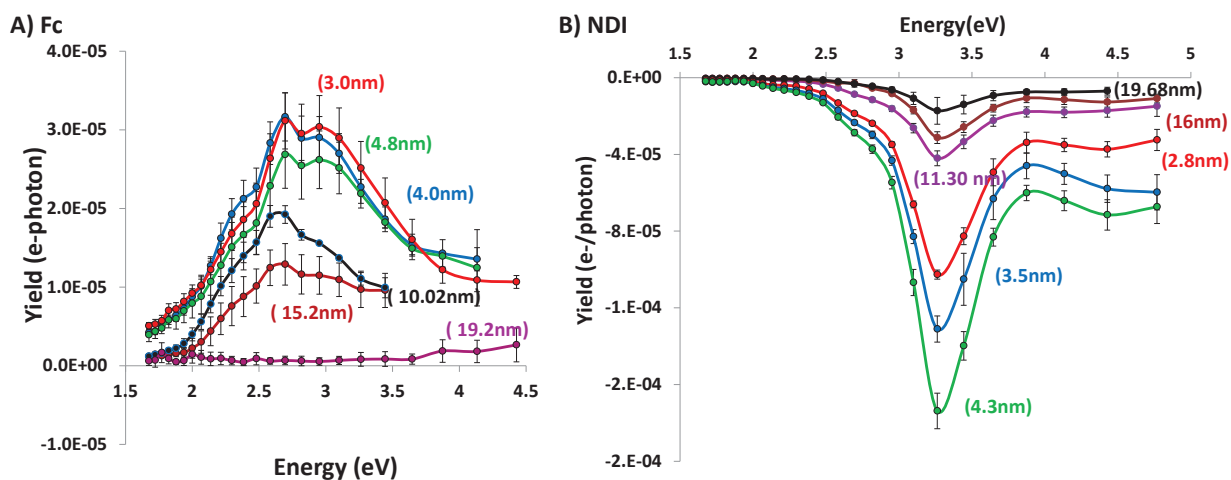


**Figure 5.7:** Photocurrent yield spectra for increasing molecular layer thickness, as indicated. (A) Fc (B) NDI.

For Fc junctions less than 5nm thick in the IPE regime (i.e., at energies less than 3eV) the photocurrent yield is independent of molecular layer thickness. Once the thickness of the molecular layer is increased above 5nm the photocurrent yield decreases dramatically. At 20nm molecular layer thickness, the observed photocurrent is so low that it becomes difficult to differentiate it from the background current. Increasing the molecular layer thickness increases the distance for the electrons to travel through the molecular layer to reach the other electrode. After travelling some distance through the molecule the electron will lose its energy and would not be able to reach other electrode i.e., a detailed analysis of photocurrent vs. thickness in the IPE regime might give us some indication about the scattering length of electrons through the molecule. A similar response in photocurrent was obtained for NDI junctions in the IPE regime (less than 3eV), when the thickness was varied from 2.5-20 nm. Photocurrent yield vs. thickness

for NDI and Fc junctions at the IPE region (2.0eV) and molecular absorption region (3.2eV) is shown in figure 5.8 (A) and 5.8(B).

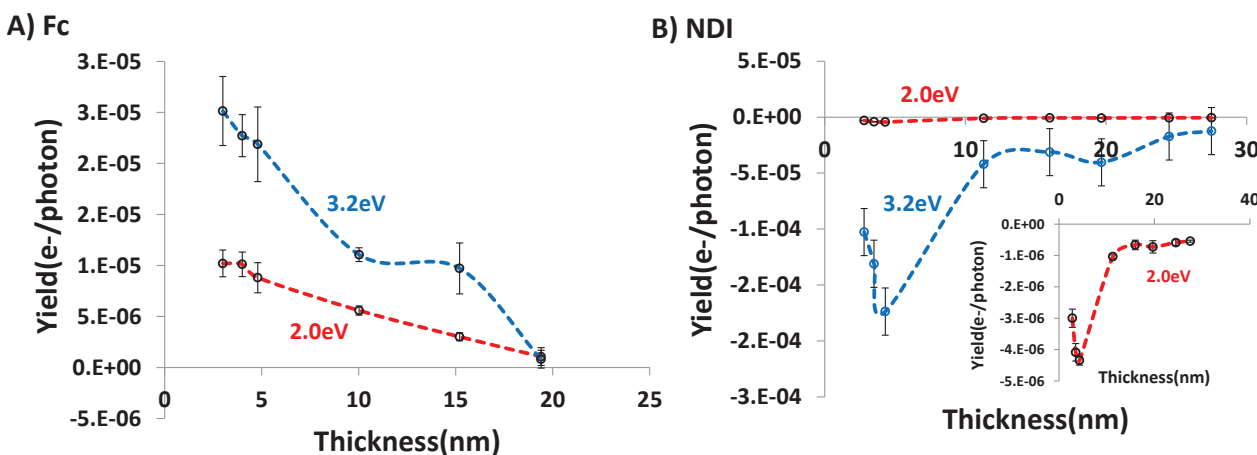


**Figure 5.8:** photocurrent yield vs. thickness plots of (A) Ferrocene (B) NDI at two different photon energies. The Inset in figure B shows the enlarged plot of NDI at 2.0 eV.

By increasing the thickness of the molecules in the energy regime where MA takes place we are increasing the number of absorbing units thereby creating more excitons. Therefore the photocurrent yield is expected to increase with increasing thickness of the molecular layer. Figure 5.8(B) shows that for the NDI molecule, the photocurrent yield decreases after certain thickness (6 nm) even in the energy region where molecular absorption takes place (3.2eV). This decrease in photocurrent yield might possible be due to the fact that with increase in molecular layer thickness we are increasing the probability of creating charged exciton state at both the electrode/molecule interface. Now the contribution of free carriers generated from the molecule/copper interface is no longer negligible and it may act in opposition with the PPF/NDI interface, thus reducing the photocurrent yield. Photocurrent yield vs. thickness behaviour in the MA regime might also give some indication about the exciton diffusion length, i.e., by increasing the molecular layer thickness we are not only increasing the absorbing units but also increasing the distance for the exciton to diffuse through the molecular layers to reach the metal/molecule

interface to disassociate into free charges (see figure 5.5). Since the bound exciton has to diffuse through larger distances to reach the interface, the probability of secondary effects such as non-radiative relaxation and geminate recombination to happen is increased. These secondary events can also play a part in reducing the photocurrent yield for increasing thickness in the MA regime.

Analyzing the observations from figure 5.7 and 5.8 together, we can conclude that carbon/molecule/Cu junctions can be used as a platform to determine the scattering length of electrons at the IPE regime ( $< 2.8\text{eV}$  for NDI and Fc) i.e., it might be able to determine how far the photoelectron can travel before scattering within the molecular junction. A detailed investigation in the energy region where MA takes place ( $> 3.0\text{eV}$  for NDI), might indicate the diffusion decay length of the excitons or possibly a change in photocurrent generation mechanism.

## **5.7 Changing the top contact:**

In single-layer organic photovoltaic devices, the difference in work function of the contact electrodes plays an important role for the generation of free charges at the electrode/organic interface. Here, the work function of carbon/molecule/Cu device is compared with that of the ITO/organic layer/Al device to investigate the role played by the built in field in carbon devices(20, 24). The reported work-function values for ITO vary between 4.6 to 5.5eV depending on the preparation conditions (time exposed to ozone gas etc.)(33) and for the Al it is 4.3eV. Considering the work function of ITO as 5.0eV (average of the reported values) and Al as 4.3 (22), a work function difference of 0.7eV is predicted which can create a built-in potential within the system (see figure 5.9A). The difference in work function for Carbon/molecule/Cu devices is 0.2eV (carbon (4.6eV) and copper (4.8eV) (see figure 5.9B), less than that of the ITO/polymer/Al system. Thus the role of built-in potential for separating the bound excitons in

carbon/molecule/Cu devices is expected to be less efficient. In addition, other factors like the electronic coupling between the molecules and the electrode also play a major role for charge separation.

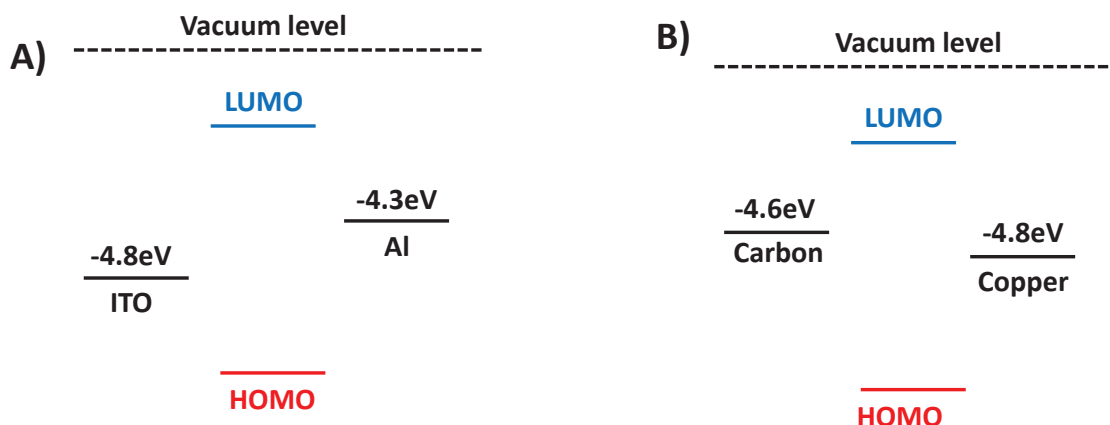


**Figure 5.9:** (A) Schematic energy-level representation for ITO/polymer/Al devices (B) Schematic energy-level representation for Carbon/molecule/copper devices. HOMO and LUMO levels are generic, i.e. not for a particular molecular structure.

In order to understand the role of built-in field (due to work function difference) for charge separation in carbon devices, we changed the top contact from copper to vapour deposited carbon (e-carbon) i.e., PPF(Carbon)/molecules/carbon(10nm)/Copper(10nm) devices were made instead of the previously studied PPF(Carbon)/molecules/Copper(20nm) junctions. Now the organic molecules are oriented between two carbon conductors (i.e., similar electrodes), therefore the difference in work function is predicted to be smaller. This change not only should provide insight into the role of the work function in free-charge generation but also about the possibility of a high built-in field of unknown origin due to dipole or trapped charges at the interface(23). If the difference in work function is playing the major role for charge separation one would expect small or negligible photocurrents from devices having carbon as both the substrate and top contact.

Previous studies have shown that metal-free all carbon molecular electronic junctions can be fabricated by orienting a layer of organic molecules between two carbon conductors with high yield and reproducibility(31). The advantage of using all-carbon devices is that it can withstand much higher voltages and current densities than Cu-containing junctions, which fail upon oxidation and/or electromigration of the copper. Carbon can resist electromigration or penetration into the molecular layer and provides enhanced stability.

### **5.7.1 Comparison of photocurrent spectrum with copper and carbon top contact:**

Keeping experimental procedures the same as described for previous experiments, photocurrent spectra for large-area aromatic molecular tunnel junctions with partially transparent carbon (10nm)/copper (10nm) top contacts were measured. Figure 5.10 shows the overlay of photocurrent yield spectra obtained from PPF(carbon)/AB(3.0nm)/carbon(10nm)/cu(10nm) and PPF(carbon)/AB(3.0nm)/Cu(20nm) devices. The sign of the photocurrent spectrum for both these devices remains the same (negative), indicating a similar mechanism of photocurrent generation. The device with carbon as top contact shows approximately 50% less yield compared to copper (see figure 5.10). Carbon being a good absorber and a bad transmitter of light, the difference in photocurrent yield can be attributed to the difference in percentage of light reaching the surface of molecules after undergoing transmission and reflection through different material layers.

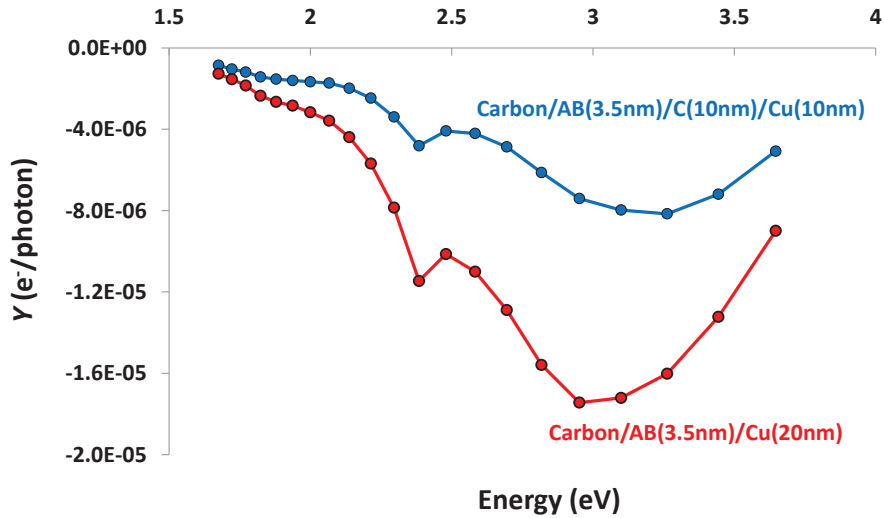


**Figure 5.10:** Comparison of photocurrent yield spectra of AB junctions with similar molecular layer thickness but different top contact. (Cu (20nm, red curve) and C(10nm)/Cu(10nm), blue curve).

### 5.7.2 Varying the thickness of carbon top contact:

Figure 5.10 shows the photocurrent yield spectra obtained for junctions with varying thickness of the carbon top contact. By keeping the overall thickness of the top contact constant (20nm), the thickness of carbon with respect to copper was varied. The experimental results show that by increasing the thickness of carbon top contact, the photocurrent yield decreases. Even though the photocurrent yield of devices with carbon top contact is less(see figure 5.10) compared to that of copper, it adds additional advantages of making highly reproducible thick junctions with very good yield and offers great stability to bias conditions(31).

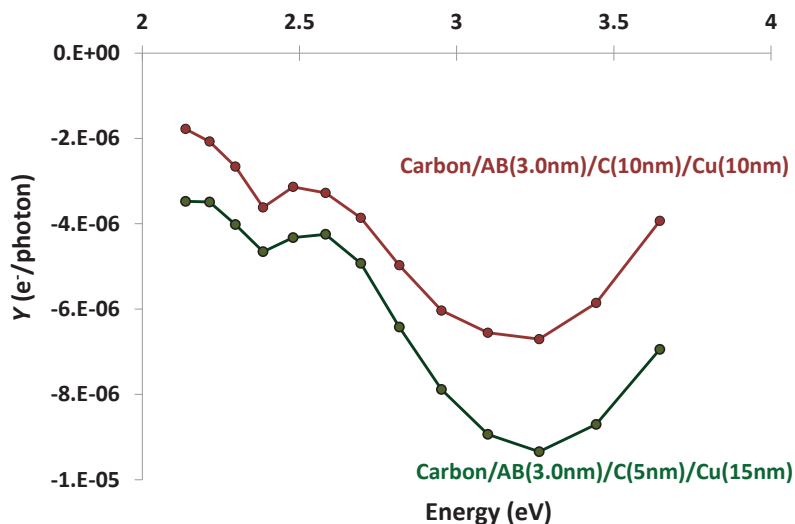


**Figure 5.11:** Comparison of photocurrent yield spectra of AB junctions with similar molecular layer thickness but different carbon top contact thickness. (C(10nm)/Cu(10nm), brown curve and C(5nm)/Cu(15nm), green curve).

### 5.7.3 Thickness study on BTB molecules using carbon top contacts:

The electronic behaviour of carbon/BTB/carbon/Cu junctions, where BTB is (bis-thienyl benzene (carbon/BTB/carbon/copper) junctions, with thickness range varying from 3-22nm has been previously reported with high yield and reproducibility (33). BTB junctions with similar layer thickness were re-fabricated on quartz using the procedure explained elsewhere (33) and were used for photocurrent experiments. Figure 5.12 (A) shows the results obtained from BTB junctions with varying thickness using vapour deposited carbon as top contact. Similar to the results obtained from NDI junctions (see figure 5.8), in the energy region where MA takes place ( $>2.0\text{eV}$ ) the photocurrent yield for BTB junctions increases with BTB film thickness up to 7nm and then gradually decreases. Varying the film thickness of NDI junctions (3-20nm) with Cu top contact, the photocurrent sign always remained negative (see figure 5.7). BTB junction shows a change in photocurrent sign at  $\sim 16\text{nm}$ , indicating a change in photocurrent generation mechanism.

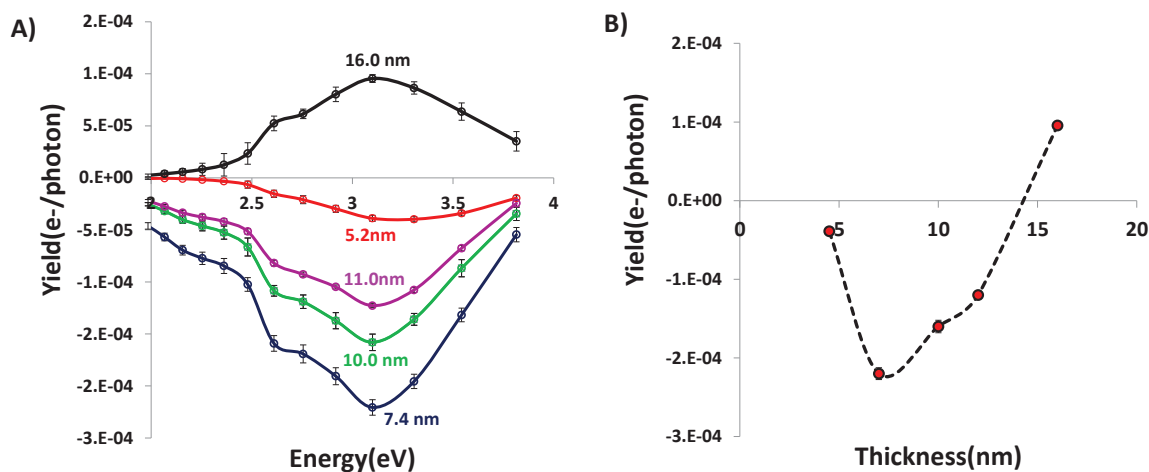


**Figure 5.12:** (A) Overlay of photocurrent yield spectra of BTB junctions with different thickness using carbon as top contact (B) Yield vs. thickness data for BTB junctions at 3.2 eV.

Referring back to the photocurrent generation mechanism in section 5.5, using vapour deposited carbon as top contact instead of Cu certain changes in photocurrent behaviour with thickness was observed. The fact that both the substrate and the top contact are covalent conductors there always exist a competition between the two interfaces to form free separate charges from charge transfer exciton which opposes each other. This might also explain lower yield for devices with carbon as top contact. The results shown in figure 5.12 shows that the photocurrent yield increases with film layer thickness up to 7nm, but when the thickness of the molecular layer is increased further (>7nm) the photocurrent yield starts to drop down and at higher thickness(16nm) the photocurrent sign become positive. One of the possible explanation is that at thickness less than 7nm, PPF(carbon)/molecule interface is dominant for charge separation giving a negative photocurrent( making PPF more negative). This might be due to the initial strong (C-C) covalent bond made between the molecule and the PPF (carbon) surface. But as the thickness of the molecular layer increases (>7nm), the molecule/e-carbon interface becomes more significant for charge separation than PPF (carbon)/molecule interface. Direct electronic coupling being the major criteria for forming charge transfer exciton, the results in

figure 5.12 indicates the direct coupling distance between the molecule and the initial PPF substrate.

## **5.8 Conclusion:**

This result presented in this chapter demonstrates that the IPE photocurrent spectrum of aromatic tunnel junctions can be augmented by a secondary photoevent where the light-induced excitation of the molecular component takes place. It is likely that the coupling of electronic states between the molecule and electrode (i.e., molecule-electrode hybrid orbitals) are involved in photoconversion. Thus, many of the optically-active transitions readily decay into conducting states in the contact, while the electronic states involved in tunneling are governed by a different set of parameters. This chapter also shows that reliable photocurrent measurements can be obtained from devices with vapour deposited carbon as the top contact. By advancing our understanding of the absorption-mediated photocurrent in these devices, we may find ways of improving the electronically active coupling of states. Such insights into the devices studied here may also be of interest in the continued quest to improve the efficiency of a variety of optically-active devices, including organic photovoltaic and optical detectors.

## 5.9 Future work:

Potential extensions of photocurrent measurements to more complex structures of interest to the photonic properties of molecular junctions include at least two approaches, described separately as follows:

### Photocurrent experiments on bilayer junctions:

It has been previously(34) demonstrated that bilayer molecular junctions can be fabricated using alkyne/azide “click” reaction on a carbon substrate(see figure 5.13), followed by deposition of a carbon top contact in a crossbar configuration. Bilayer junctions will be a good candidate for photocurrent experiments due to the fact that using click reaction on an alkyne layer formed by diazonium reduction will permit incorporation of a range of molecules into the resulting bilayer. Figure 5.13 shows different possible pathways for the formation of molecular bilayers.

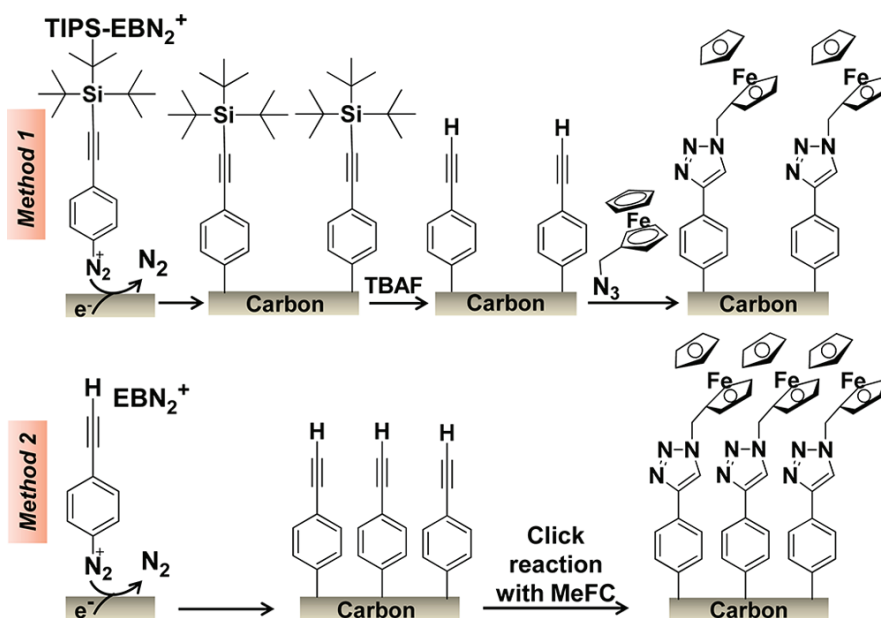


**Figure 5.13:** Different modification pathways for formation of molecular bilayers via click chemistry. Picture adopted from (34).

Bilayer molecular junctions prepared using “click” chemistry resembles two-layer photovoltaic devices (see figure 5.14). The photovoltaic properties of two-layer photovoltaic cells are significantly different from those of conventional single-layer organic photovoltaic cells (see figure 5.1). The two-layer organic photovoltaic cell differs from conventional single-layer cells in that the interface between two organic layers is crucial in determining its photovoltaic properties. The interface region is primarily responsible for the photo generation of charges (23). Whereas for single layer photovoltaic cell it was the electrode-organic interface that played the major role for the photo generation of charges (see figure 5.15). The magnitude and the polarity in the two-layer photovoltaic system show a stronger dependence on the nature of the organic-organic interface than on that of the electrode-organic interfaces. The electrodes in two-layer photovoltaic device simply provide ohmic contacts to the organic layers (23).

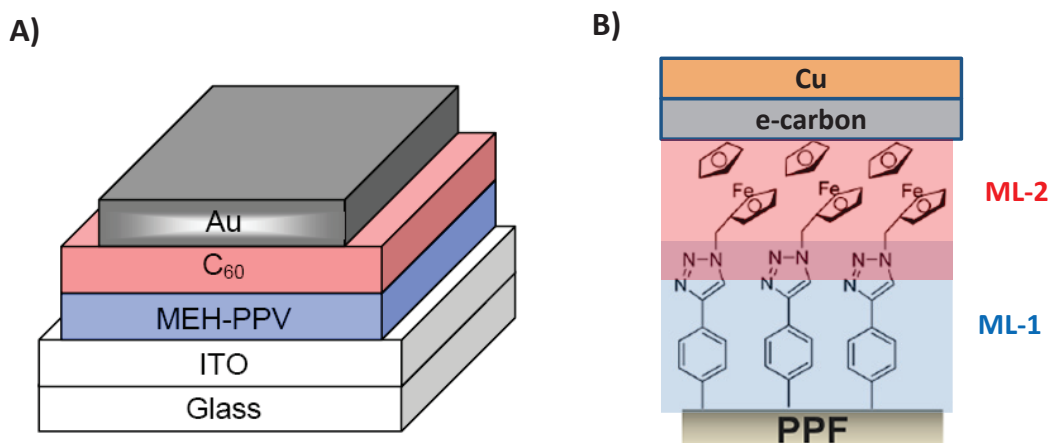


**Figure 5.14:** (A) two-layer photovoltaic cell. The electron accepting C<sub>60</sub>-layer contacts the Au electrode, while the electron donating MEH-PPV layer contacts the ITO electrode. (B) Bilayer molecular junction resembling the two-layer photovoltaic cell. Picture adopted from (21).

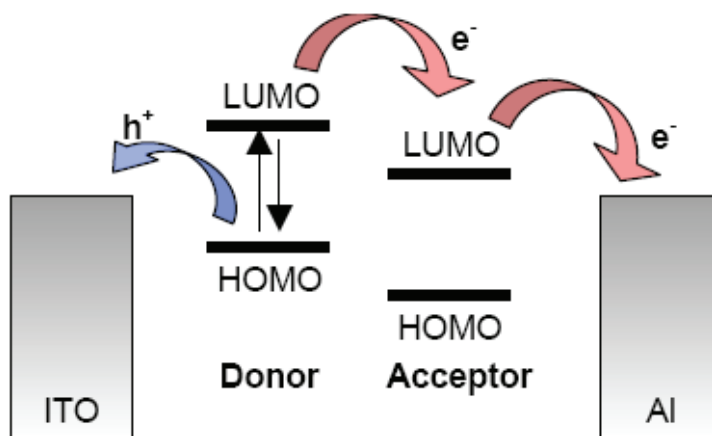


**Figure 5.15:** Exciton dissociation at the donor-acceptor interface. The electron goes to the acceptor while hole stays in the donor.

### **Molecular Photovoltaic device based on ballistic electron transport:**

In conventional solid state solar cells the electron hole pairs are created by light absorption in a semiconductor. Here a multilayer photovoltaic device structure in which the photon absorption occurs in aromatic molecules attached covalently on the surface of ultrathin metal-semiconductor junction is proposed. Photoexcited electrons are transferred to the metal and travel ballistically to-and over-the barrier, providing the photocurrent output. Unlike conventional cells, the semiconductor in this device serves only for majority charge transport and separations. The molecules attached covalently on the surface give high stability to these devices. This approach to photovoltaic energy conversion might provide the basis for high stability, low-cost solar cells using a variety of materials.

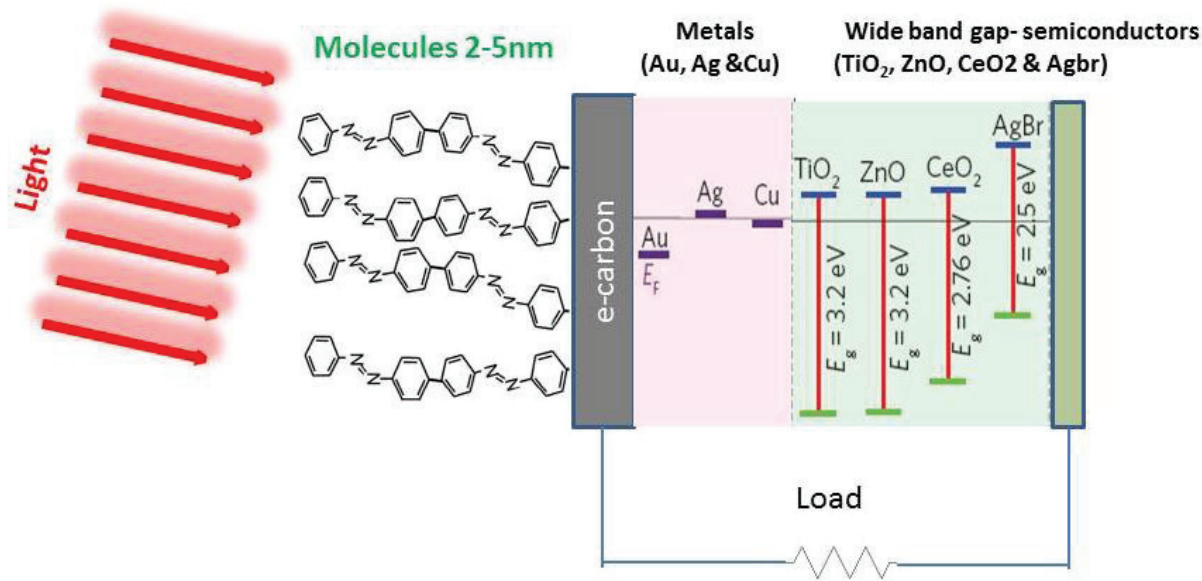


**Figure 5.16:** Schematic representation of the molecular photovoltaic device.

The bulk semiconductor is not utilized for photon absorption; thus the band gap and semiconductor thickness constraints are largely removed. The physical and electronic couplings of the chromophores to the metal conduction levels might play a crucial role to the performance of the device. The relative HOMO-LUMO energy levels in the molecules, the conductor Fermi level, the barrier height and the position of the semiconductor band edges are the points to be considered in choosing the materials for the device.

## 5.10 References:

1. Metzger R (2007) Unimolecular Electronics. *Nano and Molecular Electronics Handbook*, Nano and Microengineering Series, (CRC Press).
2. Carroll RL & Gorman CB (2002) The Genesis of Molecular Electronics. *Angew. Chem. Int. Ed.* 41:4378-4400.
3. Fan F-RF, Yang J, Cai L, Price DW, Dirk SM, Kosynkin DV, Yao Y, Rawlett AM, Tour JM & Bard AJ (2002) Charge Transport through Self-Assembled Monolayers of Compounds of Interest in Molecular Electronics. *J. Chem. Soc.* 124(19):5550-5560.
4. Tour JM (2000) Molecular Electronics, Synthesis and Testing of Components. *Acc. Chem. Res.* 33:791-804.
5. Ward DR, Halas NJ, Ciszek JW, Tour JM, Wu Y, Norlander P & Natelson D(2008) Simultaneous Measurements of Electronic Conduction and Raman Response in Molecular Junctions. *Nano Lett.* 8(3):919-924.
6. Liu Z, Ding SY, Chen ZB, wang X, Tian JH, Anema JR, Zhou XS, Wu DY, Mao BW, Xu X, Ren B & Tian QZ (2011) Revealing the Molecular Structure of Single-Molecule Junctions in Different Conductance States by Fishing-Mode Tip-Enhanced Raman Spectroscopy. *Nat. Commun.* 2:305.
7. Galperin M & Nitzan A (2012) Molecular Optoelectronics: The Interactions of Molecular Conduction Junctions with Light. *Phys. Chem. Chem. Phys.* 14:9421-9438.
8. Battacharyya S, Kibel A, Kodis G, Lidell PA, Gervaldo M, Gust D & Lindsay S (2011) Optical Modulation of Molecular Conductance. *Nano Lett.* 11:2709-2714.

9. Mangold MA, Calame M, Mayor M, & Holleitner AW (2011) Resonant Photoconductance of Molecular Junctions Formed in Gold Nanoparticle Arrays. *J. Chem. Soc.* 133(31):12185-12191.
10. Huang W, Masuda G, Maeda S, Tanaka H, & Ogawa T (2006) Molecular Junctions Composed of Oligothiophene Dithiol-Bridged Gold Nanoparticles Exhibiting Photoresponsive Properties. *Chem. Eur. J.* 12:607-619.
11. Nowak AM & McCreery RL (2004) In Situ Raman Spectroscopy of Bias-Induced Structural Changes in Nitroazobenzene Molecular Electronic Junctions. *J. Chem. Soc.* 126:16621-16631.
12. Richter CA, Hacker CA, & Richter LJ (2005) Electrical and Spectroscopic Characterization of Metal/Monolayer/Si Devices. *J. Phys. Chem. B.* 109:21836-21841.
13. Fereiro JA, McCreery RL, & Bergren AJ (2013) Direct Optical Determination of Interfacial Transport Barriers in Molecular Tunnel Junctions. *J. Chem. Soc.* 135(26):9584-9587.
14. Chamberlain GA (1983) Organic Solar Cells: A Review. *Solar cells.* 8:47-83.
15. Mahmoud AM, Bergren AJ, & McCreery RL (2009) Derivatization of Optically Transparent Materials with Diazonium Reagents for Spectroscopy of Buried Interfaces. *Anal. Chem.* 81(16):6972-6980.
16. Tang CW & Albrecht AC (1975) Photovoltaic Effects of Metal-Chlorophyll a-Metal Sandwich Cells. *J. Chem. Phys.* 62(6):2139-2149.
17. Kampas FJ & Gouterman M (1977) Porphyrin films. 3. Photovoltaic Properties of Octaethylporphine and Tetraphenylporphine. *J. Phys. Chem.* 81(8):690-695.

18. Merritt VY & Hovel HJ (1976) Organic Solar Cells of Hydroxy Squarylium. *Appl. Phys. Lett.* 29:414-415.
19. Fan FR & Faulkner LR (1978) Photovoltaic Effects of Metalfree and Zinc Phthalocyanines. 1. Dark Electrical Properties of Rectifying Cells. *J. Chem. Phys.* 69(7):3334-3340.
20. Schlenker CW & Thompson ME (2011) The Molecular Nature of Photovoltage Losses in Organic Solar Cells. *Chem. Commun.* 47:3702-3716.
21. Spanggaard H & Krebs FC (2004) A Brief History of the Development of Organic and Polymeric Photovoltaics. *Sol. Energy Mater. Sol. Cells.* 83:125-146.
22. Jain V, Rajbongshi BK, Mallajosyula AT, Bhattacharyja G, Iyer SK & Ramanathan G (2008) Photovoltaic Effect in Single-Layer Organic Solar Cell Devices Fabricated with Two new Imidazolin-5-one Molecules. *Sol. Energy Mater. Sol. Cells.* 92:1043-1046.
23. Tang CW (1986) Two Layer Organic Photovoltaic Cell. *App. Phys. Lett.* 48(2):183-185.
24. McGehee MC & Topinka MA (2006) Pictures from the Blended Zone. *Nat. Mater.* 5:675-676.
25. Bergren AJ, Harris KD, Deng F, & McCreery R (2008) Molecular Electronics using Diazonium-Derived Adlayers on Carbon with Cu Top Contacts: Critical Analysis of Metal Oxides and Filaments. *J. Phys. Condens. Matter.* 20:374117.
26. Bergren AJ, McCreery RL, Stoyanov SR, Gusarov S, & Kovalenko A (2010) Electronic Characteristics and Charge Transport Mechanisms for Large Area Aromatic Molecular Junctions. *J. Phys. Chem. C.* 114:15806-15815.
27. Anariba F & McCreery RL (2002) Electronic Conductance Behavior of Carbon-Based Molecular Junctions with Conjugated Structures. *J. Phys. Chem. B.* 106:10355-10362.

28. McGovern WR, Anariba F, & McCreery RL (2005) Importance of Oxides in Carbon/Molecule/Metal Molecular Junctions with Titanium and Copper Top Contacts. *J. Electrochem. Soc.* 152(5):E176-E183.
29. Sayed SY, Fereiro JA, Yan H, McCreery RL, & Bergren AJ (2012) Charge Transport in Molecular Electronic Junctions: Compression of the Molecular Tunnel Barrier in the Strong Coupling Regime. *Proc. Natl. Acad. Sci. U.S.A.* 109(29):11498-11503.
30. Ranganathan S, McCreery RL, Majji SM, & Madou M (2000) Photoresist-Derived Carbon for Microelectrochemical Applications. *J. Electrochem. Soc.* 147:277 - 282.
31. Yan H, Bergren AJ, & McCreery RL (2011) All-Carbon Molecular Tunnel Junctions. *J. Am. Chem. Soc.* 133(47):19168-19177.
32. Conwell EM (1996) Definition of Exciton Binding Energy for Conducting Polymers. *Synth. Met.* 83:101-102.
33. Yan H, Bergren AJ, McCreery RL, Della Rocca ML, Martin P, Lafarge P & Lacroix JC (2013) Activationless Charge Transport Across 4.5 to 22 nm in Molecular Electronic Junctions. *Proc. Natl. Acad. Sci. U.S.A.* 110(14):5326-5330.
34. Sayed SY, Bayat A, Kondratenko M, Leroux Y, Hapiot P & McCreery RL (2013) Bilayer molecular electronics: All-carbon Electronic Junctions containing Molecular Bilayers made with "Click" Chemistry. *J. Am. Chem. Soc.* 135:12972-12975.

## BIBLIOGRAPHY

1. Feynman R (1960) There's Plenty of Room at the Bottom. *Engineering and Science*. 23(5):22-36.
2. Aviram A & Ratner MA (1974) Molecular Rectifiers. *Chem. Phys. Lett.* 29(2):277-283.
3. Carroll RL & Gorman CB (2002) The Genesis of Molecular Electronics. *Angew. Chem. Int. Ed.* 41:4378-4400.
4. Binnig G & Rohrer H (1983) Scanning Tunneling Microscopy. *Surf. Sci.* 126:236-244.
5. Murray RW & Elliot CM (1976) Chemically Modified Electrodes. *Anal. Chem.* 48(8):1247-1254.
6. Murray RW (1980) Chemically Modified Electrodes. *Acc. Chem. Res.* 13:135-141.
7. Allara D & Nuzzo RG (1985) Spontaneously Organized Molecular Assemblies. 2. Quantitative Infrared Spectroscopic Determination of Equilibrium Structures of Solution-Adsorbed n-alkanoic Acids on an Oxidized Aluminum Surface. *Langmuir*. 1:52-66.
8. Porter MD, Bright TB, Allara DL, & Chidsey CED (1987) Spontaneously Organized Molecular Assemblies. 4. Structural Characterization of n-alkyl Thiol Monolayers on Gold by Optical Ellipsometry, Infrared Spectroscopy, and Electrochemistry. *J. Am. Chem. Soc.* 109(12):3559-3568.
9. McCreery RL & Bergren AJ (2009) Progress with Molecular Electronic Junctions: Meeting Experimental Challenges in Design and Fabrication. *Adv. Mater.* 21:4303-4322.
10. Cahen D, Haick H, Niitsoo O, & Ghabboun J (2007) Electrical Contacts to Organic Molecular Films by Metal Evaporation: Effect of Contacting Details. *J. Phys. Chem. C*. 111:2318-2329.

11. Wold DJ & Frisbie CD (2001) Fabrication and Characterization of Metal-Molecule-Metal Junctions by Conducting Probe Atomic Force Microscopy. *J. Am. Chem. Soc.* 123:5549.
12. Bumm LA, Arnold JJ, Dunbar TD, Allara DL, & Weiss PS (1999) Electron Transfer through Organic Molecules. *J. Phys. Chem.* 103(38):8122-8127.
13. Fan F-RF, Yang J, Cai L, Price DW, Dirk SM, Kosynkin DV, Yao Y, Rawlett AM, Tour JM & Bard AJ (2002) Charge Transport through Self-Assembled Monolayers of Compounds of Interest in Molecular Electronics. *J. Am. Chem. Soc.* 124(19):5550-5560.
14. Holmlin RE, Haag R, Chabinyc ML, Ismagilov RF, Cohen AE & Whitesides GM (2001) Electron Transport through Thin Organic Films in Metal-Insulator-Metal Junctions Based on Self-Assembled Monolayers. *J. Am. Chem. Soc.* 123:5075-5085.
15. Chabinyc ML, Holmiln RE, Jacobs H, Skulason H, Frisbie CD, Mujica V, Ratner MA, Rampi MA, Whitesides GM (2002) Molecular Rectification in a Metal-Insulator-Metal Junction Based on Self-Assembled Monolayers. *J. Am. Chem. Soc.* 124 11730-11736.
16. Chang S-C, Li Z, Lau CN, Larade B, & Williams RS (2003) Investigation of a Model Molecular-Electronic Rectifier with an Evaporated Ti-Metal Top Contact. *App. Phys. Lett.* 83(15):3198-3200.
17. Stewart DR, Ohlberg DAA, Beck PA, Stoddart JF (2004) Molecule-Independent Electrical Switching in Pt/Organic Monolayer/Ti Devices. *Nano Lett.* 4(1):133-136.
18. Ranganathan S, Steidel I, Anariba F, & McCreery RL (2001) Covalently Bonded Organic Monolayers on a Carbon Substrate: A New Paradigm for Molecular Electronics. *Nano Lett.* 1:491-494.

19. Anariba F & McCreery RL (2002) Electronic Conductance Behavior of Carbon-Based Molecular Junctions with Conjugated Structures. *J. Phys. Chem. B.* 106:10355-10362.
20. Ohtani H, Wilson RJ, Chiang S, & Mate CM (1988) Scanning Tunneling Microscopy Observations of Benzene Molecules on the Rh(111)-(3x3)(C<sub>6</sub>H<sub>6</sub>+2CO) Surface. *Phys. Rev. Lett.* 60(23):2398-2401.
21. Bain CD & Troughton EB (1989) Formation of Monolayers Films by Spontaneous Assembly of Organic Thiols from Solution onto Gold. *J. Am. Chem. Soc.* 111:321-335.
22. Laibinis PE, Whiteside GM, Parikh AN & Nuzzo R (1991) Comparison of the Structures and Wetting Properties of Self-assembled Monolayers of n-alkanethiols on the Coinage Metal Surfaces, Copper, Silver, and Gold. *J. Am. Chem. Soc.* 113(19):7152-7167.
23. Laibinis PE & Whitesides GM (1991) Attenuation of Photoelectrons in Monolayers of n-Alkanethiols Adsorbed on Copper, Silver and Gold. *J. Phys. Chem.* 95:7017-7021.
24. Li Z, Chang S-C, & Williams RS (2003) Self-Assembly of Alkanethiol Molecules onto Platinum and Platinum Oxide Surfaces. *Langmuir.* 19(17):6744-6749.
25. Love JC, Wolfe DB, Haasch R, Chabinyc ML, Paul KE, Whitesides GM & Nuzzo RG (2003) Formation and Structure of Self-Assembled Monolayers of Alkanethiolates on Palladium. *J. Am. Chem. Soc.* 125:2597-2609.
26. Magnussen OM, Ocko BM, Deutsch M, Regan MJ, Pershan PS, Abernathy D & Legrand JF (1996) Self-assembly of Organic Films on a Liquid Metal. *Nature.* 384:6606.
27. Baum T, Ye S, & Uosaki K (1999) Formation of Self-Assembled Monolayers of Alkanethiols on GaAs Surface with in Situ Surface Activation by Ammonium Hydroxide. *Langmuir.* 15(25):8577-8579.

28. Schwartzman M, Sidorov V, Ritter D, & Paz Y (2003) Passivation of InP Surfaces of Electronic Devices by Organothiolyated Self-Assembled Monolayers. *J Vac Sci Technol B: Microelectron Nanometer Struct Process Meas Phenom.* 21(1):148-155.
29. Nuzzo RG & Allara DL (1983) Adsorption of Bifunctional Organic Disulfides on Gold Surfaces. *J. Am. Chem. Soc.* 105:4481-4483.
30. Ulman A (1991) An Introduction to Ultrathin Organic Films From Langmuir-Blodgett to Self-Assembly (Academic Press, San Diego, CA) 1st Ed.
31. Schreiber F, Eberhardt A, Schwartz LP, Wetterer SM, Lavrich DJ, Berman L & Scholes G (1998) Adsorption Mechanisms, Structures, and Growth Regimes of an Archetypal Self-Assembling System: Decenethiol on Au(111). *Phys. Rev. B.* 57(19):12476-12481.
32. Nitzan A & Ratner MA (2003) Electron Transport in Molecular Wire Junctions. *Science.* 300:1384-1389.
33. Xue Y, Datta S, & Ratner MA (2001) Charge Transfer and 'Band Lineup' in Molecular Electronic Devices: A Chemical and Numerical Interpretation. *J. Chem. Phys.* 115:4292-4299.
34. Love JC, Estroff LA, Kriebel JK, Nuzzo RG, & Whitesides GM (2005) Self-Assembled Monolayers of Thiolates on Metals as a Form of Nanotechnology. *Chem. Rev.* 105:1103-1170.
35. Fisher GL, Walker AV, Hooper AE, Opila RL & Allara DL (2002) Bond Insertion, Complexation, and Penetration Pathways of Vapor-Deposited Aluminum Atoms HO- and CH<sub>3</sub>O-Terminated Organic Monolayers. *J. Am. Chem. Soc.* 124:5528-5541.

36. Walker AV, Tighe TB, Cabarcos OM, Reinard MD, Brendan C, Uppili Sundararajan & Allara DL (2004) The Dynamics of Noble Metal Atom Penetration through Methoxy-Terminated Alkanethiolate Monolayers. *J. Am. Chem. Soc.* 126(12):3954-3963.
37. Silerova R & Gyepi-Garbrah SH (2001) Probing Temperature-Dependent Behavior in Self-Assembled Monolayers by AC-Impedance Spectroscopy. *Phys. Chem. Chem. Phys.* 3:2117-2123.
38. McCreery RL (2008) Advanced Carbon Electrode Materials for Molecular Electrochemistry. *Chem. Rev.* 108(7):2646-2687.
39. Delamar M, Hitmi R, Pinson J, & Saveant JM (1992) Covalent Modification of Carbon Surfaces by Grafting of Functionalized Aryl Radicals Produced from Electrochemical Reduction of Diazonium Salts. *J. Am. Chem. Soc.* 114: 5883-5884.
40. Barbier B, Pinson J, Desarmot G, & Sanchez M (1990) Electrochemical Bonding of Amines to Carbon Fiber Surfaces Toward Improved Carbon-Epoxy Composites. *J. Electrochem. Soc.* 137(6):1757.
41. Knickerbocker T, Strother T, Schwartz MP, Russell, Smith LM & Hamers RJ (2003) DNA-Modified Diamond Surfaces. *Langmuir.* 19(6):1938-1942.
42. Ranganathan S, McCreery RL, Majji SM, & Madou M (2000) Photoresist-Derived Carbon for Microelectrochemical Applications. *J. Electrochem. Soc.* 147:277 - 282.
43. Bergren AJ, Harris KD, Deng F, & McCreery R (2008) Molecular Electronics using Diazonium-Derived Adlayers on Carbon with Cu Top Contacts: Critical Analysis of Metal Oxides and Filaments. *J. Phys. Condens. Matter.* 20:374117.

44. Mahmoud AM, Bergren AJ, Pekas N, & McCreery RL (2011) Towards Integrated Molecular Electronic Devices: Characterization of Molecular Layer Integrity during Fabrication Processes. *Adv. Funct. Mater.* 21(12):2273-2281.
45. Mahmoud AM, Bergren AJ, & McCreery RL (2009) Derivatization of Optically Transparent Materials with Diazonium Reagents for Spectroscopy of Buried Interfaces. *Anal. Chem.* 81(16):6972-6980.
46. Kumar R, Yan H, McCreery RL, & Bergren AJ (2011) Electron-Beam Evaporated Silicon as a Top Contact for Molecular Electronic Device Fabrication. *Phys. Chem. Chem. Phys.* 13:14318-14324.
47. Yan H, Bergren AJ, & McCreery RL (2011) All-Carbon Molecular Tunnel Junctions. *J. Am. Chem. Soc.* 133(47):19168-19177.
48. Bergren AJ, McCreery RL, Stoyanov SR, Gusarov S, & Kovalenko A (2010) Electronic Characteristics and Charge Transport Mechanisms for Large Area Aromatic Molecular Junctions. *J. Phys. Chem. C.* 114:15806-15815.
49. Hamers RJ, Coulter SK, Ellison MD, Hovis JS, Padowitz DF & Schwartz MP (2000) Cycloaddition Chemistry of Organic Molecules with Semiconductor Surfaces. *Acc. Chem. Res.* 33(9):617-624.
50. Reed MA, Zhou C, Muller CJ, Burgin TP, & Tour JM (1997) Conductance of a Molecular Junction. *Science.* 278:252.
51. Salomon A, Cahen D, Lindsay S, Tomfohr J, Engelkes VB, Frisbie CD (2003) Comparison of Electronic Transport Measurements on Organic Molecules. *Adv. Mater.* 15(22):1881-1890.

52. Kim B, Beebe JM, Olivier C, Rigaut S, Touchard D, Kushmerick JG, Zhu XY and Frisbie CD (2007) Temperature and Length Dependence of Charge Transport in Redox-Active Molecular Wires Incorporating Ruthenium(II) Bis(s-arylacetylide) Complexes. *J. Phys. Chem. C*.111:7521-7526.
53. Haiss W, Zalinge HV, Higgins SJ, Bethell D, Hobenreich H, Cahen D & Nichols RJ (2003) Redox State Dependence of Single Molecule Conductivity. *J. Am. Chem. Soc.* 125(50):15294-15295.
54. Sedghi G, Sawada K, Esdaile LJ, Hoffmann M, Anderson HL, Bethell D, Haiss W, Higgins SJ & Nichols RJ (2008) Single Molecule Conductance of Porphyrin Wires with Ultralow Attenuation. *J. Am. Chem. Soc.* 130(27):8582-8583.
55. Cui XD, Primak A, Zarate X, Tomhofer J, Sankey OF, Moore AL, Gust D, Harris G, Lindsay SM (2001) Reproducible Measurement of Single-Molecule Conductivity. *Science*. 294:571-574.
56. Kim, Beebe JM, Jun Y, Zhu XY, & Frisbie CD (2006) Correlation between HOMO Alignment and Contact Resistance in Molecular Junctions: Aromatic Thiols versus Aromatic Isocyanides. *J. Am. Chem. Soc.* 128(15):4970-4971.
57. McCreery RL (2009) Electron Transport and Redox Reactions in Molecular Electronic Junctions. *ChemPhysChem*. 10(14):2387-2391.
58. McCreery RL (2004) Molecular Electronic Junctions. *Chem. Mater.* 16:4477-4496.
59. Simmons JG (1971) *DC Conduction in Thin Films* (Mills and Boon Ltd., London).
60. Yamamoto H & Waldeck DH (2002) Effect of Tilt-Angle on Electron Tunneling through Organic Monolayer Films. *J. Phys. Chem. B*. 106(30):7469-7473.

61. Skourtis SS, Archontis G, & Xie Q (2001) Electron Transfer Through Fluctuating Bridges: On the Validity of the Superexchange Mechanism and Time-Dependent Tunneling Matrix Elements. *J. Chem. Phys.* 115(20):9444-9462.
62. Galperin M, Segal D, & Nitzan A (1999) Perturbation Theory Approach to Tunneling: Direct and Resonance Transmission in Superexchange Models. *J. Chem. Phys.* 111(4):1569-1579.
63. Mujica V & Ratner MA (2001) Current-Voltage Characteristics of Tunneling Molecular Junctions for Off-Resonance Injection. *Chem. Phys.* 264(3):365-370.
64. Mujica V, Roitberg AE, & Ratner M (2000) Molecular Wire Conductance: Electrostatic Potential Spatial Profile. *J. Chem. Phys.* 112(15):6834-6839.
65. Meggers E, Michel-Beyerle ME, & Giese B (1998) Sequence Dependent Long Range Hole Transport in DNA. *J. Am. Chem. Soc.* 120:12950-12955.
66. Cordes M & Giese B (2009) Electron Transfer in Peptides and Proteins. *Chem. Soc. Rev.* 38:892-901.
67. Segal D, Nitzan A, Davis WB, Wasielewski MR, & Ratner MA (2000) Electron Transfer Rates in Bridged Molecular Systems 2. A Steady-State Analysis of Coherent Tunneling and Thermal Transitions. *J. Phys. Chem. B.* 104(16):3817-3829.
68. Buttiker M & Landauer R (1982) Traversal Time for Tunneling. *Phys. Rev. Lett.* 49:1739.
69. Hwang J, Wan A, & Kahn A (2009) Energetics of Metal-Organic Interfaces: New Experiments and Assessment of the Field. *Mater. Sci. Eng. R-Rep.* 64:1-31.
70. Cahen D & Kahn A (2003) Electron Energetics at Surfaces and Interfaces: Concepts and Experiments. *Adv. Mater.* 15(4):271-277.

71. Cahen D, Kahn A, & Umbach E (2005) Energetic of Molecular Interfaces. *Mater. Today*. 8(7):32-41.
72. Salomon A, Bocking T, Gooding JJ, & Cahen D (2006) How Important Is the Interfacial Chemical Bond for Electron Transport through Alkyl Chain Monolayers? *Nano Lett.* 6(12):2873-2876.
73. Ishii H, Sugiyama K, Ito E, & Seki K (1999) Energy Level Alignment and Interfacial Electronic Structures at Organic/Metal and Organic/Organic Interfaces. *Adv. Mater.* 11(8):605-625.
74. Seki K & Ishii H (1998) Photoemission Studies of Functional Organic Materials and their Interfaces. *J. Electron. Spectros. Rel. Phenom.* 88-91:821-830.
75. Ishii H & Seki K (1997) Energy Level Alignment at Organic/Metal Interfaces Studied by UV Photoemission: Breakdown of Traditional Assumption of a Common Vacuum Level at the Interface. *IEEE. Electr. Device. L.* 44(8):1295-1301.
76. Hill IG & Kahn A (1998) Energy Level Alignment at Interfaces of Organic Semiconductor Heterostructures. *J. Appl. Phys.* 84(10):5583-5586.
77. Rhoderick EA & Williams RH (1998) *Metal-Semiconductor Contacts*. (2nd edition, Clarendon, Oxford).
78. Shen C & Kahn A (2001) The Role of Interface States in Controlling the Electronic Structure of Alq<sub>3</sub>/Reactive Metals Contacts. *Org. Electron.* 2:89-95.
79. Wan AS-C (2006) *Electrical engineering, vol. Ph.D.*, (Princeton University, Princeton).
80. Schalf R ( <http://rsl.eng.usf.edu/Documents/Tutorials/TutorialsWorkFunction.pdf>).
81. Woodruff DP & Delchar TA (1986) *Modern Techniques of Surface Science* (Cambridge University Press, Cambridge 1986).

82. Wandelt K (1987) *Thin Metal Films and Gas Chemisorption* (Elsevier, Amsterdam 1987).
83. Lang N & Kohn W (1970) Theory of Metal Surfaces: Charge Density and Surface Energy. *Phys. Rev. B.* 1(12):4555-4568.
84. Lang ND & Kohn W (1971) Theory of Metal Surfaces: Work Function. *Phys. Rev. B.* 3(4):1215-1223.
85. William R, Seki K, Kahn A & Pireaux JJ (2001) *Conjugated Polymer and Molecular Interfaces* (Marcel Dekker, Inc).
86. Hoffman R (1989) *Solids and Surfaces* (VCH NewYork, Inc).
87. Gensterblum G, Pireaux JJ, Thiry PA, Caudano R, Vigneron JP, Lambin PH & Lucas AA (1991) High-Resolution Electron-Energy-Loss Spectroscopy of Thin Films of C60 on Si(100). *Phys. Rev. Lett.* 67(16):2171-2174.
88. Wu CI, Hirose Y, Sirringhaus H, & Kahn A (1997) Electron-hole Interaction Energy in the Organic Molecular Semiconductor PTCDA. *Chem. Phys. Lett.* 272(1-2):43-47.
89. Weaver JH & Poirier DM (1994) *Solid State Physics* (Academic, NewYork).
90. Zhu XY (2002) Electron Transfer at Molecule-Metal Interfaces: A Two-Photon Photoemission Study. *Annu. Rev. Phys. Chem.* 53:221-247.
91. Probst M & Haight R (1997) Unoccupied Molecular Orbital States of Tris (8-hydroxy quinoline) Aluminum: Observation and Dynamics. *Appl. Phys. Lett.* 71(2):202-204.
92. Zhu XY (2004) Electronic Structure and Electron Dynamics at Molecule-Metal Interfaces: Implications for Molecule-Based Electronics. *Surf. Sci. Rep.* 56(1-2):1-83.

93. Taborski J, Vaterlein P, Deitz H, Zimmermann U, & Umbach E (1995) NEXAFS Investigation on Ordered Adsorbate Layers of Large Aromatic Molecules. *J. Electron. Spectrosc. Relat. Phenom.* 75:129-147.
94. Lua L, Choi SH, & Frisbie CD (2011) Probing Hopping Conduction in Conjugated Molecular Wires Connected to Metal Electrodes. *Chem Mater.* 23(3):631-645.
95. Siebbeles LDA & Grozema FC eds (2011) *Charge and Exciton Transport through Molecular Wires* (Wiley-VCH, Weinheim, Germany).
96. Kim B, Choi SH, X.-Y.Zhu, & Frisbie CD (2011) Molecular Tunnel Junctions Based on  $\pi$ -Conjugated Oligoacene Thiols and Dithiols between Ag, Au, and Pt Contacts: Effect of Surface Linking Group and Metal Work Function. *J. Am. Chem. Soc.* 133(49):19864-19877.
97. Yan H, Bergren AJ, & McCreery RL (2011) All Carbon Molecular Tunnel Junctions. *J. Am. Chem. Soc.* 133(47):19168-19177.
98. Venkataraman L, Klare JE, Nuckolls CD, Hybertsen MS, & Steigerwald ML (2006) Dependence of Single-Molecule Junction Conductance on Molecular Conformation. *Nature.* 442(24):904-907.
99. Bonifas AP & McCreery RL (2010) "Soft" Au, Pt and Cu Contacts for Molecular Junctions through Surface-Diffusion-Mediated Deposition. *Nat. Nanotechnol.* 5(8):612-617.
100. Bonifas AP & McCreery RL (2011) Assembling Molecular Electronic Junctions One Molecule at a Time. *Nano Lett.* 11(11):4725-4729.
101. Dell'Angela M, *et al.* (2010) Relating Energy Level Alignment and Amine-Linked Single Molecule Junction Conductance. *Nano Lett.* 10:2470-2474.

102. Neshet G, Vilan A, Cohen H, Cahen D, Amy F, Chan C, Hwang J & Kahn A (2006) Energy Level and Band Alignment for GaAs-Alkylthiol Monolayer-Hg Junctions from Electrical Transport and Photoemission Experiments. *J. Phys. Chem. B.* 110:14363-14371.
103. Yan H & McCreery RL (2009) Anomalous Tunneling in Carbon/Alkane/TiO<sub>2</sub>/Gold Molecular Electronic Junctions: Energy Level Alignment at the Metal/Semiconductor Interface. *ACS Appl. Mater. Interfaces.* 1(2):443-451.
104. Anariba F, Steach JK, & McCreery RL (2005) Strong Effects of Molecular Structure on Electron Transport in Carbon/Molecule/Copper Electronic Junctions. *J. Phys. Chem. B* 109(22):11163-11172.
105. McGovern WR, Anariba F, & McCreery RL (2005) Importance of Oxides in Carbon/Molecule/Metal Molecular Junctions with Titanium and Copper Top Contacts. *J. Electrochem. Soc.* 152(5):E176-E183.
106. Ranganathan S, Steidel I, Anariba F, & McCreery RL (2001) Covalently Bonded Organic Monolayers on a Carbon Substrate: A New Paradigm for Molecular Electronics. *Nano Lett.* 1(9):491-494.
107. Itoh T & McCreery RL (2002) In Situ Raman Spectroelectrochemistry of Electron Transfer between Glassy Carbon and a Chemisorbed Nitroazobenzene Monolayer. *J. Am. Chem. Soc.* 124:10894-10902.
108. Tian H, Bergren AJ, & McCreery RL (2007) Ultraviolet-Visible Spectroelectrochemistry of Chemisorbed Molecular Layers on Optically Transparent Carbon Electrodes. *Appl. Spectrosc.* 61(11):1246-1253.

109. Ranganathan S & McCreery RL (2001) Electroanalytical Performance of Carbon Films with Near-Atomic Flatness. *Anal. Chem.* 73:893-900.
110. Liu Y-C & McCreery RL (1997) Raman Spectroscopic Determination of the Structure and Orientation of Organic Monolayers Chemisorbed on Carbon Electrode Surfaces. *Anal. Chem.* 69:2091.
111. Solak AO, Eichorst LR, Clark WJ, & McCreery RL (2003) Modified Carbon Surfaces as "Organic Electrodes" that Exhibit Conductance Switching. *Anal. Chem.* 75:296-305.
112. Bergren AJ & McCreery RL (2011) Analytical Chemistry in Molecular Electronics. *Annu. Rev. Anal. Chem.* 4(1):173-195.
113. Qi Y, Yaffe O, Tirosh E, Vilan A, Cahen D & Kahn A (2011) Filled and empty states of alkanethiol monolayer on Au (111): Fermi level Asymmetry and Implications for Electron Transport. *Chem. Phys. Lett.* 511(4-6):344-347.
114. Majumdar A, Reddy P, Jang S-Y, & Segalman RA (2007) Thermoelectricity in Molecular Junctions. *Science.* 315:1568-1571.
115. Kahn A, Koch N, & Gao W (2003) Electronic Structure and Electrical Properties of Interfaces between Metals and  $\pi$ -Conjugated Molecular Films. *J. Polymer Sci.: Part B: Polymer Phys.* 41:2529-2948.
116. Lindberg B, Svensson S, malmquist PA, Basilier E, Gelius U & Siegbahn K (1976) Correlation of ESCA Shifts and Hammett Substituent Constants in Substituted Benzene Derivatives. *Chem. Phys. Lett.* 40(2):175-179.
117. Anariba F, DuVall SH, & McCreery RL (2003) Mono- and Multilayer Formation by Diazonium Reduction on Carbon Surfaces Monitored with Atomic Force Microscopy "Scratching". *Anal. Chem.* 75:3837-3844.

118. Anariba F, Viswanathan U, Bocian DF, & McCreery RL (2006) Determination of the Structure and Orientation of Organic Molecules Tethered to Flat Graphitic Carbon by ATR-FT-IR and Raman Spectroscopy. *Anal. Chem.* 78:3104-3112.
119. Salomon A, Cahen D, Lindsay S, Tomfohr J, Engelkes VB & Frisbie CD (2003) Comparison of Electronic Transport Measurement on Organic Molecules. *Adv. Mater.* 15(22):1881-1890.
120. Choi SH, Kim B, & Frisbie CD (2008) Electrical Resistance of Long Conjugated Molecular Wires. *Science.* 320:1482-1486.
121. Liu H, Wang N, Zhao J, Guo Y, Yin X, Boey FY & Zhang H (2008) Length-Dependent Conductance of Molecular Wires and Contact Resistance in Metal-Molecule-Metal Junctions. *ChemPhysChem.* 9:1416-1424.
122. Simmons JG (1963) Generalized Formula for the Electric Tunnel Effect between Similar Electrodes Separated by a Thin Insulating Film. *J. Appl. Phys.* 34(6):1793-1803.
123. Huisman EH, Guedon CM, Wees BJv, & Molen SJvd (2009) Interpretation of Transistion Voltage Spectroscopy. *Nano Lett.* 9(11):3909-3913.
124. Engelkes VB, Beebe JM, & Frisbie CD (2004) Length-Dependent Transport in Molecular Junctions Based on SAMs of Alkanethiols and Alkanedithiols: Effect of Metal Work Function and Applied Bias on Tunneling Efficiency and Contact Resistance. *J. Am. Chem. Soc.* 126:14287-14296.
125. Kock N & Vollmer A (2006) Electrode-molecular Semiconductor Contacts: Work-Function-Dependent Hole Injection Barriers versus Fermi-Level Pinning. *Appl. Phys. Lett.* 89:162107.

126. Ivanco J, Netzer FP, & Ramsey MG (2007) On Validity of the Schottky-Mott Rule in Organic Semiconductors: Sexithiophene on Various Substrates. *J. Appl. Phys.* 101:103712.
127. Yan L, Watkins NJ, Zorba S, Gao Y, & Tang CW (2001) Direct Observation of Fermi-Level Pinning in Cs-doped CuPc Film. *Appl. Phys. Lett.* 79(25):4148-4150.
128. Yan L, Watkins NJ, Zorba S, Gao Y, & Tang CW (2002) Thermodynamic Equilibrium and Metal-Organic Interface Dipole. *Appl. Phys. Lett.* 81(15):2752-2754.
129. Chen J, Markussen T, & Thygesen KS (2010) Quantifying Transition Voltage Spectroscopy of Molecular Junctions: Ab initio Calculations. *Phys. Rev. B.* 82:121412(R).
130. Heimel G, Romaner L, Bredas J-L, & Zojer E (2008) Odd-Even Effects in Self-Assembled Monolayers of w-(Biphenyl-4-yl)alkanethiols: A First-Principles Study. *Langmuir.* 24:474-482.
131. Garcia-Lastra JM, Rostgaard C, Rubio A, & Thygesen KS (2009) Polarization-Induced Renormalization of Molecular Levels at Metallic and Semiconducting Surfaces. *Phys. Rev. B.* 80:245427.
132. Zhong S, Zhong JQ, Mao HY, Zhang JL, Lin JD & Chen W (2012) The Role of Gap States in the Energy Level Alignment at the Organic-Organic Heterojunction Interfaces. *Phys. Chem. Chem. Phys.* 14:14127-14141.
133. Braun S, Salaneck WR, & Fahlman M (2009) Energy-Level Alignment at Organic/Metal and Organic/Organic Interfaces. *Adv. Mater.* 21(14-15):1450-1472.

134. Sayed SY, Fereiro JA, Yan H, McCreery RL, & Bergren AJ (2012) Charge Transport in Molecular Electronic Junctions: Compression of the Molecular Tunnel Barrier in the Strong Coupling Regime. *Proc. Natl. Acad. Sci. U.S.A.* 109(29):11498-11503.
135. Powell R (1970) Interface Barrier Energy Determination from Voltage Dependence of Photoinjected Currents. *J. Appl. Phys.* 41(6):2424.
136. Gundlach KH & Kadlec J (1975) Interfacial Barrier Height Measurement from Voltage Dependence of Photocurrent. *J. Appl. Phys.* 46(12):5286-5287.
137. DiMaria DJ & Arnett PC (1975) Hole Injection into Silicon Nitride: Interface Barrier Energies by Internal Photoemission. *Appl. Phys. Lett.* 26(12):711-713.
138. Goodman AM (1970) Photoemission of Holes and Electrons from Aluminum into Aluminum Oxide. *J. Appl. Phys.* 41(5):2176-2179.
139. Deal BE & Snow EH (1966) Barrier Energies in Metal-Silicon Dioxide-Silicon Structures. *J. Phys. Chem. Solids.* 27:1873-1879.
140. Kovacs DA, Winter J, Meyer S, Wucher A, & Diesing D (2007) Photo and Particle Induced Transport of Excited Carriers in Thin Film Tunnel Junctions. *Phys. Rev. B.* 76(23):235408.
141. Campbell IH & Smith DL (2002) Metal-Organic Schottky Energy Barriers: Measurements and Device Implications. *Conjugated Polymer and Molecular Interfaces: Science and Technology for Photonic and Optoelectronic Applications*, eds Salaneck WR, Seki K, Kahn A, & Pireaux J-J (Marcel Dekker, New York), pp 693-732.
142. Galperin M & Nitzan A (2012) Molecular Optoelectronics: The Interactions of Molecular Conduction Junctions with Light. *Phys. Chem. Chem. Phys.* 14:9421-9438.

143. Mangold MA, Calame M, Mayor M, & Holleitner AW (2011) Resonant Photoconductance of Molecular Junctions Formed in Gold Nanoparticle Arrays. *J. Am. Chem. Soc.* 133:12185-12191.
144. Huang W, Masuda G, Maeda S, Tanaka H, & Ogawa T (2006) Molecular Junctions Composed of Oligothiophene Dithiol-Bridged Gold Nanoparticles Exhibiting Photoresponsive Properties. *Chem. Eur. J.* 12:607-619.
145. Battacharyya S, Kibel A, Kodis G, Liddell PA, Gervado M, Gust D & Lindsay S (2011) Optical Modulation of Molecular Conductance. *Nano Lett.* 11:2709-2714.
146. Choi SH, Kim B, & Frisbie CD (2008) Electrical Resistance of Long Conjugated Molecular Wires. *Science.* 320(5882):1482-1486.
147. Choi SH, Kim B, & Frisbie CD (2010) Transition from Tunneling to Hopping Transport in Long, Conjugated Oligo-imine Wires Connected to Metals. *J. Am. Chem. Soc.* 132(12):4358-4368.
148. Salomon A, Boecking T, Seitz O, Markus T, Amy F, Chan C, Cahen D & Kahn A (2007) What is the Barrier for Tunneling Through Alky Monolayers? Results from n- and p--Si-Alkyl/Hg Junctions. *Adv. Mater.* 19:445-450.
149. McCreery RL, Yan H, & Bergren AJ (2013) A Critical Perspective on Molecular Electronic Junctions: There is Plenty of Room in the Middle. *Phys. Chem. Chem. Phys.* 15(4):1065-1081.
150. Afanas'ev VV (2008) *Internal Photoemission Spectroscopy: Principles and Applications* (Elsevier, London).
151. Goodman AM (1966) Photoemission of Holes from Silicon into Silicon Dioxide. *Phys. Rev.* 152(2):780-784.

152. Gundlach KH (1971) Logarithmic Conductivity of Al/Al<sub>2</sub>O<sub>3</sub>/Al Tunneling Junctions Produced by Plasma and by Thermal Oxidation. *Surf. Sci.* 27(1):125-141.
153. Deinhammer RS, Ho M, Anderegg JW, & Porter MD (1994) Electrochemical Oxidation of Amine-Containing Compounds: A Route to the Surface Modification Glassy Carbon Electrodes. *Langmuir.* 10:1306-1313.
154. Donner S, Li HW, Yeung ES, & Porter MD (2006) Fabrication of Optically Transparent Carbon Electrodes by the Pyrolysis of Photoresist Films: Approach to Single-Molecule Spectroelectrochemistry. *Anal. Chem.* 78(8):2816-2822.
155. Lee CH, Yu G, & Heeger AJ (1993) Persistent Photoconductivity in poly(p-phenylenevinylene): Spectral Response and Slow Relaxation. *Phys. Rev. B.* 47(23):15543-15553.
156. Sze SM (1981) *Physics of Semiconductor Devices* (Wiley, New York) 2nd Edition Ed.
157. Fereiro JA, McCreery RL, & Bergren AJ (2013) Direct Optical Determination of Interfacial Transport Barriers in Molecular Tunnel Junctions. *J. Chem. Soc.* 135(26):9584-9587.
158. Yaffe O, Qi Y, Scheres L, Reddy S, Segev L, Ely T, Haick H, Vilan A, Kronik L, Kahn A & Cahen D. (2012) Charge Transport Across Metal/Molecular (alkyl) Monolayer-Si Junctions is Dominated by the LUMO Level. *Phys. Rev. B.* 85:045433.
159. Malen JA, Doak P, Baheti K, Tilley TD, Segalman RA & Majumdar A (2009) Identifying the Length Dependence of Orbital Alignment and Contact Coupling in Molecular Heterojunctions. *Nano Lett.* 9(3):1164-1169.

160. Niskala JR, Rice WC, Bruce RC, Merkel TJ, Tsui F & You W (2012) Tunneling Characteristics of Au–Alkanedithiol–Au Junctions formed via nanoTransfer Printing (nTP). *J. Am. Chem. Soc.* 134:12072-12082.
161. Wang G, Kim T-W, Jo G, & Lee T (2009) Enhancement of Field Emission Transport by Molecular Tilt Configuration in Metal-Molecule-Metal Junctions. *J. Am. Chem. Soc.* 131:5980-5985.
162. Li X, He J, Hihath J, Xu B, Lindsay SM & Tao NJ (2006) Conductance of Single Alkanedithiols: Conduction Mechanism and Effect of Molecule-Electrode Contacts. *J. Am. Chem. Soc.* 128:2135-2141.
163. Segev L, Salomon A, Natan A, Cahen D, & Kronik L (2006) Electronic Structure of Si(111)-bound Alkyl Monolayers: Theory and Experiment. *Phys. Rev. B.* 74:165323.
164. Huynh WU, Dittmer JJ, Teclmariam N, Milliron DJ, & Alivisatos AP (2003) Charge Transport in Hybrid Nanorod-Polymer Composite Photovoltaic Cells. *Phys. Rev. B.* 67:115326.
165. Taylor JR (1997) *An Introduction to Error Analysis: The Study of Uncertainties in Physical Measurements* (University Science Books, Sausalito, California) 2nd Ed.
166. Metzger R (2007) Unimolecular Electronics. *Nano and Molecular Electronics Handbook*, Nano and Microengineering Series, (CRC Press).
167. Tour JM (2000) Molecular Electronics, Synthesis and Testing of Components. *Acc. Chem. Res.* 33:791-804.
168. Ward DR, Halas NJ, Ciszek JW, Tour JM, Wu Y, Norlander P & Natelson D (2008) Simultaneous Measurements of Electronic Conduction and Raman Response in Molecular Junctions. *Nano Lett.* 8(3):919-924.

169. Liu Z, Ding SY, Chen ZB, wang X, Tian JH, Anema JR, Zhou XS, Wu DY, Mao BW, Xu X, Ren B & Tian QZ (2011) Revealing the Molecular Structure of Single-Molecule Junctions in Different Conductance States by Fishing-Mode Tip-Enhanced Raman Spectroscopy. *Nat. Commun.* 2:305.
170. Mangold MA, Calame M, Mayor M, & Holleitner AW (2011) Resonant Photoconductance of Molecular Junctions Formed in Gold Nanoparticle Arrays. *J. Chem. Soc.* 133(31):12185-12191.
171. Nowak AM & McCreery RL (2004) In Situ Raman Spectroscopy of Bias-Induced Structural Changes in Nitroazobenzene Molecular Electronic Junctions. *J. Chem. Soc.* 126:16621-16631.
172. Richter CA, Hacker CA, & Richter LJ (2005) Electrical and Spectroscopic Characterization of Metal/Monolayer/Si Devices. *J. Phys. Chem. B.* 109:21836-21841.
173. Chamberlain GA (1983) Organic Solar Cells: A review. *Solar cells.* 8:47-83.
174. Tang CW & Albrecht AC (1975) Photovoltaic Effects of Metal-Chlorophyll a-Metal Sandwich Cells. *J. Chem. Phys.* 62(6):2139-2149.
175. Kampas FJ & Gouterman M (1977) Porphyrin films. 3. Photovoltaic Properties of Octaethylporphine and Tetraphenylporphine. *J. Phys. Chem.* 81(8):690-695.
176. Merritt VY & Hovel HJ (1976) Organic Solar Cells of Hydroxy Squarylium. *Appl. Phys. Lett.* 29:414-415.
177. Fan FR & Faulkner LR (1978) Photovoltaic Effects of Metal free and Zinc Phthalocyanines. 1. Dark Electrical Properties of Rectifying Cells. *J. Chem. Phys.* 69(7):3334-3340.

178. Schlenker CW & Thompson ME (2011) The Molecular Nature of Photovoltage losses in Organic Solar Cells. *Chem. Commun.* 47:3702-3716.
179. Spanggaard H & Krebs FC (2004) A Brief History of the Development of Organic and Polymeric Photovoltaics. *Sol. Energy Mater. Sol. Cells.* 83:125-146.
180. Jain V, Rajbongshi BK, Mallajosyula AT, Bhattacharyya G, Iyer SK & Ramanathan G (2008) Photovoltaic Effect in Single-Layer Organic Solar Cell Devices Fabricated with two new Imidazolin-5-one Molecules. *Sol. Energy Mater. Sol. Cells.* 92:1043-1046.
181. Tang CW (1986) Two Layer Organic Photovoltaic Cell. *App. Phys. Lett.* 48(2):183-185.
182. McGehee MC & Topinka MA (2006) Pictures from the Blended Zone. *Nat. Mater.* 5:675-676.
183. Conwell EM (1996) Definition of Exciton Binding Energy for Conducting Polymers. *Synth. Met.* 83:101-102.
184. Yan H, Bergren AJ, & McCreery RL (2013) Activationless Charge Transport Across 4.5 to 22 nm in Molecular Electronic Junctions. *Proc. Natl. Acad. Sci. U.S.A.* 110(14):5326-5330.
185. Sayed SY, Bayat A, Kondratenko M, Leroux Y, Hapiot P & McCreery RL (2013) Bilayer molecular electronics: All-carbon Electronic Junctions containing Molecular Bilayers made with "Click" Chemistry. *J. Am. Chem. Soc.* 135:12972-12975.
186. Spicer WE, Lindau I, Gregory PE, Garner CM, Pianetta P & Chye PW (1976) Synchrotron Radiation Studies of Electronic Structure and Surface Chemistry of GaAs, GaSb, and InP. *J. Vac. Sci. Technol. A* 13(4):780-785.

187. Choong VE, Mason MG, Tang CW, & Gao Y (1998) Investigation of the Interface Formation between Calcium and tris-(8-hydroxy quinoline) Aluminum. *Appl. Phys. Lett.* 72(21):2689-2691.
188. Heine V (1965) Theory of Surface States. *Phys. Rev.* 138(6A):A1689-A1696.
189. Louie SG & Cohen H (1976) Electronic Structure of a Metal-Semiconductor Interface. *Phys. Rev. B* 13(6):2461-2469.
190. Vazquez H, Flores F, Oszwaldowski R, Ortega J, Perez R & Kahn A (2004) Dipole Formation at Metal/PTCDA Interfaces: Role of the Charge Neutrality Level. *EuroPhys. Lett* 65(6):802.